KU LEUVEN

ARENBERG DOCTORAL SCHOOL
Faculty of Engineering Science

Non-rigid image registration for the assessment of myocardial deformation from 3D echocardiography

Brecht Heyde

Dissertation presented in partial
fulfillment of the requirements for the
degree of Doctor in Engineering Science

December 2013

Non-rigid image registration for the assessment of myocardial deformation from 3D echocardiography

Brecht Heyde

Jury:
Prof. dr. ir. Willy Sansen, chair
Prof. dr. Jan D'hooge, supervisor
Prof. dr. ir. Frederik Maes, co-supervisor
Prof. dr. ir. Paul Suetens
Prof. dr. ir. Dirk Vandermeulen
dr. ir. Dirk Loeckx (icoMetrix, Belgium)
Prof. dr. Piet Claus
Prof. dr. Frank Rademakers
Prof. dr. ir. Daniel Rueckert
(Imperial College London, United Kingdom)
Prof. dr. Knut Matre
(University of Bergen, Norway)

Dissertation presented in
partial fulfillment of the
requirements for the degree of
Doctor in Engineering Science

December 2013

Uitgegeven in eigen beheer, Brecht Heyde,
Herestraat 49 box 7003, 3000 Leuven, Belgium

D/2013/7515/161
ISBN 978-94-6018-780-3

"I thought of that while riding my bicycle"

Albert Einstein, on the theory of relativity

Acknowledgements

While some may claim that Leuven is a small city to live in and to spent four years pursuing a PhD, I have gradually come to realize that our world is potentially even smaller. I was fortunate to meet many remarkable people along the way from no less than 22 different countries (yes... I actually did the counting) and who have all contributed to this thesis in their own special way.

First and foremost, I would like to thank prof. Jan D'hooge, a great supervisor, inspiring scientist and good friend. Jan, thank you for so warmly welcoming me to Leuven when I first visited the lab so many years ago, and letting me be part of such a great, talented and unique research group. Your gift to motivate people when a scientific problem appears invincible is something I value deeply. I often felt privileged for the trust you put in me, your belief in my potential and the many opportunities you have given me to spread the word of my research abroad. Thank you for your guidance and the many interesting discussions, occasionally further reflected upon over a beer or two.

My thanks also goes to my co-supervisor, prof. Frederik Maes. Your guidance, vision and your eye for detail has helped to further shape the course of this work to something I am very proud of. I would also like to express my appreciation for all the support of prof. Piet Claus. Piet, while it may not have been obvious to the outside world, you have helped me tremendously all these years. Your door was always open for me for theoretical or programming questions, and your sincere answers helped me to see things from a different perspective. For this I thank you deeply.

To all the members of my jury, I would like to express my gratitude for their interest and time taken to read through my thesis. Prof. Daniel Rueckert, I'm truly honored to have you as a jury member. Your original work on deformable image registration was the driving force behind the developments described within this thesis. Prof. Knut Matre, I'm equally privileged to have you in my jury committee. I would like to thank you for the precious comments and

the kind words. I also owe many thanks to prof. Paul Suetens, prof. Dirk Vandermeulen, Dirk Loeckx and prof. Frank Rademakers. Your thoughtful questions and comments during my entire project were valued greatly. Prof. Willy Sansen, thank you for being the chairman of my jury committee.

Much of the experimental work described in this thesis would not have been possible without the fruitful collaboration with other research groups. I would like to thank prof. Krzysztof Kaluzynski, Szymon Cygan and Beata Lesniak-Plewinska from the Warsaw University of Technology for their expertise and tremendous help with the construction of the in-vitro experimental setup and the phantoms. The long working hours without daylight, hidden inside a small lab with nothing but the sound of the setup to keep us comfort, were truly memorable. I'm also very grateful for all the help during the in-vivo experiments of prof. Patrick Wouters, Stefaan Bouchez, Michael Vandenheuvel and Maria Olieslagers from the Department of Anesthesiology at the University of Ghent. Having an engineer running through an operation theatre consistently asking questions out of curiosity must have been a challenge. Helene Houle, thank you for your professional assistance and support during these challenging experiments.

To all my colleagues of the Cardiac Imaging and Dynamics Group, thank you for your friendship and sharing the daily delights of being a researcher. Daniel, 'my partner in crime', for all those great years being my neighbor. Thank you for your help in unraveling the mysteries of science, for your moral support and for the many inspiring conversations. Ruta, for being a close friend, for introducing me to the Lithuanian culture and for being the listening ear in times of need. Florence, Hang and Ling, for your everlasting good mood and pleasant company on our many travels abroad. Matilda, for being such a good friend and for the pleasant stay in Sweden. Alejandra and Natalia, for the many smiles and your enthusiasm, it was contagious. Nuno and Pedro, for the great company, your organization talent and your love for Belgian beers. Valérie, for all the entertaining sport-related conversations. Natasa, for reintroducing me to Rummikub. Martino, for the laughs and being a great new neighbor. Giovanni, for shedding light on the complexity of Italian politics and the Westvleteren. Vesselina, for all the relaxing off-topic talks. And to all the other people within cardiology whom I had the pleasure to meet and with whom I had many interesting conversations: Agnieszka, Alexander, Ana, Anca, André, Arco, Dana, Guido, Hadewich, Hon Fai, Ivan, prof. Jan Bogaert, Jan V, Jean-Yves, prof. Jens-Uwe Voigt, Jeroen, Jürgen, Kaatje, Lieven, Maja, Massimo, Miki, Ming, Nina, Oana, Paul, Pedro M, Peter, Pieter DM, Razvan, Richte, Rik, Sandro, Szymon, Tom B, Tom S and Tommy. A special thanks also goes to Christel for guiding me through the jungle of paperwork, administration and logistics that every scientist is apparently bound to face these days.

Being part of the Medical Imaging Research Center, I was fortunate to meet many people from the other research groups. To them I also owe the wonderful time I had in the Louvre: An, Anke, Annemie, Barbara, Bart, Catarina, Daan, David, Dirk, Dominique, Federica, Hans, Inga, Janaki, Jenny, Johannes, Jonatan, Jose, Katleen, Koen, Laura, Maarten, Martijn, Pieter B, Pieter S, Simon, Stijn, Thibo, Thijs, Tom H and Wouter. Thank you for the many hilarious coffee breaks in the ridiculously small but by now famous kitchen.

As most of you may know, I also developed a stubborn love for road race cycling during my research years. I am not sure if there was a correlation with the amount of time spent developing the techniques unveiled within this thesis. Thank you Stijn 'the diesel', Stijn 'the explosive climber', and Roel 'the talent' for the many enjoyable rides, memorable moments and sharing the joy of having flat tyres in the middle of nowhere. Although my training time over the last few months turned out to be inversely related with the amount of written thesis pages, I promise to make up for it next year. Szymon 'the Cancellara', you became the revelation of the year by being surprisingly proficient in bike logistics. I'm also glad I turned out not to be the only crazy person out there once the sun was traded for ice cold winds. To Jan, Valérie and Katrien, while our shared cycling kilometers were rather limited, thank you for making them so enjoyable. Also bless the bike for showing me the wonderful world from a different perspective and bringing me so many refreshing ideas.

To the fantastic Arenberg Orchestra, and the magnificent first violin section, you were my musical beacon throughout the occasional rough PhD research months. Thanks for all the unforgettable moments, intensive rehearsals, sleepless repetition weekends, and historic concerts. A noteworthy recognition goes to Elisabeth and Hannah for the many animated conversations during the rehearsals even when that meant disturbing the general order on more than a few occasions. Christine, Kristin and Stijn, for the great company and proudly being part of the senior violin gang. Annelies, Maarten, Martine, Sabine and Stijn, for your friendship even when that implied overcoming the eternal rivalry of strings versus winds.

I also want to thank my close friends from the 'West side' of the country, who saw me move to the 'other side' in pursuit of happiness and scientific greatness. Annelies, Brecht, Elise, Frederick, Julie, Liselot and Nicolas, thank you for all the visits, your support and friendship throughout these last years.

I'm thankful to the members of my family living in Canada, for their interest in my research and the many encouragements along the way. Regardless of where my future endeavors may bring me, I will always know that I have a warm and welcoming place overseas. I'm especially grateful to Ross and Rita, for making me feel I arrived at my second home when I first set foot on Canadian soil. To

Michael and Peter, for showing me the great outdoors, for the unforgettable camping, canoeing, loon and moose tracking. To Trish, Bernie and Erinn, for introducing me to the Canadian way of living and bear spotting.

I also want to express my gratitude to my family and grandparents for their continued support and encouragement. Nadine, for always being there to take care of me even from before I knew how to walk. Peter and meter, for stimulating my scientific interest during those long summer holidays when I was a child, designing and thinking about the next project to build in the garage.

My final words of thanks goes to the people closest to me. To my brother Evert, for your warm personality and refreshing sense of humor. To my parents, for your unconditional support and for all the opportunities you have given me. Thank you for being there. Always.

Brecht,

Leuven, 17 December 2013

Abstract

Non-rigid image registration for the assessment of myocardial deformation from 3D echocardiography

Cardiovascular diseases are currently the major cause of death in the world. Cardiac imaging therefore plays an essential role in the diagnosis, management and follow-up of patients with any suspected or known cardiovascular disease. Ultrasound (US) imaging is a well established imaging modality in daily clinical practice for the evaluation of cardiac morphology and function by measuring cardiac wall motion and deformation (i.e. strain). Several recent technological advancements have made a real-time assessment of the heart in three dimensions now possible, and thus offer the possibility to improve and expand on the diagnostic capabilities of the traditional two-dimensional (2D) US images. Analyzing these datasets however is a challenging endeavor as the spatial and temporal resolution is currently lower than in 2D and the large amount of data makes a manual evaluation cumbersome and subjective.

The focus of the present thesis was therefore the development of non-rigid image registration techniques able to cope with these demanding conditions. We illustrate that image registration is a viable technique for regional cardiac function estimation by validating the technique in a variety of cardiac ultrasound imaging scenarios. An in-vitro experimental setup was built in which tissue-mimicking phantoms could be deformed and imaged. Some phantoms contained stiff inclusions to investigate to what extent dysfunctional areas could be identified. An in-vivo animal study was also designed to acquire volumetric data in 17 open-chest sheep subject to conditions comparable to those encountered in clinical situations such as ischemia.

New regularisation methods were proposed to improve cardiac deformation estimates. A strategy was derived to adapt the topology of the control point grid of the non-rigid image registration method to the anatomy of the

heart. It was shown that such a model is more suited for cardiac deformation. Efforts were made to automate the strain estimation workflow to facilitate its introduction in clinical practice. Finally, excellent results were obtained at an international challenge where the performance of the proposed method was compared against the most competitive algorithms currently available.

Niet-rigide beeldregistratie voor het bepalen van de hartspiervervorming met behulp van 3D ultrasone beeldvorming

Hart- en vaatziekten vormen op dit moment de meest voorkomende doodsoorzaak over de hele wereld. Cardiale beeldvorming is van groot belang voor de diagnose van deze hart- en vaatziekten, en speelt een centrale rol bij het opvolgen van patienten tijdens de behandeling. Ultrasone beeldvorming is de meest belangrijke techniek in de dagdagelijkse klinische praktijk en laat toe om de morfologie en de functie van het hart in detail te bestuderen door onder andere de hartspiervervorming te bepalen. Verschillende recente technische ontwikkelingen hebben het ondertussen mogelijk gemaakt om het hart driedimensionaal te evalueren. Deze techniek opent heel wat mogelijkheden voor een verbeterde diagnosevorming van hart- en vaatziekten tegenover de traditionele ultrasone onderzoeken die enkel twee-dimensionele (2D) beelden opleveren. Toch blijft de analyse van deze beelden een moeilijke onderneming omdat de spatiale en temporele resolutie lager is dan 2D beelden. De grote hoeveelheid data maakt een manuele analyse ook tijdsintensief en te subjectief.

In deze thesis werden er daarom niet-rigide beeldregistratietechnieken ontwikkeld die rekening houden met deze moeilijke omstandigheden. We tonen aan dat beeldregistratie een performante techniek is die toelaat om regionaal de hartspiervervorming te bepalen in een ruime waaier van toepassingen. Zo werd er een experimentele opstelling gebouwd om de techniek te valideren met behulp van dynamische weefsel-nabootsende fantomen. Sommige fantomen bevatten een stijve inclusie om te onderzoeken hoe goed de methode dysfunctionele gebieden kon detecteren. Er werd ook een in-vivo experimentele studie opgezet om de techniek verder te valideren. Hiertoe werden beelden opgenomen in 17 schapen met een chirurgisch geopend pericard, en werd er onder andere ischemie geinduceerd.

Nieuwe regularisatie methoden werden hiernaast ook ontwikkeld om de berekening van de hartspiervervormingen te verbeteren. Zo werd de topologie van de controle punten van de niet-rigide registratie aangepast aan de anatomie

van het hart. We toonden aan dat dergelijke modellering beter geschikt is om hartvervormingen te bepalen. Hiernaast werden ook verschillende stappen gezet om het berekeningsproces verder te stroomlijnen. Dit maakt de hele methode mogelijks aantrekkelijker in de klinische praktijk. Tot slot werden ook uitstekende resultaten bekomen op een internationale wedstrijd waarin de ontwikkelde methode vergeleken werd met andere competitieve technieken.

List of Acronyms

1D	one-dimensional
2D	two-dimensional
3D	three-dimensional
3DSE	3D strain estimation
A	anterior (wall)
AFFD	anatomical free-form deformation
AL	anterolateral (wall)
AR	adjacent region
AS	anteroseptal (wall)
AVC	aortic valve closure
bpm	beats per minute
BV	biventricular (pacing)
CFFD	Cartesian free-form deformation
CL	contralateral (wall)
CT	computed tomography
CVD	cardiovascular disease
ED	end-diastole
ED2	end-diastole (second ED occuring within the image sequence)
ES	end-systole

FFD free-form deformation

HR heart rate

I inferior (wall)

IL inferolateral (wall)

IR inclusion region

IS inferoseptal (wall)

ITK insight segmentation and registration toolkit [266]

LAD left anterior descending (artery)

LAx long axis

LBBB left bundle branch block

LBFGSB limited memory Broyden-Fletcher-Goldfarb-Shanno bound constrained optimizer [36]

LCA left coronary artery

LCX left circumflex (coronary artery)

LOA limits-of-agreement

LV left ventricle

MI mutual information

MRI magnetic resonance imaging

NCC normalized cross-correlation

OF optical flow

PET positron emission tomography

PVA polyvinylalcohol

PW pulsed wave

RBBB right bundle branch block

RBF radial basis functions

RCA right coronary artery

RF	radiofrequency (signals)
ROI	region-of-interest
RR	remote region
RT3DE	real-time 3D echocardiography
RV	right ventricle
SAD	sum of absolute differences
SAx	short axis (acoustic view)
SH	spherical harmonics
SNR	signal-to-noise ratio
SPECT	single photon emission computed tomography
SR	strain rate
SSD	sum of squared differences
ST	speckle tracking
SV	stroke volume
TDI	tissue Doppler imaging
US	ultrasound
VG	velocity gradient

List of Symbols

Images

Ω	Image domain
I_f	Frame f of an image sequence in Cartesian space
$\hat{I}_f$	Frame f of an image sequence in anatomical space
I_F	Fixed image (within registration framework)
I_M	Moving image (within registration framework)
N	Number of frames within the image sequence

Image coordinates

x, y, z	Cartesian coordinates
r, l, c	Anatomical coordinates, oriented along the radial, longitudinal and circumferential cardiac direction
λ, μ, θ	Prolate spheroidal coordinates
ρ, φ, θ	Spherical coordinates
$\mathbf{r} = [x, y, z]$	Spatial coordinate in Cartesian space
$\hat{\mathbf{r}} = [r, l, c]$	Spatial coordinate in anatomical space

B-spline tensor product

$\beta^1(\cdot)$	B-spline of degree 1
$\beta^2(\cdot)$	B-spline of degree 2
$\beta^3(\cdot)$	B-spline of degree 3
σ	Control point spacing
κ	Control point location
i, j, k	Control point index in x, y and z direction
$\imath, \jmath, \varsigma$	Control point index in r, l and c direction
ξ	Placeholder for either x, y, z or $\imath, \jmath, \varsigma$
$\mathcal{N}$	Set of control points within the compact support of the B-spline
$\boldsymbol{\mu}^{ijk}$	B-spline coefficients associated with control point κ^{ijk} (transformation parameters)
$\boldsymbol{\mu}^*$	Optimal transformation parameters (after optimization)
$\boldsymbol{\mu}_{(k)}$	Values of the transformation parameters (during optimization)
$\boldsymbol{d}_{(k)}$	Search direction at iteration (k) (during optimization)
$a_{(k)}$	Gain factor at iteration (k) (during optimization)

Free-form deformation transform

$\mathbf{u}_{f \to f+1}$	Displacement field between I_f and I_{f+1}
$\tilde{\mathbf{u}}_{f \to f+1}$	Unregularised displacement field between I_f and I_{f+1}
$\hat{\mathbf{u}}_{f \to f+1}$	Displacement field between I_f and I_{f+1} in anatomical space
$\mathbf{T}_{f \to f+1}$	Transformation field between I_f and I_{f+1}
$\mathbf{J}$	Spatial Jacobian of the transformation field $\mathbf{T}$
m	Compact notation for looping index i, j, k (see appendix B) Range: m=1..M, or m=1..S
M	Total number of parameters $\boldsymbol{\mu}$ (see appendix B)
S	Total number of parameters within the compact B-spline support (see appendix B)

Cost function

C	Cost function
S	Similarity metric
R	Regularisation term
ω	Hyperparameter governing the regularisation term strength
P	Number of points used in the calculation of the cost function terms C
$\mathbf{H}$	Hessian matrix of the cost function (wrt. parameters $\boldsymbol{\mu}$)

Strain

L_0	Length between two points before tissue deformation
L	Length between two points after tissue deformation
$\boldsymbol{n}$	Placeholder for a certain direction
$\boldsymbol{n}_{\mathrm{R}}, \boldsymbol{n}_{\mathrm{L}}, \boldsymbol{n}_{\mathrm{C}}$	Radial, longitudinal and circumferential direction
$\varepsilon_{\boldsymbol{n}}$	Strain along direction $\boldsymbol{n}$
$\varepsilon_{\mathrm{RR}}$, $\varepsilon_{\mathrm{LL}}$, $\varepsilon_{\mathrm{CC}}$	Radial, longitudinal and circumferential strain
ε_{L}	Lagrangian strain (see appendix A)
ε_{E}	Eulerian strain (see appendix A)
$\varepsilon_{\mathrm{AS}}$	Area strain (see appendix A)
$\varepsilon_{\mathrm{PP},i}$	Principal strain (component i; see appendix A)
ε^{ref}	Reference strain (ground-truth)
ε^{dr}	Drift-corrected strain
$\dot{\varepsilon}$	Strain rate (see appendix A)

Continuum mechanics (appendix A)

B, b	Continuous body in the undeformed and deformed configuration respectively
$d\mathbf{X}, d\mathbf{x}$	Line segment within B and b respectively.
$\mathcal{X}$	Generic deformation acting on a continuous body B
$\mathbf{F}$	Deformation gradient tensor
$\mathbf{D}$	Displacement gradient tensor
$\mathbf{C}$	Right Cauchy-Green deformation tensor
$\mathbf{E}$	Lagrangian finite strain tensor
$\mathbf{e}$	Infinitesimal strain tensor
$\mathbf{N}$	Strain direction in the undeformed configuration

Segmentation and fitting

P_{qm}	Legendre functions
Y_{qm}	Spherical harmonics basis functions
c_{qm}	Spherical harmonics expansion coefficients
$\mathbf{S}$	Endocardial surface
$\mathbf{B}$	Endocardial border
α	Diffusivity (chapter 6)
$\bar{\kappa}$	Mean local curvature of a surface
$\psi(\theta, \varphi)$	Explicit function defining the endocardial border (chapter 11)
$\phi(\mathbf{x})$	Level-set like function controlling the segmentation (chapter 11)

Contents

Chapter 1

Introduction

1.1 Cardiac anatomy and function

The heart, shown schematically in Fig. 1.1, is one of the most vital organs of the human body and ensures a continuous blood circulation. As such, it contributes in supplying organs with oxygen and essential nutrients, and assists in removing carbon dioxide and other waste products from cells. It is enclosed by the pericardium, a double-layered sac responsible to anchor the heart to the surrounding tissue structures. The pericardium contains pericardial fluid which facilitates cardiac motion and reduces resistance with the outer layer of the heart, the epicardium. The myocardium forms the the bulk of the heart and is composed mainly of cardiac muscle cells (cardiomyocytes). The inner layer is the endocardium and consists of endothelial cells.

Four chambers can be distinguished in the heart: the left and right atrium (also called the upper chambers), and the left and right ventricle (or lower chambers). Both sides of the heart are separated by the septum. The right atrium collects deoxygenated blood coming from the systemic circuit through the inferior and superior vena cava and pumps it to the right ventricle through the tricuspid valve. The right ventricle (RV) then expells the blood through the pulmonary valve into the pulmonary circuit. The pulmonary arteries lead the blood to the lungs where carbon dioxide and oxygen are interchanged. Oxygen-rich blood then returns to the left atrium and is directed into the left ventricle (LV) through the mitral valve. Finally, the LV pumps the blood again into the systemic circuit through the aortic valve. The wall of the LV is approximately three times thicker then the RV, since the blood through

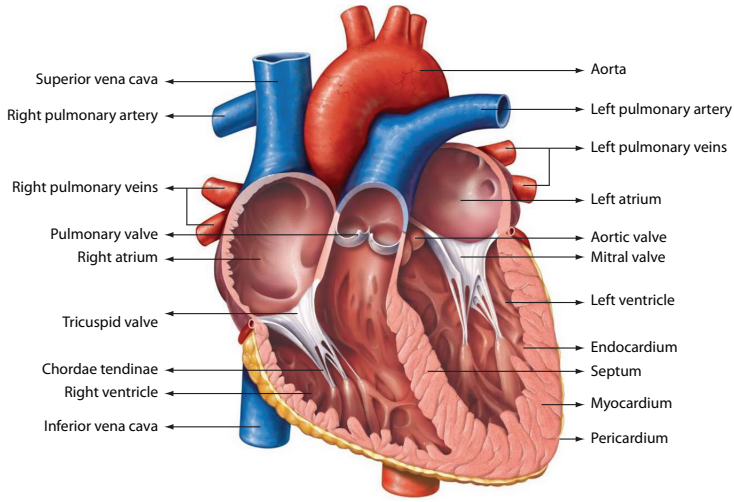

Figure 1.1: Overview of cardiac anatomy. Modified from [156] with permission.

the systemic circulation encounters approximately five times more friction. The valves at the in- and outflow tract of the ventricles prevent retrograde flow. The leaflets of the atrio-ventricular valves, i.e. the mitral valve and the tricuspid valve, are connected to the papillary muscles with chordae tendineae. The papillary muscles contract with the ventricle to prevent the valves from protruding in the atria [156].

The myocardium is oxygenated by the coronary circulation which originates at the root of the aorta. The left coronary artery (LCA) runs towards the left side of the heart and branches off into the left anterior descending artery (LAD), supplying blood to the LV anterior wall and the septum, and the left circumflex artery (LCX) which guarantees blood flow in the LV lateral wall. The right coronary artery (RCA) is responsible to maintain blood flow within the LV inferior wall and nearly the whole RV [37].

1.2 Cardiac mechanics

Each cardiomyocyte contains bundles of myofibrils which are further organised into sarcomeres, the basic contractile unit of the muscle. Two protein filaments (myofilaments) form the main actors within a sarcomere: a thick filament composed of myosine molecules and a thin filament consisting of actine molecules. During contraction, the heads of the myosine molecules form cross

bridges with the actin molecules and bend. This results in a sliding motion of the actin filament past the myosin filament which is translated to muscle contraction on a macroscopic level.

The effective pumping action of the heart requires a precise, coordinated contraction of all the cardiomyocytes. This is possible through a network of specialized cells forming the electrical conduction system of the heart. Impulses start at the sinoatrial node and stimulate the atria to contract. The atrioventricular node delays this impulse to ensure that the atria can complete their contraction before the ventricles respond. The stimulus then continues through the His bundle, branches off into the left and right bundle, and into Purkinje fibers towards the apex. Finally, the impulse spreads from cell to cell through gap-junctions, leading to the ventricular contraction. From a global point of view, the heart performs a twisting motion during contraction due to the helical orientation of the myocardial fibers [217]. Looking up from the apex, the base undergoes a clockwise motion around its long axis while the apex rotates in the opposite direction. From an anterior point of view, the base of the heart moves downwards to the apex.

The cardiac cycle can be divided into two phases: systole (contraction) and diastole (relaxation). Systole starts with an isovolumetric contraction phase which builds up pressure inside the ventricles, followed by ejection into the pulmonary arteries and aorta. The ventricles then begin to relax, pressure drops inside the cavity and the aortic/pulmonary valve closes, marking the end of systole. Diastole begins with an isovolumetric relaxation phase of the ventricles, followed by a rapid passive filling phase when the atrio-ventricular valves open, and ending with active filling when the atria contract. When the electrical stimulus propagates to the ventricles again, the cardiac cycle starts over.

1.3 Cardiovascular diseases

Cardiovascular diseases (CVDs) are a group of disorders affecting the heart and blood vessels, and is currently the leading cause of death globally [262]. These disorders include coronary artery disease (usually caused by atherosclerosis in which coronary arteries narrow due to the deposit of fatty materials), myocardial infarct (heart attack due to an acute blockade of coronary arteries), cerebrovascular disease (usually caused by hypertension in which arteries supplying the brain get permanently damaged), stroke (sudden loss in blood supply to the brain due to ischemia or a hemorrhage), cardiomyopathy (often leading to heart failure), cardiac arrhythmias, cardiac conduction abnormalities (such as left bundle branch block), congenital heart defects (a defect present at

birth), etc. The majority of deaths were due to coronary heart disease (42%) and stroke (36%), and are mostly caused by atherosclerosis and hypertension. Behavioural risk factors include physical inactivity, unhealthy diet, smoking and harmful use of alcohol [262].

1.4 Cardiac Imaging

Cardiac imaging plays an essential role in the diagnosis, management and follow-up of patients with any suspected or known CVD. The most commonly used clinical imaging modalities are ultrasound imaging (US), single photon emission computed tomography (SPECT), computed tomography (CT) and magnetic resonance imaging (MRI). Cardiac CT is mostly used in angiography to investigate myocardial perfusion and visualize the blood vessels in the presence of coronary artery disease [261]. It has a relatively high spatial resolution but delivers a significant radiation dose during scanning. SPECT is mainly used to assess myocardial perfusion and viability as it creates functional images with a high SNR. However, similar to CT, these examinations result in a radiation exposure since the tracer molecules carrying the unstable isotopes accumulate in organs and can take several days to fully decay [220]. MRI on the other hand does not make use of ionizing radiation, and provides an excellent spatial and contrast resolution. It is ideally suited for the assessment of cardiac morphology, myocardial perfusion and infarction [48]. However, the temporal resolution is relatively low, and MRI examinations are time-consuming and expensive.

In daily clinical practice, ultrasound imaging is a well established and often preferred imaging modality for the evaluation of cardiac morphology and function as it is non-invasive, relatively inexpensive, portable and provides an excellent temporal resolution [167]. The present thesis therefore focused on ultrasonic assessment of the left ventricular function, which is vital in supplying the body with oxygenated blood. Nevertheless, in comparison with the other modalities, US image quality is typically lower due to the presence of image artefacts such as reverberations, rib shadowing, signal dropouts and near-field artefacts. Manual analysis and objective interpretation of these images can therefore be challenging. The techniques developed in this thesis aim to facilitate this process.

1.5 Ultrasound imaging

1.5.1 Basic principles

Diagnostic ultrasound imaging is based on the propagation and reflection of high frequency compression waves in human tissues. Ultrasound waves, having a frequency above the audible range of human hearing, are both generated and detected by piezoelectric crystals embedded within a transducer. These crystals deform under the influence of a sinusoidal electrical field generating US waves. As the US waves propagate deeper into the body, they get partly reflected when they encounter local density and/or compressibility inhomogeneities. When the US waves encounter a distinct surface, significantly larger then the US wavelength, a specular reflection occurs which will result in a bright signal on the US images. When these inhomogeneities (i.e. scatterers) are small relative to the US wavelength, US waves get scattered in all directions. The resulting interference pattern will give rise to the characteristic speckle pattern seen in US images. Upon receiving the reflected US waves in the transducer, the piezoelectric crystals deform and induce an electrical field. The detected signals are called radiofrequency (RF) signals since the involved frequencies correspond to the radio waves range in the electromechanical spectrum. A transducer can only generate and receive a limited band of frequencies, called the bandwidth of the transducer. The central frequency of the transducer is the center of this bandwidth.

Axial resolution of US imaging depends on the pulse length (or equivalently the bandwidth of the transmitted pulse). Lateral resolution is determined by the US beamwidth. It can be improved by increasing the transducer aperture or by increasing the central frequency of the transmitted pulse, but at the cost of a lower penetration depth due to signal attenuation. For transthoracic cardiac applications, a central transmit frequency of 2.5 MHz is typically used. The axial resolution is typically around 0.5 mm [228].

1.5.2 Image formation

In order to generate an image, multiple pulses have to be transmitted in different directions. Linear array transducers consist of a 1D array of crystals which fire pulses successively, but are typically only used in cases where the acoustic window is large (i.e. in vascular imaging and obstetrics). Phased-arrays on the other hand have a smaller footprint and are preferred in cardiology because the acoustic window between the ribs is small. The US beam can be directed and/or focused by electronically modifying the firing

delays of each crystal element individually. Transmit beamforming thus allows modifying beamwidth (affecting lateral resolution) as well as the focus depth. Similarly, beamforming can also be performed on receive by applying the right delays on the incoming signals. If these delays are modified over time, one can (artificially) focus along a given image line without sacrificing temporal resolution (i.e. dynamic focusing). The frame rate depends on the field of view (scanning deeper requires a longer time interval between subsequent pulses) and the line density. Typical frame rates of 2D cardiac images are between 50-80 Hz, allowing real-time scanning.

A series of steps is performed to reconstruct ultrasound images from RF data [228]: filtering to remove high-frequency noise, envelope detection to generate a grayscale or B-mode image (B stands for brightness), attenuation correction (also called time gain compensation), log-compression to reduce the large dynamic range, and scan conversion to create a sector scan image (see Fig. 1.2). Image quality in grayscale images is typically deteriorated by image artefacts such as near-field reverberations (received echoes which bounce back at the transducer towards the tissue) and the presence of side lobes in the US beams (introducing information from another direction in the received signals). These artefacts can be reduced by using second harmonic imaging in which the fundamental low-frequency band is filtered. Harmonic imaging is based on the occurence of nonlinear wave propagation. Transmit pulses get distorted the further they propagate in the tissue, and higher frequencies built up. Echos originating from superficial reverberations therefore do not contain harmonics, and harmonics from side lobes are generally too low in amplitude to show up [235]. Typical cardiac harmonic imaging takes place using transducers operating at a 1.7 MHz transmit frequency and 3.4 MHz receive frequency (i.e. the second harmonic frequency). The main disadvantage is that transducers require a sufficient bandwidth to perform harmonic imaging.

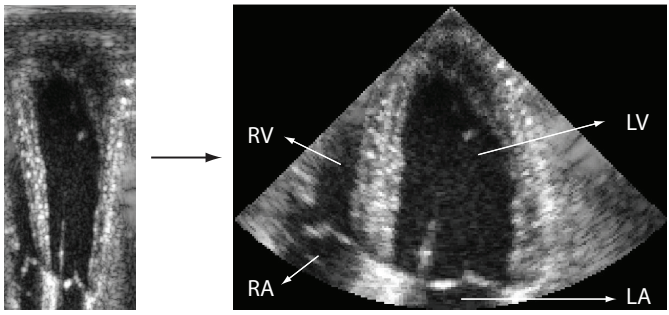

Figure 1.2: Example of a 2D B-mode US dataset showing the 4 chambers of the heart: (left) before and (right) after scanconversion.

1.5.3 Volumetric imaging

Since myocardial motion and deformation is truly three-dimensional, the main drawbacks of quantitative methods relying on two dimensional images are their inability to follow out-of-plane movement, the possibility of foreshortening and the need of geometric assumptions for volume calculations. The easiest way to construct 3D images is by mechanically translating, tilting or rotating conventional phased-array transducers to sweep over the anatomy of interest. This approach however limits the speed of volume acquisition considerably [69]. The mechanical motion can be replaced by electronically steering the US beams using a 2D phased-array transducer. The first real-time 3-dimensional echocardiography system was developed at Duke University in the early 90's [221]. With the developments in ultrasound transducer technology, microelectronic techniques and both hardware and software computing, systems capable of acquiring real-time full volumetric data of the left ventricle have now become widely available (Fig. 1.3). However, due to the increased field of view, spatial and temporal resolution is typically lower compared to 2D imaging. Cardiac subvolumes acquired over subsequent heart cycles, are therefore often stitched together to increase the frame rate without sacrificing the field of view and spatial resolution. Typical clinical frame rates of volumetric US images acquired with stitching are around 25–35 Hz. Advances in parallel beamforming techniques (multiline acquisition and multiline transmit) can further aid in increasing the frame rate of 3D imaging [243][255], with some commercial systems already reporting real-time volumetric acquisition rates around 60 Hz without the need for stitching [248].

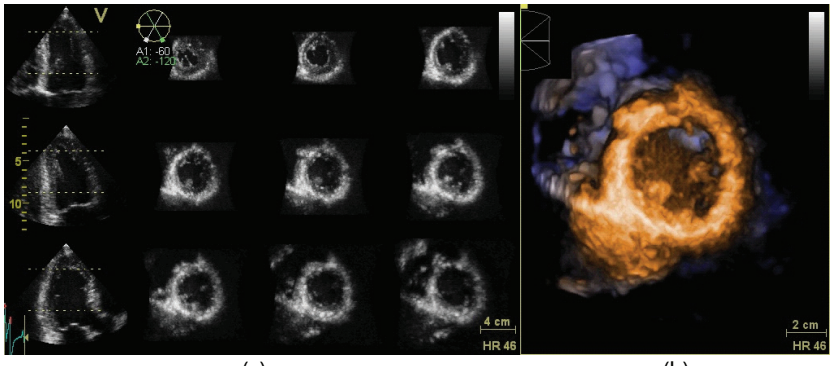

Figure 1.3: Example of a clinical 3D B-mode US dataset: (a) several cross sections through the volumetric dataset and (b) corresponding 3D rendering of the left ventricle.

1.5.4 Assessment of cardiac function

Ultrasound imaging cannot only be used to visualize cardiac anatomy, but also allows for an objective assessment of myocardial function. For example, the end-diastolic volume, end-systolic volume, ejection fraction (fractional shortening in 2D) and stroke volume are traditional parameters of global cardiac morphology and function [241], and have been shown to be important predictors for morbidity and mortality [182][197][260]. Several studies have shown that 3D echocardiography allows to assess these measures more accurately and with a lower inter-observer variability compared to 2D ultrasound imaging [110][166][172].

However, as many diseases result in regional dysfunction, looking into regional rather than global function is of primary attention. Traditionally, regional function has often been derived by visual inspection of segmental wall motion (i.e. by wall motion scoring). However, this methodology is semi-quantitative, depends considerably on the expertise of the operator [191] and has a relatively high inter-observer variability [98]. Classic M-mode echocardiography can also be used to evaluate local thickening parameters but only in one dimension and for a limited number of regions since the ultrasound beam has to be perpendicular to the investigated segment [81]. As an alternative, tissue Doppler imaging (TDI) can resolve all myocardial velocities along each imaging line [234]. However, as with all Doppler techniques, only the axial velocity component is measured. Furthermore, regional velocity estimates will be affected by overall heart motion, rotation and adjacent contracting segments, and may thus not necessarily reflect local contraction.

To solve some of the aforementioned problems, myocardial strain (i.e. the relative lengthening or shortening of the myocardial segment expressed as a percentage of its initial length) and strain rate imaging (i.e. the rate of this lengthening or shortening) was introduced [86][114]. Ultrasonic myocardial deformation imaging offers the possibility to study myocardial deformation in a multitude of clinical scenarios [52][133][232]. For example, it is widely used for the detection of myocardial ischemia [21][40][83] and has been proposed as a tool to predict infarct size after coronary reperfusion [251], to detect heart disease at its preclinical stage [163], to quantify dyssynchrony and predict response to cardiac resynchronization therapy [229], and to monitor therapy [75]. Several studies have since then also tried to establish a normal range of strain values [133][159][265].

1.6 Objectives and outline of this thesis

Three-dimensional US acquisitions now offer the possibility to improve and expand on the diagnostic capabilities of the traditional two-dimensional (2D) US images. Nevertheless, the large amount of image data increases computational load, and their limited temporal and spatial resolution compared to 2D images makes tracking tissue and estimating regional cardiac deformation challenging. The aim of this thesis was therefore to develop advanced image processing strategies able to cope with these challenging conditions. More specifically, the focus of this thesis was:

- To develop an accurate 3D strain estimation method
- To develop new regularization methods to further improve cardiac deformation estimates
- To set up different experimental studies to validate the developed 3D strain estimation method
- To demonstrate its applicability in clinical practice
- To compare its performance against other state-of-the-art strain estimation algorithms

The manuscript is structured as follows. First, a broad overview of ultrasound-based cardiac deformation techniques is given in chapter 2. One-dimensional (1D), 2D and 3D strain estimation methods are discussed. Chapter 3 highlights two of these techniques which have proven successfull for 2D strain estimation, i.e. non-rigid image registration based on Cartesian free-form deformations (CFFD) and speckle tracking (ST), and contrasts them directly in an in-vivo experimental setup. The open-chest animal setting used for this purpose is described in detail. Given the potential of CFFD to outperform 2D ST in this study, further efforts were made to extend CFFD to 3D in the next two chapters. In chapter 4, a validation setup using univentricular cardiac phantoms was built to assess 3D strain accuracy. Furthermore, the resolving power of the method to identify regions containing stiff inclusions, i.e. mimicking a dysfunctional region, was investigated. Chapter 5 continues with the validation process by applying the method on in-vivo datasets.

While the 3D CFFD method provided encouraging results, improvements could still be made from a theoretical point of view. Indeed, the CFFD model treats the myocardium and the blood pool in a similar way, and smoothed motion along non-physiological directions rather than along the 'anatomical' directions of interest for strain estimation, i.e. along the radial, longitudinal

and circumferential direction of the heart. In order to model cardiac motion in a more natural way, the control point grid of the FFD model was adapted to match the anatomy of the heart. The implementation of this anatomical free-form deformation (AFFD) model for the analysis of 2D US images is formulated in chapter 6. Its performance is also compared against a 2D CFFD model on in-vivo datasets. Its extension to the evaluation of 3D cardiac deformation is the subject of chapter 7. Chapters 8 and 9 continue by comparing the developed 3D AFFD model first with other academic implementations of 3D strain estimation techniques and then with its CFFD equivalent model, in both cases using simulated data. An alternative regularisation term based on myocardial volume conservation is investigated further in chapter 10. Chapter 11 proposes automating the strain estimation workflow, hereby facilitating its applicability in clinical practice. Finally, chapter 12 concludes and provides outlooks for the future. The thesis structure is shown schematically in Fig. 1.4.

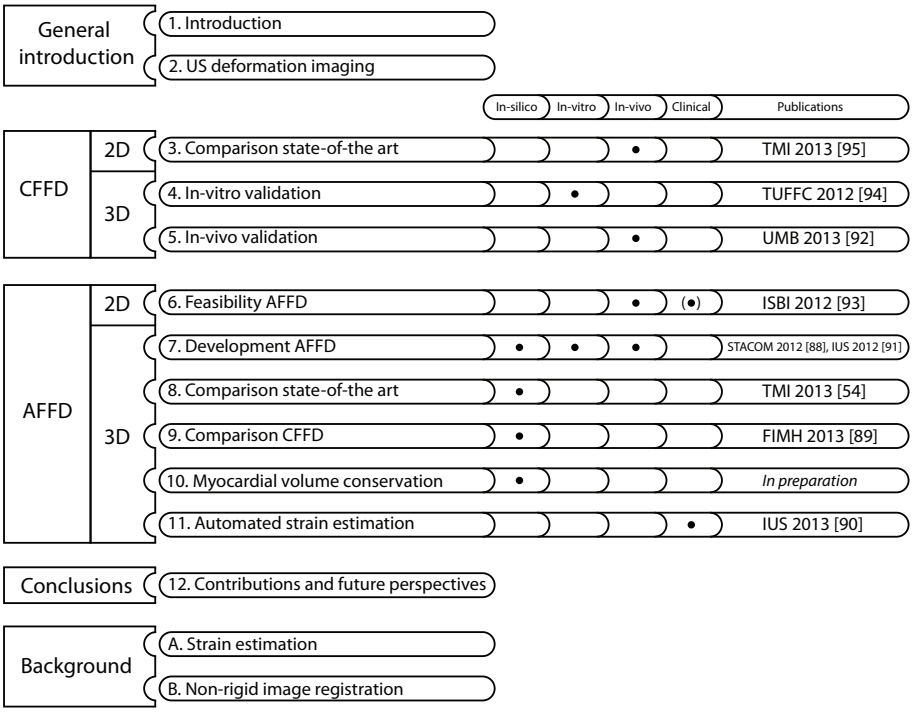

Figure 1.4: Schematic overview of the structure of this thesis, highlighting the validation setting and the associated publications of each chapter.

Chapter 2

Ultrasound-based cardiac deformation imaging

2.1 Overview

A vast amount of methods have been developed in the field of medical imaging for applications which require estimating deformation between images, e.g. in multi-modality fusion, in longitudinal studies where anatomical changes are investigated or to recover motion from image sequences. Several reviews are available on this topic, e.g. [99][225]. More specifically, cardiac motion and deformation estimation has received widespread attention as covered by a number of review papers, e.g. a broad overview of the developed methodologies for a wide range of modalities is given in [72][151], and a detailed overview regarding techniques developed specifically for cardiac MRI analysis is treated in [256]. While a variety of techniques were covered, few were classified or discussed from an ultrasound point of view. The present chapter therefore aims to provide a (non-exhaustive) overview of US-based cardiac deformation techniques and proposes a classification to conceptually group them (Fig. 2.1).

Traditionally, US-based cardiac deformation estimates depended on Doppler techniques only. Non-Doppler based methods emerged later and can be divided into two categories depending on the way they represent the deformation field. They can be classified as being non-parametric if they are inspired from physical models, or as parametric models if they represent deformation using a set of basis functions. Non-parametric models can be further grouped into optical flow methods, biomechanical models and statistical models. Finally, a selected number of segmentation-based methods are highlighted.

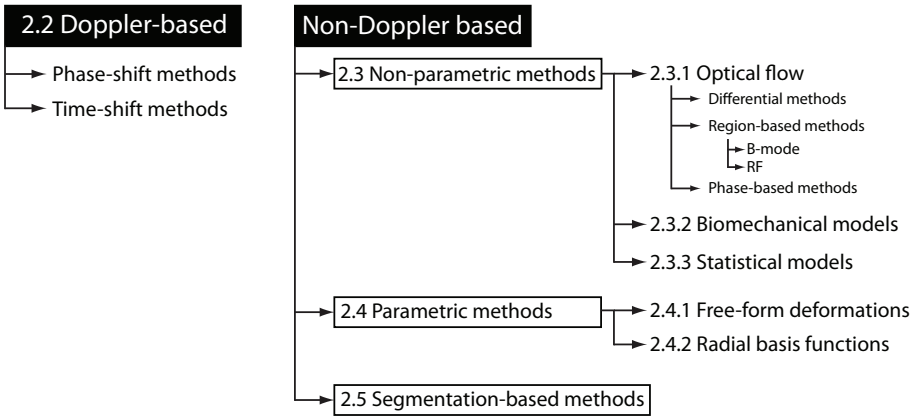

Figure 2.1: Proposed classification of ultrasound-based cardiac motion and deformation techniques. The numbers preceding the classes refer to the respective sections within this chapter.

2.2 Doppler-based methods

Due to the Doppler effect, tissue motion causes a frequency shift in the detected US echos, proportional to the tissue velocity parallel to the US beam. This frequency shift can be estimated directly from a continuous US signal (as in continuous wave Doppler) but does not provide spatial information. As an alternative, it could be estimated from sampling the returned echos of repetitive US pulses at a fixed time point after transmit (i.e. the range gate). This is called pulsed wave tissue Doppler imaging (PW TDI). However, this only results in a local tissue velocity measure. Measuring tissue velocities at different locations requires adjusting the range gate [233].

In order to obtain tissue velocities from multiple locations simultaneously, color tissue Doppler imaging (color TDI, also called Doppler myocardial imaging) was developed. It is based on the same principles as color flow mapping to visualise blood velocities, but filters the high blood velocity signals and retains those originating from tissue. In this method, US pulses are transmitted along a certain line at a constant pulse repetition frequency. Two groups of methods exist to estimate motion from the returned echo: phase-shift methods and time-shift methods. In both cases, it is assumed that the reflected echo signal is a scaled, delayed replica of the transmitted pulse [59].

Phase-shift methods use an autocorrelation estimator to relate the phase shift of the returned echo signals to the velocities. It should be noted that these methods are subject to velocity aliasing [111]. Due to the assumption that RF signals do not change between acquisitions, data acquisition at a sufficiently high pulse repetition frequency is required (5 kHz for cardiac applications). This is possible when the sector scan is reduced sufficiently. In practice, it is reduced until it covers only a ventricular wall. The resulting frame rate is typically around 200-300 Hz [27]. The estimated tissue velocities are usually color coded on top of the B-mode image, with red and blue representing velocities towards and away from the transducer respectively. It can be shown that strain rate can be calculated using the spatial velocity gradient (see appendix A.1.2), either by sampling velocities over a fixed offset along the beam [86] or as the slope of a regression line through multiple velocities estimated within a certain distance [71]. Strain can then be obtained by temporally integrating the strain rate curves.

Time-shift methods use several functions to determine motion of signal patterns, e.g. sum of squared differences, sum of absolute differences, cross-correlation, etc. [254]. While these techniques do not suffer from aliasing when tissues move at a high velocity, they are computationally intensive making real-time processing difficult. They generally require interpolation techniques to achieve subsample resolution [38].

TDI has several limitations: the velocity estimation is angle dependent, not all strain components can be measured in all myocardial segments [157], and the presence of noise is amplified in the strain rate calculation. The non-Doppler methods described in the next sections, attempt to adress these limitations. Despite these disadvantages, TDI is a well validated technique in a wide range of imaging scenarios (in phantoms [23], in animals [80][106][246], and in clinical practice [66]). Furthermore, it has a wide range of clinical applications [232][238].

2.3 Non-parametric models

2.3.1 Optical flow

Optical flow (OF) is the apparent motion of brightness patterns within an image sequence. Many techniques for computing optical flow from an image sequence have been proposed: differential methods, region-based methods and phase-based methods [5][20].

Differential methods

Differential or gradient-based OF methods rely on the assumption that the intensity of a particular point in a moving pattern does not change with time. They compute velocity from spatiotemporal derivatives of image intensities [20]. This constant intensity assumption can be expressed as [100]:

$$\nabla I_f(\mathbf{r}) \cdot \mathbf{v} = I_m(\mathbf{r}) - I_f(\mathbf{r}) \tag{2.1}$$

where $I_f(\mathbf{r})$ and $I_m(\mathbf{r})$ are the voxel intensities of the fixed image (the initial frame) and moving image (the consecutive frame) respectively, ∇I denotes the spatial derivatives of I_f, and $\mathbf{v}$ represents the unknown velocity components of the optical flow field. Since the number of components of $\mathbf{v}$ is at least two, this single equation is insufficient to be solved without additional constraints. This is known as the aperture problem.

Two popular approaches exist to solve this underdetermined problem. The Horn-Schunck algorithm is a global method and imposes smoothness in the flow across the whole image as an additional constraint [100]. The Lucas-Kanade method estimates the motion locally, assuming that the velocity field is constant within a small image region [149]. Both techniques were shown to be reliable in estimating motion on synthetic US images [12]. The Horn-Schunck OF approach has been formulated as a variational problem for 3D motion estimation in [170]. The Lucas-Kanade OF has been applied to clinical datasets in e.g. [44][126].

Suhling *et al.* proposed an extension of the Lucas-Kanade method in which they introduced a local spatio-temporal affine motion model in order to better capture the typical myocardial motion modes such as contraction, expansion, rotation and shear [230]. This approach was further extended to 3D in [17] to track the endocardial borders.

Thirion *et al.*, inspired by Maxwell's demons, were the first to regard motion estimation as a diffusion problem [240]. In this method, object boundaries in one image I_f are modelled as membranes through which the other image I_m is allowed to diffuse under the influence of 'demons' placed on these membranes (i.e. entities which determine whether or not diffusion should take place). The forces of the demons are given by the optical flow equation:

$$\mathbf{v} = \frac{[I_m(\mathbf{r}) - I_f(\mathbf{r})] \cdot \nabla I_f(\mathbf{r})}{[\nabla I_f(\mathbf{r})]^2} \tag{2.2}$$

However, in regions where the image gradient $\nabla I_f(\mathbf{r})$ is very small, the flow will become unstable ($\mathbf{v}$ becomes very large). Therefore Thirion stabilized the vector-flow field first by underestimating the flow field at these locations [214]:

$$\mathbf{v} = \frac{[I_m(\mathbf{r}) - I_f(\mathbf{r})] \cdot \nabla I_f(\mathbf{r})}{[\nabla I_f(\mathbf{r})]^2 + [I_m(\mathbf{r}) - I_f(\mathbf{r})]^2} \tag{2.3}$$

Gaussian smoothing is then performed to compensate for this underestimation and to ensure that the vector flow field diffuses from regions having a strong gradient to regions with small gradients. These two steps are solved iteratively for every voxel. A number of modifications have been proposed to the original demons formulation. For example, Somphone *et al.* replaced the standard Gaussian smoothing of the displacement field by a normalized convolution within a predefined myocardial mask and demonstrated its feasibility on simulated 3D US datasets [223]. Vercauteren *et al.* proposed the logDemons algorithm in which the spatial transform was completely represented in the log-domain to become diffeomorphic [252]. Mansi *et al.* later introduced an incompressibility constraint within this framework (leading to the formulation of the iLogDemons algorithm; [154]). The iLogDemons method was evaluated on simulated and clinical 3D cardiac US images in [195] and [161] respectively. A poly-affine variant was proposed in [162] to reduce the amount of parameters required to represent cardiac deformation.

Region-based methods

Region-based methods or block matching methods estimate motion of a certain point by shifting a local neighborhood around this point and determining the best fit within the next frame. Finding the best match amounts to maximizing a similarity measure. They are based on the assumption of a stable local speckle pattern between subsequent frames. For this reason, block matching techniques applied on B-mode data are therefore often termed speckle tracking techniques. Block matching techniques can also be applied directly on the radiofrequency

(RF) data. In these methods, strain is typically obtained as the spatial gradient of the motion, with strain rate being obtained after temporal derivation [60].

Applying block matching on **B-mode data** has been a popular approach in the ultrasound society due to its conceptual simplicity and high computational speed. Trahey *et al.* were the first to successfully apply block matching to track blood motion [244], later followed by Bohs *et al.* who applied the technique to track 2D tissue motion. It has been extensively validated by several research groups, e.g. [4][22][123][130][193][200]. Several of these 2D speckle tracking methods have become commercially available and proven useful in the clinical setting, e.g. in [11][40][159][229]. Additionally, ventricular rotation and twist as parameters to describe LV function could be determined [8][87][183]. The performance of a commercial speckle tracking technique against the techniques developed within this thesis is the topic of chapter 3.

Early work to extend block matching to 3D was performed in [169]. Three-dimensional block matching has been applied in an open-chest animal setting [62][224] and in clinical practice [50]. A straightforward extension of block matching from 2D to 3D is challenging primarlily due to the increased processing time: in order to produce a dense motion field, the amount of tracking points has to increase significantly. Strategies to cope with this problem are limiting the search region in the next frame [50] or using similarity measures with a lower calculation cost (such as sum of absolute differences), or by using an efficient implementation on GPUs to increase processing speed [116]. Several commercial implementations of 3D block matching are currently available [117][190][199][204][205][268].

As an alternative, 2D tissue tracking can be performed directly on the **raw RF data** by defining a 1D or 2D kernel over the RF signal and finding the optimal shift within a certain 2D search region in the next frame [113][128][144][148]. Several studies have shown that due to the high frequency content of the RF signals, more accurate sub-pixel motion estimates can be obtained in the axial direction, given that the deformation between frames is sufficiently low [198][267]. It is therefore often applied in applications associated with small deformations, e.g. in elastography. An extension to 3D cardiac applications is therefore challenging given the current low volumetric acquisition rate [146]. The main disadvantage of RF tracking over B-mode tracking is its higher processing cost. B-mode data hold much lower frequency content and the sampling frequency can therefore be reduced, resulting in a drastic reduction in computation time. In [43], several techniques are proposed to reduce the computational load of 3D RF tracking. To increase the resolution in both non-axial directions, additional beams are sometimes reconstructed by interpolation. To account for shearing, some authors allowed the RF regions to deform non-rigidly [144].

There are several **other topics** worth mentioning in this context. The most commonly used similarity measures in block matching are the sum of absolute differences (SAD), sum of squared differences (SSD) and the normalized cross-correlation (NCC). Several studies comparing the performance of these metrics have been presented, e.g. [29][73][128][254]. Other authors have proposed alternative metrics taking into account speckle statistics [46]. Subpixel displacements can be found by either interpolating the similarity functions, e.g. by fitting a parabole or cosine near the peak [38], or by exploiting phase information from the complex cross-correlation function in RF tracking [148].

Finally, because the motion estimates are typically performed independently from one another, they are usually noisy. Without further processing this would lead to noisy strain estimates. An *a posteriori regularisation step* is therefore typically required, e.g. by median filtering [226] or wavelet denoising [9] of the initial displacement estimates, by averaging the strain images [250], or by using least-square strain estimators in 1D (linear curve fitting through the displacement estimates; [112]) or in 2D (plane fitting; [142]). Several authors have also derived strategies to incorporate confidence measures, and only retain the motion estimates with a high tracking quality, e.g. [50][113][131].

Phase-based methods

Some authors have proposed to solve the optical flow equation using the phase information as it should give more robust motion estimates [2][31]. They argued that, compared to intensity-based tissue tracking, using phase information should be less sensitive to brightness fluctuations and more strictly correlated with the image structure. This could be helpful especially in volumetric US images where speckle decorrelation occurs due to the low frame rate, or when temporal variations in the local echo strength occur due to changes in the angle between the myocardial fibers and propagation direction of the US beam [180].

Tautz *et al.* applied a set of quadrature filters in several directions to extract phase information from volumetric US datasets. These are combined into a displacement estimate by using confidence measures extracted from the individual filter responses [237]. Alessandrini *et al.* do not require chosing a direction to extract phase information as they applied the OF equation directly on the phase of the monogenic signal, which is implicitely computed along the direction of maximum energy variation, i.e. along the monogenic orientation [1]. These methods have been recently validated on simulated US datasets, in 2D [1] and in 3D [2][237].

2.3.2 Biomechanical models

These techniques exploit our knowledge about the deformation properties of tissues and construct biomechanical deformation models to mimic their properties and behaviour. The main advantage of these models is their use of informed priors about biomechanical properties that allow to estimate a complex deformation with few degrees of freedom.

Papademetris *et al.* adopted a transversely isotropic linear elastic model for the myocardium, taking into account fiber directions, to generate a dense motion field within the myocardium from the motion estimates obtained at the endo- and epicardial surfaces. The motion estimates on these surfaces were obtained from a shape-tracking approach [189][188]. Sermesant *et al.* presented an electromechanical model of the heart, able to simulate the electrical propagation and the mechanical contraction. By deforming the model to fit the myocardial boundaries present in the US images, it could be used to estimate cardiac deformation [211][212].

2.3.3 Statistical models

This class of methods introduces a-priori knowledge in the motion estimation process by off-line training a statistical model describing cardiac deformations from a large annotated database. Myocardial motion in a new dataset can then be estimated online guided by the statistical model. The advantage of these models is their ability to reduce computational complexity while achieving a robust performance. It is important to note that the set of images used during the learning stage should be representative for the expected range of deformations in the population that it aims to analyze later.

Wang *et al.* proposed a learning-based framework where information from multiple cues is fused together, such as speckle patterns, image boundaries and motion statistics [257][258]. Leung *et al.* used a statistical model of cardiac motion trained from endocardial segmentations to regularize optical flow results [135]. Finally, Duchateau *et al.* constructed an atlas using a database of 2D US images from normal volunteers. This database was subsequently used to quantify the response to cardiac resynchronization therapy in patients by comparing their cardiac motion with the atlas [65].

2.4 Parametric models

Parametric models do not rely on physical models but instead model the deformation using a set of basis functions. By adjusting the coefficients of the basis functions, different deformation fields can be represented. A wide range of basis functions have been employed in medical imaging (e.g. see [99]). This section will concentrate only on those currently used for the analysis of cardiac US images: free-form deformations and radial basis functions.

2.4.1 Free-form deformations

Free-form deformations (FFDs) are one of the most common types of transformation models in medical imaging. A rectangular control point grid is typically superimposed on the image which gets deformed under the influence of the movement of these control points. They were first popularized in the computer graphics community [208], and gained wide acceptance in the medical imaging community when combined with cubic B-splines [125][203]. For the sake of clarity, (2D) displacement can be modelled using a tensor-product of B-splines in the following way:

$$\mathbf{u}_{f\rightarrow f+1}(\mathbf{r}) = \sum_{i\in\mathcal{N}_i}\sum_{j\in\mathcal{N}_j} \boldsymbol{\mu}^{ij}\beta_x^3(\frac{x-\kappa_x^{ij}}{\sigma_x})\beta_y^3(\frac{y-\kappa_y^{ij}}{\sigma_y}) \tag{2.4}$$

with κ_ξ^{ij} and σ_ξ the control point location and spacing respectively, and N_ξ the set of control points within the compact support $\mathcal{N}$ of the B-spline β_ξ ($\xi \in \{x, y\}$).

FFDs have been adopted for assessing cardiac deformation by several research groups. It was first applied by Ledesma *et al.* on 2D US images [132], and its feasibility for 3D motion estimation was illustrated by Elen *et al.* on simulated datasets [67]. The following chapters of this thesis will demonstrate its performance in more realistic imaging scenarios, e.g. [92][94], and propose an alternative control point topology adapted to the cardiac morphology and motion, e.g. [89][90]. The method has been extended to include the time dimension by either formulating the transformation as a diffeomorphism as illustrated by De Craene *et al.* [55][192] and Zhang *et al.* [269], or by explicitely adding a regularization term imposing smoothness in time [270]. Myronenko *et al.* also proposed to incorporate a segmentation-based energy in the cost function [175], and applied the FFD algorithm on pre scan-converted B-mode data in [176].

2.4.2 Radial basis functions

The displacement $\mathbf{u}$ of a certain point $\mathbf{r}$ using radial basis functions (RBF) is given as a function of its distance to every basis function centre κ^i [33]:

$$\mathbf{u}_{f\to f+1}(\mathbf{r}) = \sum_{i\in\Omega} \boldsymbol{\mu}^i F(\left\|\mathbf{r} - \kappa^i\right\|) \tag{2.5}$$

where the contribution of every RBF was summed over the whole image domain Ω. A popular choice for F are thin-plate splines. Please note that a similar nomenclature was used compared to the FFD model in the previous section to highlight similarities. The advantage of RBFs is that the center points can be placed anywhere within the image, as opposed to the regular placement on a grid for the FFD models. Their main disadvantage is that they have a global support which may be undesirable when seeking local transformations.

Radial basis functions have been used in 3D echocardiography to interpolate motion estimates originating from several inputs. For example, Compas *et al.* used RBFs to combine motion estimates from speckle tracking and shape tracking [47]. Duan *et al.* used a block matching approach to estimate motion on the endo- and epicardial surface only, and obtained a dense motion field by applying a RBF interpolation [63].

2.5 Segmentation-based methods

The scope of this chapter is extended slightly to include segmentation-based techniques, which allow tracking myocardial borders over time. However, they typically do not allow to estimate regional cardiac deformation since no point-correspondences exist between segmentations at different frames, and no motion estimates are available within the myocardium unless an interpolation strategy as proposed in [188] would be employed. Nevertheless, they can be used to assess global functional parameters. Providing an extensive review regarding US-based image segmentation is beyond the scope of this section. The reader is therefore referred to reviews by Noble *et al.* [180] and Leung *et al.* [135] for a more in-depth treatment of this topic.

A couple of methods worth mentioning in the context of segmenting myocardial borders from static 2D US images are those that used active contours [39], active shape models [104], active appearance motion models [30] or level-set like formulations [14]. Several of these techniques have been extended to 3D, e.g. in [6][16][179][249], with some of them being commercially available [84][105][222]. Finally, segmentation can also be used to dynamically track myocardial borders from 3D US sequences, e.g. as described in [17][184].

Chapter 3

Non-rigid image registration to assess 2D myocardial deformation: Comparison against speckle tracking

This work was published in:
B. Heyde, R. Jasaityte, D. Barbosa, V. Robesyn, S. Bouchez, P. Wouters, F. Maes, P. Claus, and J. D'hooge. Elastic image registration versus speckle tracking for 2D myocardial motion estimation: a direct comparison in-vivo. *IEEE Trans Med Imaging*, 32(2):449–459, 2013.

3.1 Motivation

Despite the availability of multiple solutions for assessing myocardial strain from ultrasound (US) images (see chapter 2), little is currently known about the performance of the different methods relative to each other. Indeed, such information would have potential implications for the interpretation and applicability of these approaches in clinical practice. In the present chapter we therefore sought to contrast two popular techniques which have proven successful for regional strain estimation. This chapter focuses on 2D strain estimation since it is currently well accepted in clinical practice. Its application to 3D US data will be discussed in chapters 4 and 5.

On the one hand, optical flow methods have been proposed to estimate local myocardial movement. As the name implies, these methods share the same underlying principle: motion is characterized by a flow of pixels with constant intensity. In the *ultrasound community* a particular subgroup of solutions, termed block matching techniques or speckle tracking methods, have received wide-spread attention and have been successfully used to analyze B-mode data [22][29][263]. Several speckle tracking methods have become commercially available and proven useful in the clinical setting [11][40][159][229].

On the other hand, non-rigid image registration techniques, popular in the *image processing community*, have also been suggested to determine myocardial motion. The myocardial deformation field can be parametrized using smooth basis functions, e.g. B-splines [125][132][203]. The motion is then typically regularized by adding extra cost terms to the energy function to be optimized. It has also been shown successful for 2D US cardiac motion estimation [132].

To the best of our knowledge, no studies have been reported on the relative performance of these methods using the same image data. The performance of both techniques was therefore compared in an in-vivo setting against a known ground-truth.

This chapter is organized as follows. Section 3.2 presents the experimental protocol and describes how the image data was gathered. Section 3.3 continues with briefly reviewing both tracking methods, gives details regarding their application on the current data, followed by the performed statistical analysis. Section 3.4 highlights the results and our findings are discussed in section 3.5.

3.2 In-vivo animal setup

This section describes the in-vivo animal setup which will be used as a validation setting in the present chapter, but also in several other upcoming chapters of this thesis.

This investigation conforms to the Guide for the Care and Use of Laboratory Animals published by the US National Institutes of Health (NIH Publication No. 85-23, revised 1996) and was approved by a local Ethics Committee (Ethische Commissie Dierproeven, Ghent University, Ghent, Belgium).

3.2.1 Animal preparation

Fourteen Suffolk sheep (44.3 ± 10.4 kg) were premedicated with an intragluteal injection of ketamine (10 mg/kg) and piritramide (1 mg/kg). They were placed in a dorsal recumbancy on a surgical table and anesthesia was induced via the cephalic vein with an intravenous infusion of propofol (10 mg/kg) and a bolus of sufentanil (0,5 μg/kg). The trachea was intubated and the sheep were mechanically ventilated throughout the procedure with a mixture of sevoflurane, oxygen and room air to maintain normocapnia and normoxia (tidal volume of 8 mL/kg and respiratory rate of 12 times/minute). A gastric tube was positioned to evacuate excess gas and fluids from the reticulorumen. Anesthesia was maintained by a continuous infusion of sufentanil (1 μg/kg/h) and an end-tidal sevoflurane concentration of 2.5%.

A bi-lumen catheter was inserted into the left jugular vein to allow measurement of the central venous pressure and administration of drugs. Furthermore, a catheter-tipped pressure transducer (Millar, Houston, Texas, USA) was advanced into the left ventricle (LV) via the right carotid artery for continuous monitoring of the left ventricular pressure and its first temporal derivative (dP/dt). The systemic arterial pressure was measured in the proximal aorta via a fluid-filled side-line of the arterial sheet.

Ten minutes before surgical incision, a bolus of cisatracurium (20 mg) was administered. A sternotomy was then performed, and the heart was suspended in a pericardial cradle to maintain a normal anatomic configuration. Cardiac output was monitored with a flow probe positioned around the pulmonary artery.

In order to have an independent measure of the ventricular wall deformation throughout the cardiac cycle, a sonomicrometry system (Sonometrics Corporation, London, Ontario, Canada) was used. Microcrystals are small piezoelectric crystals (2 mm) that can emit and detect ultrasonic pulses. By

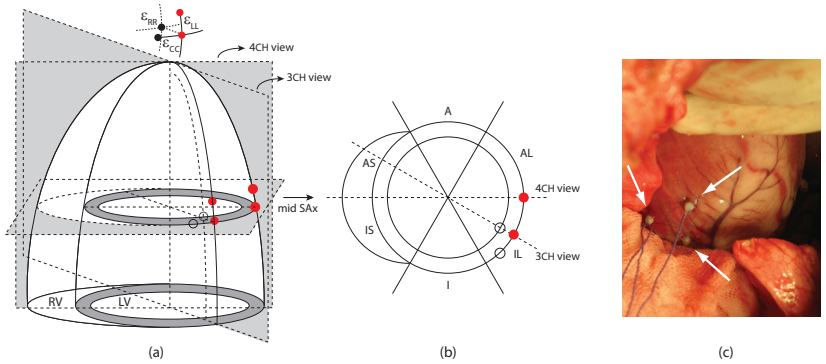

Figure 3.1: (a) Sonomicrometry crystal locations to obtain reference myocardial deformation and the associated 2D image acquisition planes (SAx: short-axis view; 3CH: 3 chamber apical view; 4CH: 4 chamber apical view). (b) Detail of the crystal locations in the mid short-axis plane. Crystal pairs used to obtain the longitudinal strain estimates are colored in red. (c) Corresponding in-vivo locations of the three epicardial IL crystals.

using the speed-of-sound and the time-of-flight between ultrasound emission in one crystal and detection in a neighboring crystal, inter-crystal distance can be calculated continuously at a time resolution of 1 ms and with a spatial resolution of 15.4 μm. In all animals, reference radial ($\varepsilon_{\mathrm{RR}}$), longitudinal ($\varepsilon_{\mathrm{LL}}$) and circumferential ($\varepsilon_{\mathrm{CC}}$) strain components were obtained using four ultrasonic microcrystals attached to the myocardium in the mid-inferolateral (IL) wall in a tetrahedral configuration (see Fig. 3.1a). Three crystals were sutured to the epicardium, resulting in two crystal pairs along the circumferential and longitudinal direction respectively (see Fig. 3.1c), while a fourth crystal was placed subendocardially just radially to the center crystal. The latter was introduced in an oblique way to limit damage to the myocardium under investigation. In two animals, an additional longitudinal crystal pair was placed more laterally towards the anterolateral (AL) wall.

3.2.2 Data acquisition

A GE Vivid7 ultrasound scanner (GE Vingmed, Horten, Norway) equipped with a 2-D matrix transducer (3V probe) was used to acquire volumetric data at a frame rate of 25–32 Hz with electrocardiographic gating over four cardiac cycles. The left ventricle was scanned from an apical position. The optimal combination of spatial and temporal resolution was achieved by decreasing the

volume size and depth to the smallest setting possible, while keeping the whole left ventricle within the field of view.

After volumetric imaging, a 2.5 MHz transducer (M4S) was used to acquire mid short-axis (SAx) B-mode data (frame rate 50-70 Hz). The probe was again positioned on the apex to acquire three-chamber (3CH) and four-chamber (4CH) apical views (frame rate 50-70 Hz). The images were recorded in a plane just parallel to the crystal pairs in order to avoid the crystals showing up as bright spots in the ultrasound data (Fig. 3.1).

A piece of a liver was used as a stand-off to ensure the full left ventricle was always visible in the ultrasound sector and not cut off near the apex (apical planes) or cut off at the anterior wall (short-axis planes).

Image data was collected both at rest and during acute ischemia induced by ligating a distal branch of the left circumflex (LCX) coronary artery. Prior to induction of acute ischemia, the range of strain values was modulated by reducing the inotropic state with esmolol infusion and subsequently increasing it with dobutamine infusion. A physiological target was set to a 50% reduction in $(\mathrm{dP/dt})_{max}$ and a 100% increase in $(\mathrm{dP/dt})_{max}$ relative to baseline for esmolol and dobutamine respectively. Infusion rates were titrated continuously according to this target.

Due to the overlapping frequency bands of the microcrystals and the ultrasound system, both systems could not be operated simultaneously. Therefore, crystal data were acquired immediately before and after each US recording, and the system was switched off during US acquisitions. Crystal data was typically collected over a period of 10-15 cardiac cycles to ensure that enough good quality traces were available for ground truth strain estimation.

3.2.3 Sonomicrometry

Reference strain curves were obtained by post-processing the recorded crystal traces using custom-made software. The following steps were performed successively for all traces: data outliers were removed automatically by median-filtering, parts of the crystal traces with a low quality (e.g. due to signal loss) could be removed manually if required, the ED of every consecutive cardiac cycle was identified based on the onset of the simultaneously recorded LV pressure and the reference displacements were averaged over different cycles.

Strain $\varepsilon_{\boldsymbol{n},\,\mathrm{ED}\to f}$ in every point along a certain cardiac direction $\boldsymbol{n}$ was calculated according to:

$$\varepsilon_{\boldsymbol{n},\,\mathrm{ED}\to f} = \frac{L_{\boldsymbol{n}}(f) - L_{\boldsymbol{n}}(\mathrm{ED})}{L_{\boldsymbol{n}}(\mathrm{ED})} \tag{3.1}$$

Table 3.1: Number of analysed in-vivo datasets

	Segment	B	E	D	I	All
$\varepsilon_{\mathrm{RR}}$	IL	3	4	5	5	17
$\varepsilon_{\mathrm{CC}}$	IL	5	5	5	5	20
$\varepsilon_{\mathrm{LL}}$	IL	5	5	5	5	20
$\varepsilon_{\mathrm{LL}}$	AL	2	1	2	0	5

The datasets are summarized for every stage individually (B: baseline, D: dobutamine, E: esmolol, I: ischemia) and over all stages (All). Reference $\varepsilon_{\mathrm{LL}}$ is recorded in the IL and the AL segment.

where $L_{\boldsymbol{n}}(f)$ is the distance between two adjacent crystals in either the radial, longitudinal or circumferential direction at frame f, and $L_{\boldsymbol{n}}(\mathrm{ED})$ is the respective initial distance at end-diastole (ED).

End-systolic (ES) strain values were determined at aortic valve closure (AVC), defined by $(\mathrm{dP/dt})_{min}-20$ ms [239]. In order to account for any physiological changes occurring during the course of the procedure, reference ES strain values were obtained by averaging recordings made before and after the acquisition of the US data.

3.3 Methods

In this study, 2D image data collected from the last 5 animals (42 ± 8 kg) was used to compare the speckle tracking method and the registration method. The volumetric data of all animals is further analysed in chapter 5.

For the block-matching based approach a well-validated commercially available software package (EchoPac, GE Vingmed, Horten, Norway) was chosen [130][200] that was also extensively used in numerous clinical studies [101][133]. The non-rigid image registration method was implemented within the framework of ITK, a collection of C++ image analysis libraries well-known in the medical imaging analysis society [266]. For both methods, tracking and strain estimation was performed on data from one cardiac cycle.

Three $\varepsilon_{\mathrm{RR}}$ traces in the IL wall and one $\varepsilon_{\mathrm{LL}}$ trace in the AL wall had to be excluded from analysis due to a bad trace quality of the reference crystal data. Furthermore, 4CH views were not recorded during the ischemic case. Table 3.1 summarizes the number of datasets thus available for analysis.

3.3.1 Speckle tracking

A schematic overview of speckle tracking in 2D B-mode image data is shown in Fig. 3.2a. This technique is based on the assumption of a stable local speckle pattern between frames to extract local tissue motion from the displacement of intensity patterns. Displacement of a point $\mathbf{r}$ within a certain region-of-interest (ROI) in one frame I_f is found by a template matching scheme in a search region of the subsequent frame I_{f+1}. An image similarity metric (e.g. sum of squared differences, normalized cross-correlation) is used to determine the matching quality. The position of the best matching block within the search region indicates the most likely tissue displacement $[dx, dy]$. Repeating this procedure for all the points-of-interest within the investigated myocardial tissue, leads to the displacement field $\tilde{\mathbf{u}}_{f\to f+1}(\mathbf{r})$. However, these different motion estimates are performed independently from each other. Without further processing this would lead to noisy strain estimates. An *a posteriori regularisation step* is therefore typically required, e.g. by median filtering [226] or wavelet denoising [9] of the initial displacement estimates, by averaging the strain images [250], or by using least-square strain estimators in 1D (linear curve fitting through the displacement estimates; [112]) or in 2D (plane fitting; [142]).

A trained cardiologist used the EchoPac software to analyze all images. After manual delineation of the endocardial border at end-diastole (ED) identified by the R-peak of the ECG signal, and selecting the appropriate myocardial thickness, the myocardium was tracked throughout the cardiac cycle. The default settings for the spatial and temporal smoothing were used.

The SAx images were automatically divided into 6 equally sized segments around the circumference of the LV. The segments were rotated around the circumference such that the inferior insertion point of the right ventricle marked the border between the inferior and inferoseptal wall. Upon visual inspection of the tracking results by a trained cardiologist, the software allowed to reposition the initial delineation or modify the myocardial thickness if required (e.g. when the automatic tracking quality index supplied by the software was low, or when the tracked borders did not follow the myocardium properly during systole). In practice, all datasets could be adequately tracked and analyzed. End-systole was automatically defined at aortic valve closure (AVC) and manually adjusted if required. End-systolic (ES) $\varepsilon_{\mathrm{RR}}$ and $\varepsilon_{\mathrm{CC}}$ strain values in the IL wall were then exported for further analysis.

A similar process was used to analyze the 3CH and 4CH apical views. Estimated ES $\varepsilon_{\mathrm{LL}}$ values in the walls containing crystal pairs were then selected for further analysis. The software automatically performed a drift-correction.

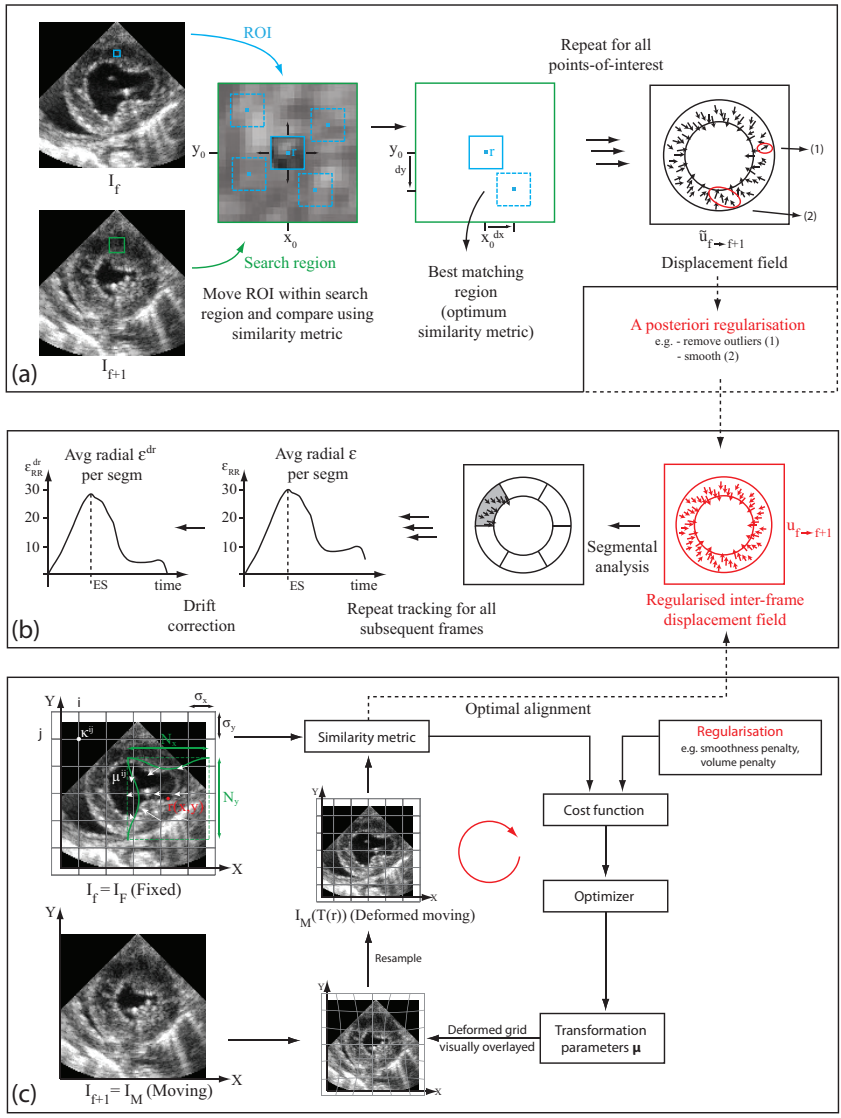

Figure 3.2: Principle of cardiac motion estimation in short-axis B-mode ultrasonic image data for two methods: (a) speckle tracking using a block-matching technique and (c) non-rigid image registration approach using a B-spline transformation field (the B-spline support kernel is represented by a green square). Regularization steps are indicated in red. (b) Both methods follow the same stages to estimate cardiac strain once a regularized inter-frame displacement field is obtained. ROI = region-of-interest

3.3.2 Registration

The same datasets were then processed using a non-rigid registration approach developed in our lab. The current choices for the different components in the registration framework have all been proven useful for myocardial motion estimation from ultrasound data [132]. A more elaborate mathematical background can be found in appendix B.

The inter-frame myocardial displacement was modelled with a two-dimensional third order B-spline tensor-product [203], defined on a rectangular lattice (see Fig. 3.2c):

$$\mathbf{u}_{f\to f+1}(\mathbf{r}) = \sum_{i\in\mathcal{N}_i}\sum_{j\in\mathcal{N}_j} \boldsymbol{\mu}^{ij}\beta_x^3(\frac{x-\kappa_x^{ij}}{\sigma_x})\beta_y^3(\frac{y-\kappa_y^{ij}}{\sigma_y}) \tag{3.2}$$

with κ_ξ^{ij} and σ_ξ the control point location and spacing respectively, and N_ξ the set of control points within the compact support $\mathcal{N}$ of the B-spline β_ξ ($\xi \in \{x, y\}$).

Since image intensities at corresponding points between two consecutive frames are similar for intra-modality registration, the sum of squared differences (SSD) was used as an image similarity metric. Regularization was performed during the optimization process by the addition of a smoothness penalty based on the bending energy of a 2D thin sheet of metal [203] in the cost function C:

$$\begin{aligned} C = \frac{1}{P}\sum_{\mathbf{r}\in I_f}\left[I_f(\mathbf{r}) - I_{f+1}(\mathbf{T}(\mathbf{r}))\right]^2 \\ + \omega\cdot\frac{1}{P}\sum_{\mathbf{r}\in I_f}\sum_{\xi\in(x,y,z)}\left(\frac{\partial^2 T_\xi}{\partial x^2}\right)^2 + 2\left(\frac{\partial^2 T_\xi}{\partial x\partial y}\right)^2 + \left(\frac{\partial^2 T_\xi}{\partial y^2}\right)^2 \end{aligned} \tag{3.3}$$

with P the number of points $\mathbf{r}$, and ω a hyperparameter controlling the influence of the smoothness penalty. In every frame, pixels outside the ultrasound sector were masked to assure that this part of the image did not contribute to the cost function in the registration process.

The optimal transformation field $\mathbf{T}_{f\to f+1}(\mathbf{r}) = \mathbf{r} + \mathbf{u}_{f\to f+1}(\mathbf{r})$ was estimated iteratively with a limited memory Broyden-Fletcher-Goldfarb-Shanno optimization routine with simple bounds (LBFGSB, [36]). This optimizer uses an approximation of the inverse of the Hessian matrix during the optimization routine. Due to its resulting low memory requirement it is well suited for optimization of a large amount of parameters. In order to capture small deformations, the model complexity was gradually increased in three stages by refining the B-spline grid with a factor of two in every stage.

In practice, subsequent images in the cardiac cycle were registered to each other in a pairwise fashion. To find the transformation field $\mathbf{T}$ between frame f with respect to the frame corresponding with ED, inter-frame transformation fields were cumulated as follows:

$$\mathbf{T}_{ED\to f}(\mathbf{r}) = \mathbf{T}_{f-1\to f}(\mathbf{r}) \circ \cdots \circ \mathbf{T}_{2\to 3}(\mathbf{r}) \circ \mathbf{T}_{ED\to 2}(\mathbf{r}) \tag{3.4}$$

In order to assess strain within a certain ROI, a procedure similar to the one used in the EchoPac software was followed. The endocardium was first manually contoured in the ED frame using custom-made software (Speqle3D, KU Leuven, Belgium). A ROI for strain estimation was then created by expanding the endocardial contour along its normal to represent the myocardium. Care was taken to ensure that this ROI was as close as possible to the one used by the speckle tracking method. For the SAx images, this region was subsequently populated in the radial and circumferential direction with 5 and 60 sample points respectively, and given a label corresponding to one of the 6 equally spaced segments around the circumference. Similarly, 5 and 60 sample points were used in the apical images to populate the ROI in the radial and longitudinal direction respectively. Segments were labeled according to one of three equally spaced longitudinal levels from base to apex, either on the septal or lateral side, thus leading to 6 segments.

Using the obtained inter-frame displacement fields from the registration results, the manually delineated ED contours could be propagated over the cardiac cycle. Similarly, the cumulative displacement could be calculated in every sample point. Strain $\varepsilon_{\boldsymbol{n},\,\mathrm{ED}\to f}$, where $\boldsymbol{n}$ corresponds to either the radial, circumferential or longitudinal direction, was then calculated according to Eq. (3.1), corresponding to the procedure used in the processing of the crystal data. Similar to what is typically performed in EchoPac, the estimated strain curves were then drift compensated to obtain values of zero strain at the end of the cardiac cycle (ED2) by distributing the remaining strain offset $\varepsilon_{\boldsymbol{n},ED\to ED2}$ uniformly over the cardiac cycle (containing N frames). The drift compensated strain $\varepsilon^{dr}_{\boldsymbol{n},\,\mathrm{ED}\to f}$ in frame f thus becomes:

$$\varepsilon^{dr}_{\boldsymbol{n},\,\mathrm{ED}\to f} = \varepsilon_{\boldsymbol{n},\,\mathrm{ED}\to f} - \frac{f-1}{N-1}\,\varepsilon_{\boldsymbol{n},\,\mathrm{ED}\to\mathrm{ED2}} \tag{3.5}$$

Finally, strain values were averaged within each segment and ES strain values were extracted in the IL wall. Similar to the speckle tracking method, the ES frame was visually defined by AVC. A schematic overview of the strain calculation process is shown in Fig. 3.2b.

3.3.3 Statistical analysis

For the SAx images, the Pearson correlation coefficient was used to compare the estimated end-systolic $\varepsilon_{\mathrm{RR}}$ and $\varepsilon_{\mathrm{CC}}$ values in the mid IL wall with those obtained from sonomicrometry. Similarly, reference end-systolic $\varepsilon_{\mathrm{LL}}$ strain values obtained by the crystal pairs in the IL and AL segment were compared against the estimated strain values in the corresponding image planes. Results from both segments were combined in one correlation plot. Bland-Altman analysis was performed for all three components.

Fisher's z-transformation was used to compare the strengths of different correlations, whereas a t-test was used to assess differences in the regression slope of both methods. For the Bland-Altman plots, a t-test was used to compare the bias and an F-test was employed to analyze differences in the limits of agreement (LOA).

In order to have a more robust look at the strain behaviour over the entire cycle, 20 strain values were extracted at equidistant time points. Correlations against sonomicrometry were then calculated by using a linear mixed model which accounted for repeated measurements (i.e. the dependency of the measurements over the different time points within the same dataset, and the dependency of the measurements over the different stages within the same animal).

In addition to these measures, five SAx and five apical images were reanalyzed to assess intra-observer variability. Variability was expressed as the mean difference $\pm$ standard deviation between two observations.

3.4 Results

Fig. 3.3 shows the correlation between the ES radial strain values obtained by sonomicrometry and those measured by speckle tracking (panel a) and registration (panel b). The correlation coefficients were 0.64 ($p=0.005$) and 0.85 ($p<0.001$) for the speckle tracking and registration method respectively. Bland-Altman analysis revealed a bias of 18.52% and 4.65% for the speckle tracking (Fig. 3.3c) and registration method respectively (Fig. 3.3d). Limits of agreement are also indicated in the respective plots.

In the circumferential direction, the correlations were 0.73 ($p<0.001$) for the speckle tracking method and 0.80 ($p<0.001$) for the registration method (Fig. 3.4a-b). The bias was –7.72% and –9.68% respectively (panels c and d).

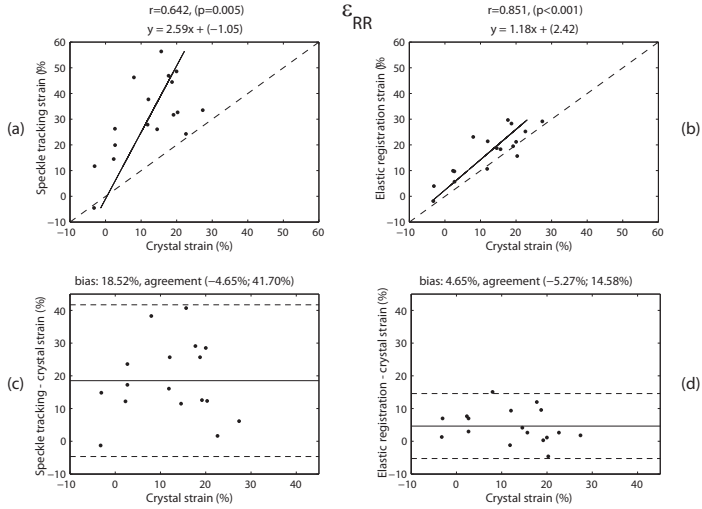

Figure 3.3: Scatter plots of $\varepsilon_{\mathrm{RR}}$ measured by (a) speckle tracking and (b) the registration method against reference crystal strain. The dotted line represents the line of identity. (c-d) Corresponding Bland-Altman plots of estimated $\varepsilon_{\mathrm{RR}}$ for speckle tracking and the registration method respectively.

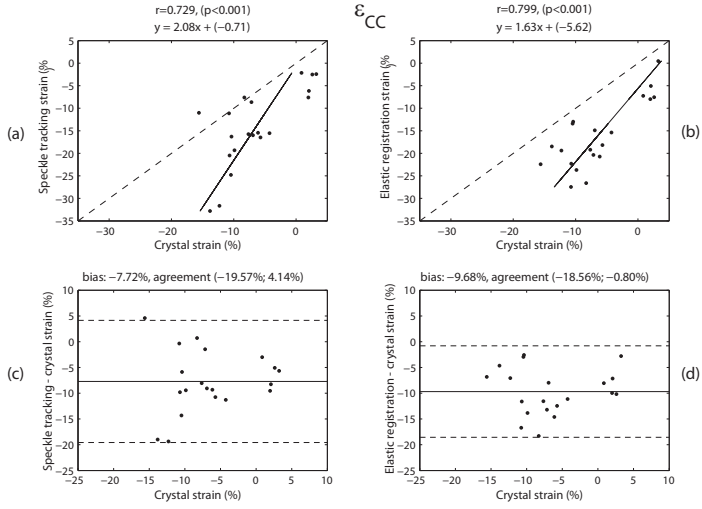

Figure 3.4: Scatter plots of $\varepsilon_{\mathrm{CC}}$ measured by (a) speckle tracking and (b) the registration method against reference crystal strain. The dotted line represents the line of identity. (c-d) Corresponding Bland-Altman plots of estimated $\varepsilon_{\mathrm{CC}}$ for speckle tracking and the registration method respectively.

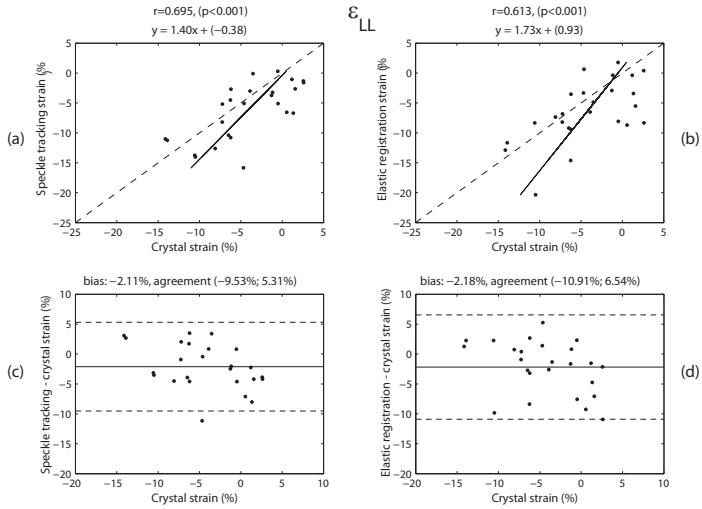

Figure 3.5: Scatter plots of $\varepsilon_{\mathrm{LL}}$ measured by (a) speckle tracking and (b) the registration method against reference crystal strain. The dotted line represents the line of identity. (c-d) Corresponding Bland-Altman plots of estimated $\varepsilon_{\mathrm{LL}}$ for speckle tracking and the registration method respectively.

Correlation coefficients for the longitudinal component were 0.70 ($p<0.001$) and 0.61 ($p<0.001$) respectively (Fig. 3.5a-b), while the bias was –2.11% and –2.18% respectively (panels c and d).

Over the entire cardiac cycle correlations for $\varepsilon_{\mathrm{RR}}$ were 0.59 ($p<0.001$) and 0.74 ($p<0.001$) respectively, for $\varepsilon_{\mathrm{CC}}$ they were 0.56 ($p<0.001$) and 0.76 ($p<0.001$) respectively, and for $\varepsilon_{\mathrm{LL}}$ they were 0.47 ($p<0.001$) and 0.53 ($p<0.001$) respectively.

For the speckle tracking method, variability was $9.6 \pm 7.4\%$, $3.4 \pm 3.3\%$ and $1.4 \pm 1.3\%$ for $\varepsilon_{\mathrm{RR}}$, $\varepsilon_{\mathrm{CC}}$ and $\varepsilon_{\mathrm{LL}}$ respectively. Similarly, intra-observer variability for the registration method was $1.8 \pm 1.5\%$, $1.8 \pm 1.4\%$ and $1.1 \pm 1.0\%$ resp.

Example strain curves obtained by sonomicrometry and the estimated strain curves by both methods are shown in Fig. 3.6. Table 3.2 summarizes the results of the statistical analysis.

Table 3.2: Statistical analysis ST vs Reg

	Correlation strength			Regression slope		
	ST	Reg	p	ST	Reg	p
ε_{RR}	0.642	0.851	0.09	2.59	1.18	<0.01*
ε_{CC}	0.729	0.799	0.31	2.08	1.63	<0.01*
ε_{LL}	0.695	0.613	0.32	1.40	1.73	0.07

	Bland-Altman bias			Bland-Altman LOA		
	ST	Reg	p	ST	Reg	p
ε_{RR}	18.52	4.65	<0.001*	–4.65 .. 41.7	–5.27 .. 14.58	<0.001*
ε_{CC}	–7.72	–9.68	0.13	–19.57 .. 4.14	–18.56 .. –0.8	0.11
ε_{LL}	–2.11	–2.18	0.48	–9.53 .. 5.31	–10.91 .. 6.54	0.22

P-values comparing speckle tracking (ST) and registration (Reg) in terms of correlation coefficient, slope of the regression line, Bland-Altman bias and Bland-Altman limits of agreement (LOA). $p < 0.05$ was considered significant and is indicated with a $*$.

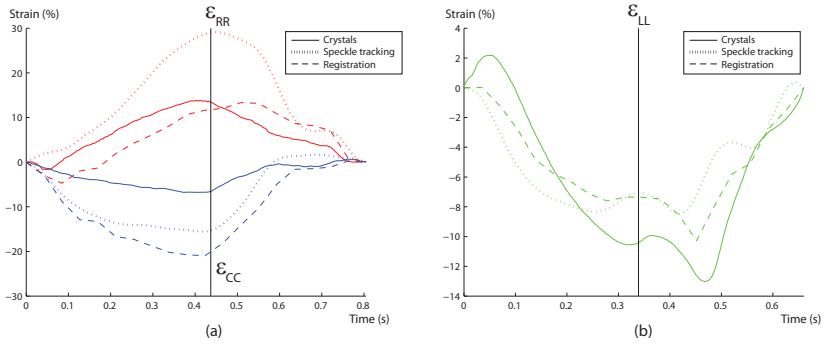

Figure 3.6: (a) Example radial and circumferential strain curve (from a mid short-axis acquisition) and (b) example longitudinal strain curve (from an apical three-chamber view) as obtained from the microcrystals (full line) and estimated by the speckle tracking method (dotted line) and the registration method (dashed line). The end-systolic timing is indicated with a vertical line.

3.5 Discussion

In this chapter, a speckle tracking method and a non-rigid image registration technique were compared in-vivo against a known ground-truth. To the best of our knowledge, no studies have been reported on the relative performance of these methods using the *same* image data.

3.5.1 Short-axis views

The above results suggest that the image registration method is the preferred method over speckle tracking for the assessment of radial strain. Only a moderate $\varepsilon_{\mathrm{RR}}$ correlation was found for the block-matching method, whereas the image registration method performed considerably better (on the edge of being statistically significant, p=0.09). Furthermore, the limits of agreement were also narrower (p<0.001), and the bias was also smaller (p<0.001). Perfect agreement between the ground truth and a strain estimation method occurs when all points lie along the line of equality. The slope of the $\varepsilon_{\mathrm{RR}}$ regression line measured with the registration method lay closer to this ideal line than the block matching method (Fig. 3.3c; p<0.01).

On the other hand, both methods seem competitive for the $\varepsilon_{\mathrm{CC}}$ component, with a slight preference for the image registration method. A good correlation was obtained for both methods against sonomicrometry (Fig. 3.4a-b), with a higher correlation coefficient for the registration method, but this was not statistically significant (p=0.31). Moreover, no statistically significant difference in $\varepsilon_{\mathrm{CC}}$ bias (p=0.13) nor LOA spread (p=0.11) was found, although the LOA spread was narrower for the registration method (Fig. 3.4c-d). However, the slope of the $\varepsilon_{\mathrm{CC}}$ correlation line measured with the registration method lay closer to the line of equality (p<0.01).

These findings may be explained in terms of the underlying tracking principle which is different for both methodologies. Block-matching methods rely on selecting stable speckles within a certain ROI and tracking them on a frame-by-frame basis throughout the cardiac cycle employing correlation criteria. Registration methods on the other hand, use a more global approach in which the cardiac motion is resolved by finding the optimal deformation field between consecutive frames. During registration, regularization is therefore intrinsically embedded in the optimization process (e.g. the recovered transformation field should be smooth), whereas block-matching methods usually need a post-processing regularization step (e.g. median filtering of the motion estimates or discarding estimates having a low tracking quality). In addition to tracking local features ('speckles'), registration methods also

take global features into account (e.g. strong endocardial and epicardial borders). Registration methods may therefore retrieve motion better when large displacements occur as the associated decorrelation of the speckle pattern may lead to undesirable results for the speckle tracking method.

Our correlation findings and the fairly large limits of agreement for $\varepsilon_{\mathrm{RR}}$ in the block-matching method are in agreement with previous studies. Reant *et al.* performed a similar in-vivo experiment and found a correlation of 0.61 (versus 0.64 in the present study) for radial strain estimation in SAx images [200]. Moreover, Koopman *et al.* reported significantly different $\varepsilon_{\mathrm{RR}}$ values and wide limits of agreement between different block-matching methods [122]. Similar observations were made by Bansal *et al.* [10]. This suboptimal performance could be related to the fact that the spatial motion gradient has to be calculated over a relatively small region due to the limited wall thickness. Since block-matching methods only make use of local image information, radial strain might thus be more prone to error. The obtained $\varepsilon_{\mathrm{CC}}$ correlation for the block matching method (r=0.73) is also in line with the findings of Reant *et al.* (r=0.69) [200].

As can be deduced from table 3.2, both methods seem to overestimate the excursions in the radial and circumferential direction with respect to the ground truth. From a methodological point-of-view this is counterintuitive as the presence of decorrelation should not introduce a bias (random errors lead to zero bias) and the embedded regularization steps shouldn't increase the measured strain values. It is therefore more likely that the strain measured in the imaging planes did not accurately reflect the implanted crystal pair distances. The endocardial crystal of the radial crystal pair was placed subendocardially by an experienced cardiac anesthesiologist and its position was echographically verified. Since the short-axis images were acquired at a mid-ventricular level, the movement of trabecular tissue and papillary muscles during systole naturally contributes to the apparent wall thickening in the acquired ultrasound images. As such, it is therefore likely that strain was extracted over a larger myocardial extent compared to the actual reference crystal pair distance during systole, causing an overestimation of the radial strain component. Circumferential strain on the other hand was measured in the mid myocardium for both methods, whereas the reference measures were extracted from an epicardial placed crystal pair. Some studies suggest a heterogeneous strain distribution exists transmurally with the lowest circumferential strain located at the epicardium [28]. This is in correspondence with our findings and may thus explain the observed $\varepsilon_{\mathrm{CC}}$ overestimation by both methods.

Another possible cause of error could be a mismatch in timing between the reference measurements (based on pressures), and the strain estimation methods (based on the ECG for ED and AVC for ES). However, we believe this

mismatch should be small given that we followed the methodology described by Theroux *et al.* [239]. Finally, strain is also sensitive to the exact investigated location, especially in the radial and circumferential direction where the transmural gradient is known to be large [28]. Therefore, another source of error between both methods could have resulted from differences in ROI and segment definitions, even though care was taken to avoid this as much as possible.

3.5.2 Apical views

As can be inferred from table 3.2, no statistical differences for the correlation coefficient, regression slope, bias and LOA between both methods could be made for the apical views. Surprisingly, the $\varepsilon_{\mathrm{LL}}$ correlation was only moderate in comparison with other validation studies looking into regional longitudinal strain estimation. In this chapter we found a correlation of r=0.7 for the speckle tracking method ($p<0.001$) and r=0.61 for the registration method ($p<0.001$). On the other hand, higher correlations were reported by e.g. Langeland *et al.* in an animal study (r=0.94 for a 3CH view and r=0.86 for a parasternal view in [130]), by Reant *et al.* (r=0.81 in [200]) or by Pirat *et al.* (r=0.83 in [193]).

There are several reasons which may explain this discrepancy. According to the reference strain measurements, the majority (80%) of the $\varepsilon_{\mathrm{LL}}$ strain values lie between [−7.25%..2.6%] strain. Since the strain range is already low, outliers influence the correlation strength intrinsically more, making it harder to achieve a high correlation. Moreover, these values are also low compared to what could typically be expected. By means of comparison, normal longitudinal strain values in human subjects are typically in the order of –20% [101]. These low strain values may be explained in terms of physiological changes induced by the surgical procedure. It is well known that performing a pericardiotomy, can have an impact on regional myocardial function [7] and influences the longitudinal motion of the heart [219]. Furthermore, the cardio-depressive effects of the anesthesia could have further decreased the range of the observed strain values [24][152]. Finally, we observed that longitudinal strain in our open-chest, open-pericardium sheep model was spatially inhomogeneous (Fig. 3.7). This may have introduced additional variability in the measurements, and lead to the relatively low observed correlation values. Similar findings were reported in other studies, e.g. in open-chest pigs radial strain was higher in the anterior wall compared to the posterior wall [160][165], in volunteers longitudinal strain was higher in the anterior wall compared to the posterior wall [147], and regional strain inhomogeneities were found in a clinical US [107] and MRI study [28].

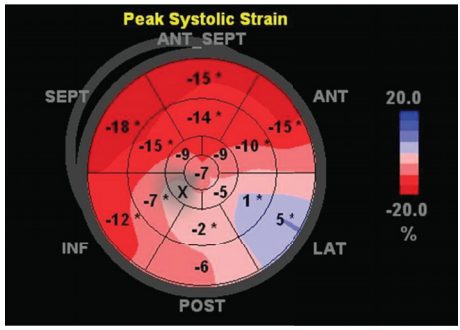

Figure 3.7: Example bullseye plot as exported from EchoPac by analyzing the three apical views. Longitudinal strain values for an animal at baseline conditions before implanting crystals, are indicated using the color scheme on the right. Numbers represent the average value for each segment. The cross refers to unfeasible tracking near the apex.

3.5.3 General remarks

In the present study, the performance of both methods was evaluated using scan converted B-mode data. As an alternative, motion estimation could be performed on data before scan conversion, i.e. on the enveloppe detected data or even on the raw radio frequency (RF) data. This avoids the introduction of interpolation errors in the image which is inherent to the scan conversion process. B-mode images on the other hand are more widely available, easier to interpret and also depict true distances. Elen *et al.* performed non-rigid image registration on enveloppe data but showed that avoiding the interpolation step did not significantly improve the results of the motion estimation [67]. Early studies have shown that algorithms which work on RF data can achieve more accurate, sub-pixel axial motion estimates but at a higher computation cost compared to B-mode tracking. The lack of RF speckle patterns in the lateral direction also results in a poorer spatial resolution compared to the beam direction [29]. Several speckle tracking methods have since been developed using RF data (e.g. [129][144]). In theory, registration methods could also be performed on the same data but the increased computational cost may be impractical. Thus far, RF methods have been studied exclusively in research environments and are not clinically available. To the authors' best knowledge no direct comparisons between B-mode and RF tracking methods have been reported. Given the above arguments and in order to keep the comparison fair, the same underlying data was used in this study, i.e. scan converted B-mode data.

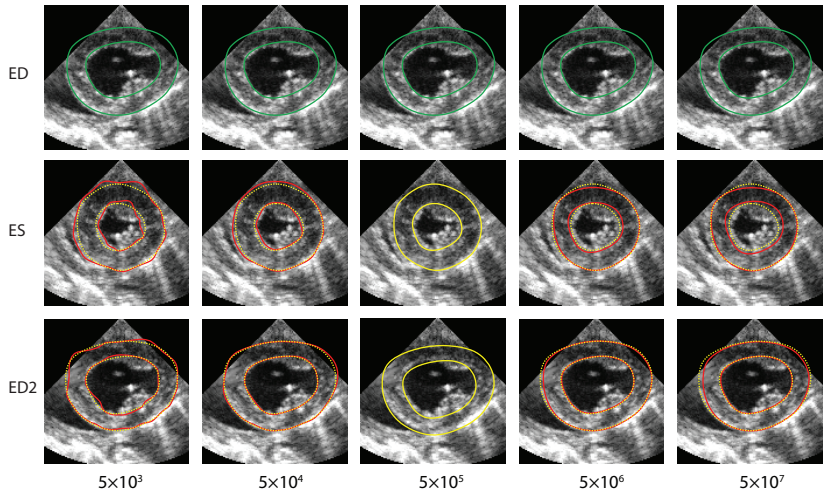

Figure 3.8: Influence of the smoothness factor weight ω for a short-axis dataset showing the tracking results at several phases during the cardiac cycle: end-diastole (ED, top), end-systole (ES, middle) and at the end of the cardiac cycle (ED2, bottom). The colored contours visualise the tracking results: (green) delineation of the region-of-interest (ROI) at ED; (yellow) propagated ROI at ES and ED2 for the preferred weight ($\omega = 5{\times}10^5$) overlayed on neighboring images as a dotted line; (red) propagated ROI for the other considered weights.

The weight of the smoothness factor ω in the registration method may lead to improbable tracking results if set improperly. In this study, it was fixed to 5×10^5 for both SAx and apical images, and was determined by visually assessing the tracking results of three SAx and three apical datasets. Increasing the influence of the smoothness constraint too much restricts the motion while decreasing it leads to too much degrees of freedom. From Fig. 3.8 it is clear that low ω values result in unphysiological propagated contours as they become too wrinkled, whereas barely any movement is visible for high ω values. No systematic further finetuning with respect to the ground truth was performed in order not to overtrain the registration method and to allow for a fair comparison with the commercially available speckle tracking software package.

In terms of computational speed, the commercial speckle tracking method of EchoPac is clearly faster as it takes roughly 5–10 s to estimate motion for a full cardiac sequence. In comparison, our current non-optimized implementation of the registration method takes roughly 150–180 s for a full cycle while running on a laptop equipped with a 2.8 GHz Intel Core i7-2640M CPU. Within this context, it is worth noting that the EchoPac software only estimates motion in

a predefined ROI guided by stable speckle pattern motions. The registration method on the other hand, produces a dense motion field over the complete image irrespective of the chosen ROI. The ROI is used afterwards to indicate which parts of the motion field should be used for strain estimation. As such, it is intrinsically more computationally intensive but also uses neighboring information (e.g. papillary muscle or pericardial motion) to guide the solution. A lot of research efforts have been made in speeding up registration tasks by moving computations to GPUs or even across multiple GPUs through horizontal parallelization [216]. For example, some authors report up to a 50 fold calculation speed improvement compared to CPU-based implementations [173]. This would already make these registration methods competitive in terms of computation time.

3.5.4 Limitations

The major limitation of the present study is the delineation of the region-of-interest in both methods. Due to technical limitations of the EchoPac software, the exact endocardial and epicardial contour could not be exported into the software used for the registration method (Speqle3D). Care was taken to ensure the borders matched as closely as possible by visually comparing both contours. In order to assess how robust the measurements are to changes in the placement of the contours, measurements were repeated for five SAx and five apical views. Variability was expressed as the mean difference $\pm$ standard deviation between the two observations. For the registration method, intra-observer variability was low: $1.8 \pm 1.5\%$, $1.8 \pm 1.4\%$ and $1.1 \pm 1.0\%$ for $\varepsilon_{\mathrm{RR}}$, $\varepsilon_{\mathrm{CC}}$ and $\varepsilon_{\mathrm{LL}}$ respectively. Variability for the EchoPac software was markably higher: respectively $9.6 \pm 7.4\%$, $3.4 \pm 3.3\%$ and $1.4 \pm 1.3\%$. As mentioned above in section 3.5.3, this may be related to the fact that the registration method produces a dense motion field for the complete image irrespective of the chosen ROI, whereas the EchoPac software only estimates motion in a predefined ROI. Reanalyzing the data with a slightly different ROI may thus result in a different selection of stable speckle patterns, intrinsically leading to a higher intra-observer variability. The higher variability of the EchoPac software is also in line with previous studies where radial strain measures had the highest variability [122][199] and variability on a segmental level was considerably higher compared to those on a global level [242].

Another limitation is that the performance of the methods was compared only in one region for all strain components. However, the amount of crystals that can be acquired simultaneously is limited by the sonomicrometry system (in our case this was 7 crystals) and it also prolongs the surgical procedure. We choose to implant the crystals at the infero-lateral side to ensure the crystals

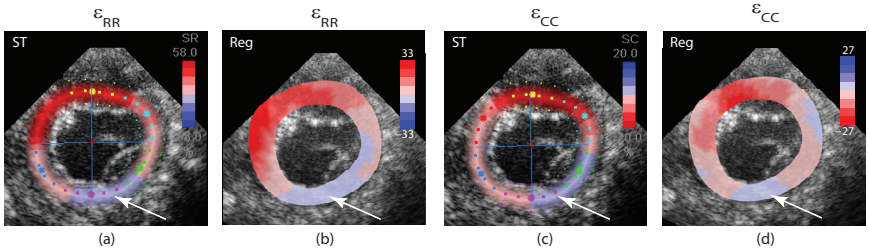

Figure 3.9: Qualitative comparison of (a-b) $\varepsilon_{\mathrm{RR}}$ and (c-d) $\varepsilon_{\mathrm{CC}}$ strain maps at end-systole for an ischemic dataset as tracked by: ST = speckle tracking of EchoPac, Reg = registration. Ischemia was induced by ligation of the left circumflex artery. Blue regions in the infero(-lateral) segments (white arrow) highlight the ischemic area.

(and the wires) would not interfere with the positioning of the probe when scanning the SAx images from the anterior side. Alternatively, tagged MRI images are often used in clinical studies to provide reference values in multiple regions. However, given the current length of the open chest surgery (over 8 hours) and complexity of the procedure this was unfeasible.

In the present study, both methods were not quantitatively compared in terms of their spatial resolution, or in other words in terms of their resolving power to identify and assess the size of dysfunctional regions. It remains unclear to the authors how ground truth estimates can be obtained in an animal setting that would allow to perform such a comparison. An example of a qualitative comparison for an ischemic dataset is shown in Fig. 3.9. While both methods identified the region of abnormal (negative) $\varepsilon_{\mathrm{RR}}$ and (positive) $\varepsilon_{\mathrm{CC}}$ strain in the ischemic area (blue zone), it is hard to judge which method is superior in terms of spatial resolution. However, according to the authors' best knowledge no such comparison studies have been performed thus far. There are indications in literature that both methods are able to detect dysfunctional regions [94][194], but it may still be too early to predict whether these findings have prognostic value in clinical practice [171].

3.6 Conclusions

In this chapter, the performance of two methods for cardiac strain estimation was compared against each other in an in-vivo animal setup, using sonomicrometry as a gold standard reference measurement. While the correlation and limits of agreement of a block matching approach and the non-rigid image registration method were comparable for the $\varepsilon_{\mathrm{CC}}$ and $\varepsilon_{\mathrm{LL}}$ component, imposing regularization during the motion estimation process (i.e. as embedded in the non-rigid image registration), showed to be advantageous for radial strain estimation as it improved performance considerably. Moreover, the bias and the limits of agreement were also smaller in this direction. The registration method also had a lower intra-observer variability. Whether one method outperforms the other in detecting dysfunctional regions remains the topic of future research.

Chapter 4

Non-rigid image registration to assess 3D myocardial deformation: Experimental validation in tissue-mimicking phantoms

This work was published in:
B. Heyde, S. Cygan, H. Choi, B. Lesniak-Plewinska, D. Barbosa, A. Elen, P. Claus, D. Loeckx, K. Kaluzynski, and J. D'hooge. Regional cardiac motion and strain estimation in three-dimensional echocardiography: A validation study in thick-walled univentricular phantoms. *IEEE Trans Ultrason Freq Control*, 59(4):668–682, 2012

4.1 Motivation

Three-dimensional (3D) echocardiography has relatively recently matured as a clinical imaging technique to overcome several limitations of conventional 2D echocardiographic imaging, such as foreshortening and out-of-plane motion. As discussed in chapter 2, several 2D strain estimation methods have been extended to 3D motion and strain estimation, e.g. by segmentation of the myocardium [185][188], by 3D speckle tracking (ST) on B-mode data [50][62] or on RF-data [143][145], by non-rigid image registration [56][67][175][270], by combining differential optical flow with statistical modeling [135] or by fusing segmentation with block matching formulated in a Bayesian framework [258].

Given the encouraging results of image registration for 2D strain estimation as obtained in chapter 3, we aimed to further explore the possibilities of this technique for 3D strain estimation. An initial feasibility study on simulated sequences had been performed by Elen *et al.* within our lab [67]. This method was shown to be reliable in extracting *global* LV functional parameters in simulated datasets [67] and in a clinical setting [19]. It was also shown to be accurate in assessing global LV functional indices, such as stroke volume (SV) and ejection fraction [18]. However, a thorough validation on a *regional* level was still lacking.

The aim of the present study was therefore to validate this methodology experimentally in a more realistic imaging scenario by (i) comparing the estimated 3D strain tensor with a reference method on a regional level and by (ii) investigating to what extent regions of abnormal deformation could be accurately detected by image registration techniques.

The second goal is of particular interest when a strain estimation methodology is to be employed in a clinical setting where understanding the resolving power of an automated method is crucial for an objective diagnosis, i.e. the required strain contrast with the surrounding tissue and the minimal size of a dysfunctional region such that it can still be detected. To our knowledge and at the time of writing, *quantitative* studies of this matter had not yet been performed for any of the cardiac strain methodologies mentioned above, including the 2D speckle tracking approaches. More qualitatively, the proof-of-principle was demonstrated only by Crosby *et al.* using bullseye plots. They showed that their 3D speckle algorithm was able to detect areas of reduced strain in patients with a myocardial infarction [50]. However, no quantitative analysis was carried out and results were lumped for two cases. As such, this research area still remains largely uncharted terrain, which the present chapter attempts to explore.

4.2 In-vitro phantom setup

4.2.1 Phantom construction

Univentricular phantoms with realistic LV dimensions were manufactured similar to the methodology previously described by Lesniak-Plewinska *et al.* [134]. The phantoms had the shape of a truncated thick-walled ellipsoid as an approximation of the LV shape. Stress-free model geometry and dimensions are shown in Fig. 4.1a. The base-to-apex length was 100 mm, while the major and minor ellipse axes were 60 mm and 40 mm respectively. Wall thickness was uniform across the phantom and equal to 10 mm. At the basal level, the model extended eccentrically to form a collar used to fix the phantom into the setup (see next section). The intracavity volume equaled 100 mL in unloaded conditions.

To mimic appropriate mechanical and acoustic properties, a deionized water solution consisting of 10 mass% (m%) polyvinylalcohol (PVA; Sigma Aldrich, St. Louis, USA) and 10 m% glycerin (Chempur, Piekary Slaskie, Poland) was used. Qualitatively, the added glycerin gave the phantom a more detailed speckle pattern, which may be due to the influence of the glycerin on the gelation process [49]. The PVA solution was slowly heated in an oven to 80°C and stirred until it became fully dissolved. The hot solution was then poured into a mold made of casting polyurethane elastomer (UR 3435/45, Axson, France, Fig. 4.1b) and allowed to cool down to room temperature.

This PVA solution becomes a cryogel when subjected to freezing. Its properties are among others dependent on the PVA concentration, the number of freeze-thaw cycles, the freeze temperature and the freezing/thawing rate [231]. Its stiffness increases with the number of freeze/thaw cycles [74]. Two freeze-thaw cycles were found to give the desired stiffness. Each cycle consisted of a 24 hours freezing period in a closed laboratory freezer at –25°C, followed by a 48 hours thawing period (see Fig. 4.1c). At the end of the freezing stage, the freezer was turned off and temperature was allowed to slowly increase back to room temperature. During freezing, the mold cover was not completely tightened to allow the material to bulge on the side of the fixing collar. Due to a very slow thawing process over 48 hours and a high thermal conductance of the PVA due to the high water content, any present temperature gradient throughout the phantom wall would be negligible.

Some phantoms were homogeneous (Fig. 4.1d) while others had a cylindrical harder inclusion embedded to mimic a dysfunctional region. The latter models were produced in two stages. Initially, a donor phantom was manufactured as described above, being subjected to either two (for the soft inclusion) or four

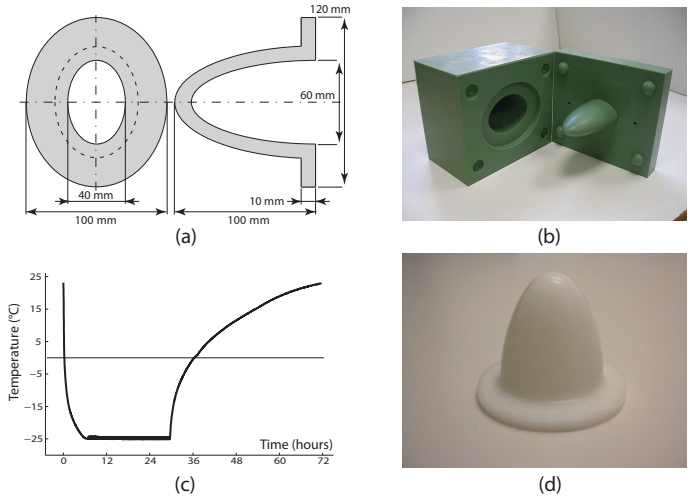

Figure 4.1: PVA phantom construction: (a) stress-free geometry and dimensions, (b) mold used for PVA casting, (c) temperature inside the freezer during one freeze-thaw cycle and (d) resulting phantom.

freeze-thaw cycles (for the hard inclusion). Then, a circular inclusion was cut from the donor phantom and placed at its corresponding location into the mold of the acceptor phantom. The production process was then repeated and two additional freeze-thaw cycles were used. In total, two homogeneous phantoms and six heterogeneous phantoms were constructed by varying the inclusion stiffness, location and size (as shown in table 4.1). The evaluated combinations were defined prospectively. In order to reduce the amount of heterogeneous phantoms that needed to be manufactured, no large and stiff inclusion variant was made. Moreover, it was expected that the regional abnormality in this phantom variant would be easiest to detect.

In order to assess the stiffness of the uniform phantoms and the inclusions, small cubic samples were made by casting the PVA solution in a thick-walled silicone-rubber mold with inner cavity dimensions approx. 54×40×22 mm. The samples were manufactured by subjecting them to the same freeze-thaw cycles as the phantoms. Sample stiffness was assessed using a basic uniaxial compression test with a pressure column. Measurements were taken dynamically, with approximately two steps of compression per second, each step corresponding to a displacement of 0.75 mm. For every compression step, the stress-strain relationship was then calculated according to Hooke's law. The Young's modulus was estimated according to the methodology outlined in [74] as an average of three compression measurements.

Table 4.1: Constructed heterogeneous phantoms

	Size [Diameter]		
	Small (9 mm)	Medium (17 mm)	Large (27 mm)
Stiffness			
Hard	•	• ⋆	
Soft	•	•	•

Different heterogeneous phantoms were constructed to investigate the influence of inclusion size, stiffness and position on the 3D strain estimates. The symbol represents the inclusion location in Fig. 4.5b: • (basal position, 30mm from fixing collar), ⋆ (apical position, 60mm from fixing collar).

4.2.2 Experimental setup and instrumentation

An experimental setup to mount and cyclically deform the phantoms was built in collaboration with the University of Warsaw, Poland [134]. A schematic representation is shown in Figs. 4.2 and 4.3a.

All phantoms were submerged in a deionized water-filled plexiglas tank and mounted in the setup by fixing the PVA collar between two polyethelene plates (item 8). Prior to phantom deformation, bonding between the inclusion and surrounding phantom tissue was manually and visually checked. In order to balance the speed-of-sound differences at the water-phantom interface and to obtain additional attenuation in the surrounding phantom solution, 10 m% glycerin (Acros Organics, Geel, Belgium) was added to the water in the tank and the tubing system. Because the phantom also contained glycerin, there was no osmotic pressure difference which would otherwise dehydrate the phantom.

During operation, a step motor (QMOT QSH6018-65-28-210, Trinamic Motion Control, Hamburg, Germany) controlled by a microprocessor, powered two reciprocally moving pistons to cyclically deform the model (items 1 to 4). A closed circulation was thus created with the undeformed resting state of the phantom corresponding to end-systole; and end-diastole being reached at a maximum displacement of the pistons. The SV, heart rate (HR), systole-diastole time ratio and volume waveform could be modified. The tank walls were covered with linings featuring high attenuation and low reflection of ultrasound (Aptflex F28, Precision Acoustics, Dorchester, UK) to prevent echoes from the plexiglas tank (item 7).

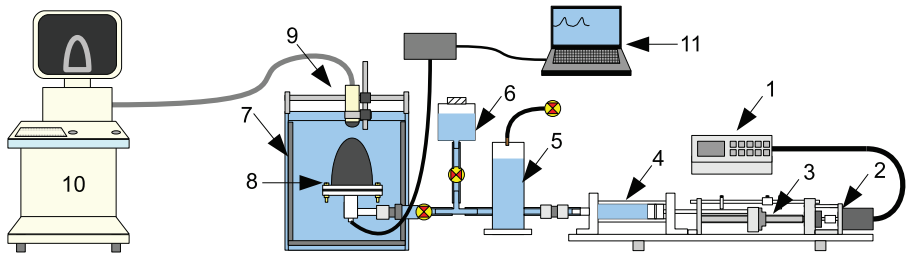

Figure 4.2: Schematic overview of the experimental setup: 1-Pump control unit, 2-Stepper motor, 3-Driving mechanism, 4-Piston (2x), 5-Windkessel, 6-Preloading reservoir, 7-Container with US absorbing tank linings, 8-Phantom and fixing collar, 9-US probe, 10-US scanner, 11-Pressure registration system.

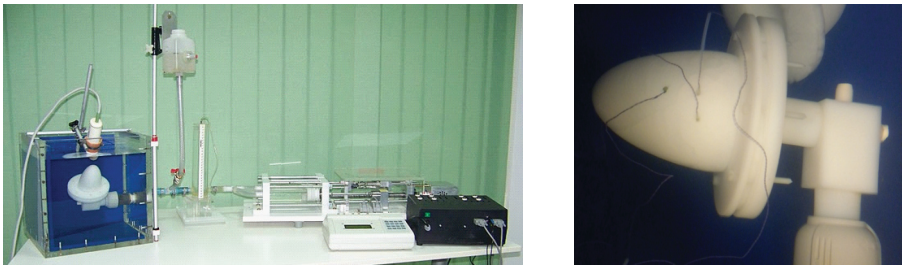

Figure 4.3: Actual experimental setup: (a) with mounted PVA phantom, and (b) close-up of homogeneous phantom with glued epicardial crystals.

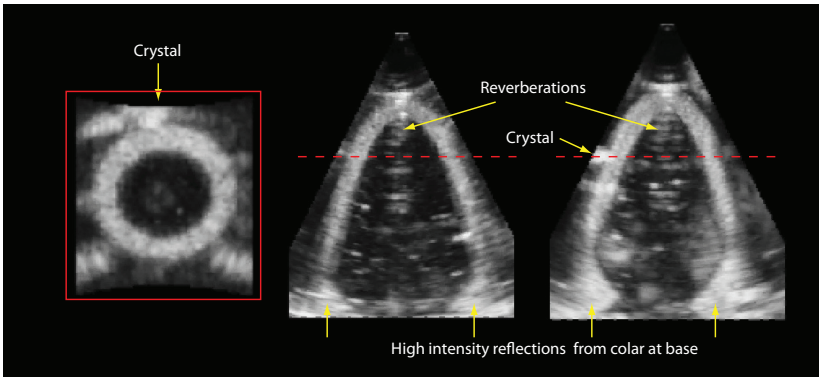

Figure 4.4: Example of a volumetric B-mode dataset showing three cross-sections through a uniform phantom.

The model was fixed with the apex pointing upwards to allow scanning from an apical view, parallel to the main long axis of the ellipsoidal phantom. Volumetric B-mode data at a frame rate of 14 ± 2 Hz and with a 50° opening angle was acquired using a GE VividE9 equipped with a 2.5 MHz transducer (3V or 4V matrix array, dimensions: 21×24 mm; GE Vingmed, Horten, Norway) fixed at the top of the tank (items 9 and 10). For each time frame we thus obtained a scan-converted dataset of $119 \times 119 \times 192$ voxels with a spatial resolution of $0.9 \times 0.9 \times 0.7$ mm in the azimuth, elevation and axial direction respectively (Fig. 4.4). Gain and focus depth were modified to minimize the effect of acoustic artifacts and optimize quality of the phantom image. The trigger signal from the pump controller was connected to the electrocardiogram input of the scanner in order to provide a synchronization signal for data processing.

Other parts of the system included a Windkessel reservoir to eliminate excessive pressure vibrations (item 5) and a constant pressure reservoir to modify the preload conditions (item 6). The preload was set until the movement of the apex was stable and no wobbling motions occurred during deformation. No apical sagging occurred during the low pressure state.

Cavity pressure could be monitored by using a micromanometer-tipped catheter (Millar Instruments, Houston, TX, USA) introduced from an access at the base of the fixing collar (item 11). It was captured and analyzed on a PC workstation with a commercially available software package (PowerLab/Chart, ADInstruments, Mountain View, CA, USA). As previously reported by Lesniak-Plewinska *et al.*, output flow and cavity pressure were highly reproducible [134].

4.2.3 Sonomicrometry

Similar to the in-vivo animal setup of chapter 3, a sonomicrometry system (Sonometrics Corporation, London, Ontario, Canada) was used to obtain an independent measure of the phantom wall deformation throughout the deformation cycle. In this study, only the homogeneous phantoms were instrumented with crystals (Fig. 4.3b).

Reference radial ($\varepsilon_{\mathrm{RR}}$), longitudinal ($\varepsilon_{\mathrm{LL}}$) and circumferential ($\varepsilon_{\mathrm{CC}}$) strain components could be calculated independently using 4 ultrasonic microcrystals which were glued to the wall having the lowest curvature, i.e. either in position 1 or 2 of Fig. 4.5a. Microcrystals are small piezoelectric crystals (2 mm) that can emit and detect ultrasonic pulses. By using the speed-of-sound and the time-of-flight between ultrasound emission in one crystal and detection in a neighboring crystal, inter-crystal distance can be calculated continuously at a time resolution of 1 ms and with a spatial resolution of 15.4 μm. Due to the

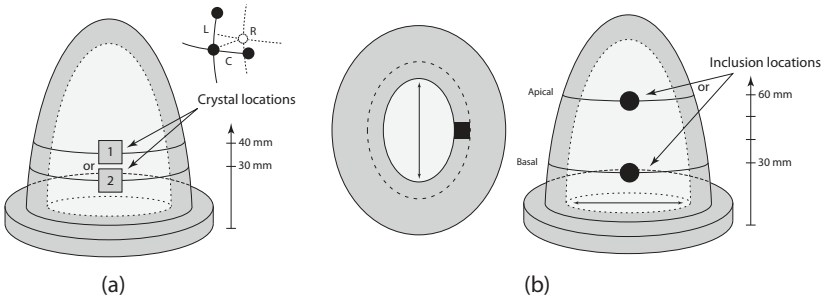

Figure 4.5: Phantom types: (a) configuration of the 4 crystals attached to the homogeneous phantoms, either at position 1 or 2 (used in Experiment A), (b) position of the cylindrical inclusion in the heterogeneous phantoms, either located at a basal or apical position (used in Experiment B).

overlapping frequency bands for the microcrystal system and the ultrasound system, the two systems could not be operated simultaneously. The system was therefore switched off during the acquisition of the volumetric data, and microcrystal data were recorded immediately afterwards. The raw crystal data was processed similarly to what is described in section 3.2.3.

Strain $\varepsilon_{\boldsymbol{n},\,\mathrm{ED}\to f}$ in every point along a certain cardiac direction $\boldsymbol{n}$ was calculated according to:

$$\varepsilon_{\boldsymbol{n},\,\mathrm{ED}\to f} = \frac{L_{\boldsymbol{n}}(f) - L_{\boldsymbol{n}}(\mathrm{ED})}{L_{\boldsymbol{n}}(\mathrm{ED})} \tag{4.1}$$

where $L_{\boldsymbol{n}}(f)$ is the distance between two adjacent crystals in either the radial, longitudinal or circumferential direction at frame f, and $L_{\boldsymbol{n}}(\mathrm{ED})$ is the respective initial distance at end-diastole (ED).

4.3 Non-rigid image registration

4.3.1 Motion estimation

Estimating cardiac motion between two volumetric US images can be accomplished by employing a three-dimensional (3D) extension of the 2D methodology proposed in section 3.3.2.

Similar to the formulation of Eq. (3.2), the inter-frame myocardial displacement was modelled with a 3D third order B-spline tensor-product [203], defined on a rectangular lattice:

$$\mathbf{u}_{f\to f+1}(\mathbf{r}) = \sum_{i\in\mathcal{N}_i}\sum_{j\in\mathcal{N}_j}\sum_{k\in\mathcal{N}_k} \boldsymbol{\mu}^{ijk}\beta_x^3(\frac{x-\kappa_x^{ijk}}{\sigma_x})\beta_y^3(\frac{y-\kappa_y^{ijk}}{\sigma_y})\beta_z^3(\frac{z-\kappa_z^{ijk}}{\sigma_z}) \quad (4.2)$$

with κ_ξ^{ijk} and σ_ξ the control point location and spacing respectively, and N_ξ the set of control points within the compact support $\mathcal{N}$ of the B-spline β_ξ ($\xi \in \{x, y, z\}$).

The optimal transformation field $\mathbf{T}(\mathbf{r}) = \mathbf{r} + \mathbf{u}(\mathbf{r})$ was found by maximizing an overall cost function C consisting of mutual information (MI) as a similarity measure and two additional weighted penalties to regularize the transformation field: a smoothness penalty R_{sm} [203] and a local volume penalty R_{vol} [140]:

$$C = \mathrm{MI}(I_f, I_{f+1}; \boldsymbol{\mu}) - \omega_{sm}R_{sm}(\boldsymbol{\mu}) - \omega_{vol}R_{vol}(\boldsymbol{\mu}) \quad (4.3)$$

The input images I_f and I_{f+1} are the scan-converted and log-compressed B-mode volumetric data as exported directly from the US scanner. The registration method is automated and requires no prior manual contouring. It has previously been described in detail by Elen *et al.* [67] and in [139]. The reader is referred to appendix B for a more extensive treatment of this technique and for more details regarding R_{sm} and R_{vol}.

The algorithm contains a significant amount of parameters, which can all be chosen differently. In [67] these parameters were optimized based on simulated data sets. These parameters were subsequently fine-tuned for the in-vivo application [13] and used for the phantom application in this study. This resulted in the following settings. Initial grid spacings were $\Delta x = 32$ voxels (or 28.8 mm), $\Delta y = 32$ voxels (or 28.8 mm) and $\Delta z = 64$ voxels (or 44.8 mm) in the azimuth, elevation and axial (parallel to the long axis of the model) direction respectively. The initial axial grid size was larger to make sure the greater longitudinal phantom movement could be accurately captured and thus to avoid the algorithm being stuck in a local optimum. Four refinement steps were used during optimization, halving the grid size in each direction with every step. The full resolution data set was used in every refinement stage. Third degree B-splines were used in all directions. B-spline basis functions have a limited span such that the 3D transformation in each image point is determined by at most 64 control points thus yielding computational efficiency. The penalty weights were adopted from [67] and were respectively $\omega_{vol} = 0.01$ and $\omega_{sm} = 100$.

4.3.2 Strain estimation

One-dimensional strain ε between two points of interest can be defined as

$$\varepsilon = \frac{L - L_0}{L_0} = \frac{L}{L_0} - 1 \tag{4.4}$$

where L_0 and L are the initial and deformed length between both points respectively.

From continuum mechanics theory, an equivalent strain definition can be formulated that takes full advantage of the analytic form of the estimated displacement field [153]. Strain along a certain direction, represented by the corresponding unit vector $\boldsymbol{n}$, is defined as:

$$\varepsilon_{\boldsymbol{n}} = \frac{\|d\mathbf{x}\|}{\|d\mathbf{X}\|} - 1 = \sqrt{\boldsymbol{n}^{\mathrm{T}} \cdot \mathbf{F}^{\mathrm{T}} \cdot \mathbf{F} \cdot \boldsymbol{n}} - 1 \tag{4.5}$$

where $d\mathbf{X}$ is an arbitrary material line segment along $\boldsymbol{n}$ which is deformed to $d\mathbf{x}$. In the context of the registration algorithm, the deformation gradient tensor $\mathbf{F}$ is the spatial gradient of the transformation field and is thus given by the spatial Jacobian $\partial\mathbf{T}(\mathbf{r})/\partial\mathbf{r}$ of the transformation field $\mathbf{T}(\mathbf{r})$. It can be shown that the strain definitions of Eqs.(4.4) and (4.5) are equal (see appendix, section A.2.4).

In practice, the inner- and outer phantom wall were first manually contoured in end-diastole using in-house developed software (Speqle3D, KU Leuven) to indicate the region-of-interest for strain estimation. The same software was used for least-square surface fitting using a fifth order spherical harmonic expansion [115]. Subsequently, a 3D myocardial mesh of 16000 points was generated. The mesh consisted of 5 samples in the radial direction, 80 samples circumferentially, and 40 samples longitudinally from base-to-apex (base-to-base resulting in the same number of samples as the circumferential direction; Fig. 4.6b top). In each point, the directions $\boldsymbol{n}$ corresponding to the directions of a local cardiac coordinate system (radial, longitudinal and circumferential) were calculated [59]. The generated mesh was then subsequently tracked over the cardiac cycle using the computed transformation field as outlined in section 4.3.1.

Since we are interested in cardiac strains throughout the cardiac cycle, the transformation field must be accumulated across multiple frames. Because consecutive frames were registered pairwise, strain $\boldsymbol{\varepsilon}_{\boldsymbol{n},\,\mathrm{ED}\to k}$ along a certain direction $\boldsymbol{n}$ between end-diastole (ED) and frame f, was then calculated according to Eq. (4.5) using the cumulated deformation gradient tensor $\mathbf{F}_{\mathrm{ED}\to f}$:

$$\mathbf{F}_{\mathrm{ED}\to f} = \mathbf{F}_{f-1\to f} \circ \ldots \circ \mathbf{F}_{2\to 3} \circ \mathbf{F}_{\mathrm{ED}\to 2} \tag{4.6}$$

with $\mathbf{F}_{f-1\rightarrow f}$ corresponding to the spatial Jacobian of the transformation field from frame $f-1$ to f. A drift correction was performed for each strain curve such that the drift-corrected strain $\boldsymbol{\varepsilon}_{\boldsymbol{n}}^{dr}$ at the end of the cardiac cycle, i.e. the second end-diastole (ED2), returned to zero. In contrast with chapter 3 and as mentioned in [67], this correction was only applied to the second part of the strain curve from end-systole (ES) to ED2. Possible strain drift caused by the fast cardiac motion during the rapid filling phase which might be more difficult to track, can thus be limited. The remaining strain offset at ED2 was distributed over the second part of strain curve according to

$$\varepsilon_{\boldsymbol{n},\,\mathrm{ED}\rightarrow f}^{dr} = \boldsymbol{\varepsilon}_{\boldsymbol{n},\,\mathrm{ED}\rightarrow f}^{dr} = \boldsymbol{\varepsilon}_{\boldsymbol{n},\,\mathrm{ED}\rightarrow f} - \frac{f-\mathrm{ES}}{\mathrm{ED2}-\mathrm{ES}} \cdot \boldsymbol{\varepsilon}_{\boldsymbol{n},\,\mathrm{ED}\rightarrow\mathrm{ED2}} \;(f > \mathrm{ES}) \quad (4.7)$$

Finally, the resulting strain was averaged over certain areas (further defined in section 4.4) and could be visualized in Speqle3D by means of a 3D surface strain map or selected strain curves (Fig. 4.6b). The size of the regions considered in this study is similar to those defined in common clinical practice where the LV is usually divided in 16 segments [206], 17 segments [37] or 18 segments [102].

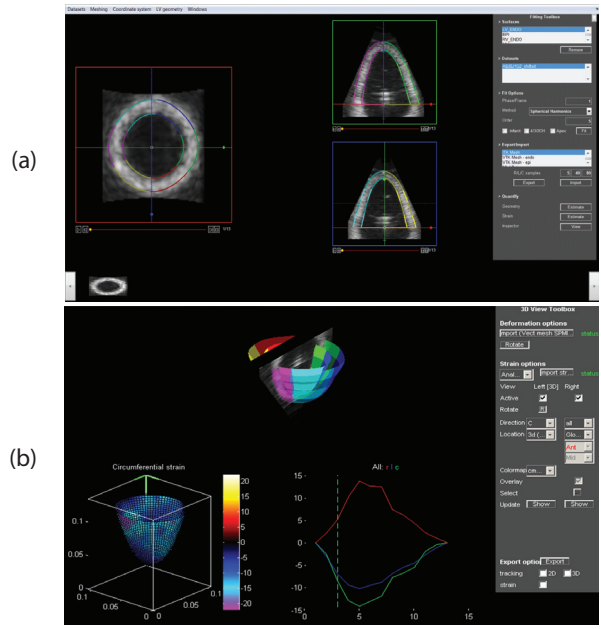

Figure 4.6: Speqle3D interface to (a) manually contour the phantom wall and (b) generate a mesh (represented by an 18 segment surface; top panel) and extract strain values with visual feedback (lower left and right panel).

4.4 Experiments

The performance of the non-rigid registration algorithm was evaluated in two different experiments. Regional strain accuracy was assessed in homogeneous phantoms by comparison against sonomicrometry as a reference method (experiment A). Next, we assessed strain in heterogeneous phantoms containing a stiff inclusion, to investigate to what extent our 3DSE-method could accurately identify dysfunctional regions (experiment B).

4.4.1 Experiment A: Regional strain against sonomicrometry

To obtain a broad strain range at the location of the crystals, two similar homogeneous phantoms (differing in the location of the crystals) were deformed. The first one was deformed at a rate of 70 beats per minute (bpm) with a SV that was changed in steps of 15 mL (75–90–105 mL) with the central crystal attached at 3 cm from the fixing collar (see Fig. 4.5a, position 1) and the second one was deformed at a rate of 60 bpm but with a broader SV range (25–65–105–150 mL) with the central crystal attached at 4 cm from the fixing collar (see Fig. 4.5a, position 2). Strain values for the volumetric datasets were calculated for all cardiac directions through Eq. (4.5) and spatially averaged within each segment according to an 18 segment cardiac model typically used in echocardiography [102]. The calculated peak strain values $\boldsymbol{\varepsilon}^{dr}_{\boldsymbol{n},\,\mathrm{ED}\rightarrow\mathrm{ES}}$ in the segment with the attached crystals were then correlated with the reference strain values $\boldsymbol{\varepsilon}^{ref}_{\boldsymbol{n},\,\mathrm{ED}\rightarrow\mathrm{ES}}$ obtained from sonomicrometry.

The absolute systolic strain error $\Delta\boldsymbol{\varepsilon}_{\boldsymbol{n},\,\mathrm{ED}\rightarrow\mathrm{ES}}$, defined as:

$$\Delta\boldsymbol{\varepsilon}_{\boldsymbol{n},\,\mathrm{ED}\rightarrow\mathrm{ES}} = \left|\boldsymbol{\varepsilon}^{ref}_{\boldsymbol{n},\,\mathrm{ED}\rightarrow\mathrm{ES}} - \boldsymbol{\varepsilon}^{dr}_{\boldsymbol{n},\,\mathrm{ED}\rightarrow\mathrm{ES}}\right| \tag{4.8}$$

was also assessed for $\varepsilon_{\mathrm{RR}}$, $\varepsilon_{\mathrm{LL}}$ and $\varepsilon_{\mathrm{CC}}$, for all the performed experiments. In addition, the amount of strain drift in all three directions was quantified by omitting the second term in Eq. (4.7), yielding the non-drift compensated strain $\boldsymbol{\varepsilon}_{\boldsymbol{n},\,\mathrm{ED}\rightarrow\mathrm{ED2}}$ at the end of the cardiac cycle.

Finally, it should be noted that the presence of crystals might introduce a substantial bias in the tracking algorithm. Since the crystals show up as bright spots in the volumetric data it might well be possible that the tracking is facilitated by the movement of these bright markers. To investigate this, strain in the contralateral (CL) wall was measured. This wall is located at a mirrored position (with respect to the long axis of the phantom) from the wall containing the crystals, and should deform similarly due to symmetry reasons. Therefore,

the calculated peak strain values $\varepsilon^{dr}_{\boldsymbol{n},\,\mathrm{ED}\rightarrow\mathrm{ES}}$ in the CL wall could be correlated with those obtained from sonomicrometry. In addition, the absolute strain error $\Delta\varepsilon_{\boldsymbol{n},\,\mathrm{ED}\rightarrow\mathrm{ES}}$ in the CL wall was calculated.

4.4.2 Experiments B: Detection of inclusions in heterogeneous phantoms

We assessed strain in phantoms containing a stiff inclusion, to investigate the discriminative power of our 3DSE-method to detect regional differences in strain, i.e. to what extent such dysfunctional regions could be accurately identified. The influence of different parameters on strain outcomes was therefore considered: (i) the inclusion location (apical or basal as shown in Fig. 4.5c), (ii) the stroke volume (75 mL to 105 mL) and (iii) the inclusion size (9–17–27mm, i.e. small–medium–large) and inclusion stiffness (2 or 4 additional freeze-thaw cycles, i.e. a soft or hard inclusion), with the evaluated combinations summarized in table 4.1.

Strains were spatially averaged within the inclusion region (IR), an adjacent region (AR) and remote region (RR) as shown in Fig. 4.8d. The location and size of the IR corresponds to the location and size of the present inclusion. The RR is located at the contralateral side of the IR, mirrored with respect to the long axis of the phantom. The AR region makes a 10 degrees opening angle with the IR on the projected surface. Differences in peak strain values between regions were assessed using ANOVA with Tamhane's T2 post-hoc analysis [236].

4.5 Results

4.5.1 Experiment A: Regional strain against sonomicrometry

An example of the full strain curves obtained from sonomicrometry and calculated by our 3DSE-method is shown in Fig. 4.7a. Figures 4.7b-d show the segmental peak strain correlation of our method against sonomicrometry (SV range = 25–150 mL). Correlations of 0.98, 0.96 and 0.92 were obtained for $\varepsilon_{\mathrm{RR}}$, $\varepsilon_{\mathrm{LL}}$ and $\varepsilon_{\mathrm{CC}}$ respectively.

The absolute strain error $\Delta\varepsilon_{\boldsymbol{n},\,\mathrm{ED}\rightarrow\mathrm{ES}}$ in the segment containing the crystals is presented in table 4.2. Results for the contralateral wall (absolute strain error and correlation with the crystal data) are summarized in the same table for ease of comparison. Finally, table 4.3 quantifies the strain drift $\varepsilon_{\boldsymbol{n},\,\mathrm{ED}\rightarrow\mathrm{ED2}}$ in the segment containing the crystals.

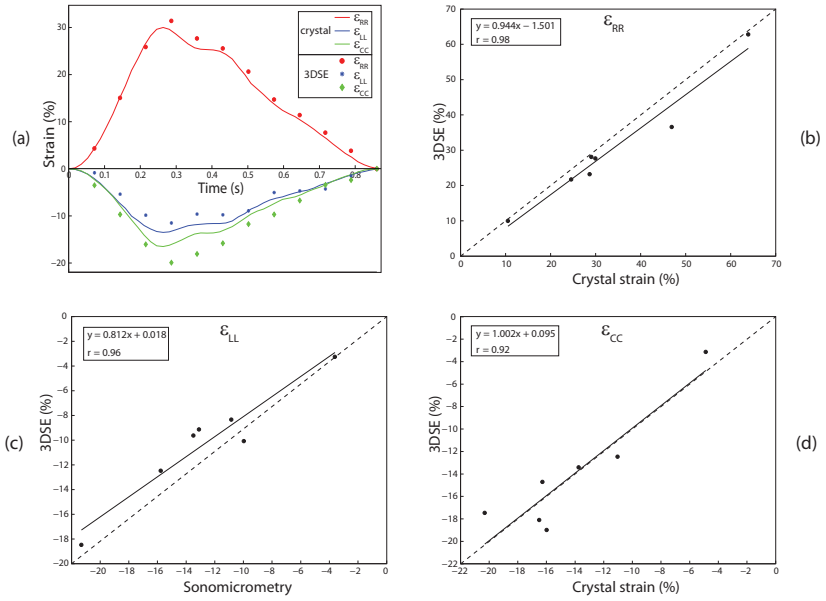

Figure 4.7: Experiment A - Regional strain against sonomicrometry. (a) Example of full strain curves as obtained by the microcrystals (full line) and our 3DSE-method (samples) for the phantom with the crystals located in position 1, deformed at HR=70 bpm and SV=105 mL. (b)-(d) Segmental peak strain correlation of our method against sonomicrometry in the (b) radial, (c) longitudinal and (d) circumferential direction. The dotted line represents the line of identity.

Table 4.2: Experiment A - Crystal vs contralateral wall

	Correlation (r^2)		$\Delta\varepsilon_{\boldsymbol{n},\,\mathrm{ED}\to\mathrm{ES}}$					
			Mean (%)		Min (%)		Max (%)	
	C wall	CL wall	C wall	CL wall	C wall	CL wall	C wall	CL wall
$\varepsilon_{\mathrm{RR}}$	0.98	0.96	3.37	4.23	0.54	0.29	10.34	11.08
$\varepsilon_{\mathrm{LL}}$	0.96	0.73	2.42	5.28	0.10	1.16	3.96	16.03
$\varepsilon_{\mathrm{CC}}$	0.92	0.95	1.79	2.67	0.35	0.91	3.00	5.15

Comparison between the strain results obtained at the wall containing the crystals (C) and the contralateral (CL) wall, expressed in terms of correlation with the crystals (r^2) and the absolute strain error $\Delta\varepsilon_{\boldsymbol{n},\,\mathrm{ED}\to\mathrm{ES}}$. Minimum, maximum and mean values are reported in % strain.

Table 4.3: Experiment A - Strain drift

	$\varepsilon_{\boldsymbol{n},\,\mathrm{ED}\to\mathrm{ED2}}$		
	Min (%)	Max (%)	Mean (%)
$\varepsilon_{\mathrm{RR}}$	0.64	7.55	3.05
$\varepsilon_{\mathrm{LL}}$	–1.74	0.06	–1.05
$\varepsilon_{\mathrm{CC}}$	–2.67	0.96	–1.33

Strain drift $\varepsilon_{\boldsymbol{n},\,\mathrm{ED}\to\mathrm{ED2}}$ at the end of the cardiac cycle (defined in section 4.4.1). Minimum, maximum and mean values are reported in % strain.

4.5.2 Experiment B: Detection of inclusions in heterogeneous phantoms

Stiffness of the phantoms increased approximately linearly with the amount of freeze-thaw cycles. The uniform phantom (subjected to two freeze-thaw cycles) had a Young's modulus of 28.05 ± 2.09 kPa. The soft and hard inclusions, in total subjected to respectively four and six freeze-thaw cycles, had a Young's modulus of respectively 50.68 ± 6.6 kPa and 67.47 ± 3.99 kPa, resulting in approximately a 2:1 and 5:2 stiffness ratio with the surrounding material.

The influence of stroke volume on regional strain estimates is presented in Fig. 4.8a and 4.8b for a medium-sized hard inclusion. To facilitate vertical axis scaling, absolute values of the true negative $\varepsilon_{\mathrm{LL}}$ and $\varepsilon_{\mathrm{CC}}$ values are displayed. For both $\varepsilon_{\mathrm{LL}}$ and $\varepsilon_{\mathrm{CC}}$, an increasing strain gradient was found when moving from the IR, over the AR, to the RR. Moreover, this increasing gradient became steeper at a higher SV. For $\varepsilon_{\mathrm{RR}}$, strain was only statistically lower in the IR compared to the RR for a low SV. This pattern was reversed at a high SV.

The influence of the inclusion location can be seen in Fig. 4.8a and 4.8c. Moving the inclusion to a more basal position resulted in a less pronounced strain gradient for $\varepsilon_{\mathrm{LL}}$ and $\varepsilon_{\mathrm{CC}}$, but strain was still significantly lower in the IR compared to the RR. $\varepsilon_{\mathrm{RR}}$ was only statistically lower in the IR for phantoms containing an apical inclusion (Fig. 4.8a), not for a basal inclusion (Fig. 4.8c).

Finally, the influence of inclusion size and stiffness on regional strain estimates is summarized in table 4.4. The heterogeneous phantoms with a medium-sized hard inclusion, and a large-sized soft inclusion had statistically lower strain values in the IR compared to the RR for both $\varepsilon_{\mathrm{LL}}$ and $\varepsilon_{\mathrm{CC}}$. Moreover, phantoms with a small-sized hard inclusion and a medium-sized soft inclusion also showed statistically lower strain values in the IR compared to the RR for $\varepsilon_{\mathrm{CC}}$.

An example of 3D $\varepsilon_{\mathrm{LL}}$ and $\varepsilon_{\mathrm{CC}}$ bullseye plots is presented in Fig. 4.9a-b. The phantom contains a medium-sized hard inclusion located in an apical position (see Fig. 4.5a). In this representation, the phantom is viewed from the apex and the strain in every sampled point along the surface of the phantom is projected onto the basal plane. As such, a 2D donut-shaped colored strain map is created with the inner white circle serving as the apical cap where no strain measurements were made. Points near the center represent strain values originating from a more apical level, whereas points near the edges arise from the basal phantom level. Both panels show a decreased strain pattern at the location of the inclusion as indicated by the black full arrow. Moreover, the normal opposite wall, containing no inclusion (black dotted arrow), has higher strain values. Qualitatively, a gradual increase in strain from apex to base can be seen for both directions, which dropped of slightly near the base for $\varepsilon_{\mathrm{LL}}$.

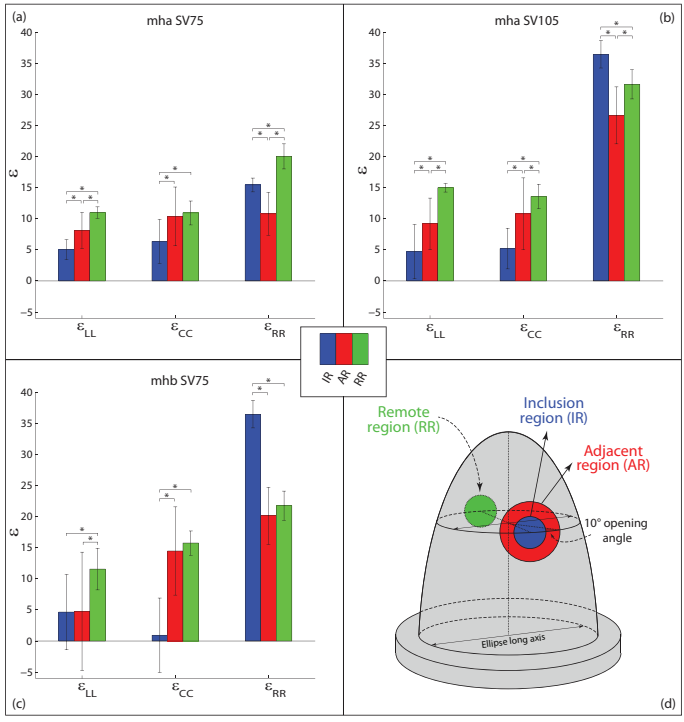

Figure 4.8: Experiment B - Impact of SV and inclusion location on strain outcomes for a phantom containing a medium sized (17 mm diameter) hard inclusion (mh). The cylindrical inclusion was located at either a basal (mhb) or apical position (mha) as illustrated in Fig. 4.5c. The phantom was deformed at either a low SV (75 mL) or a high SV (105 mL). (a-c) Peak longitudinal ($\varepsilon_{\mathrm{LL}}$), circumferential strain ($\varepsilon_{\mathrm{CC}}$) and radial strain ($\varepsilon_{\mathrm{RR}}$) were averaged over the segments as defined in (d). To facilitate vertical axis scaling, absolute values of the true negative $\varepsilon_{\mathrm{LL}}$ and $\varepsilon_{\mathrm{CC}}$ values are displayed. The remote area is located at the same position of the inclusion and identical in size, but on the contralateral side. Statistically different values are indicated above the graph: $^{*}p < 0.01$. Error bars represent the variation of the calculated end-systolic strain values within the considered segments.

Table 4.4: Results experiment B - Remote vs Inclusion region

	Size (diameter)					
	Small (9 mm)		Medium (17 mm)		Large (27 mm)	
Stiffness	IR (%)	RR (%)	IR (%)	RR (%)	IR (%)	RR (%)
ε_{LL}						
Hard	–0.17 ± 1.67	–3.71 ± 4.00	–4.66 ± 6.06*	–11.59 ± 3.37	–	–
Soft	–8.44 ± 0.72	–6.05 ± 1.55	–11.07 ± 4.38	–7.94 ± 2.37	–8.45 ± 3.52*	–11.21 ± 7.32
ε_{CC}						
Hard	–16.28 ± 1.94*	–26.82 ± 2.32	–0.94 ± 5.99*	–15.78 ± 1.95	–	–
Soft	–19.15 ± 0.99	–18.00 ± 1.63	–16.68 ± 1.89*	–19.49 ± 1.72	–11.90 ± 5.01*	–22.62 ± 6.25

Effect of inclusion size and stiffness on ε_{LL} and ε_{CC} for an inclusion located at a basal position as shown in Fig. 4.5b. Strain is averaged over the inclusion region (IR) and the remote region (RR) defined as in Fig. 4.8d. The phantoms were deformed with a HR of 70 bpm and a SV of 75 mL. Inclusions which could be detected are indicated in the table: *significantly lower strain values compared to the remote region, $p < 0.01$.

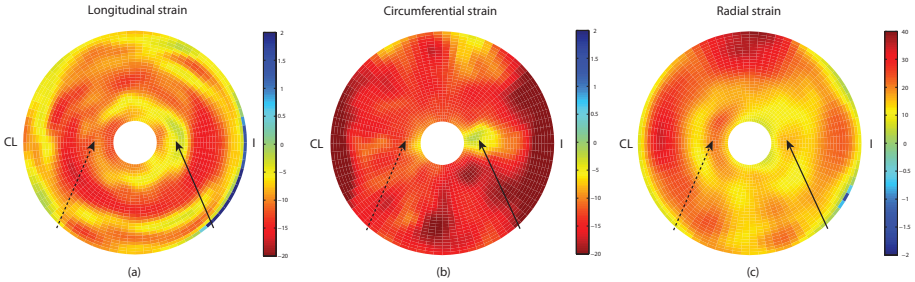

Figure 4.9: Experiment B - Spatial strain distribution. Bullseye plots of (a) peak $\varepsilon_{\mathrm{LL}}$ and (b) peak $\varepsilon_{\mathrm{CC}}$ and (c) peak $\varepsilon_{\mathrm{RR}}$ of a phantom containing a medium-sized hard inclusion in an apical position. The bullseye plot is oriented with the inclusion side (I) located at the right side and the contralateral wall (CL) on the left. The phantom was deformed at a HR of 70 bpm and a SV of 75 mL. The full arrow indicates the center of the inclusion location. The dotted arrow indicates the corresponding location at the opposite wall.

4.6 Discussion

4.6.1 Experiment A: Regional strain against sonomicrometry

In this experiment, we validated our 3DSE-method against sonomicrometry as a reference method. Good agreement between both methods was found on a regional level as is evident from the high correlations (Fig. 4.7), low absolute mean error with respect to the ground truth (table 4.2) and low mean strain drift (table 4.3). Radial strain revealed the highest correlation but also showed the highest errors. This is likely due to the fact that the range for $\varepsilon_{\mathrm{RR}}$ in Fig. 4.7 is higher compared to the other two directions, making the influence of outliers on the correlation strength intrinsically lower. Overall, the absolute errors of the different components are small compared to normal strain values encountered in clinical practice, e.g. according to [101] in the order of 38%, –20% and –23% for $\varepsilon_{\mathrm{RR}}$, $\varepsilon_{\mathrm{LL}}$ and $\varepsilon_{\mathrm{CC}}$ respectively. They are also small compared to the typical changes induced by pathology, e.g. in an in-vivo animal setup [259], $\varepsilon_{\mathrm{RR}}$ dropped from $59 \pm 3\%$ to $32 \pm 6\%$ in the inferolateral wall of animals having a non-transmural myocardial infarct and dropped from $58 \pm 2\%$ to $3 \pm 3\%$ for those animals developing a transmural infarct.

As mentioned previously, the presence of the crystals, showing up as bright markers in the volumetric data (see Fig. 4.4), might introduce a substantial bias in the tracking algorithm. This issue is easily resolved in two dimensions,

where the imaging plane can be chosen in a parallel, neighboring plane [127]. However, in volumetric data this is not possible. If no bias is introduced, correlations and mean absolute strain error in the CL wall should be comparable to those of the wall containing the crystals. This is the case for $\varepsilon_{\mathrm{RR}}$ and $\varepsilon_{\mathrm{CC}}$ (table 4.2). However, the correlation for $\varepsilon_{\mathrm{LL}}$ was poor (0.96 vs 0.73 in the CL wall), and the mean absolute error was also higher (2.42% vs 5.28% in CL). By visually verifying the tracking result, this could be attributed to two outliers at a high SV that were caused by static reverberations near the CL wall (as also illustrated by the high maximum $\varepsilon_{\mathrm{LL}}$ strain error of the CL wall in table 4.2). Removing these outliers resulted in a correlation of 0.97 for $\varepsilon_{\mathrm{LL}}$. These observations thus suggest that no additional bias was introduced by the crystals.

4.6.2 Experiment B: Detection of inclusions in heterogeneous phantoms

In this experiment we investigated the ability of our 3DSE-method to detect dysfunctional regions. Comparing strain between the inclusion region (IR) and the remote region (RR) permits us to assess the accuracy of the method in detecting dysfunctional regions, whereas comparison between the IR and the adjacent region (AR) informs us about the method's precision to resolve the inclusion from the surrounding tissue. As shown in Fig. 4.8a, a medium-sized inclusion in an apical position deformed at a moderate SV (75 mL), can be accurately detected in all directions: the strain is statistically lower in the IR compared to the RR. However, the method is only able to resolve the inclusion with $\varepsilon_{\mathrm{LL}}$ and $\varepsilon_{\mathrm{CC}}$: the strain is statistically lower in the IR compared to the AR.

The impact of SV on strain outcomes is in the line of expectations (Fig. 4.8a-b). Increasing the stroke volume resulted in more deformation in all directions. In accordance with the phantom deformation at a low SV (panel 4.8a), only the $\varepsilon_{\mathrm{LL}}$ and $\varepsilon_{\mathrm{CC}}$ direction allowed to accurately detect the inclusion and resolve it from the surrounding tissue at a higher SV (panel 4.8b).

Likewise, when the same type of inclusion was located at a more basal position (compare panel a and c in Fig. 4.8), only $\varepsilon_{\mathrm{LL}}$ and $\varepsilon_{\mathrm{CC}}$ showed statistically lower strain in the IR compared to the RR. However, standard deviations in both directions also increased. In this case, only $\varepsilon_{\mathrm{CC}}$ was able to resolve the inclusion from the surrounding material (strain is lower in the IR with respect to the AR). As such, basal inclusions seem to be harder to find. Likely, this was due to image quality problems. Acquiring images of sufficient quality in volumetric imaging is challenging. Compared to typical clinical images, the phantom images had a more prominent 'wall-blood pool' border which may be easier to follow (see

Fig. 4.4). Furthermore, the models were not surrounded by other tissues. In clinical images, this tissue can negatively influence tracking performance as they can introduce image artefacts or apparent heart motion. These tracking advantages over clinical images were nevertheless somewhat balanced due to the presence of static artifacts. These were mostly prominent near the base as a result of imaging in a low attenuating medium containing strong reflectors (i.e. the walls of the container and the fixing collar of the PVA model, Fig. 4.4). Reverberation artifacts of this strength are atypical for clinical data. This phenomenon could affect strain outcomes in most experiments, especially in the heterogeneous phantoms having basal inclusions. For example, during ejection the basal parts display no (or even positive) strain due to these static artifacts. This is evident from the standard deviations crossing the horizontal axis in Fig. 4.8c in $\varepsilon_{\mathrm{LL}}$ and $\varepsilon_{\mathrm{CC}}$.

As can be noted from Fig. 4.8, the behavior of $\varepsilon_{\mathrm{RR}}$ is not entirely as expected: panels b and c show higher strain values in the inclusion region. There are several reasons for this unexpected behavior. First of all, spatial lateral and elevational resolution is typically coarser compared to the axial direction. Due to the orientation of the phantom in the image volume, beam density and therefore spatial resolution is lower in the radial direction than the longitudinal direction. This effect becomes more pronounced near the base (as is the case in panel c), making the estimation of radial strain challenging. Secondly, it should be noted that the dimension of the phantom in the radial direction is small with respect to the dimensions in the other cardiac directions. For example, the phantom thickness is only 10 mm (i.e. in the radial direction), whereas the diameter of a large inclusion is 27 mm (i.e. in the circumferential direction). This makes it intrinsically harder to detect motion gradients in the radial direction. In addition, as already mentioned $\varepsilon_{\mathrm{RR}}$ was negatively influenced especially at the base due to the presence of the basal artifacts. Finally, it is worth mentioning that strain estimation in the radial direction has until the present day typically been more difficult and prone to errors even with techniques assessing two-dimensional strain as reported by numerous studies [101][130]. Recently, these observations were also confirmed in a clinical setting for 3D strain [109].

The above shows that the performance of $\varepsilon_{\mathrm{RR}}$ is not optimal for detecting spatial differences in strain. As such, $\varepsilon_{\mathrm{RR}}$ was not further reported in table 4.4. It might thus be better to calculate $\varepsilon_{\mathrm{RR}}$ from the other two components by assuming volume conservation during phantom deformation as proposed by several other authors (see appendix A.3 and chapter 10). In the future, results for $\varepsilon_{\mathrm{RR}}$ might improve due to advances in transducer technology leading to a higher image quality in terms of a higher line density and frame rate.

The severity of a dysfunctional region, both in terms of size and stiffness, will dictate how easily such a region can be detected. Intuitively, regions which have a large stiffness difference with the surrounding tissue (i.e. stiff inclusions having a large strain contrast with the surrounding tissue) will be easier to identify. Likewise, the larger the dysfunctional regions, the easier they should be to detect. Table 4.4 confirms both these statements. When the inclusion was soft (approximately a 2:1 inclusion-surrounding tissue stiffness ratio), spatial resolution of our 3DSE-method was adequate to resolve full transmural dysfunctional regions with a diameter of 27 mm in both the longitudinal and circumferential direction. Increasing the inclusion-surrounding tissue stiffness ratio to 5:2, made inclusion identification easier as it now allowed the method to distinguish smaller inclusions down to 17 mm. In addition, ε_{CC} appeared more sensitive since it could also identify small-hard, and medium-soft inclusions. The above findings also suggest that a large and stiff inclusion should be detectable (this phantom was not manufactured) since both the harder-to-detect medium-hard and large-soft versions were found.

More qualitatively, at the inclusion location, the ε_{LL} and ε_{CC} bullseye plots (Fig. 4.9a and b) clearly identified the inclusion as an island of reduced strain which is not visible at the contralateral wall. Especially at the basal part, an additional strain distribution along the circumference can be distinguished, with the highest strain in the anterior and posterior wall having the lowest curvature. This would be in agreement with Laplace's law which describes a linear relationship between low curvature and a higher wall stress (and thus a higher strain). The ε_{LL} bullseye also shows a decreasing base-to-apex strain gradient although a ring of lower strain values at the base could be noted. Likely, this is again due to image quality problems at the base. A similar ring of low (negative) strain values can be noticed in the ε_{RR} bullseye plot (panel c), especially at the inclusion side. Radial strain values in the inclusion area are lower compared to those in the contralateral wall, but this difference is not so prominent compared to the other two panels.

4.6.3 Comparison with other strain estimation techniques

Extrapolating and comparing results from this study to those obtained with alternative techniques is difficult since methods are technically different and publications related to the performance of regional 3D strain estimation are sparse. Clinically, 3D speckle tracking currently seems to be the most popular technique, but it has only been compared on a global level with 2D strain estimation techniques [190][205]. Three dimensional ultrasound typically comes at the expense of reduced temporal resolution with associated speckle decorrelation between subsequent volumes. This presents challenges for 3D

speckle tracking techniques based on (RF-based) block matching. Indeed, the results of Byram *et al.* indicate that high volume acquisition rates are required for accurate motion estimation using block matching approaches [35]. Their results show tracking improvements at frame rates up to 200 Hz. With current state-of-the-art clinical ultrasound systems, acquiring volumetric datasets with sufficient field-of-view at such a high frame rate is currently impossible. For this exact reason, non-rigid image registration methods may be of benefit as they attempt to capture motion and deformation in a more global optimization approach. Indeed, during registration regularization is intrinsically embedded in the framework (e.g. smoothness of the recovered transformation field as was imposed here), whereas speckle tracking usually needs a post-processing regularization step (e.g. median filtering of the motion estimates, or discarding estimates having a low tracking quality as in [50]). Registration methods may also better retrieve motion when large displacements occur, whereas speckle tracking could yield undesirable results due to decorrelation of the speckle pattern or the algorithm getting stuck in local optima. However, these registration approaches might not make optimal use of the available local image information whereas speckle tracking would. On the other hand, using RF data instead of speckle tracking on the enveloppe-detected data, is in 2D theoretically more accurate [198]. Whether this remains true for suboptimal 3D image quality remains to be proven. Feasibility of 3D RF tracking was recently shown in [145]. However, no validation was performed and computational load was high compared to 3D speckle tracking on voxel data.

A related method using B-splines for cardiac motion tracking but from MRI images is the one of Chandrashekara *et al.* [42]. In this work, information from 2D short and 2D long axis tagged images was combined to produce a dense 4D motion field. One of the major differences with the work presented in this chapter, was the used registration scheme. Every frame of the sequence was registered with the ED frame (as opposed to mapping consecutive frames in this chapter). This has also implications with respect to the way that the transformation fields were cumulated throughout the image sequence to obtain cardiac motion. Chandrashekara *et al.* summed the FFD contributions from the previously registered image pairs with the FFD governing the to-be-registered image pair coming next in the sequence. In this chapter, all consecutive image pairs were registered independently from each other and the transformation between ED and any frame in the sequence was then obtained by concatenating the respective transforms. The multilevel approach of [42] may be more robust to drift or accumulation of errors since information from a previous pair is taken into account. However, this does not allow to process registrations in parallel, in contrast to the method described in this chapter.

4.6.4 Limitations and closing remarks

A limitation of the current study is the absence of any rotational or twisting movement due to the lack of structural anisotropy in the phantom wall. Any shearing components which are normally present in myocardial tissue, could thus not be validated. However, no difficulties are expected to assess shearing components since our 3DSE-method assesses the full 3D myocardial strain tensor. Previously we showed already on simulated data that differences in the rotation resulting from torsion between base and apex could be found [67].

Moreover, in our setup the apex was cyclically moving and the base was fixed, whereas in reality this situation is reversed. Adapting the setup to fix the apex is far from trivial as acoustical access to the apex is still required to acquire apical images. Furthermore, in order to address the high ultrasound reflections coming from the fixing collar, it might be better to scan the apex from a more oblique position to avoid the presence of static artifacts at the basal level. However, a larger opening angle, and thus a lower frame rate, might then be required to fit the complete phantom within the image. In addition, this would also not properly reflect clinical scanning conditions where the heart is normally scanned from an apical position.

Another potential limitation of the study is the volume conservation penalty which was applied on the whole image during registration. Since the temporal resolution is quite low, volume changes from frame-to-frame might not be negligible between all pairs of images in the image sequence. Chapter 10 therefore investigates whether imposing volume conservation on the myocardium alone improves strain estimates. This in turn however, requires a segmentation of the myocardium, which may be a time-consuming process and subject to considerable observer variability if contoured manually. Chapter 11 tackles this problem.

Please note that MI was used in this chapter as a similarity measure, in contrast with SSD which was the similarity metric of choice in all the other chapters. This is mainly related to the chronological development of the algorithms: at the time of performing these experiments, we adopted the implementation that was used to test the feasibility of CFFD in-silico by Elen *et al.* [67]. This in-vitro study was the next logical validation step, and the same cost function was therefore used. Since mutual information does not make limiting assumptions about the nature of the relationship between image intensities of corresponding voxels between two images, it is especially suited for inter-modality registration. However, given the presence of speckle correlation between subsequent US frames, SSD was used as an intra-modality image similarity metric in the other chapters. We have currently no reasons to believe that SSD would

underperform greatly in this setup if these experiments were to be repeated using SSD instead of MI. Nevertheless, it may be interesting to investigate the influence of the similarity criterion on the strain accuracy for US applications, e.g. by following a strategy as proposed in [247], but this remains the topic of future research.

Finally, in clinical practice the presence of a dysfunctional region is unknown and averaging strain over the segments as performed in this manuscript (Fig. 4.8d) is thus not possible. Clearly, the ultimate goal is to solve the *reverse* problem, i.e. to detect any present dysfunctional region(s), given a 17 or 18 segment model. With this definition, it may well be possible that small infarctions lie on the border of these segments [50], further complicating the analysis. In this paper, we presented the first step in tackling this challenging problem, by assessing the method's performance when the presence of the inclusion is known. To the authors best knowledge this is the first paper to quantitatively do so. Solving the second step, i.e. the reverse problem, remains the topic of future work.

4.7 Conclusions

In this chapter, a 3D strain estimation methodology based on non-rigid image registration of voxel data was further validated on a regional level. High correlations were obtained against sonomicrometry in all directions. Absolute strain errors and strain drift were low for $\varepsilon_{\mathrm{LL}}$ and $\varepsilon_{\mathrm{CC}}$, and slightly higher for $\varepsilon_{\mathrm{RR}}$. The discriminative power of our methodology was adequate to resolve full transmural inclusions down to 17 mm in diameter, although the inclusion-surrounding tissue stiffness ratio was required to be at least 5:2. When the inclusion-surrounding tissue stiffness ratio was lowered to approximately 2:1, only larger inclusions down to 27 mm in diameter could still be identified. Radial strain was found not reliable in identifying dysfunctional regions.

Chapter 5

Non-rigid image registration to assess 3D myocardial deformation: Experimental validation in an animal model

This work was published in:
B. Heyde, S. Bouchez, S. Thieren, M. Vandenheuvel, R. Jasaityte, D. Barbosa, P. Claus, F. Maes, P. Wouters, and J. D'hooge. Elastic image registration to quantify 3D regional myocardial deformation from volumetric ultrasound: Experimental validation in an animal model. *Ultrasound Med Biol*, 39(9):1688–1697, 2013.

5.1 Motivation

Although real-time 3D echocardiography (RT3DE) has been available for several years, ongoing advances in both transducer hardware and ultrasound (US) computer software have sparked research interest, not only academically but also commercially, as most major vendors of clinical echocardiographic imaging systems currently offer RT3DE solutions. These developments hold promise as it potentially allows for a faster and more accurate assessment of global and regional ventricular dynamics, while overcoming the intrinsic limitations associated with 2D strain estimation such as out-of-plane motion. The superiority of RT3DE over previously used 2D techniques in terms of assessing *global* myocardial function has already been shown [178]. Nesser *et al.* demonstrated that RT3DE is more accurate and reproducible in estimating LV volumes and ejection fraction compared with 2D techniques

Various methods have been developed to estimate motion and deformation from volumetric ultrasound sequences as reviewed in chapter 2. While all these 3D strain estimation methods measure the same deformation of the heart, they do it in different ways, e.g. by using different regularization choices or postprocessing steps [158]. This was demonstrated in a recent study by Gayat *et al.* [77], showing a high intervendor dependency of strain measures. Therefore, it is essential that every method is validated individually before being introduced into clinical practice.

Despite the abundance of papers demonstrating regional 3D strain estimation within a clinical context, only a limited number of studies have validated these 3D strain algorithms in an in-vivo experimental setting (see table 5.1). This setup is favorable over simulated images or phantom experiments as it gives a more realistic motion pattern and image quality is closer to what is seen in clinical practice.

In this chapter we continue the development of a registration-based strain estimation methodology. In chapter 3, we showed that this technique outperformed block matching based methods in an animal setting on 2D US data [95]. Furthermore, in chapter 4 we illustrated the encouraging performance of this approach on volumetric data obtained from tissue mimicking phantoms on a regional level [94].

The aim of the present study was to further validate this methodology in 3D using an animal model by comparing the estimated strain values with a known ground truth, obtained through sonomicrometry.

Table 5.1: Overview of in-vivo validation studies to quantify 3D regional myocardial deformation

Approach	Study	#[1]	Segments[2]	ε_{RR}	ε_{LL}	ε_{CC}	ϵ_{AS}[3]	ϵ_{PP}[4]
Block matching	[64]*	3	Single	–	–	–	–	0.83 – 0.91 (1.8±3.56%)
	[210]	10	Multiple	0.84 (3±14%)	0.89 (2±10%)	0.9 (–3±13%)	–	–
			Separataly	0.59 – 0.7	0.65 – 0.68	0.71 – 0.78	–	–
	[209]	8	Multiple	–	–	–	0.87 (0.45±17.8%)	–
Registration	[176]*	5	Multiple	–	–	–	–	0.88 – 0.93
	[96]*	5	Single	0.21[(5)]	0.63	0.60	–	–
	Ch.5**	14	Single	0.69 (0.02±13.01%)	0.64 (–1.48±6.36%)	0.62 (–4.21±9.40%)	–	–
Model-based	[189]	4	Multiple	–	–	–	–	0.89

Methods were classified according to Jasaityte *et al.* [108]. The reported values are the correlation coefficients (r) against sonomicrometry. Values between brackets indicate the limits of agreement expressed as the mean bias ± 1.96 SD, if reported in the associated study.
[1]Number of animals in the validation study. [2]Some validation studies used multiple crystal pairs placed in different segments to assess a particular strain component. Correlations can therefore be reported using *multiple* segments together, or for every segment *separately* leading to a range of correlation values. In all other cases, only one crystal pair for each strain component was available and the correlation was reported in a *single* segment. [3]Area strain (as a substitute for ε_{RR}, also see appendix A). [4]Principal strain (per component or as an average of all three principal strain components, also see appendix A). [5]Not significant ($p = 0.42$). *Proceedings paper presented at a conference. **Study of the present chapter.

5.2 Materials and Methods

5.2.1 In-vivo animal setup

The same animal setup as the one presented in chapter 3 was used for the in-vivo validation of the registration-based strain estimation technique. For an extensive description of the animal preparation and the followed protocol, the reader is therefore referred to section 3.2.

Volumetric US data was recorded in 14 open-chest sheep during four stages: at baseline, during negative (esmolol) and positive (dobutamine) inotropic stimulation and during acute ischemia (ligation of the circumflex coronary artery; LCX). Sonomicrometric crystals were implanted in a tetrahedral configuration in the mid inferolateral (IL) wall, resulting in three crystal pairs, providing a reference measure for $\varepsilon_{\mathrm{RR}}$, $\varepsilon_{\mathrm{LL}}$ and $\varepsilon_{\mathrm{CC}}$.

Ischemia measurements could not be completed in three animals and esmolol data was lacking in two others. Two datasets had to be excluded from the analysis due to image dropout artefacts in the IL region (one dataset during dobutamine, and one dataset during ischemia). Overall, 49 datasets could thus be included for further analysis (see table 5.2).

The crystal data was processed according to the procedure described in section 3.2.3, and reference strain was calculated according to Eq. (3.1). End-systolic (ES) reference strain values were determined at aortic valve closure (AVC), defined by $(\mathrm{dP/dt})_{min}-20$ ms [239].

Table 5.2: Number of analysed in-vivo datasets

	Segment	B	E	D	I	All
$\varepsilon_{\mathrm{RR}}$	IL	14	12	13	10	49
$\varepsilon_{\mathrm{LL}}$	IL	14	12	13	10	49
$\varepsilon_{\mathrm{CC}}$	IL	14	12	13	10	49

The datasets are summarized for every stage individually (B: baseline, E: esmolol, D: dobutamine, I: ischemia) and over all stages (All). 3D strain estimates were compared in the IL segment.

5.2.2 Non-rigid image registration

Motion estimation

Motion was estimated in a similar fashion as in chapter 4. Inter-frame myocardial displacement was modeled with a 3D third-order B-spline tensor-product [203]:

$$\mathbf{u}_{f\rightarrow f+1}(\mathbf{r}) = \sum_{i\in\mathcal{N}_i}\sum_{j\in\mathcal{N}_j}\sum_{k\in\mathcal{N}_k} \boldsymbol{\mu}^{ijk}\beta_x^3(\frac{x-\kappa_x^{ijk}}{\sigma_x})\beta_y^3(\frac{y-\kappa_y^{ijk}}{\sigma_y})\beta_z^3(\frac{z-\kappa_z^{ijk}}{\sigma_z}) \quad (5.1)$$

with κ_ξ^{ijk} and σ_ξ the control point location and spacing respectively, and N_ξ the set of control points within the compact support $\mathcal{N}$ of the B-spline β_ξ ($\xi \in \{x, y, z\}$).

For reasons mentioned in section 4.6.4, the sum of squared differences (SSD) was used as an image similarity metric. Regularization was performed during the optimization process by the addition of a smoothness penalty R_{sm} based on the 3D equivalent of the bending energy of a 2D thin sheet of metal [203] in the cost function C:

$$\begin{aligned} C &= \text{SSD} + \omega R_{sm} \\ &= \frac{1}{P}\sum_{\mathbf{r}\in\mathbf{I}_f}\left[\mathbf{I}_f(\mathbf{r}) - \mathbf{I}_{f+1}(\mathbf{T}(\mathbf{r}))\right]^2 + \frac{\omega}{P}\sum_{\mathbf{r}\in\mathbf{I}_f}\left\|\frac{\partial^2\mathbf{T}(\mathbf{r})}{\partial\mathbf{r}\partial\mathbf{r}^T}\right\|_F^2 \end{aligned} \quad (5.2)$$

with P the number of points $\mathbf{r}$ and ω a factor to modulate the influence of the smoothness penalty. The parameter ω was set to 5.10^5, which was chosen empirically by visual inspection of the tracking results. In every frame, pixels outside the ultrasound sector were masked to assure that this part of the image did not contribute to the calculations in the registration process. The current choices for the different components in the registration framework have all been proven useful for myocardial motion estimation from ultrasound data [55][67][132]. Further details regarding the optimization process and its interplay with SSD and R_{sm} can be found in appendix B. In contrast with chapter 4, the method was reimplemented completely within the framework of ITK, a collection of open-source C++ image analysis libraries [266].

Strain estimation

In practice, subsequent images in the cardiac cycle were first registered to each other in a pairwise fashion. To find the transformation field $\mathbf{T}$ in frame f with respect to end-diastole (ED), inter-frame transformation fields were cumulated:

$$\mathbf{T}_{\mathrm{ED}\to f}(\mathbf{r}) = \mathbf{T}_{f-1\to f}(\mathbf{r}) \circ \cdots \circ \mathbf{T}_{2\to 3}(\mathbf{r}) \circ \mathbf{T}_{\mathrm{ED}\to 2}(\mathbf{r}) \tag{5.3}$$

To assess strain within a certain region-of-interest (ROI), the endo- and epicardial borders were first manually contoured in a number of slices at end-diastole using custom-made software (Speqle3D, KU Leuven, see Fig. 5.1). A least-square surface fitting procedure with a fifth order spherical harmonics expansion was used to generate endo- and epicardial surfaces [45] which were subsequently labeled corresponding to a standard 18-segment LV model (Fig. 5.1, [37]). Next, this ROI was populated with a 3D myocardial mesh of 9000 points, sampled along the directions of a local cardiac coordinate system (5, 30 and 60 samples in the radial, longitudinal and circumferential direction respectively). Finally, the generated mesh was propagated over the cardiac cycle using the estimated inter-frame transformation fields.

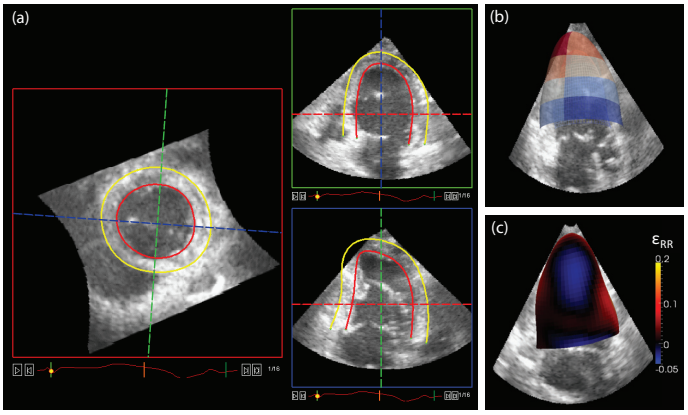

Figure 5.1: General workflow to assess 3D strain: (a) The region-of-interest is manually delineated using custom-made software (Speqle3D, KU Leuven) in a select number of image slices. (b) Next, a 3D myocardial mesh is created using these contours (the colors indicate the 18 segment LV model). (c) Using the image registration results, this mesh is deformed over the cardiac cycle and strain is calculated (the color overlay shows the end-systolic radial strain in a dataset during acute ischemia in the mid infero-lateral wall).

Please note that this mesh contained less points compared to the one used in chapter 4 (where $5 \times 40 \times 80$ points were defined). This was to ensure that segments contained an equal and integer amount of sampling points in the longitudinal direction (3 levels of 10 points), and circumferential direction (6 segments of 10 points), without sacrificing too much strain resolution, while at the same time speeding up the calculations.

Strain was then estimated similarly to sonomicrometry as in Eq. (3.1), and a drift compensation was performed according to Eq. (3.5). Finally, strain values were averaged within each segment and end-systolic (ES) strain values were extracted in the infero-lateral wall. The end-systolic frame was visually defined based on the timing of aortic valve closure (AVC).

5.2.3 Statistical analysis

The calculated 3D end-systolic strain values were correlated with the reference ES strain values obtained with sonomicrometry using the Pearson correlation coefficient. They were considered statistically significant when p-values were lower than 0.05. The agreement between the two methodologies was evaluated using Bland-Altman analysis of the systolic strain values.

Eight randomly selected datasets (i.e. two datasets during baseline, dobutamine, esmolol and ischemia conditions) were recontoured and processed again using the non-rigid image registration method for the assessment of 3D strain reproducibility. Intra-observer variability was expressed as the mean percent error (absolute difference divided by the mean of the two measurements).

5.3 Results

The correlation coefficients between the estimated ES strain and the reference ES strain values were r=0.69 for $\varepsilon_{\mathrm{RR}}$ (p<0.001), r=0.64 for $\varepsilon_{\mathrm{LL}}$ (p<0.001) and r=0.62 for $\varepsilon_{\mathrm{CC}}$ (p<0.001), as shown in Fig. 5.2. Bland-Altman analysis revealed the bias and the 95% limits of agreement for the radial, longitudinal and circumferential component to be $0.02 \pm 13.01\%$, $-1.48 \pm 6.36\%$ and $-4.21 \pm 9.40\%$ respectively (Fig. 5.3).

Examples of strain curves obtained with the registration method and sonomicrometry are shown in Fig. 5.4 during baseline conditions and acute ischemia. Fig. 5.5 illustrates the strain changes occuring during acute ischemia.

Intra-observer variability was 8.5%, 5.8% and 3.5% for $\varepsilon_{\mathrm{RR}}$, $\varepsilon_{\mathrm{LL}}$ and $\varepsilon_{\mathrm{CC}}$ resp.

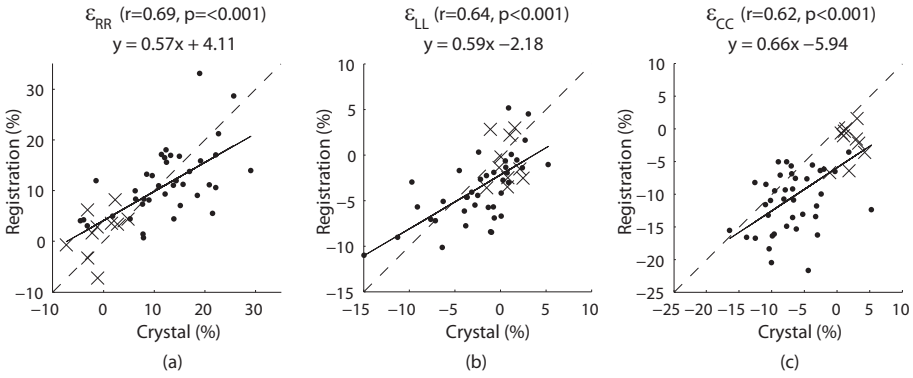

Figure 5.2: Estimated end-systolic strain by the registration method against the reference end-systolic strain calculated from sonomicrometry in the (a) radial, (b) longitudinal and (c) circumferential direction. Crossed points originate from datasets acquired during acute ischemia. The dashed line represents the line of identity.

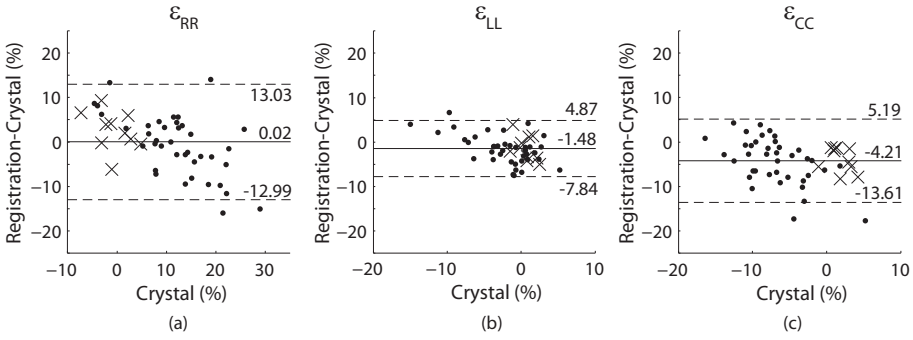

Figure 5.3: Bland-Altman plot of the end-systolic strain values obtained with the registration method and sonomicrometry in the (a) radial, (b) longitudinal and (c) circumferential direction. Crossed points originate from datasets acquired during acute ischemia. The dashed horizontal lines represent the limits-of-agreement ($\mu \pm 1.96\sigma$).

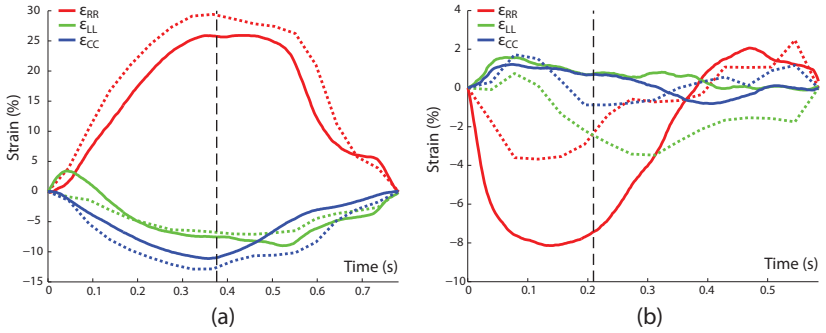

Figure 5.4: Estimated strain (dotted line) against reference strain values (full line) for (a) a dataset at baseline conditions and (b) during acute ischemia.

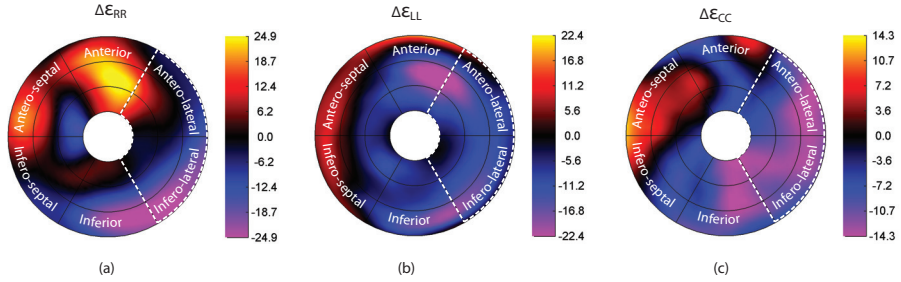

Figure 5.5: Bullseye plot illustrating the spatial distribution of the change in end-systolic (a) radial, (b) longitudinal and (c) circumferential strain during acute ischemia of the left circumflex artery (LCX) compared with baseline conditions ($\Delta\varepsilon = |\varepsilon_{ischemia}| - |\varepsilon_{baseline}|$). The typical LCX perfusion area is indicated with a dashed line [187].

5.4 Discussion

Despite the abundance of papers demonstrating regional 3D strain estimation within a clinic context, only a limited number of studies have validated these 3D strain algorithms in an in-vivo experimental setting (see table 5.1). This setup is favorable over simulated images or phantom experiments as it gives a more realistic motion pattern and image quality is closer to what is seen in clinical practice. The aim of the present study therefore was to validate our previously proposed 3D strain estimation methodology on a segmental level in an animal model for which a ground truth deformation estimate is available.

Significant and encouraging correlations were obtained for all cardiac directions, with slightly higher values in the radial (r=0.69) direction compared to the other directions (r=0.64 for $\varepsilon_{\mathrm{LL}}$, and r=0.62 for $\varepsilon_{\mathrm{CC}}$). Compared to our previous preliminary results [96], radial correlation was much better (from r=0.21 to r=0.69). This is probably due to the increased number of animals (from five to fourteen) and the increased $\varepsilon_{\mathrm{RR}}$ range as more ischemic datasets were available (originally only three were analysed).

These findings are in agreement with the current state-of-the-art commercial 3D speckle tracking methods, which typically rely on block-matching based algorithms. In a study by Seo *et al.* [210], regional correlations of r=0.59–0.70 for $\varepsilon_{\mathrm{RR}}$, r=0.65–0.68 for $\varepsilon_{\mathrm{LL}}$ and r=0.71–0.78 for $\varepsilon_{\mathrm{CC}}$ were obtained against sonomicrometry in an animal population of 10 sheep.

A comparable registration method developed by Myronenko *et al.* [176] gave high correlations (r=0.88–0.93) against sonomicrometry traces. It is important to note that these strain values were calculated between crystal pairs which were spread out over multiple segments, and which were not necessarily aligned to the cardiac directions. In contrast, in the present study all crystal pairs were located within one segment and oriented along the cardiac directions.

As can be seen from the Bland-Altman plots (Fig. 5.3), the method seemed to overestimate excursions specifically in the circumferential direction (–4.21%), while bias in the longitudinal direction was lower (–1.48%), and even negligible for the radial direction (0.02%). Nevertheless, the limits-of-agreement (LOA) were largest for the radial component, while the smallest variability was seen for $\varepsilon_{\mathrm{LL}}$. The observed $\varepsilon_{\mathrm{CC}}$ bias may be explained by the fact that circumferential strain was averaged over the myocardial wall while the crystal pair was placed epicardially. Indeed, it is well known that a heterogeneous transmural strain distribution exists with the lowest circumferential strain located at the epicardium [28]. The large variability in the radial direction could be related to the fact that the spatial motion gradient has to be estimated within a relatively small region due to the limited wall thickness. Furthermore, since the LV is typically scanned from an apical view in 3D echocardiography, beam density and consecutively spatial resolution is lower in the radial direction than in the longitudinal direction. It is also worth mentioning that even with 2D strain estimation techniques radial strain estimation has been more difficult and prone to errors [130].

Comparing the observed LOA to literature is difficult since no other studies have reported this on a segmental level. In the study by Seo *et al.* [210] using a block-matching based approach, Bland-Altman plots were only made for all segments simultaneously. Nevertheless, the LOA were narrower in all directions for our registration method (table 5.1: 13% vs 14%; 6% vs 10%; and 9% vs

13% for ε_{RR}, ε_{LL} and ε_{CC} respectively). As mentioned previously in section 3.5.1, these findings may be explained in terms of the underlying tracking mechanism which is different for both techniques.

Intra-observer variability was remarkably lower for our registration method compared to the reproducibility reported by Seo *et al.* [210]: 8.5% vs 13.5% for ε_{RR}, 5.8% vs 7.8% for ε_{LL} and 3.5% vs 8.9% for ε_{CC} respectively. As noticed previously in section 3.5.3, this may be related to the fact that the registration method produces a dense motion field for the complete image irrespectively of the chosen ROI, whereas the block-matching based method typically estimates motion in a predefined ROI only. Reanalyzing the data with a slightly different ROI may thus result in a different selection of stable speckle patterns, which may lead to a higher intra-observer variability.

Fig. 5.5 illustrates that the registration method is able to detect deformation changes occurring in the perfusion area of a coronary artery during an acute occlusion. Indeed, as can be noted from Fig. 5.5, end-systolic ε_{RR} dropped considerably in the LCX perfusion area. Similarly, both ε_{LL} and ε_{CC} estimates decreased, i.e. became less negative, during artery occlusion. This is in correspondence with the expected strain behavior during ischemic episodes [25].

5.4.1 Limitations

In the present study only strain values within the infero-lateral wall were assessed as this was the only segment in which reference values were available. Although in theory more crystal pairs could be implanted, the amount of crystals that could be acquired simultaneously was limited by the sonomicrometry system (in our case maximum 7 crystals). Moreover, it would have also prolonged an already complex experimental protocol.

Aligning US acquisitions and crystal traces in time is challenging given that both acquisition systems interfere and can thus not operate simultaneously. In the present study, aortic valve closure was visually identified on the echocardiographic recordings in order to define end-systole in the ultrasound sequence. On the other hand, for the crystal data, AVC was selected based on simultaneously recorded LV pressures in analogy to the method described by Theroux *et al.* (taking $(dP/dt)_{min}-20$ ms; [239]). These different approaches towards the definition of end-systole may have induced small timing errors with corresponding errors for the end-systolic strain values.

In order to improve this temporal registration process in future experiments, it may be better to continuously record pressure data. In this way, the ultrasound images could be temporally aligned with the pressure data by cross-

correlation of the ECG signals recorded simultaneously by both acquisition systems (i.e. the ultrasound scanner and the physiologic data acquisition system). As such, AVC could always be defined on the pressure traces and then imposed on the (time registered) ultrasound images and the sonomicrometry signals (intrinsically time aligned as these signals are sampled by the same physiologic data acquisition system). Of course, this approach would imply that the physiology of the animal does not change between the ultrasound and sonomicrometry recordings which is a reasonable assumption given the recordings are made immediately after one another. In the current study, this timing approach could not be used given that the whole physiologic data acquisition system was switched off during ultrasound recordings rather than the sonomicrometry system alone.

Whether 3D non-rigid image registration performs better than 3D block-matching based methodologies still remains to be proven. Nevertheless, as 3D ultrasound typically comes at the expense of temporal resolution with associated de-correlation between subsequent volumes, non-rigid image registration may be more robust as it utilizes a more global motion estimation approach.

Also worth noting is that in general, motion estimation approaches rely on good image quality. Since volumetric data was acquired through a sternotomy, only two datasets had to be excluded from analysis. In clinical practice however, the quality of the volumetric images may be inferior (feasibility ranges from 63% to 83%; [108]) and may thus affect tracking quality. Indeed, in clinical practice, 3D strain values have been compared to 2D techniques, e.g. by Maffessanti *et al.* who only found moderate segmental correlations of r=0.49 and r=0.43 for $\varepsilon_{\mathrm{LL}}$ and $\varepsilon_{\mathrm{CC}}$ respectively [150], whereas radial correlation was poor (r=0.24). These observations are consistent with a previous clinical study in which we compared the 3D segmental strain estimates against those obtained with 2D techniques (r=0.63 for $\varepsilon_{\mathrm{LL}}$, r=0.41 for $\varepsilon_{\mathrm{CC}}$ and no significant correlation for $\varepsilon_{\mathrm{RR}}$)[109].

5.4.2 Future perspectives

Despite the great potential of 3D echocardiography to quantify regional cardiac function, some emerging shortcomings may potentially hamper a widespread use in clinical practice in the future. First of all, a recent study demonstrated that inter-vendor variability of commercially available software packages to assess 3D strain was high [77]. Apart from using different underlying tracking algorithms, this may also be due to a lack of standardization (e.g. Should peak or ES strain be reported? How is ED defined? Should strain be measured in the sub-endocardium, sub-epicardium or mid-myocardium?) It is worth

mentioning that a working group of experts has recently been formed by the European Association of Cardiovascular Imaging and the American Society of Echocardiography to work on the standardization of 2D strain estimation software. Extending the focus to 3D strain estimation would thus be beneficial.

Furthermore, validating and comparing different 3D strain methodologies has been difficult due to a lack of benchmark data. Very recently, De Craene *et al.* [53] initiated the construction of publicly available 3D benchmark data. Currently, the database consists of simulated data covering healthy, ischemic and left bundle branch block images. The validation protocol presented in this chapter may be inspirational to further extend the database to include more realistic images.

5.5 Conclusions

In this study, we have demonstrated that all strain components could be estimated with acceptable accuracy from volumetric ultrasound datasets in an animal model. These findings are comparable to the performance of the current state-of-the-art commercial 3D speckle tracking methods. Furthermore, the shape of the strain curves, timing of peak values and location of dysfunctional regions were identified well. Whether 3D non-rigid image registration performs better than 3D block-matching based methodologies still remains to be proven.

Chapter 6

Non-rigid image registration using a transformation model adapted to the heart: Quantifying myocardial function from 2D US images

This work was published in:
B. Heyde, P. Claus, R. Jasaityte, D. Barbosa, S. Bouchez, M. Vandenheuvel, P. Wouters, F. Maes, and J. D'hooge. Motion and deformation estimation of cardiac ultrasound sequences using an anatomical B-spline transformation model. In *ISBI - International Symposium on Biomedical Imaging*, pages 266–269, Barcelona, Spain, 2-5 May 2012 [93].

6.1 Motivation

In the previous chapters we demonstrated the potential of non-rigid image registration based on a B-spline free-form deformation (FFD) model in quantifying regional cardiac function from both 2D and 3D ultrasound image sequences by validating this technique in two realistic validation settings. Furthermore, its success for cardiac strain estimation has also been shown by other researchers on both scan-converted US data (e.g. [132]) and non-scan-converted data (e.g. [68] [176]). In these models, myocardial deformation was parametrized using a rectangular shaped FFD lattice defined in Cartesian space, abbreviated as CFFD in the upcoming chapters (see Fig. 6.1a).

While the performance of these techniques was encouraging, there are several reasons to believe that improvements related to the transformation model could still be made from a theoretical point of view. First of all, *the resolution of the FFD lattice* will intrinsically influence the smoothness of the retrieved deformations. A coarse control point grid will result in capturing only global and intrinsically smooth deformation patterns, whereas lowering the grid spacing allows to retrieve more local deformations, but at a higher computational cost and often requiring a higher level of regularisation to keep the deformations physiologically relevant. Adding more myocardial specific regularisation terms (e.g. volume conservation) may improve motion estimates.

Secondly, *the control point topology* for a given resolution level will indirectly dictate the range of deformations that can be modelled. For example, in order to capture the inward concentric motion pattern seen in short axis US images during systole, it may require less control points and potentially increase the convergence rate during optimization, if the grid topology would be adapted to the expected motion (e.g. as shown in Fig. 6.1b) compared to the more traditional regular grid organisation (as in Fig. 6.1a). Even for the CFFD model, it was demonstrated that adopting a non-uniform control grid spacing could already result in a significant reduction in registration-time without compromising performance [207].

In this light, other transformation models more closely matching the left ventricular motion have been proposed for the analysis of MR images (Fig. 6.1b), by using a cylindrical FFD (e.g. [41] [57]), a prolate spheroidal FFD (e.g. [136]) or an extended cylindrical FFD (e.g. [137]). However, these geometrical transformation models do not necessarily follow the true anatomy of the heart and are often applied to stacks of 2D short-axis MR data, where motion is not estimated in the apical regions. Furthermore, their application for function quantification in echocardiography remains currently underexplored.

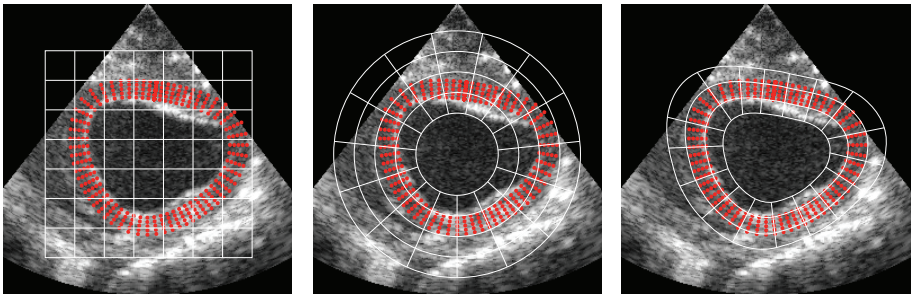

Figure 6.1: Different B-spline support grid topologies used in non-rigid registration: (a) Cartesian grid, (b) Polar grid (equal to 3D slice of cylindrical and prolate spheroidal grid) and (c) proposed anatomical grid. The points within the region-of-interest for strain estimation are highlighted in red.

In this chapter, we propose an anatomical free-form deformation model (AFFD) as shown in Fig. 6.1c, which is locally adapted to the LV shape. In this model, the B-spline basis functions are locally oriented along the cardiac directions of the endocardial surface, i.e. the radial, longitudinal and circumferential direction. This arrangement has several advantages. It naturally enforces smoothness in the physiologically relevant directions. In contrast, CFFD models enforce smoothness in the image directions (x, y, z), which do not relate to the LV anatomy nor correspond to the principal motion directions. Moreover, since the CFFD grid covers the LV cavity completely, it incorrectly treats the blood pool and the myocardium in a similar way whereas the AFFD grid covers the myocardium more efficiently and allows for imposing more selective boundary conditions. Finally, given its more efficient myocardial coverage, it leads to a reduced amount of parameters, potentially reducing the registration time.

This chapter focuses on the feasibility of this AFFD model for the extraction of strain from 2D US image sequences. The implementation of the AFFD model is discussed first. Its performance is then compared against the CFFD model in an in-vivo setting, and the tracking for both methods is scored by several clinicians. Its application on 3D echocardiography is the subject of chapter 7.

6.2 Anatomical FFD registration

General principles

The AFFD B-spline grid is organized according to the shape of the endocardium, both in short axis (SAx) and apical views (Fig. 6.2a). Due to the locally varying grid topology, it becomes evident that the mathematical formulation of the B-spline grid locations, their local neighborhood and grid refinement schemes are complex. In effect, the definition of a B-spline tensor product, as defined in Eq. (3.2), and its evaluation in this local coordinate system is not straightforward. Some authors define the control grid after performing a *global* coordinate transform, e.g. as in [41]. Our formulation differs in the sense that we aim to determine an *anatomical* transform which aligns the B-spline grid *locally* to the cardiac radial (r), longitudinal (r) and circumferential (c) directions.

An alternative implementation for such an anatomical organized grid is to transform the images to anatomical coordinates first, such that the overlying grid becomes a rectangular lattice similar to the Cartesian formulation where standard registration techniques can be applied. This anatomical unfolding process is shown schematically in Fig. 6.2b-d, and is discussed in the next sections.

Endocardial sampling strategy

In practice, the endocardium was first manually contoured in the end-diastolic (ED) frame using custom-made software (Speqle3D, KU Leuven). This contour was then sampled in a fixed number of points. In this feasibility study, a total of 360 points was used. For the SAx images, this corrsponds to one point for each degree of an imaginary polar grid with the origin being the center of the endocardium, resulting in an approximate uniform distribution of sampling points along the circumference. Similarly, the endocardial border of the apical images was sampled in 360 points, but equally distributed along the longitudinal direction based on the arclength of the contour, rather then adopting a polar transform similar to the SAx images as this would lead to a lower sampling rate near the apex. By using a linear interpolation scheme for the image intensities at these sampling points, the image along this curved contour could be transformed into anatomical space, i.e. it was unfolded and could be mapped onto a straight line (Fig. 6.2b-c, red line).

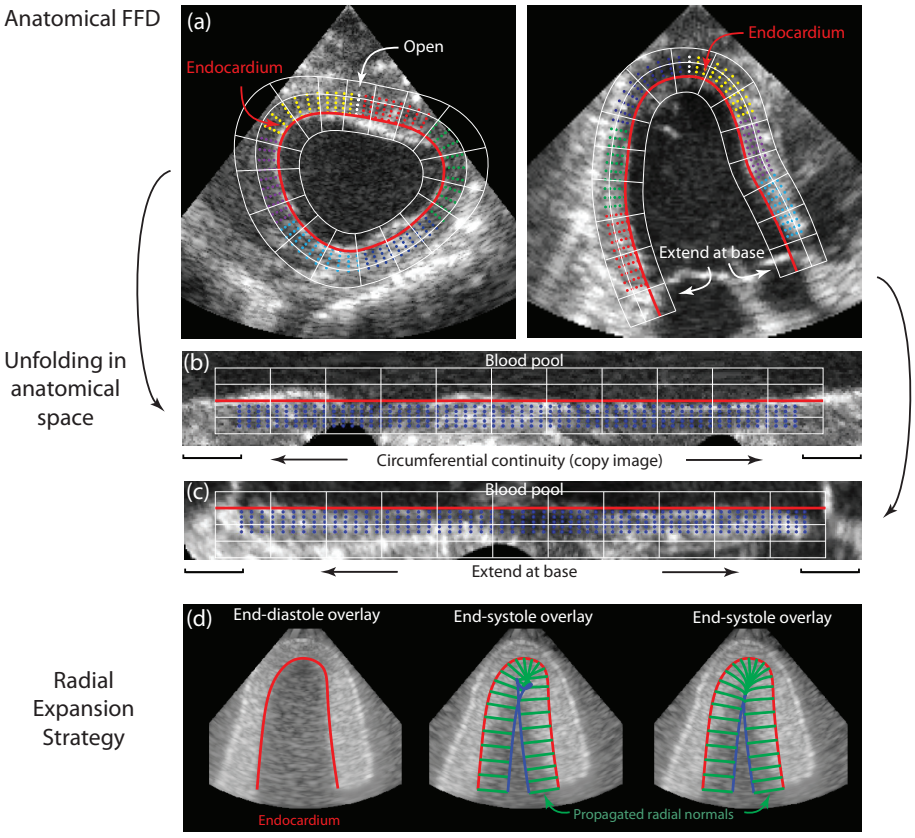

Figure 6.2: Overview of the anatomical unfolding process

Radial sampling strategy

The Cartesian image was then further resampled along the normals of the endocardial contour. In this feasibility study, a fixed number of points (50) was used for this purpose. The normals extend both inward towards the blood pool and outward towards the epicardium to ensure that the full myocardium remains inside the transformed image during the whole cardiac cycle. However, simply expanding the contour towards the blood pool along a fixed normal direction may lead to tissue folding in Cartesian space. This situation often occurs near the apex or at locations with a high curvature (see Fig. 6.2d mid). This direction, corresponding to the radial direction $\boldsymbol{n}_{\mathrm{R}}(x,y) = [n_{\mathrm{R}x}(x,y), n_{\mathrm{R}y}(x,y)]$, should therefore not be kept constant, but rather evolve dynamically towards the inner cavity.

In practice, this can be solved by posing this propagation process as a diffusion problem for each component of $\boldsymbol{n}_{\mathrm{R}}(x,y)$. For example, for $n_{\mathrm{R}x}(x,y)$ this requires solving the following differential equation:

$$\frac{\partial n_{\mathrm{R}x}(x,y,t)}{\partial t} = \alpha \nabla^2 n_{\mathrm{R}x}(x,y,t) \tag{6.1}$$

with

$$\begin{cases} n_{\mathrm{R}x}(x,y,0) = n_{\mathrm{R}x}^{\mathbf{B}} & \text{if } (x,y) \in \mathbf{B} \\ n_{\mathrm{R}x}(x,y,0) = 0 & \text{if } (x,y) \notin \mathbf{B} \\ n_{\mathrm{R}x}(x,y,t) = n_{\mathrm{R}x}^{\mathbf{B}} & \text{if } (x,y) \in \mathbf{B} \end{cases} \tag{6.2}$$

and where α represents the diffusivity, and $n_{\mathrm{R}x}^{\mathbf{B}}$ corresponds to the x-component of the radial direction on the endocardial border $\mathbf{B}$. This simple heat equation is solved by an explicit forward difference scheme in t and a central difference scheme for the spatial derivatives. In practice, 100 iterations proved to be a good trade-off between calculation time and desired accuracy. Following the calculated streamlines, the contour is propagated in both the direction of the blood pool (as shown in Fig. 6.2d right), and towards the epicardium.

Boundary conditions

To ensure circumferential spatial continuity of the deformation field in the SAx images at the position where the contour was opened, a small part of the transformed image (10%) was copied on either side (Fig. 6.2b). In order to account for longitudinal motion near the base, the endocardial contour of the apical images was oversampled by extending the mesh (by 10%) along the longitudinal direction of the base (Fig. 6.2c).

Motion estimation

Using the process outlined above, all images in the recorded image sequence I are transformed to an anatomical equivalent image sequence $\hat{I}$ in $[r,c]$ or $[r,l]$ coordinates for the SAx and the apical views respectively. The same transform is used for all frames of the cardiac cycle. This process can be performed prior to registration since it is only dependent on the position of the endocardial contour at ED. Motion between subsequent frames can then be expressed in anatomical coordinates using the standard FFD techniques employed in the previous chapters. For example, adapting Eq. (3.2) for the SAx views leads to

$$\hat{\mathbf{u}}_{f \to f+1}(\hat{\mathbf{r}}) = \sum_{i \in \mathcal{N}_i} \sum_{j \in \mathcal{N}_j} \boldsymbol{\mu}^{ij} \beta_r^3\left(\frac{r - \kappa_r^{ij}}{\sigma_r}\right) \beta_c^3\left(\frac{c - \kappa_c^{ij}}{\sigma_c}\right) \tag{6.3}$$

with a similar expression in $[r, l]$ coordinates for the apical views. To indicate that motion is estimated in anatomical space, the ($\hat{}$)-symbol was used. The same registration components from chapter 3 were used: sum of squared differences as a similarity criterion, bending energy as a regularisation term, and the LBFGSB optimizer to find the optimal deformation field. The regularisation weight was determined empirically. For more details, the reader is referred to section 3.3.2 and appendix B.

Strain estimation

A region-of-interest (ROI) for strain estimation can be created by expanding the endocardial contour at ED along its normal to represent the myocardium. Please note that the myocardium is not necessarily required to have a constant thickness in this framework. For the SAx images, this region was subsequently populated in the radial and circumferential direction with 5 and 60 points respectively, and given a label corresponding to one of the 6 equally spaced segments around the circumference (Fig. 6.2a left, colored points). These points define the locations where strain values will be extracted. For the apical images this region was populated in a similar fashion, with 3 equally spaced segments stretching from base to apex on both sides of the LV (Fig. 6.2a right, colored points). This ROI is then mapped into anatomical space (Fig. 6.2b-c blue points).

Using the frame-to-frame registration results, the transformed ROI is propagated in the resampled image sequence and then transformed back to Cartesian space. Strain was then estimated as in Eq. (3.1) and a drift compensation was performed to obtain values of zero strain at ED by distributing the remaining strain offset uniformly over the cardiac cycle, as in Eq. (3.5). Finally, strain values were averaged within each segment and end-systolic (ES) strain values were extracted in the infero-lateral (IL) wall.

6.3 Experiments

To validate the proposed anatomical registration and to compare its performance against conventional Cartesian registration, myocardial deformation was estimated with both methods in an in-vivo setup where sonomicrometry was used as a ground-truth. The reader is referred to section 3.2 for an extensive description of the animal setup, the location of the sonomicrometry crystals and the ultrasound scanning protocol.

In section 3.3, data from five open-chest Suffolk sheep (39±5 kg) were processed using the CFFD model (see table 3.1). The same data was reprocessed using the AFFD model described in this chapter. Care was taken to ensure that parameters of the registration were chosen as similar as possible for both methods, e.g. same similarity measure (SSD and smoothness penalty), same optimizer (LBFGSB), same B-spline order, same amount of model refinement stages, comparable amount of B-spline grid point covering the myocardium in the final refinement stage and same strain calculation.

The performance of both registration methods was evaluated by correlating the obtained systolic strain values with the reference strain values obtained by sonomicrometry using the Pearson correlation coefficient and by performing a Bland-Altman analysis. Fishers z-transformation was used to compare the strengths of different correlations whereas the bias between the Bland-Altman plots was compared with a paired t-test. The F-test was used to compare the limits of agreement between the Bland-Altman plots. P-values lower or equal to 0.05 were considered significant.

In addition, a qualitative clinical validation was performed. Three cardiologists with a varying degree of experience were asked to compare the registration methods: either the AFFD model was visually more appealing, the CFFD model was visually more appealing or no tracking method was preferred over the other. The image data was randomized and blinded for each observer. A Wilcoxon signed-rank test was used to assess whether one method was preferred over the other.

6.4 Results

The correlations between the estimated ES strain and the reference ES strain values for the AFFD model were r=0.77, r=0.82 and r=0.63 for $\varepsilon_{\mathrm{RR}}$, $\varepsilon_{\mathrm{CC}}$ and $\varepsilon_{\mathrm{LL}}$ respectively. For the CFFD model they were r=0.85, r=0.80 and r=0.61 respectively (see Fig. 6.3). Results for the Bland-Altman analysis, as well as the registration time are summarized in table 6.1. Finally, the tracking performance as judged by the cardiologists is shown in table 6.2.

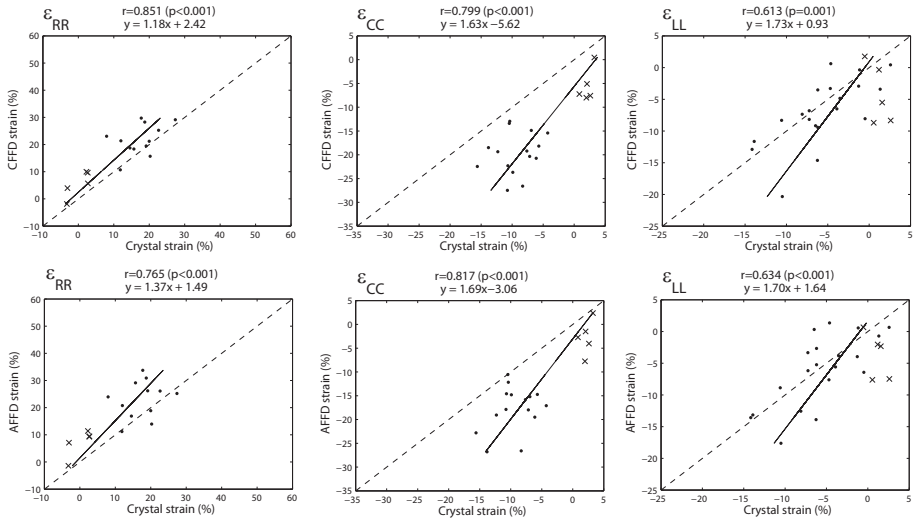

Figure 6.3: Scatter plots of estimated (left) $\varepsilon_{\mathrm{RR}}$, (mid) $\varepsilon_{\mathrm{CC}}$ and (right) $\varepsilon_{\mathrm{LL}}$ for (top) Cartesian registration (CFFD) and (bottom) anatomical registration (AFFD) against sonomicrometry. The dotted line is the line of identity. Points marked with a $\times$ indicate ischemic datasets.

Table 6.1: Comparison of the cffd and affd model

	Correlation			Bias (%)			Time (s)
	$\varepsilon_{\mathrm{RR}}$	$\varepsilon_{\mathrm{CC}}$	$\varepsilon_{\mathrm{LL}}$	$\varepsilon_{\mathrm{RR}}$	$\varepsilon_{\mathrm{CC}}$	$\varepsilon_{\mathrm{LL}}$	
CFFD	0.851	0.799	0.613	4.65	–9.68	–2.18	7.47±3.80
AFFD	0.765	0.817	0.634	6.08	–7.50	–1.36	5.39±0.55*
p	0.27	0.44	0.46	0.24	0.07	0.26	< 0.01*

	Limits-of-agreement (%)		
	$\varepsilon_{\mathrm{RR}}$	$\varepsilon_{\mathrm{CC}}$	$\varepsilon_{\mathrm{LL}}$
CFFD	–5.27 .. 14.58	–18.56 .. –0.80	–10.91 .. 6.54
AFFD	–6.70 .. 18.86	–16.63 .. 1.63	–9.94 .. 7.22
p	0.16	0.55	0.47

Comparison in terms of the correlation coefficient (Fisher's z-transform), bias (t-test), limits-of-agreement (F-test). The inter-frame registration time was compared using a t-test. $p < 0.05$ was considered significant and is indicated with a $*$.

Table 6.2: Qualitative clinical validation

	Experience	Tracking preference		
		CFFD	AFFD	None
SAx views				
Cardiologist 1	+++	1	11*	4
Cardiologist 2	++	3	8*	5
Cardiologist 3	+	7	6	3
Mean preference		3	9*	4
Apical views				
Cardiologist 1	+++	0	18*	2
Cardiologist 2	++	3	12*	5
Cardiologist 3	+	10	6	4
Mean preference		1	14*	5

Number of datasets with preference for the CFFD/AFFD tracking method judged by cardiologists with varying degree of experience. Statistically significant results are indicated with a $*$.

6.5 Discussion

From Fig. 6.3 and table 6.1, it can be noted that the AFFD model slightly underperforms for the radial strain: the correlation is somewhat lower, the bias is slightly higher, and the limits-of-agreement are wider. However, this trend is never statistically significant. The radial movement in the SAx images might have been restricted too much by the circumferential movement in the AFFD model as the bending energy is currently isotropic. Due to the anatomical unfolding, both motion modes are after all intrinsically linked together. In the future it may thus be better to consider an anisotropic bending energy for example. The longitudinal and circumferential strain for both models are on par with each other, with the bias being on the edge of being statistically smaller for the AFFD model. The correlation for the longitudinal strain component only increased slightly, but was still surprisingly low compared to other validation studies. The reader is referred to section 3.5.2 for a discussion on this topic. It is important to note that these measures all describe the tracking performance of only one particular region (containing the crystals) and at only one instance of the cardiac cycle (end-systole).

In order to assess the tracking performance in more regions, and at more time points, three cardiologists were asked to indicate their preference. Overall,

table 6.2 showed a strong preference of the tracking with the AFFD model, especially for the apical views. The clinical experts only favored the CFFD model in a minority of cases (in 19% for the SAx views, and in 5% for the apical views). It is also worth noting that a trend was visible in terms of tracking preference and the experience of the cardiologist. Senior cardiologists favored the AFFD model more then cardiologists in training. This seems to indicate that differences between both tracking methods were sometimes subtle and ambiguous. This can be appreciated from Fig. 6.4 in which the tracking results of both methods are superimposed at several time instances of the cardiac cycle. Please note that the AFFD model is always shown in green in this figure, but these colors were randomized when they were presented to the cardiologists. Examples are shown for cases with either a distinct preference for the AFFD model, or no preference at all. In the former case, yellow arrows highlight the biggest differences. For the SAx images the epicardial septal border in the CFFD model was often pushed too far inside due to the inward motion of the right ventricle (RV) during systole (Fig. 6.4a). This did not occur in the AFFD model due to the 'natural' masking of the RV during anatomical unfolding. In the apical views, the AFFD model appeared to better cope with fast motions during the cardiac cycle (Fig. 6.4c). The CFFD model lagged behind during systole, and drifted towards the blood pool at the end of the cardiac cycle.

The major rationale behind this work is that an AFFD model offers several advantages over the CFFD model. First of all, the organisation of the B-spline grid more closely matches the shape and motion of the heart. CFFD has a shape mismatch which can cause B-spline spans to contain few or no myocardial displacement measurements, and which may cause additional errors. While the performance of both methods is comparable, the AFFD model is able to do so through a more efficient myocardial grid coverage, thus using less parameters and leading to a reduced inter-frame registration time (5.39 ± 0.55 s versus 7.47 ± 3.80 s for the CFFD model). Moreover, since the CFFD grid covers the LV cavity completely, it incorrectly treats the blood pool and the myocardium in a similar way, whereas an AFFD model allows to impose conditions more closely coupled to the LV physiology, e.g. the smoothness penalty is naturally aligned with the fibre and cross-fibre directions in the myocardium. It also allows to include a-priori knowledge in a more straight-forward manner, e.g. by imposing volume conservation on the myocardium only. The effect of this cost function on tracking performance is discussed in chapter 10.

A potential limitation of the present feasibility study is that all images were currently transformed to anatomical space using a fixed number of sampling points irrespective of the physical size of the ventricle. This implies that larger ventricles may lose resolution compared to smaller ventricles. This will be tackled in chapter 7. Furthermore, circumferential continuity is currently

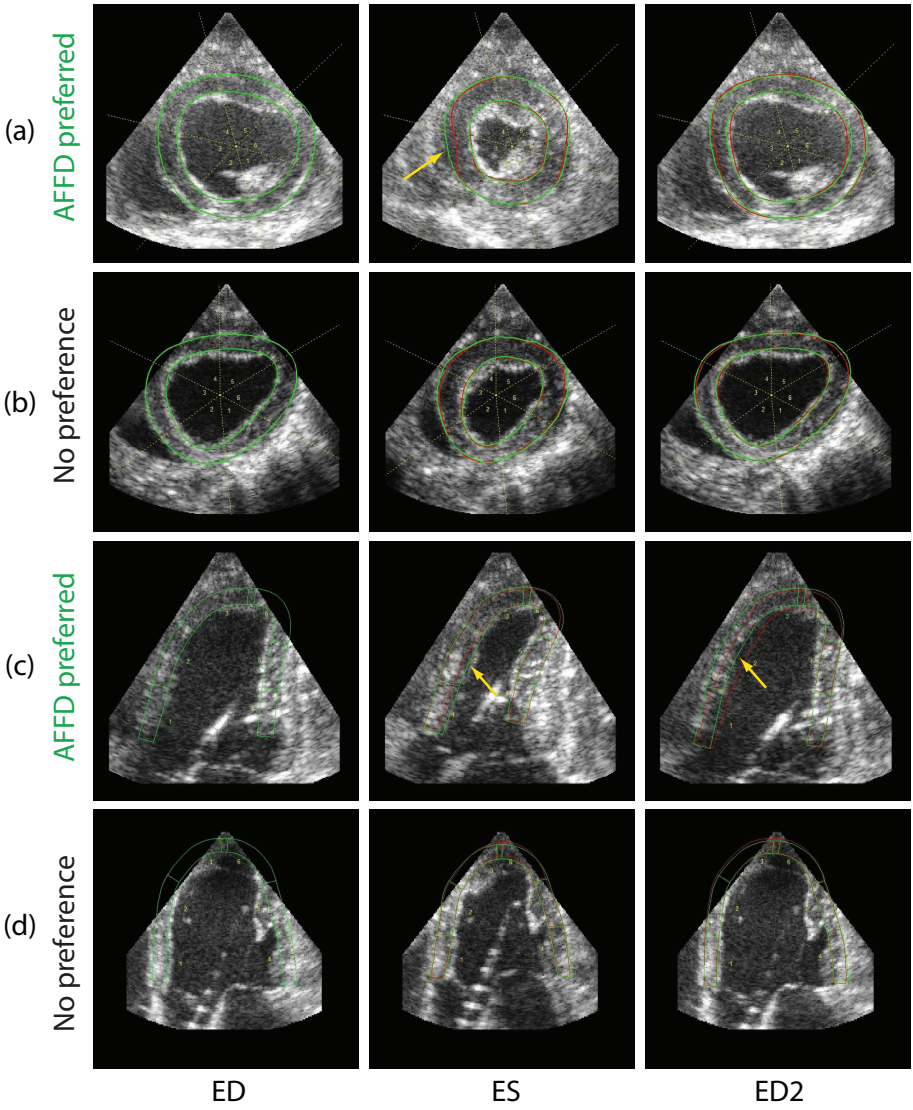

Figure 6.4: Representative examples of tracking results with the (red) CFFD and (green) AFFD model at three time points during the cardiac cycle: (left) end-diastole, (middle) end-systole, and (right) end-diastole at the end of the recorded image sequence. Tracking preference by the three cardiologists is shown on the left. Yellow arrows indicate at which regions the AFFD model was preferred over the CFFD model.

imposed by simply copying a fixed part of the image. This does not necessarily enforce true cyclicity of the recovered transformation field. This is also computationally inefficient, as the cost function needs to be evaluated over a large number of redundant points. This subject is further treated in chapter 9. Finally, the anatomical unfolding process involves an interpolation procedure which results in a spatially varying voxel size. This effect has not been taken account into the cost function in this chapter, but is investigated further in chapter 10. Consequently, the speckle appearance also changes under this transformation. The effect of the interpolation method on the speckle pattern, and the impact on tracking performance remains the topic of future research.

6.6 Conclusions

In this chapter, we demonstrated the feasibility of strain estimation using an anatomical transformation model. We demonstrated that regional end-systolic strain values assessed with the AFFD model are comparable with CFFD, but with a higher computational efficiency. Furthermore, tracking using AFFD was visually more appealing to clinical experts.

Chapter 7

Non-rigid image registration using a transformation model adapted to the heart: Quantifying myocardial function from 3D US images

This work was published in:

Experiments on simulated datasets

B. Heyde, D. Barbosa, P. Claus, F. Maes, and J. D'hooge. Three-dimensional cardiac motion estimation based on non-rigid image registration using a novel transformation model adapted to the heart. In *International Workshop on Statistical Atlases and Computational Models of the Heart (STACOM): Motion tracking challenge*, volume 7746, pages 142–150, Nice, France, 5 October 2012.

Experiments on in-vitro & in-vivo datasets

B. Heyde, D. Barbosa, R. Jasaityte, S. Bouchez, P. Wouters, F. Maes, P. Claus, and J. D'hooge. Three-dimensional myocardial strain estimation from volumetric ultrasound data using a novel transformation model adapted to the heart. In *IEEE International Ultrasonics Symposium*, pages 1086–1089, Dresden, Germany, 7-10 October 2012.

7.1 Motivation

In chapter 6, we investigated the feasibility of using a two-dimensional anatomical free-form deformation model (AFFD) to assess regional cardiac function from 2D US images. Given the true three-dimensional nature of cardiac deformation, and the ability to image this motion in three dimensions, it seems natural to extend this AFFD model to three dimensions.

As mentioned in chapter 6, several related FFD transformation models more closely matching the LV shape and motion have been suggested for the analysis of MR images (cylindrical e.g. [41][57], prolate spheroidal e.g. [136], or extended cylindrical e.g. [137]). However, these geometrical transformation models do not necessarily follow the true anatomy of the heart and were often applied to stacks of 2D short-axis MR data, where motion was not estimated in the apical regions. The latter brings along specific difficulties which will be covered in this chapter. Furthermore, their application on 4D echocardiography has currently not been demonstrated.

In this chapter, we extend the proposed 2D AFFD model of the previous chapter and orient the basis functions locally according to the radial (r), longitudinal (l) and circumferential (c) direction of the endocardium. The topological differences with the classical FFD model defined on a cubic lattice are shown in Fig. 7.1. Please note that our description in $[r, l, c]$ coordinates is different compared to the description in prolate spheroidal coordinates $[\lambda, \mu, \theta]$ by Li *et al.* [136] since the local r-direction does not neccesarily coincide with the λ-direction as the LV shape is only approximately prolate spheroidal. The LV shape shown in Fig. 7.1b was simplified to a prolate spheroid only for ease of visualisation, no specific geometrical assumptions of the LV shape are made. Moreover, in this work subsequent frames are registered with each other as opposed to the methodology described by Li *et al.* in which the model is always deformed towards the initial (undeformed) state. While this may be reliable for MR, a frame-to-frame registration may be better for echocardiography due to speckle decorrelation over the cardiac cycle. Finally, our model also allows to track tissue in the apical regions, whereas this was not reported in the mentioned MR studies.

The present chapter discusses the implementation details of the 3D AFFD model first. It is then applied on a variety of imaging scenarios, starting with simulated images, and continuing with a validation on both in-vitro and in-vivo datasets. This process is similar to the strategy used to develop and validate the CFFD model in the previous chapters.

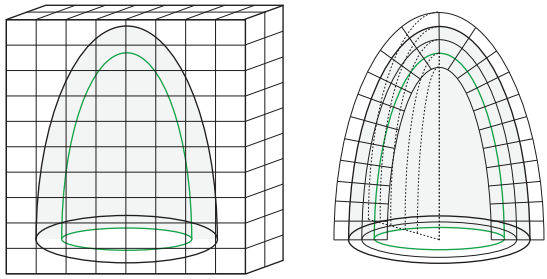

Figure 7.1: Free form deformations with the B-spline support (a) defined on a cubic lattice in Cartesian space or (b) shaped according to the endocardium in anatomical space.

7.2 Anatomical FFD registration

General principles

The 3D AFFD model was implemented by transforming the images to anatomical coordinates first, similar to what was described in chapter 6 for 2D images. However, this anatomical unfolding is less straightforward in 3D and several improvements were made compared to the 2D AFFD model:

- The endocardium is now parametrized analytically using a spherical harmonics representation of the radial component of the surface. In chapter 6, the endocardium was represented only by an explicit contour.
- This parametrization in turn allows for a uniform sampling of the surface taking the physical size of the LV into account. In chapter 6, every image was unfolded using the same amount of sampling points, irrespective of the LV size.
- The unfolding process in the SAx and apical views described in chapter 6 is combined into one unfolding framework.
- Boundary conditions near the apex and in the circumferential direction are imposed simultaneously to retain the topology of the endocardium after anatomical unfolding.

Endocardial surface parametrization

In order to map the curved endocardial surface to a plane, an elegant parametrization is required which allows a uniform sampling along the l- and c-direction. Given the ellipsoidal shape of the LV, a natural choice to describe its geometry would be in prolate spheroidal coordinates $[\lambda, \mu, \theta]$ (Fig. 7.2a left).

$$\mathbf{r} = \begin{bmatrix} x \\ y \\ z \end{bmatrix} = \begin{bmatrix} d\ sinh(\lambda)\ sin(\mu)\ cos(\theta) \\ d\ sinh(\lambda)\ sin(\mu)\ sin(\theta) \\ d\ cosh(\lambda)\ cos(\mu) \end{bmatrix} \tag{7.1}$$

In order to account for local shape differences, λ is parametrized as a spherical harmonics (SH) expansion series [115]:

$$\lambda(\mu, \theta) = \sum_{q=0}^{\infty} \sum_{m=-q}^{q} c_{qm}\, Y_{qm}(\mu, \theta) \tag{7.2}$$

with Y_{qm} being the SH basis functions, defined in terms of the Legendre functions P_{qm} as

$$Y_{qm} = \sqrt{\frac{2q+1}{4\pi} \frac{(q-m)!}{(q+m)!}} P_{qm}(cos\,\mu) e^{im\theta} \tag{7.3}$$

This SH parametrization has several advantages. It is efficient as it can generate a wide variety of shapes even for low SH orders q (Fig. 7.2a right) and surface derivatives can be calculated analytically. Given a sparse sampling of the LV surface with d points, the expansion coefficients c_{qm} completely define the endocardial surface and can be found by minimizing the following objective function:

$$F(\lambda) = \sum_{d} \left[\lambda(\mu_d, \theta_d) - \lambda_d(\mu_d, \theta_d)\right]^2 \tag{7.4}$$

where λ_d is the λ coordinate of the dth point. These points can come from manual contouring (in clinical practice) or from a given mesh. Please note that the considered endocardial surface is not necessarily a prolate spheroid.

In this chapter, the endocardium was manually contoured in several short-axis and apical views. The LV surface can thus be constructed by applying Eq. (7.4). Nevertheless, this step is time-consuming and may therefore jeopardize its introduction in daily clinical routine. Chapter 11 further addresses this issue.

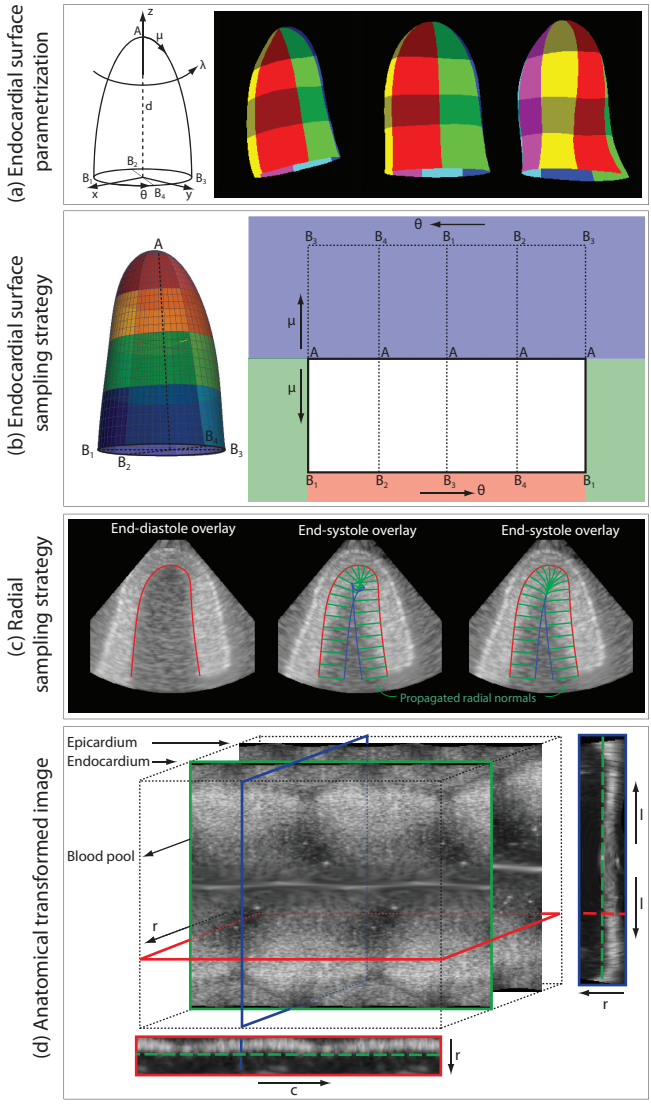

Figure 7.2: Overview of the different steps to unfold the left ventricle into anatomical space. (a) Endocardial surface parametrization, with examples showing the variety of shapes that can be represented analytically. The different segments are color-coded. (b) Endocardial surface sampling strategy in Cartesian space (left) with the corresponding surface being mapped unto a plane in anatomical space (right). (c) Radial expansion strategy in Cartesian space, and (d) The resulting transformed volumetric image in anatomical space.

Endocardial surface sampling strategy

After surface parametrization, the endocardium is sampled uniformly along the l and c direction, by sampling of $\mu \in \left[0, \frac{\pi}{2}\right]$ and $\theta \in [0, 2\pi]$ respectively. In order to keep a comparable resolution after unwrapping the surface, the number of θ samples is equal to the mid-ventricular circumference length in voxels, and the number of μ samples is equal to the average base-to-apex length along the surface in voxels (Fig. 7.2b, white zone).

In order to account for longitudinal motion near the base, the endocardium is oversampled in the μ direction by extending the mesh along the longitudinal direction of the base. In this study all images were extended by 20% (Fig. 7.2b, red zone).

It is important that the mapping also preserves the topology of the endocardium. In order to enforce circumferential continuity at the θ=0, θ=2π borders, a small part of the image was copied on either side (Fig. 7.2b, green zone). The size of this copy was equal to the third-order B-spline support extent at the coarsest transformation model scale, i.e. $[-2\sigma, 2\sigma]$ voxels, with σ the spacing between the B-spline knots at the coarsest transformation level. Longitudinal continuity near the apex was ensured by mirroring a shifted ($\Delta\theta$=π) copy of the current image at the apex (Fig. 7.2b, blue zone).

Radial expansion strategy

The image is further resampled by propagating the endocardial surface S along the surface normal. This corresponds to the radial direction $\boldsymbol{n}_{\mathrm{R}}(\mathbf{r})$:

$$\boldsymbol{n}_{\mathrm{R}}(\mathbf{r}) = \boldsymbol{n}_{\mathrm{R}}(x, y, z) = \begin{bmatrix} n_{\mathrm{R}x}(x, y, z) \\ n_{\mathrm{R}y}(x, y, z) \\ n_{\mathrm{R}z}(x, y, z) \end{bmatrix} \tag{7.5}$$

As such, the endocardial surface $\mathbf{S}$ is propagated both inwards towards the blood pool as outwards towards the epicardium to ensure that the full myocardium remains inside the transformed image during the whole cardiac cycle.

By taking the SH parametrization into account of Eq. (7.2), the normals of the surface $\boldsymbol{n}_{\mathrm{R}}(\mathbf{r}), \boldsymbol{n}_{\mathrm{L}}(\mathbf{r}), \boldsymbol{n}_{\mathrm{C}}(\mathbf{r})$ can be calculated analytically:

$$\boldsymbol{n}_{\mathrm{L}}(\mathbf{r}) = \frac{\partial \mathbf{r}}{\partial \mu} = \frac{\partial \mathbf{r}}{\partial \lambda}\frac{\partial \lambda}{\partial \mu} + \frac{\partial \mathbf{r}}{\partial \theta}\frac{\partial \theta}{\partial \mu} + \frac{\partial \mathbf{r}}{\partial \mu}\frac{\partial \mu}{\partial \mu} \tag{7.6}$$

$$\boldsymbol{n}_{\mathrm{C}}(\mathbf{r}) = \frac{\partial \mathbf{r}}{\partial \theta} = \frac{\partial \mathbf{r}}{\partial \lambda}\frac{\partial \lambda}{\partial \theta} + \frac{\partial \mathbf{r}}{\partial \theta}\frac{\partial \theta}{\partial \theta} + \frac{\partial \mathbf{r}}{\partial \mu}\frac{\partial \mu}{\partial \theta} \tag{7.7}$$

$$\boldsymbol{n}_{\mathrm{R}}(\mathbf{r}) = \boldsymbol{n}_{\mathrm{L}}(\mathbf{r}) \otimes \boldsymbol{n}_{\mathrm{C}}(\mathbf{r}) \tag{7.8}$$

As mentioned in chapter 6, simply expanding the surface towards the blood pool along a fixed direction may lead to tissue folding in Cartesian space. This situation often occurs near the apex or at locations with a high curvature (Fig. 7.2c, middle). The radial direction should therefore not be kept constant, but rather evolve dynamically towards the inner cavity. Similar to chapter 6, we solve three differential equations, one for each component of $\boldsymbol{n}_{\mathrm{R}}(x, y, z)$. For example, for $n_{\mathrm{R}x}(x, y, z)$ the following differential equation is obtained:

$$\frac{\partial n_{\mathrm{R}x}(x, y, z, t)}{\partial t} = \alpha \nabla^2 n_{\mathrm{R}x}(x, y, z, t) \tag{7.9}$$

with

$$\begin{cases} n_{\mathrm{R}x}(x, y, z, 0) = n^{\mathbf{S}}_{\mathrm{R}x} & \text{if } (x, y, z) \in \mathbf{S} \\ n_{\mathrm{R}x}(x, y, z, 0) = 0 & \text{if } (x, y, z) \notin \mathbf{S} \\ n_{\mathrm{R}x}(x, y, z, t) = n^{\mathbf{S}}_{\mathrm{R}x} & \text{if } (x, y, z) \in \mathbf{S} \end{cases} \tag{7.10}$$

and where α represents the diffusivity, and $n^{\mathbf{S}}_{\mathrm{R}x}$ corresponds to the x-component of the radial direction on the endocardial surface $\mathbf{S}$. This simple heat equation is solved by an explicit forward difference scheme in t and a central difference scheme for the spatial derivatives. In practice, 200 iterations proved to be a good trade-off between calculation time and desired accuracy. Following the calculated streamlines, the surface is propagated in both directions as shown schematically for a 2D cross-section of the endocardial propagation in Fig. 7.2c (right panel).

This expansion strategy can also be thought of in terms of electrostatics in which the endocardial surface would have a constant charge. Accordingly, isopotential surfaces can be computed by solving the Laplace equation. Expanding the endocardial surface then becomes equivalent to moving this surface along the electrical field lines, i.e. along the normals of these isosurfaces.

Motion estimation

In practice, motion is estimated by transforming the image sequence I to an anatomical equivalent image sequence $\hat{I}$ in $[r, l, c]$ coordinates as described above. The resulting 3D stack in anatomical space can be seen in Fig. 7.2d. A linear interpolation procedure is used to resample the original image. Subsequent images are then registered in a pairwise fashion by extending the formulation of Eq. (6.3) to 3D:

$$\hat{\mathbf{u}}_{f\rightarrow f+1}(\hat{\mathbf{r}}) = \sum_{i\in\mathcal{N}_i}\sum_{j\in\mathcal{N}_j}\sum_{k\in\mathcal{N}_k} \boldsymbol{\mu}^{ijk}\beta_r^3(\frac{r-\kappa_r^{ijk}}{\sigma_r})\beta_l^3(\frac{l-\kappa_l^{ijk}}{\sigma_l})\beta_c^3(\frac{c-\kappa_c^{ijk}}{\sigma_c}) \quad (7.11)$$

The ($\hat{}$)-symbol was used to indicate that motion is estimated in anatomical space. The same registration components as used in chapter 6 were used here: SSD as a similarity criterion, bending energy as a regularisation term, and the LBFGSB optimizer to find the optimal deformation field. The regularisation weight was tuned using simulated data (see sections 7.3 and 7.4). For more details, the reader is referred to section 3.3.2 and appendix B.

Strain estimation

A region-of-interest (ROI) for strain estimation was made by populating the myocardium with a series of points $\mathbf{r}_f$ along the cardiac directions (5 points radially, 30 longitudinally, and 60 circumferentially). In practice, this was performed at the end-diastolic frame, i.e. $f = \text{ED}$. Next, the LV surface was subdivided into 18 segments to allow quantification of regional function (see Fig. 7.2a, right). For this purpose, the LV was partitioned into 6 equal parts along the circumference, and 3 levels were defined longitudinally while dropping the apical cap [37]. As such, every segment contained 10-by-10 evenly distributed strain estimation points along the surface, and 5 points equally spaced radially throughout the myocardium. Using the same anatomical mapping strategy defined above, these points were mapped to $\hat{\mathbf{r}}_f$ and propagated over time using the obtained registration results yielding $\hat{\mathbf{r}}_{f+1}$. After mapping them back to Cartesian coordinates $\mathbf{r}_{f+1}$, strain could be estimated as the unit length extension defined in e.g. Eq. (3.1).

7.3 Experiments

Simulated datasets

The performance of the AFFD model was tested on in-silico datasets which were released in the context of the cardiac motion tracking challenge at STACOM (2012), a satellite workshop of MICCAI. The results presented in this chapter are based on a preliminary release of synthetic validation data [53].

In this challenge, in-silico datasets were produced by combining two image simulation techniques. First, an electromechanical model was used to simulate cardiac conduction abnormalities, such as left and right bundle branch blocks (LBBB and RBBB respectively), and different pacing scenarios such as biventricular (BV) pacing. In total, 10 sequences were simulated by modifying both the electrical activation sites and conductivity parameters of the model, the latter controlling the myocardial conduction velocity. In addition, the contractility parameters governing the maximum fibre stress were also modified. A biventricular mesh was used to represent the LV and RV (see Fig. 7.3a). Table 7.1 (in the results section) gives a more detailed overview of all the investigated cases. For more details the reader is referred to [155][211].

Secondly, scatterers were randomly placed within the myocardium and displaced according to the output of the electromechanical model. Scatterers in the background, i.e. within the blood pool and outside the myocardium, were randomly placed within every frame to ensure no speckle correlation occured within these regions (shown schematically in Fig. 7.3b). Scatterers with a higher reflectivity were placed just outside the epicardium to simulate the pericardium moving at a different speed than the underlying myocardium. By introducing the scatterer positions in a fast ultrasound simulator called COLE [76], volumetric B-mode datasets could be generated by convolving the scatterer locations with the point spread function of the simulated US system. An example of a generated US dataset is shown in Fig. 7.3c.

All the simulated datasets provided for this challenge ($355 \times 355 \times 267$ voxels) were transformed to anatomical space with 191 θ-samples and 327 μ-samples. In order to evaluate the performance of the AFFD technique, the ground truth displacement $\mathbf{T}(\mathbf{r}_f^{ref})$ of the reference mesh and the corresponding calculated displacements $\mathbf{T}(\mathbf{r}_f)$ were compared in every frame f according to

$$\|\Delta \mathbf{r}_f\| = \left\| \mathbf{T}(\mathbf{r}_f^{ref}) - \mathbf{T}(\mathbf{r}_f) \right\| \tag{7.12}$$

Only points of the ground truth mesh belonging to the left ventricle (segments 1-17) were considered. Please note that the LV was divided into 17 segments

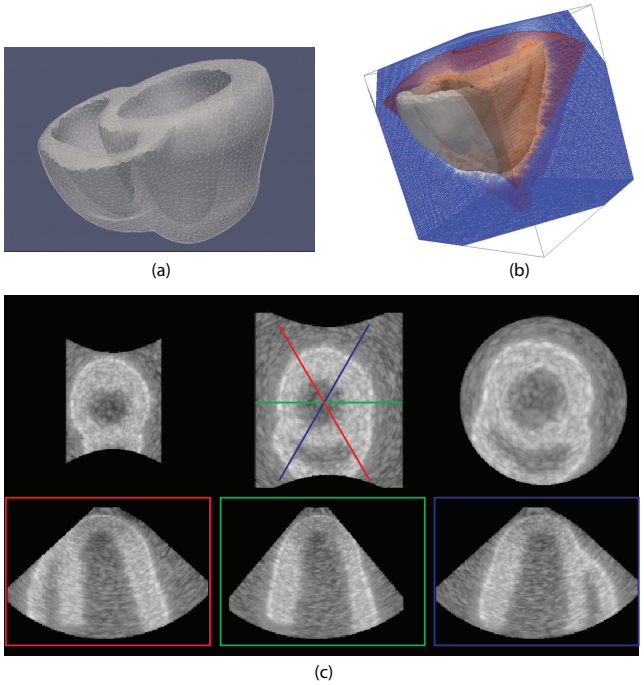

Figure 7.3: Generating the in-silico datasets: (a) initial biventricular geometry with underlying electromechanical model [155], (b) populating the model with scatterers in the US simulator [76], and (c) the generated volumetric image.

for the simulated datasets of the motion tracking challenge (base:1–6, middle: 7–12, apex: 13–16, apical cap: 17).

First, the bending energy penalty weight ω was optimized using two training datasets. Next, all datasets were processed using the optimal weight, and the error $\mathbf{r}_f$ over the cardiac cycle was assessed using Eq. (7.12).

In-vitro and in-vivo datasets

The 3D AFFD registration method was also applied both on phantom images and on in-vivo sheep data. For a full description of the experimental protocol in these setups, the reader is referred to chapter 4 and 3 respectively. Briefly, volumetric US images were recorded in gel phantoms and in open-chest sheep, from an apical view using a GE VividE9 equipped with a 2.5 MHz transducer (3V) at a frame rate of 13–17 Hz and 25–32 Hz respectively. The gel phantoms were submerged in a water-filled tank and deformed using a hydraulic pumping

system. The strain range was modulated by increasing the stroke volume (between 25–150 mL) resulting in 7 datasets which could be further analysed. In the open-chest animal setup, images were taken during four stages: at baseline conditions, during pharmacological inotropic modulation (dobutamine and esmolol) and during an acute ischemic phase induced by ligating circumflex coronary artery (mostly affecting the inferolateral segments). A subset of 5 animals from the study population was used in this study, thus leading to 20 datasets. In both setups, reference strain values ($\varepsilon_{\mathrm{RR}}/\varepsilon_{\mathrm{LL}}/\varepsilon_{\mathrm{CC}}$) were obtained using 3 sonomicrometry crystal pairs located in the mid wall of the gel phantoms having the lowest curvature (see Fig. 4.5) or sutured in the mid inferolateral segment for the sheep data (see Fig. 3.1). The estimated end-systolic strain values, averaged over the segments containing the crystals, were correlated against those obtained with sonomicrometry.

7.4 Results

Simulated datasets

First, the weight of the bending energy ω was optimized using two training datasets with a normal motion pattern (case 1) and motion in the presence of a LBBB (case 3) by varying its contribution between 1E5 and 1E7. An optimal weight of ω=5E5 was found (Fig. 7.4a).

Next, all datasets were processed using these parameter settings and the overall error $\|\Delta\mathbf{r}\|$ was assessed by averaging Eq. (7.12) over the cardiac cycle. The dispersion of the errors and the resulting strain curves for two cases are shown in Fig. 7.4b and Fig. 7.4c respectively. Fig. 7.5 shows the registration results for case 1. Finally, table 7.1 summarizes the obtained accuracy results, and analyses which segments contain the largest errors. The amount and range of the outliers is also indicated.

In-vitro and in-vivo datasets

Correlation coefficients for $\varepsilon_{\mathrm{RR}}$, $\varepsilon_{\mathrm{LL}}$ and $\varepsilon_{\mathrm{CC}}$ were 0.98, 0.62 and 0.94 respectively in the phantom data and 0.87, 0.65 and 0.74 respectively in the sheep data (Fig. 7.6). The left panels in Fig. 7.7 show strain curves for a phantom dataset and in sheep data at baseline conditions and during acute ischemia. The spatial strain distribution over the LV at end-systole is shown in the associated bullseye plots in the right panels.

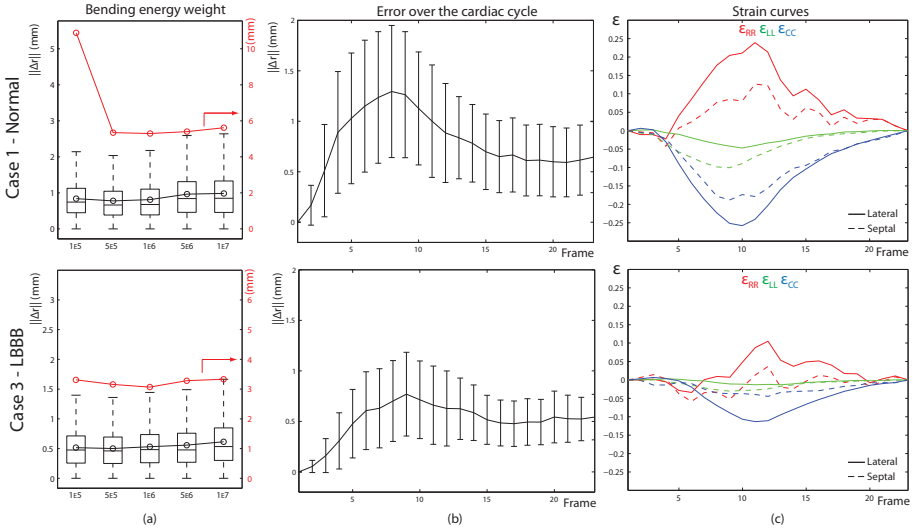

Figure 7.4: (a) Influence of the bending energy weight ω on the error $\|\Delta\mathbf{r}\|$ (mm) for (top) case 1 and (bottom) case 12. The black and red line correspond to the average and the maximum error over the cardiac cycle respectively, (b) The dispersion of the errors ($\mu \pm \sigma$) and (c) the resulting strain curves in the lateral and septal segment (for ω=5E5).

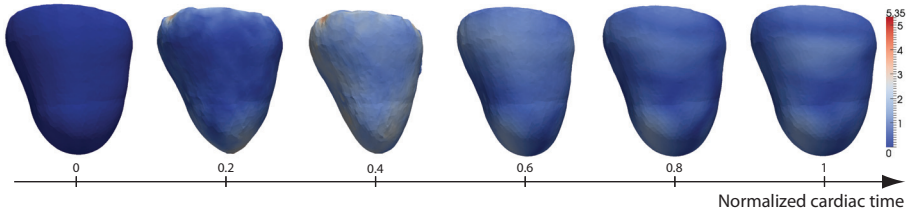

Figure 7.5: Visualisation of the registration results for case 1 (lateral view). The color overlay on the deformed LV represents the magnitude of the registration error $\|\Delta\mathbf{r}_f\|$ (mm).

Table 7.1: Simulated datasets results

Case	Description	$\mu \pm \sigma$[mm]	Outliers[mm]				
			min	max	count	segments(%)	
1*	Normal	0.78±0.57	2.04	5.35	3.67	17(24)	13(21)
2	RBBB	0.51±0.35	1.35	2.99	2.47	17(18)	6(13)
3	LBBB	0.50±0.35	1.36	3.16	2.29	17(18)	1(15)
4	LBBB (Pacing 5)	0.51±0.35	1.37	2.98	2.23	17(18)	1(13)
5*	LBBB (Pacing 6)	0.75±0.57	2.08	4.76	3.11	17(17)	13(16)
6	LBBB (Pacing 7)	0.51±0.35	1.39	3.24	2.01	17(21)	1(16)
7	LBBB (Pacing 12)	0.51±0.35	1.40	3.14	2.15	17(22)	1(15)
8	RBBB (Pacing 9)	0.50±0.34	1.29	3.17	2.83	17(18)	1(12)
9	BV (Pacing 3+6)	0.50±0.34	1.36	2.88	2.08	17(21)	1(14)
10	BV (Pacing 14+7)	0.48±0.35	1.34	3.54	2.35	1(17)	17(15)

Mean(μ)±std(σ) $\|\Delta\mathbf{r}\|$ errors in mm for the different datasets. The number of outliers (in %), their range ($min - max$, in mm) and the two segments (17 segment model, 17=apical cap) containing the most outliers are also indicated. Models with a higher simulated contractility are indicated with a *.

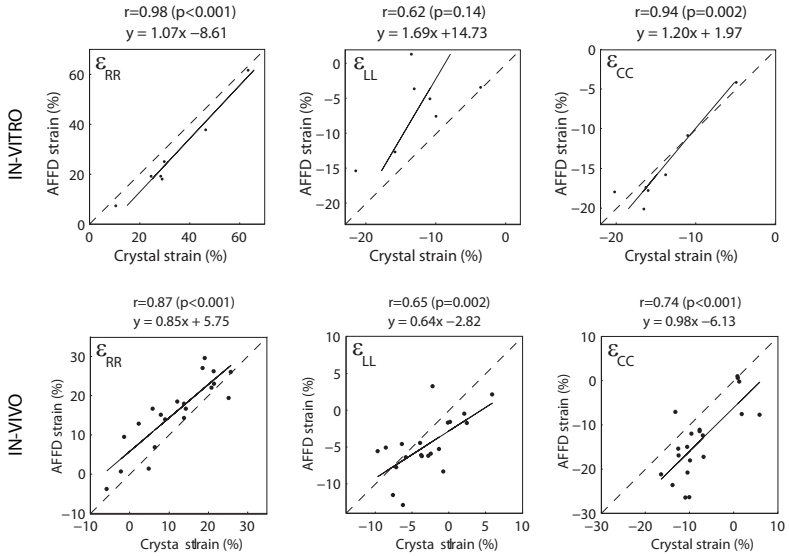

Figure 7.6: Scatter plots of estimated $\varepsilon_{\mathrm{RR}}$ (left), $\varepsilon_{\mathrm{LL}}$ (mid) and $\varepsilon_{\mathrm{CC}}$ (right) with the 3D AFFD model against reference crystal strain in the phantom data (top) and in the sheep data (bottom). The dotted line is the line of identity.

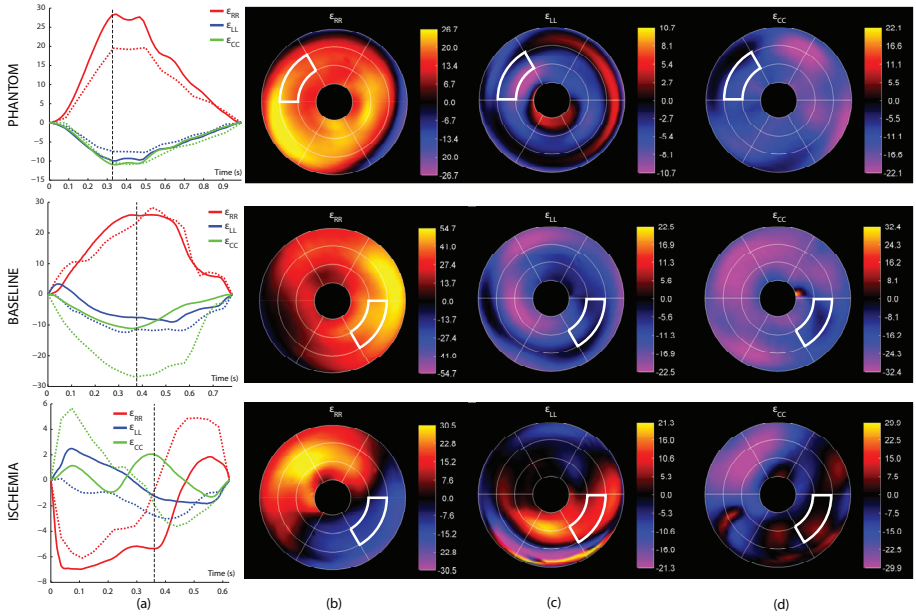

Figure 7.7: (a) Estimated strain (dotted line) against reference strain values (full line) for (top) phantom deformed at 60 Hz with a stroke volume of 65 mL, (mid) sheep at baseline conditions and (bottom) during acute ischemia. The corresponding bullseye plots at end-systole (vertical dotted line in panel a), are shown in panels (b-d). The segment containing the crystals is highlighted.

7.5 Discussion

Simulated datasets

Table 7.1 shows that the obtained average errors for all the processed data were in the sub-mm range. For the datasets with a high contractility (case 1 and 22), errors were 0.8±0.6 mm (this corresponds to an error relative to the present motion of approximately 10%), while the error was 0.5±0.4 mm for the other datasets with a lower global contractility (relative error approximately 15%).

Our method was also able to detect differences in model contractility. An example of the obtained strain curves is given in Fig. 7.4c (case 1 vs case 12). However, for the LBBB dataset (case 12) we did not observe any peak strain timing differences between the lateral and septal wall. The underlying reasons remain unclear since no specific details of the applied electromechanical model were given for this initial challenge data release (e.g. the affected segments, the

contractility delay or the degree of impairment). Furthermore, the apparent small motion amplitude from the model makes it intrinsically harder to assess strain differences between segments.

Two other observations can be inferred from table 7.1. First, the average errors within the two data groups, i.e. low and high contractility, are very similar. This may be due to the low intra-model variability. For example, looking at the ground truth data of case 12 (no pacing) and case 36 (with pacing), both models only differ at most 1 mm in segment 12 (where the pacing occurs). Given the fact that the average thickness of this segment is 15 mm and that the motion difference is very localized, this subtle difference may be too difficult to pick up, most likely because of the particularly low SNR of these datasets (as shown in Fig. 7.3c).

Secondly, the largest errors mostly occured in the apical region (segments 17 and 13), where the method underestimated motion during systole. Segment 1 (base) was another site with major errors. This may be due to an unsmooth motion of the ground truth mesh at the base. This particular electromechanical model behavior remains unclear as no further specifications were supplied.

Moreover, Fig. 7.4a showed that the obtained average errors are robust to changes in the bending energy penalty weight within the currently assessed range, which was preselected based on experience. In this in-silico setup, the contribution of this term thus appears low. This may be due to the low ground truth deformations, intrinsically leading to a low inter-frame bending energy. Indeed, in the high contractility model (case 1, Fig. 7.4a top), the influence becomes higher. The maximum error increased substantially up to 10.9 mm (left) and 5.62 mm (right). It is expected that this trend continues beyond the assessed range. Obviously, increasing the influence of the smoothness constraint too much restricts the motion while decreasing it leads to too much degrees of freedom.

In-vitro and in-vivo datasets

The obtained correlation coefficients in this study are encouraging and highlight that non-rigid registration using an anatomical oriented grid is also feasible in more realistic imaging scenarios. Similar experiments were performed previously using a CFFD model (see table 7.2). In phantom data, correlations were 0.98, 0.96 and 0.92 for $\varepsilon_{\mathrm{RR}}$, $\varepsilon_{\mathrm{LL}}$ and $\varepsilon_{\mathrm{CC}}$ respectively (see chapter 3 and [94]), while the correlations in sheep data were 0.69, 0.64 and 0.62 respectively (see chapter 5 and [92]). It is important to note that for the CFFD method data from 14 sheep was analysed, whereas only a subset of five animals was currently used for the AFFD model. Seo *et al.* reported similar findings in

Table 7.2: Comparison cffd and affd models

	ε_{RR}	ε_{LL}	ε_{CC}	Reference
In-vitro				
CFFD	0.98	0.96	0.92	Chapter 4, [94]
AFFD	0.98	0.62	0.94	Chapter 7, [91]
In-vivo				
CFFD	0.69	0.64	0.62	Chapter 5, [92]
AFFD	0.87	0.65	0.74	Chapter 7, [91]

Comparison of both FFD models in terms of correlation coefficient with respect to sonomicrometry reference data

an in-vivo setup using a state-of-the-art commercially available 3D speckle tracking method that typically relies on block-matching based algorithms to track tissue motion (r=0.59–0.70 for ε_{RR}, r=0.65–0.68 for ε_{LL} and r=0.71–0.78 for ε_{CC} [210]). The AFFD model thus appears to outperform these methods for the radial strain component while also being competitive for ε_{CC}. However, ε_{LL} performance was only moderate although comparable to the existing Cartesian approach on in-vivo data.

This could be related to the way the data is reorganised in anatomical space. After unwrapping, the endocardial wall becomes a plane, usually having a prominent white-to-black transition into the blood pool (Fig. 7.2d, green dotted line in the red/blue plane). As such, radial thickening during the cardiac cycle (and also circumferential shortening) is translated into a prominent orthogonal motion to this plane, which may be easier to pick up compared to tracking in Cartesian space. Given the influence of this prominent edge in the image, it may be harder to pick up subtle longitudinal tissue motion compared to motion in the r-/c-direction as such motion will change the similarity metric only slightly. This may explain the suboptimal ε_{LL} performance. A direct comparison with a CFFD model using the same underlying data is the topic of chapter 9 and may shed more light on these issues.

As can be seen from Fig. 7.7 (left), the shape of the strain curves, and timing of peak values were recovered well. The bullseye plots of the phantom data (top) and sheep at baseline conditions (middle) have a uniform strain distribution. The basal areas of the phantom data however showed a reversed strain pattern, but this may be related to the presence of image artefacts [94]. The dysfunctional area was also located well for the ischemic dataset (bottom) as illustrated by the island of blue/red strain for ε_{RR} and $\varepsilon_{CC}/\varepsilon_{LL}$ respectively in the inferior/inferolateral segments. However, the ε_{LL} estimates near the base appeared noisy and more difficult to assess as already mentioned above.

7.6 Conclusions

This chapter presented the implementation details of a 3D registration approach using a transformation model adapted to the heart shape. When applied to in-silico datasets, we obtained an encouraging accuracy with average errors of 0.8 ± 0.6 mm and 0.5 ± 0.4 mm compared to the ground truth in high and low contractility models respectively. In more realistic imaging scenarios, good agreement was obtained when comparing strain measurements against sonomicrometry in a phantom setup and in an in-vivo setting. Moreover, the shape of the strain curves, timing of peak values and location of dysfunctional regions were also recovered well.

Chapter 8

Non-rigid image registration using a transformation model adapted to the heart: Comparison against other 3D strain estimation methods

Large parts of this work was published in:
M. De Craene, S. Marchesseau, **B. Heyde**, H. Gao, M. Allesandrini, O. Bernard, G. Piella, A. Porras, E. Saloux, L. Tautz, A. Hennemuth, A. Prakosa, H. Liebgott, O. Somphone, P. Allain, S. Makram Ebeid, H. Delingette, M. Sermesant, and J. D'hooge. 3D strain assessment in ultrasound (straus): A synthetic comparison of five tracking methodologies. *IEEE Trans Med Imaging*, 2013. *In press.*

8.1 Motivation

In chapters 6 and 7, an anatomical transformation model for non-rigid image registration was proposed to measure regional cardiac deformation. The present chapter aims to compare its performance against other state-of-the-art tracking methodologies. The in-silico benchmark database, constructed in the context of the cardiac motion tracking challenge at STACOM (2012) forms a fair basis for this purpose [54]. An overview of the images within this database is given in section 8.2. The ranking of the AFFD model with respect to the other participants of the motion tracking challenge is the subject of section 8.3.

While the comparison within this tracking challenge was limited to in-silico images, it is important to note that this database and the results of this validation study can provide a platform to adress the growing source of concern regarding the high inter-vendor and inter-software variability of commercially available systems in clinical practice [77]. Furthermore, it may also allow extending the efforts towards standardization of 2D strain measurements [158].

8.2 In-silico benchmark database

The simulated images were generated according to the methodology described in section 7.3, but the following improvements were made:

- A more realistic mesh, obtained through segmentation of MR images from a healthy volunteer, was used to represent the left and right ventricle (see Fig. 8.1a, left).
- In addition to simulating conduction abnormalities, myocardial stiffness in the electromechanical model could be modified locally to simulate datasets with acute ischemia.
- In order to address the low intermodel variability of the models described in section 7.3, parameters of the electromechanical model were varied over a larger range.
- Blood pool scatterer strength was modified in the ultrasound simulator to simulate images with different signal-to-noise ratios.

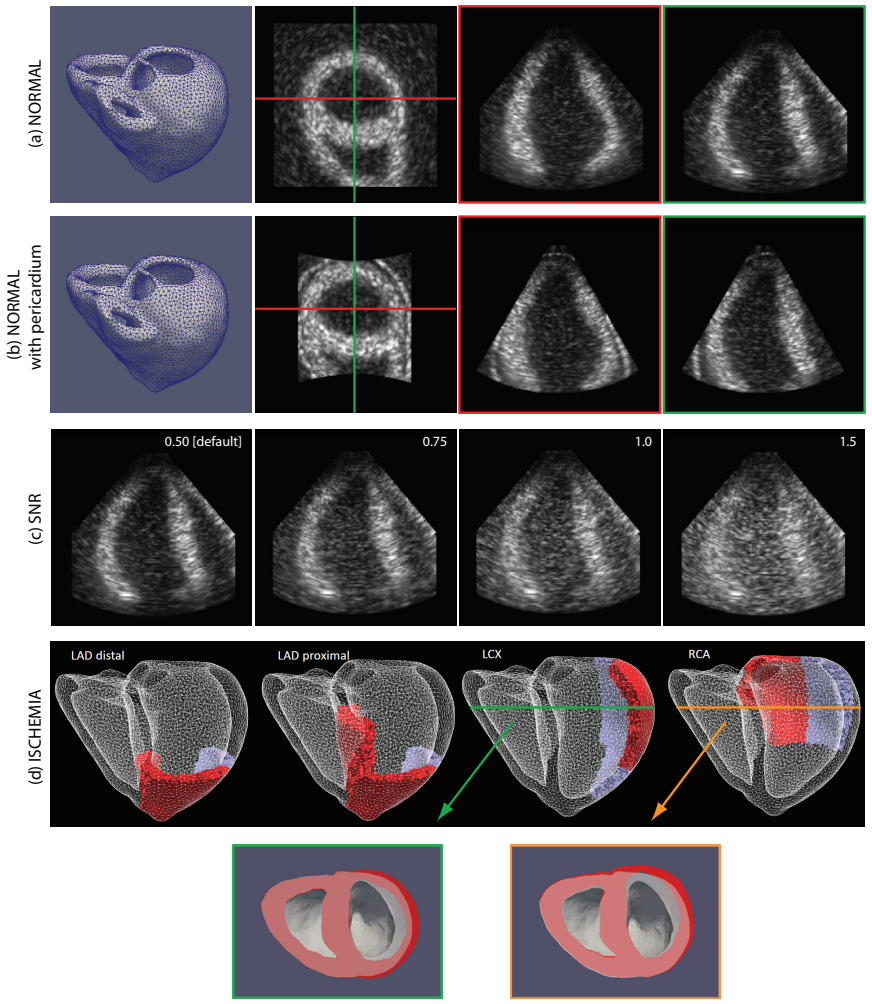

Figure 8.1: Examples of the benchmark database: (a) Normal case without pericardium showing the model geometry (left) and three cross-sections of the resulting 3D image (right), (b) Normal case with pericardium and a smaller field-of-view, (c) Normal case without pericardium at different signal-to-noise ratios (the value indicates the blood pool scatterer strength with respect to the scatterers within the myocardium), (d) Four simulated scenarios of coronary occlusion (LAD = left anterior descending, LCX = left circumflex, RCA = right coronary artery) with the affected regions highlighted in red. Blue areas indicate mildly affected regions. The cross-sections show the difference at end-systole between the ischemic models (red) vs the normal models (white).

By varying the model parameters of the electromechanical model, several datasets were simulated, representing a variety of myocardial conditions. First, a normal scenario was simulated with similar stiffness in all segments and synchronized contraction (Fig. 8.1a). A second version of this dataset was generated to study the influence of an intense pericardial layer (Fig. 8.1b). Next, four **acute ischemia** scenarios were simulated by modifying peak contractility and stiffness in different coronary artery territories (Fig. 8.1d). Simulations were performed both in the presence and the absense of a pericardial layer. Secondly, **dyssynchrony** as induced by LBBB, was modeled by progressively removing areas of early activation from the LV. Three datasets belonging to this category were simulated. Finally, the relative scatterer strength between the blood pool relative to the myocardium was modified to 0.5 (default), 0.75, 1.0 and 1.5 to study the influence of the **signal-to-noise ratio** (SNR) on tracking performance (Fig. 8.1c). An overview of all datasets is given in table 8.1.

Table 8.1: Overview in-silico benchmark database

	No pericardium	With pericardium
Acute ischemia		
Normal	•*	•
LAD distal	•	•
LAD proximal	•	•
RCA	•	•
LCX	•	•
Dyssynchrony		
Synchronuous	•	
Partial LBBB	•	
Total LBB	•	
SNR		
0.5	•*	
0.75	•	
1.0	•	
1.5	•	

The simulated datasets are grouped in three categories. The SNR represents the relative scatterer strength of the blood pool with respect to the myocardium. The dataset indicated with a (*) is the same dataset, but was used in two test scenarios.

8.3 Comparison against other state-of-the-art strain estimation techniques

8.3.1 Evaluated methods

Five research teams participated in the motion tracking challenge (Fig. 8.2). The underlying tracking algorithms are summarized very briefly here. For more details the reader is referred to the respective papers indicated below:

- **Creatis**: Alessandrini *et al.* estimate motion by solving the optical flow equation on the monogenic phase of the ultrasound images, rather than on the image intensities as in the classical formulation. A multiscale iterative displacement estimate is used to account for large cardiac motion [2].
- **KU Leuven**: This is the AFFD model described in chapter 7 [88].
- **Mevislab**: Tautz *et al.* adopt the Morphons algorithm originally proposed by Knutsson *et al.* for 2D motion estimation. This method applies quadrature filters on the images first to obtain the local phase. These image features are used both to drive the image registration, and to estimate a confidence measure used in the accumulation of the displacement fields. Regularisation is performed by Gaussian smoothing. Tautz *et al.* extended the method to 3D by sampling the sequence in a sparse set of long axis and short axis planes for computational efficieny reasons. These 2D displacement estimates are then combined to obtain the final 3D motion field [237].
- **Philips**: Somphone *et al.* proposed an algorithm inspired by Thirion's demons algorithm [240]. Motion is estimated iteratively by minimizing the SSD between subsequent images. Regularization is performed by replacing the standard Gaussian smoothing of the displacement field by a normalized convolution within a predefined myocardial mask [223].
- **UPF**: Piella *et al.* use another extension of the CFFD model to include the temporal dimension. They proposed a diffeomorphic FFD registration algorithm which is driven by a combination of two image similarity metrics: the first calculated between sequential frames based on speckle statistics, and the second estimated between the initial frame and the current frame to avoid drift [192]. As such, this is conceptually the closest algorithm to the AFFD model developed in this thesis.

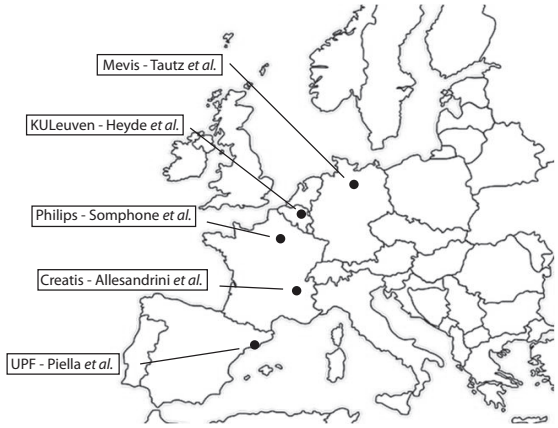

Figure 8.2: Research teams that participated in the cardiac motion tracking challenge at STACOM (2012).

8.3.2 Evaluation criteria

The sequence of volumetric meshes, given as input to the US simulator, defines the ground truth. Only the LV (divided in 17 segments) was considered for assessing **displacement and strain accuracy**. Displacement errors with respect to the ground truth were estimated first in every vertex of the mesh, and then averaged per segment in every frame. Ground truth strain values were obtained by approximating the transformation within each tetrahedron of the mesh as an affine transformation $\mathbf{T}$. Strain was then derived using the Lagrangian finite strain tensor (see appendix A.20):

$$\mathbf{E} = \frac{1}{2}(\mathbf{F}^{\mathrm{T}} \cdot \mathbf{F} - \mathbf{I}) \tag{8.1}$$

where $\mathbf{F}$ is the deformation gradient tensor of the transformation $\mathbf{T}$. The individual strain components were then assessed by projecting the strain tensor onto the cardiac directions:

$$\varepsilon_{\mathbf{N}} = \mathbf{N}^{\mathrm{T}} \cdot \mathbf{E} \cdot \mathbf{N} \tag{8.2}$$

Ground truth strain estimates were averaged on a segmental level. Segmental strain values for every method were extracted using the same expressions. As such, segmental strain errors could be estimated for every frame. Overal displacement errors $\|\Delta\mathbf{r}\|$ and strain errors $|\varepsilon_{\boldsymbol{n}}|$ were assessed over all acute ischemic and dyssynchrony datasets (13 in total, see table 8.1). Aiming at highlighting differences between methodologies, the strain curves were not post-processed, smoothed or drift-compensated.

Please note that this strain formulation is different compared to the Lagrangian strain adopted in this thesis, e.g. as in Eq. (A.1). This difference is further highlighted in the appendix, see Eq. (A.22). The strain definition of Eq. (8.2) was chosen by the organisers of the challenge.

The ability to **detect dysfunctional areas** could be investigated by generating bullseye plots of end-systolic strain for every individual method. The **influence of the SNR** on tracking performance was investigated by calculating displacement and strain errors in 4 datasets (see table 8.1). Finally, **the computational cost** of every individual method was also compared.

8.3.3 Results

Displacement and strain accuracy are reported in tables 8.2 and 8.3 respectively. Please note that the paper summarizing the results of the STACOM challenge was limited to the analysis of the average error over the whole cardiac cycle only [54]. Performance measures at end-systole (given the clinical interest in assessing systolic function) and at the end of the cardiac cycle (giving a measure of drift) were added in this chapter as well.

A bullseye plot of end-systolic strain in a dataset simulating the occlusion of an LCX coronary artery is shown in Fig. 8.3. The influence of the SNR on displacement and strain accuracy at end-systole is illustrated in Fig. 8.4. Compared to the original analysis in [54] which was limited to ε_{CC} only, results for ε_{RR} and ε_{LL} were also added in this figure. Finally, table 8.4 summarizes the computation time to process a full image sequence.

Table 8.2: Displacement accuracy

	$\|\Delta\mathbf{r}\|$ [mm]		
	All	ES	ED2
KU Leuven	0.49±0.25	0.63±0.20	0.50±0.55
Creatis	0.60±0.49	0.79±0.39	0.50±0.66
Philips	0.65±0.34	0.76±0.28	0.73±0.85
UPF	0.77±0.70	0.92±0.68	0.77±0.97
Mevis	0.83±0.50	1.10±0.41	0.83±0.96

Displacement errors expressed in mm, averaged over the whole cardiac cycle (all), at end-systole (ES) or at the end of the cardiac cycle (ED2), for the datasets representing ischemia and dyssynchrony.

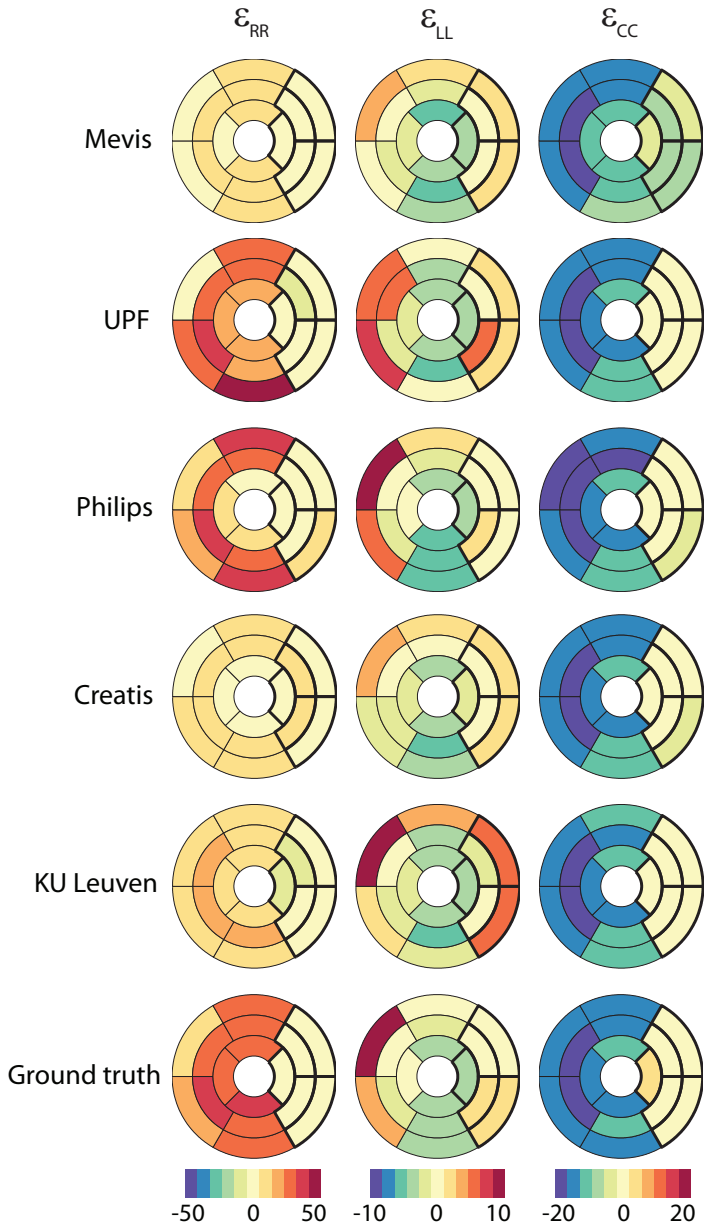

Figure 8.3: Bullseye plots of end-systolic strain for a dataset representing ischemia due to LCX occlusion. Ischemic segments in the simulations are outlined in bold.

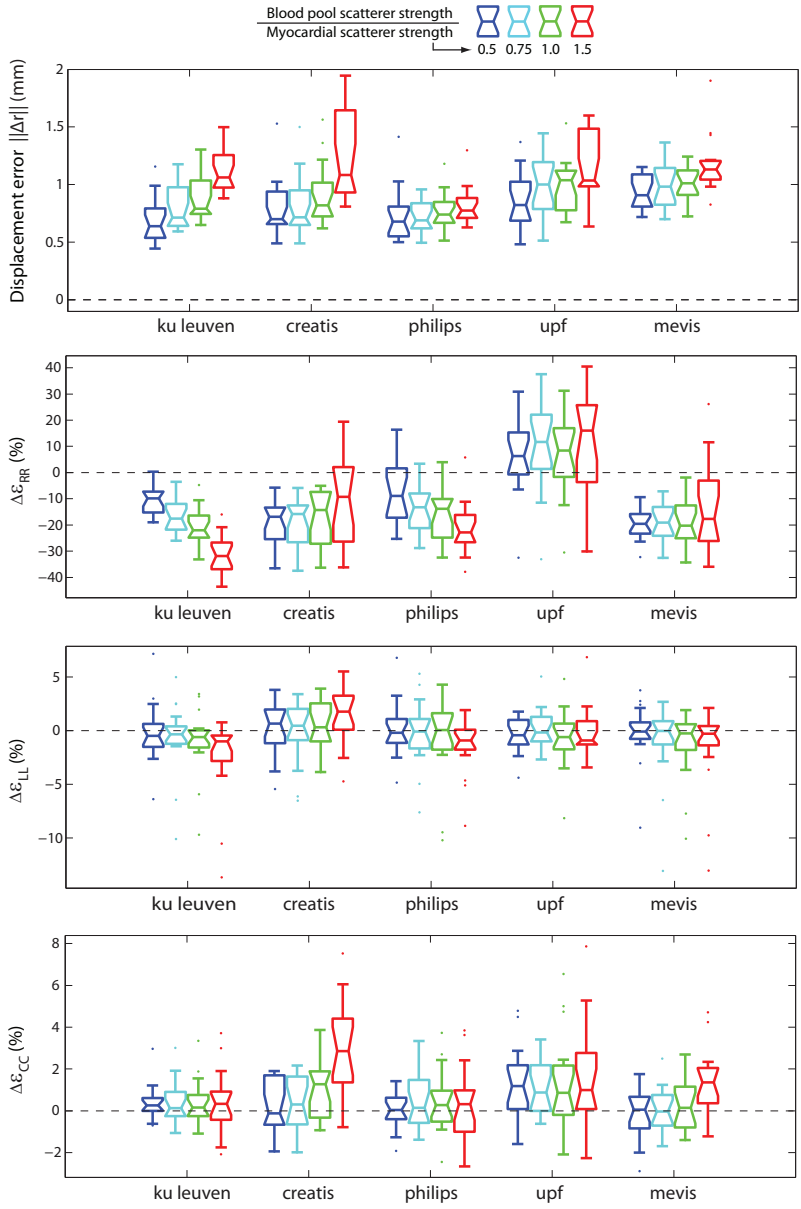

Figure 8.4: Sensitivity of end-systolic displacement and end-systolic strain accuracy to different SNRs: (a) displacement errors, (b) $\varepsilon_{\mathrm{RR}}$ errors, (c) $\varepsilon_{\mathrm{LL}}$ errors, and (d) $\varepsilon_{\mathrm{CC}}$ errors. The highest SNR is shown in blue, the lowest in red (see Fig. 8.1c).

Table 8.3: Strain accuracy

	$\Delta\varepsilon_{RR}$ [%]		$\Delta\varepsilon_{LL}$ [%]		$\Delta\varepsilon_{CC}$ [%]	
	All	ES	All	ES	All	ES
KU Leuven	–3.53±6.74	–5.67±8.35	–0.10±1.82	–0.28±2.35	0.20±1.10	0.20±1.29
Creatis	–4.44±9.22	–10.23±11.94	0.30±2.30	–0.01±2.92	0.39±1.67	0.47±1.97
Philips	–2.85±10.20	–5.45±11.49	0.21±2.45	0.00±2.43	–0.17±1.50	–0.30±1.66
UPF	1.77±9.94	1.21±11.79	1.44±5.77	1.61±6.40	0.61±2.33	0.55±2.58
Mevis	–4.31±8.35	–10.64±10.38	0.45±3.10	0.19±3.96	0.29±2.21	–0.30±2.81

Radial (ε_{RR}), longitudinal (ε_{LL}) and circumferential (ε_{CC}) errors expressed as percent strain, averaged over the whole cardiac cycle (all) or at end-systole only (ES), for the datasets representing ischemia and dyssynchrony.

Table 8.4: Computational efficiency

	Time	CPU	Environment
KU Leuven	∼120 min	2.80 GHz, 4 cores	C++
Creatis	∼40 min	3.47 GHz, 6 cores	Matlab
Philips	∼0.75 min	2.50 GHz, 4 cores	C++
UPF	∼480 min	2.66 GHz, 4 cores	C++
Mevis	∼90 min	3.00 GHz, 8 cores	C++/Python

Computational cost in minutes to process a full image sequence (27 frames, 296×296×296 voxels).

8.3.4 Discussion

Displacement and strain accuracy

All evaluated methods had an overall displacement error under 1 mm (table 8.2). Mean errors increased towards ES, and dropped off slightly towards the end of the cycle. Error dispersion increased for all methods at the end of the cardiac cycle. This may indicate drift in the estimated trajectories.

In general, the accuracy of radial strain was lower compared to the circumferential and longitudinal components (table 8.3). Most methods (apart from UPF) underestimated the radial strain, most likely due to a spatial oversmoothing which tends to reduce peak radial deformation. Error dispersions were also largest in the radial direction. This is in accordance with previous observations, e.g. in chapter 5 or in [150]. This suboptimal performance could be related to the fact that the spatial motion gradient must be calculated over a relatively small region because of the limited wall thickness, in combination with limited spatial resolution. Furthermore, because of the orientation of the LV in the volumetric data, beam density and consequently spatial resolution is lower in the radial direction compared to the other directions.

Relative to the peak strain values of the ground truth (peak $\varepsilon_{\text{RR}} \sim 40\%$, peak $\varepsilon_{\text{LL}} \sim -5\%$ and peak $\varepsilon_{\text{CC}} \sim -20\%$), the standard deviation in the longitudinal direction appears too large to be reliable to differentiate dysfunctional areas. However, it is important to note that the observed peak longitudinal strain in these models was fairly low compared to the normal expected range of values, which is typically in the order of -20% [265]. As such, estimating ε_{LL} becomes intrinsically more susceptible to tracking errors. Improving the electromechanical model (e.g. optimizing and personalising pressure constraints on the mesh) may therefore shed further light on the projected performance of this strain component.

In terms of displacement errors, the AFFD model showed the highest accuracy, and also had the smallest error dispersion (table 8.2). The latter trend continued for every strain component with the AFFD model showing the smallest error dispersion. The ES errors for the ε_{CC} component were also the lowest for the AFFD model.

Detecting ischemia

Fig. 8.3 shows that ischemic segments are well discriminated using circumferential strain. This was not the case for the longitudinal component due to the

low values of the ES longitudinal strains in combination with the moderate precision of the measurement. Radial strain values were consistently lower in the diseased segments. With the exception of UPF, all challengers also underestimated radial strain as mentioned already above. Furthermore, it can also be noted that the basal septal wall exhibited an inversed longitudinal strain pattern while not being considered ischemic in the ground truth simulations. Therefore, there is still room for further improvements in the electromechanical model. Nevertheless, this peculiarity was identified clearly by all methods.

Influence of the image signal-to-noise ratio on tracking performance

Overall, and as expected, errors increased when lowering the SNR (Fig. 8.4a). Philips appeared to be least sensitive to these changes when displacement errors were used as a quality measure. Breaking this error down to the individual strain components revealed that most of the performance loss occured in the radial direction. For the AFFD model, $\varepsilon_{\mathrm{RR}}$ error dispersion was fairly constant when lowering the SNR, but accuracy decreased greatly (Fig. 8.4b). This may be related to the fact that in anatomical space radial motion is translated into a horizontal motion of a bright black-to-white transition (transition of the blood pool to the myocardium as shown in Fig. 7.2d). When lowering the SNR, the appearance of this border becomes less evident potentially leading to an underestimation of the motion. Chapter 10 proposes an alternative regularisation scheme to address this undesired behaviour. Accuracy for the other strain components in the AFFD model remained fairly constant over the analysed SNR range. The AFFD model had the highest accuracy for the circumferential strain component, closely followed by Philips.

Computational efficiency

Compared to the other methods, the AFFD model was fairly slow (table 8.4), but also showed the best accuracy in terms of displacement error as mentioned earlier. Several improvements can still be made to speed up the registration process. Currently, the calculation of the regularisation terms, i.e. the bending energy, is computationally intensive since it is calculated in every voxel, e.g. see appendix Eq. (B.12). Closed-form integrals, where the bending energy is calculated directly for the whole B-spline support, can greatly speed up solving the registration problem, e.g. as proposed in [139] [215]. Other authors have suggested speeding up the registration process by using a stochastic optimizer, which only requires metric values and derivatives in a subset of voxels during every iteration of the optimization process [118][119].

Improving the simulated images

Several improvements to the simulations can still be made. For example, real images could be used to learn ultrasound artifacts and to simulate more realistic speckle patterns, e.g. as proposed by Alessandrini *et al.* [3] or by Prakosa *et al.* [196]. Furthermore, strategies to spatially vary the contrast between the myocardium and the blood pool could be integrated to increase realism, e.g. as proposed in the study of Barbosa *et al.* [16].

8.4 Conclusions

In this chapter, simulated data from a cardiac motion tracking challenge were used to demonstrate that the AFFD model had the highest displacement accuracy and smallest error dispersion among the other state-of-the-art methods. In terms of strain, end-systolic circumferential strain errors were the lowest. In addition, the strain dispersion errors were also the smallest for all cardiac directions. However, when lowering SNR, radial strain accuracy was negatively affected more than other methods. Accuracy for the circumferential strain component on the other hand remained fairly constant over the analysed SNR range, and was the highest among the investigated methods. Compared to the other techniques, the AFFD model remained fairly slow in computing cardiac deformation.

Chapter 9

Non-rigid image registration using a transformation model adapted to the heart: Comparison against a Cartesian transformation model

This work was published in:
B. Heyde, D. Barbosa, P. Claus, F. Maes, and J. D'hooge. Influence of the grid topology of free-form deformation models on the performance of 3D strain estimation in echocardiography. In *Functional Imaging and Modeling of the Heart*, volume LNCS 7945, pages 308–315, London, UK, 20-22 June 2013.

9.1 Motivation

The added value of adopting an anatomical grid topology remains to be proven, despite having several theoretical advantages which were described in section 6.1. In this chapter, the two FFD grid topologies used throughout this thesis (CFFD and AFFD), are compared using the datasets described in section 8.2 to investigate whether adopting an AFFD model provides an added value over a standard CFFD model. Furthermore, a more efficient implementation of the original 3D AFFD model described in chapter 7 is proposed in this chapter by introducing cyclicity within the B-spline transform formulation.

9.2 Evaluated methods

9.2.1 AFFD

The AFFD model has been described previously in chapter 6 for 2D applications and in chapter 7 for the analysis of 3D images. Circumferential boundary conditions were imposed by copying part of the original image on both sides. In chapter 6, this copy initially had a fixed size, and was later dynamically adapted to take the B-spline support grid size σ_c into account in chapter 7, i.e. the size of the copied image was $2\sigma_c$ on either side. The latter formulation only enforces circumferential cyclicity in the recovered motion field (and thus continuity) if the B-spline grid is also centered over the original image, and only if the outer control points κ_c^1 and κ_c^{max} are spaced $\frac{\sigma_c}{2}$ from the border in every refinement scale (see Fig. 9.1, top). Furthermore, this formulation is also computationally inefficient, as the cost function needs to be evaluated over a large number of redundant points.

A more efficient alternative is to let the B-spline polynomials wrap around the circumferential direction to encode circumferential cyclicity directly inside the B-spline transform (see Fig. 9.1, bottom). This is possible by first centering the grid in this direction, and ensuring that the outer control points κ_c^1 and κ_c^{max} are spaced $\frac{\sigma_c}{2}$ from the border in every refinement scale. Furthermore, we adapt the definition of the control point neighbourhood $\mathcal{N}_c$ in the following cases:

$$\begin{cases} \mathcal{N}_c = \{\kappa_c^{max}, \kappa_c^1, \kappa_c^2, \kappa_c^3\}, & \frac{\sigma_c}{2} \leq c < \frac{3\sigma_c}{2} \\ \mathcal{N}_c = \{\kappa_c^{max-1}, \kappa_c^{max}, \kappa_c^1, \kappa_c^2\}, & 0 \leq c < \frac{\sigma_c}{2} \\ \mathcal{N}_c = \{\kappa_c^{max-1}, \kappa_c^{max}, \kappa_c^1, \kappa_c^2\}, & c_{max} - \frac{\sigma_c}{2} \leq c < c_{max} \\ \mathcal{N}_c = \{\kappa_c^{max-2}, \kappa_c^{max-1}, \kappa_c^{max}, \kappa_c^1\}, & c_{max} - \frac{3\sigma_c}{2} \leq c < c_{max} - \frac{\sigma_c}{2} \end{cases} \tag{9.1}$$

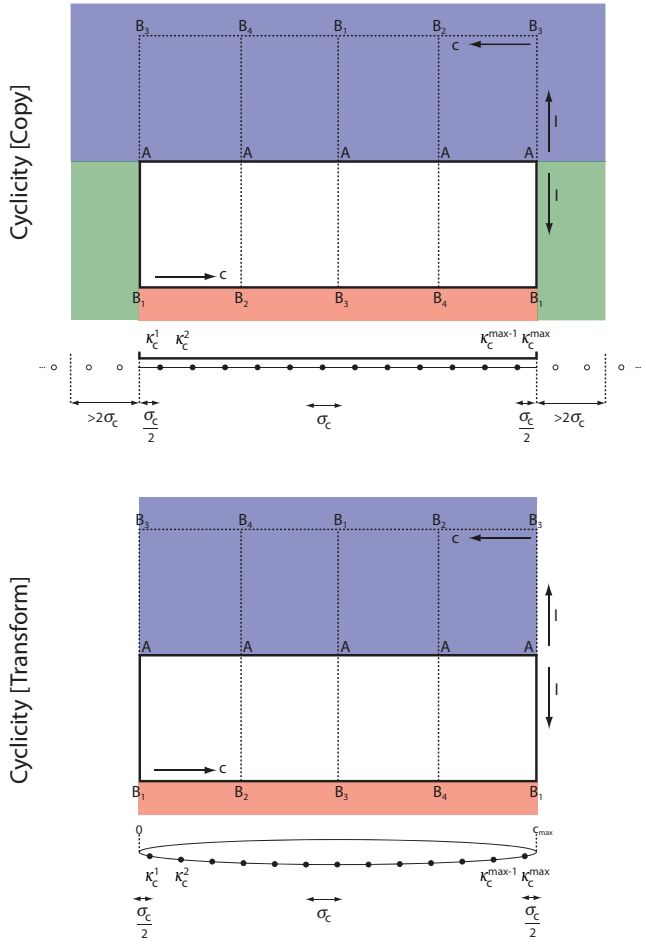

Figure 9.1: Circumferential cyclicity in anatomical space can be enforced by (top) copying part of the image on either side or (bottom) by implicitly encoding cyclicity in the B-spline transform by wrapping around the control points in the circumferential direction (bottom).

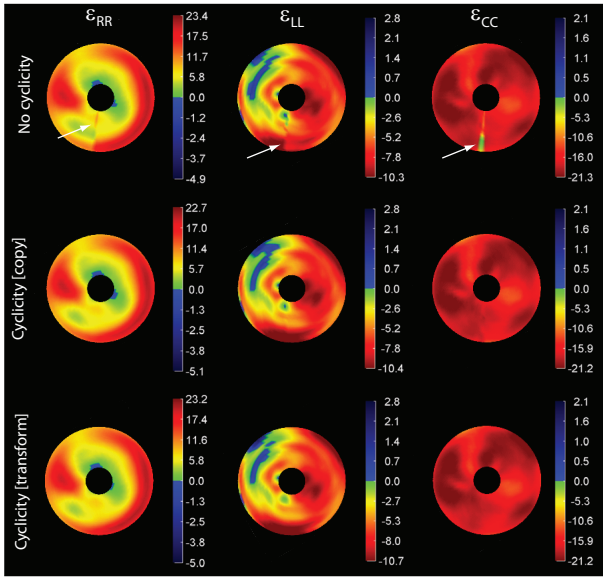

Figure 9.2: Spatial distribution of end-systolic strain of a synthetic dataset with a normal strain pattern, in the absence of circumferential cyclicity (top), or when circumferential cyclicity is imposed by copying part of the image (middle panel), or when encoded in the B-spline transform.

The effect of adopting a cyclical B-spline formulation on strain outcomes within a synthetic dataset with a normal motion pattern from the STACOM challenge (see table 8.1), is shown in Fig. 9.2. If no circumferential cyclicity is imposed near the boundaries, then discontinuities in the strain field can clearly be distinguished (white arrows, top row). These flaws dissappear when circumferential cyclicity is imposed by either copying part of the image (middle row) or by encoding it explicitly in the B-spline transform respectively (bottom). From these plots, it is clear that both the strain pattern and the peak values are similar for both approaches. However, it is important to note that the computational advantage of using a cyclical B-spline transform is quite substantial. Depending on the image size and initial grid spacing, computation time can be reduced by 30%. The low end-systolic $\varepsilon_{\mathrm{RR}}$ and the apparently inversed $\varepsilon_{\mathrm{LL}}$ pattern in the septal wall were already discussed in section 8.3.4.

9.2.2 CFFD

The implementation details of the 3D CFFD model can be found in chapter 5. A more extensive background is given in appendix B.

9.3 Evaluation criteria and results

In order to evaluate the performance of both FFD models, a simulated dataset with a normal underlying motion pattern from the STACOM challenge (table 8.1) was used. Displacement errors with respect to the ground truth were estimated first in every vertex of the mesh, and were then averaged for the whole ventricle in every frame. Strain was calculated according to Eq. (8.2). Strain errors were estimated first in every vertex of the mesh, and then averaged on a segmental level in every frame. The overall displacement error $\|\Delta\mathbf{r}\|$ and overall strain error $|\Delta\varepsilon_{\boldsymbol{n}}|$ were assessed by averaging over all frames.

The influence of the bending energy weight ω on these errors is shown in Fig. 9.3a and Fig. 9.3d-f respectively. The spatial distribution of $|\Delta\varepsilon_{\boldsymbol{n}}|$, grouped per segment, is shown in Fig. 9.4. Both methods were also compared in terms of their computation time and the amount of required grid points in every refinement scale (Fig. 9.3b-c). Differences between both methods were assessed using a paired t-test. Finally, a simulated dataset having a left circumflex artery occlusion (see table 8.1) was analysed in order to assess their ability to detect dysfunctional regions. Fig. 9.5 shows bullseye plots of end-systolic $\varepsilon_{\boldsymbol{n}}$ values.

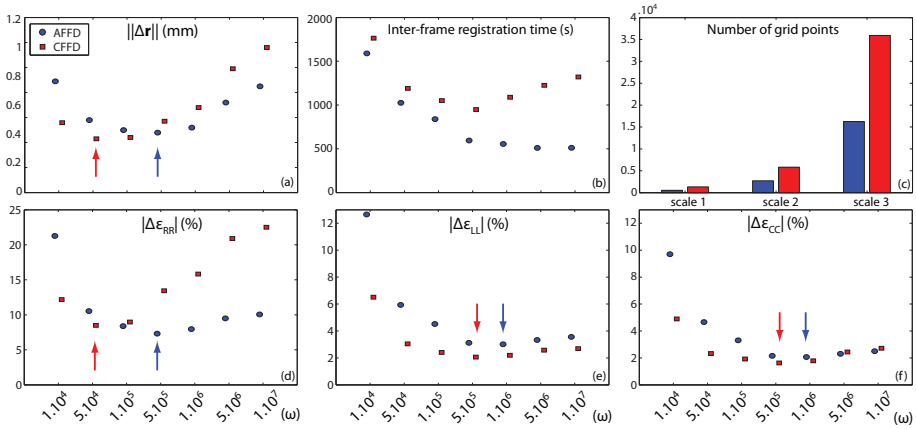

Figure 9.3: Comparison of the CFFD and AFFD model in terms of (a) the displacement error $\|\Delta\mathbf{r}\|$, (d) the strain error $|\Delta\varepsilon_{\mathrm{RR}}|$, (e) $|\Delta\varepsilon_{\mathrm{LL}}|$ or (f) $|\Delta\varepsilon_{\mathrm{CC}}|$ expressed in function of the bending energy weight ω, (b) the computation time per frame and (c) the amount of required grid points for every refinement scale. Arrows indicate minima.

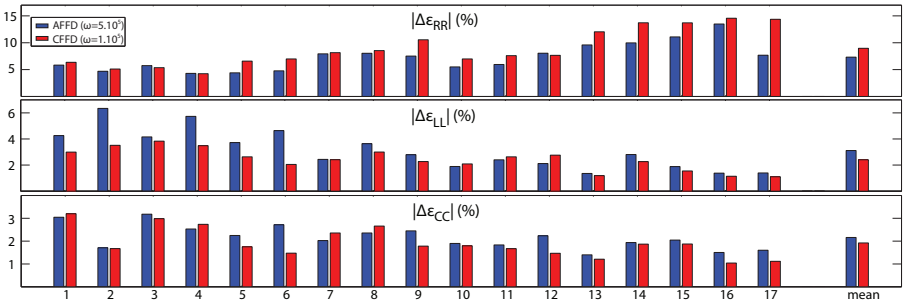

Figure 9.4: Spatial distribution of (a) the strain errors $|\Delta\varepsilon_{\mathrm{RR}}|$, (b) $|\Delta\varepsilon_{\mathrm{LL}}|$ and (c) $|\Delta\varepsilon_{\mathrm{CC}}|$, grouped per segment number (1–6=base, 7–12=middle, 13–17=apex).

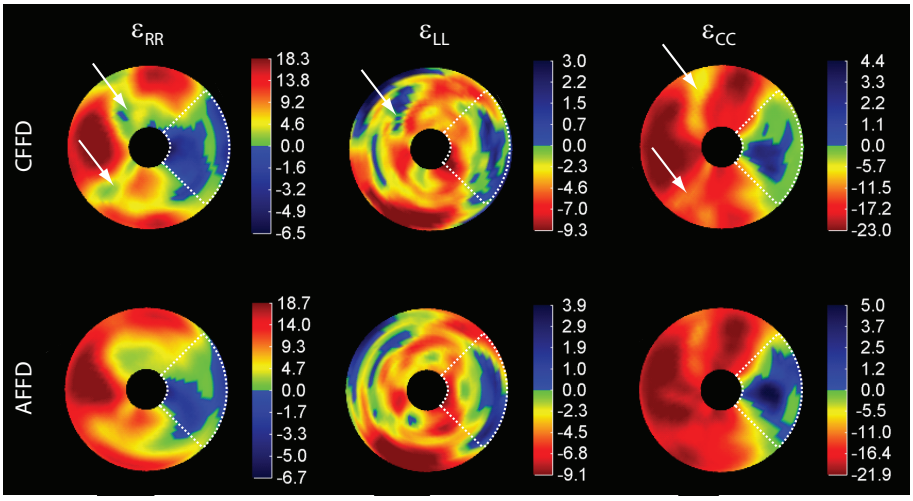

Figure 9.5: Bullseye plots of end-systolic (a) $\varepsilon_{\mathrm{RR}}$, (b) $\varepsilon_{\mathrm{LL}}$ and (c) $\varepsilon_{\mathrm{CC}}$ for the CFFD (top, $\omega = 1.10^5$) and AFFD model (bottom, $\omega = 5.10^5$). The simulated dysfunctional area is outlined. White arrows denote noisier strain areas in the CFFD model.

9.4 Discussion

By analyzing the motion tracking errors as shown in Fig. 9.3a, it is evident that the CFFD and AFFD grid topologies are competitive with a slight disadvantage for the AFFD grid ($\|\Delta\mathbf{r}\|$=0.44mm vs 0.48mm resp.; p<0.01). The CFFD model reaches its optimal accuracy at lower bending energy weights compared to the AFFD model. This trend continues for the strain accuracy (Fig. 9.3d-f). Also worth noting is that the AFFD model appears less sensitive to changes in this weight for ε_{RR}. Taking both motion and strain accuracy into account, optimal bending energy weights are ω=1.10^5 and ω=5.10^5 for the CFFD and AFFD model respectively. Examining strain errors at these weights shows that the AFFD model performs better in the r-direction ($|\Delta\varepsilon_{\text{RR}}|$=9.0% vs 7.3% resp; p<0.01), but performs suboptimal in the l-direction ($|\Delta\varepsilon_{\text{LL}}|$=2.4% vs 3.1% resp; p<0.01). Differences in the c-direction are smaller ($|\Delta\varepsilon_{\text{CC}}|$=1.9% vs 2.2% resp; p<0.05). Further breaking down $|\Delta\varepsilon_{\boldsymbol{n}}|$ on a segmental level (Fig. 9.4), shows that the improvements of the AFFD model for ε_{RR} are located mostly at the apex, but that detecting longitudinal motion is more difficult at a basal level. No significant spatial dependence for $|\Delta\varepsilon_{\text{CC}}|$ was observed.

As remarked earlier in section 7.5, performance in the ε_{LL} direction was suboptimal. It was hypothesised that this could be due to the fact that it may be harder to pick up subtle longitudinal motion compared to the prominent motion (in the r-/c-direction) of a black-to-white interface representing the myocardium. Given that myocardial-specific regularisation terms, such as volume conservation, can be imposed more naturally in an AFFD formulation, further improvements may still be possible (see chapter 10). It was also noted in section 8.3.4 that the peak ε_{LL} in these models ($\sim -5\%$) is much lower than what could be expected in clinical scenarios ($\sim -20\%$). Repeating these experiments in the future with an improved motion model in the simulations may provide further insight into the behaviour of this strain component.

In terms of computation time and model complexity, the AFFD model clearly outranks the CFFD model (Fig. 9.3b-c). Less then half the amount of parameters need to be optimized, the average inter-frame computation time is almost halved (t=1051 s for ω=1.10^5 in CFFD vs t=595 s for ω=5.10^5 in AFFD) and convergence is reached faster especially at higher bending energy weights.

Finally, both methods are clearly able to identify the location of a dysfunctional region (Fig. 9.5). However, bullseye plots of the CFFD model appeared more noisy at certain location (see white arrows), most likely related to the fact that the optimal bending energy weight was lower.

9.5 Conclusions

While both motion and strain accuracy were competitive for the CFFD and AFFD model, moving to an anatomically oriented grid topology appeared better suited for cardiac deformation estimation as model complexity and computation time was reduced considerably. The AFFD model had a tendency to perform better for $\varepsilon_{\mathrm{RR}}$, but this trend was reversed for the other two components.

Chapter 10

Non-rigid image registration using a transformation model adapted to the heart: Embedding a myocardial-specific regulariser

B. Heyde, *Manuscript in preparation*

10.1 Motivation

The myocardium consists of an inter-connected network of muscle fibers and collagen fibers, embedded in a matrix. Given that the myocardium is perfused with blood, myocardial volume changes can occur during the cardiac cycle. A number of studies have been performed to quantify these changes [32][97][138][264]. Hoffman *et al.* pioneered a series of canine experiments and found the variation of the myocardial volume between ED and ES to be around 2% [97]. Bowman *et al.* confirmed these findings in humans by using cardiac MRI and noticed a change of approximately 5% during the cardiac cycle [32]. This implies that the myocardium is nearly incompressible and that this is an important physical property which should be taken into account when extracting cardiac deformation from ultrasound images.

While the AFFD model ranked highly among other state-of-the art techniques, section 8.2 also showed that when lowering image SNR, radial strain accuracy was more susceptible than the other methods. The aim of this chapter was therefore to investigate whether incorporating a volume conservation penalty would improve cardiac strain estimates, and explores whether this decreases strain sensitivity to image SNR as well.

10.2 Volume preserving deformations

Several strategies exist to extract volume preserving deformations in which imaged anatomical structures are known to be incompressible and where all changes are either due to motion or intensity changes caused by the presence of a contrast agent.

Local compression or expansion caused by a certain deformation can be calculated using the Jacobian determinant of the transform. This determinant is equal to one if the deformation is incompressible, greater than one in case of local expansion, and smaller than one when compression occurs. In order to register pre- and post-contrast enhanced MR breast lesion images, a volume penalty term consisting of the absolute logarithm of the Jacobian determinant was proposed by Rohlfing *et al.* [201]. As an alternative, Haber *et al.* solved the registration problem by imposing that the determinant of the transformation should be equal to one [82].

Volume preserving deformations for the analysis of cardiac deformation have almost exclusively been applied to cardiac MR images. Bistoquet *et al.* proposed divergence-free radial basis functions to model the cardiac

displacements in cine MRI sequences and showed that this naturally enforces near-incompressibility. In addition, a hard constraint penalizing deviations from incompressibility larger than 4% was incorporated in the objective function [26]. Mansi *et al.* ensured strong incompressibility by constraining the stationary velocity fields, which parametrize the transformations, to be divergence-free [154]. The penalty is integrated within the logDemons framework proposed by Vercauteren *et al.* [253] and was used to determine cardiac deformation and strain in cine MRI. Its performance was subsequently evaluated in two feasibility studies on simulated and clinical 3D ultrasound images, described in [195] and [161] respectively. A poly-affine variant was proposed shortly thereafter in [162], which could significantly reduce the amount of required parameters to represent cardiac deformation.

As an alternative, some commercial solutions have proposed to estimate radial strain from the other strain components by *a-posteriori* assuming volume conservation of the motion, e.g. in [85][199][209]. A more extensive background regarding this strategy can be found in the appendix, section A.3.

Finally, a related class of problems worth mentioning in this context are those that require the incorporation of rigidity constraints into the image registration process. In this case, the anatomical structures to be registered should not only preserve volume but have to be treated as rigid objects which do not change shape after image registration. This results in additional regularisation terms in the cost function (e.g. by imposing that the deformation should be orthonormal). Applications include registering images containing bony structures which should not locally deform (such as calcifications in vessels from CT angiography [141]), registering vessels before and after contrast injection without compressing the contrast enhanced structures (e.g. in CT angiography [227]), or monitoring structural changes over time such as tumor growth which should not be compensated for by the registration algorithm (e.g. in PET [141] or CT [227]).

From this overview it can be seen that volume-preserving deformation models remain currently underexplored for the analysis of echocardiographic images. The next section discusses how this constraint can be incorporated within the AFFD model developed in the previous chapters.

10.3 Volume preserving anatomical mapping

Consider two US images I_{F} (fixed image) and I_{M} (moving image) as shown in Fig. 10.1. The deformation of the myocardium from I_{F} to I_{M} can be described with the obtained transformation field $\mathbf{T}$ from image registration.

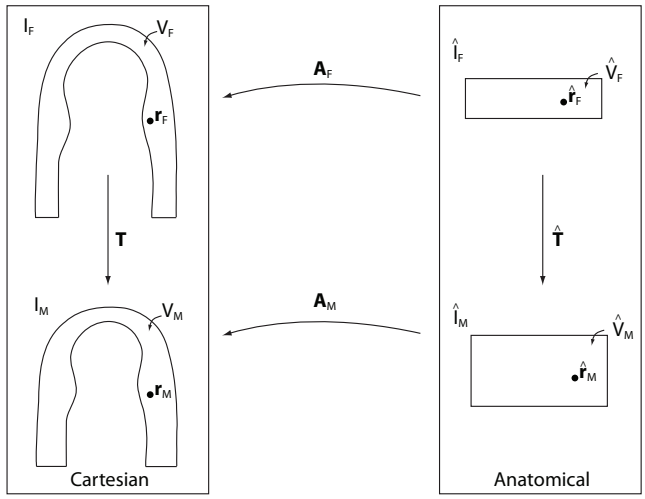

Figure 10.1: Definitions used to derive expressions for the volume conservation penalty

The myocardial volume $\mathrm{V_F}$ before deformation is equal to the myocardial volume $\mathrm{V_M}$ after deformation if the following equation holds true:

$$\int_{\mathrm{V_F}} d\mathbf{r}_{\mathrm{F}} = \int_{\mathrm{V_M}} d\mathbf{r}_{\mathrm{M}} \tag{10.1}$$

Expressing the infinitesimal volume element $d\mathbf{r}_{\mathrm{M}}$ in the initial state of image I_{F} yields:

$$\int_{\mathrm{V_F}} d\mathbf{r}_{\mathrm{F}} = \int_{\mathrm{V_F}} \det(\mathbf{J_T}(\mathbf{r}_{\mathrm{F}}))\, d\mathbf{r}_{\mathrm{F}} \tag{10.2}$$

where $\mathbf{J_T}(\mathbf{r}_{\mathrm{F}})$ is the spatial Jacobian of the transformation field $\mathbf{T}$ evaluated in the coordinates of the fixed image I_{F}. An expression for the volume penalty R_{vol} in Cartesian coordinates can thus be obtained by performing a discrete approximation of the continuous integral over P samples $\mathbf{r}_{\mathrm{F}}$, corresponding to the voxels within the myocardium of the reference image I_{F} [201]:

$$R_{vol} = \frac{1}{P} \sum_{\mathbf{r}_{\mathrm{F}} \in \mathrm{V_F}} \left[\det(\mathbf{J_T}(\mathbf{r}_{\mathrm{F}})) - 1\right]^2 \tag{10.3}$$

In the AFFD model, these images are transformed to anatomical space by the respective transforms $\mathbf{A}_{\mathrm{F}}$ and $\mathbf{A}_{\mathrm{M}}$, with the myocardium becoming a 'slab' as shown schematically in Fig. 10.1. Simply applying the same equation used in

Cartesian space to express preservation of myocardial volume would lead to:

$$\int_{\hat{\mathrm{V}}_{\mathrm{F}}} d\hat{\mathbf{r}}_{\mathrm{F}} = \int_{\hat{\mathrm{V}}_{\mathrm{M}}} d\hat{\mathbf{r}}_{\mathrm{M}} \tag{10.4}$$

With similar reasoning, volume conservation $\hat{R}_{vol}$ in anatomical coordinates would therefore be calculated as

$$\hat{R}_{vol} = \frac{1}{P} \sum_{\hat{\mathbf{r}}_{\mathrm{F}} \in \hat{\mathrm{V}}_{\mathrm{F}}} \left[\det(\mathbf{J}_{\hat{\mathbf{T}}}(\hat{\mathbf{r}}_{\mathrm{F}})) - 1 \right]^2 \tag{10.5}$$

However, this expression does not take the volume changes due to the anatomical unfolding into account. For example, motion of the endocardium in the direction of the blood pool in the anatomical space (e.g. radial inward motion during systole) will result in a higher myocardial compression compared to the same motion at an epicardial level.

This effect can be taken into account by starting from the volume conservation expression in Cartesian coordinates:

$$\int_{\mathrm{V}_{\mathrm{F}}} d\mathbf{r}_{\mathrm{F}} = \int_{\mathrm{V}_{\mathrm{M}}} d\mathbf{r}_{\mathrm{M}} \tag{10.6}$$

and using the spatial Jacobians $\mathbf{J}_{\mathbf{A}_{\mathrm{F}}}$ and $\mathbf{J}_{\mathbf{A}_{\mathrm{M}}}$ associated with the anatomical unfolding transformations $\mathbf{A}_{\mathrm{F}}$ and $\mathbf{A}_{\mathrm{M}}$, to convert the expression to anatomical space:

$$\int_{\hat{\mathrm{V}}_{\mathrm{F}}} \det(\mathbf{J}_{\mathbf{A}_{\mathrm{F}}}(\hat{\mathbf{r}}_{\mathrm{F}}))\, d\hat{\mathbf{r}}_{\mathrm{F}} = \int_{\hat{\mathrm{V}}_{\mathrm{M}}} \det(\mathbf{J}_{\mathbf{A}_{\mathrm{M}}}(\hat{\mathbf{r}}_{\mathrm{M}}))\, d\hat{\mathbf{r}}_{\mathrm{M}} \tag{10.7}$$

Finally, the infinitesimal volume element $d\hat{\mathbf{r}}_{\mathrm{M}}$ in the right hand side of Eq. (10.7) is again expressed in the initial state of image $\hat{I}_{\mathrm{F}}$ to yield:

$$\int_{\hat{\mathrm{V}}_{\mathrm{F}}} \det(\mathbf{J}_{\mathbf{A}}(\hat{\mathbf{r}}_{\mathrm{F}}))\, d\hat{\mathbf{r}}_{\mathrm{F}} = \int_{\hat{\mathrm{V}}_{\mathrm{F}}} \det(\mathbf{J}_{\mathbf{A}}(\hat{\mathbf{r}}_{\mathrm{M}})) \cdot \det(\mathbf{J}_{\mathbf{T}}(\hat{\mathbf{r}}_{\mathrm{F}}))\, d\hat{\mathbf{r}}_{\mathrm{F}} \tag{10.8}$$

where the notation $\mathbf{A} = \mathbf{A}_{\mathrm{F}} = \mathbf{A}_{\mathrm{M}}$ was introduced given that the same transformation for the anatomical unfolding is used for every image of the sequence. As such, a modified expression for volume conservation in anatomical space is obtained:

$$\hat{R}_{vol} = \frac{1}{P} \sum_{\hat{\mathbf{r}}_{\mathrm{F}} \in \hat{\mathrm{V}}_{\mathrm{F}}} \left[\det(\mathbf{J}_{\mathbf{A}}(\hat{\mathbf{r}}_{\mathrm{F}})) - \det(\mathbf{J}_{\mathbf{A}}(\hat{\mathbf{r}}_{\mathrm{M}})) \cdot \det(\mathbf{J}_{\hat{\mathbf{T}}}(\hat{\mathbf{r}}_{\mathrm{F}})) \right]^2 \tag{10.9}$$

Please note that $\det(\mathbf{J}_{\mathbf{A}})$ is evaluated in the fixed image in the first term, whereas it is evaluated in the mapped position of the same point in the second term. An example of $\det(\mathbf{J}_{\mathbf{A}}(\hat{\mathbf{r}}_{\mathrm{F}}))$ is shown in Fig. 10.2. It illustrates that voxels towards the blood pool, and towards the apex have a smaller volume after unwrapping compared to those located more towards the epicardium and the base.

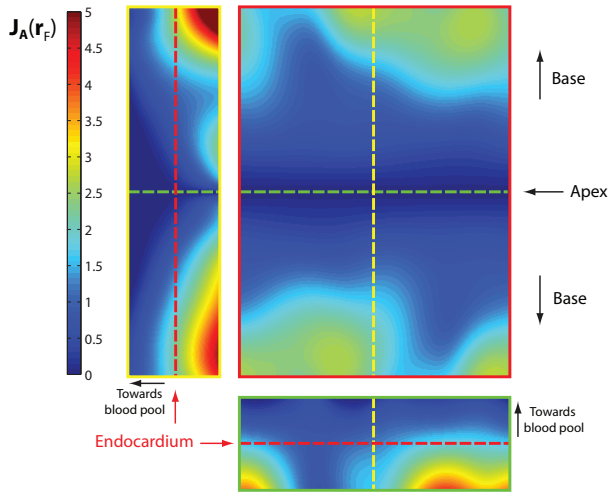

Figure 10.2: Illustration of $\det(\mathbf{J_A}(\hat{\mathbf{r}}_F))$ in anatomical space.

10.4 Experiments and Results

The AFFD model with the circumferential cyclicity features described in chapter 8 was used to test the performance of the volume conservation penalty derived in the previous section. In practice, this could simply be done by replacing the bending energy penalty term with the regularization term proposed in Eq. (10.9). Please note that this penalty term was only evaluated over the myocardial mask $\hat{V}_F$, whereas SSD was used as a similarity metric over the whole image. The myocardial mask was delineated manually in this chapter, but this could be automated by following the strategy proposed in chapter 11. The method was evaluated on a simulated dataset with a normal underlying motion pattern (SNR=0.75, see table 8.1).

The influence of modifying the volume conservation penalty from the initial formulation in Eq. (10.5) to the final formulation taking the Jacobian in Eq. (10.9) into account, is shown in Fig. 10.3.

Both regularisation strategies were compared quantitatively using the same dataset. Displacement errors with respect to the ground truth were estimated first in every vertex of the mesh, and were then averaged for the whole ventricle in every frame. Strain was calculated according to Eq. (8.2). Strain errors were estimated first in every vertex of the mesh, and then averaged on a segmental level in every frame. The overall displacement error $\|\Delta\mathbf{r}\|$ and overall strain error $\Delta\varepsilon_{\boldsymbol{n}}$ were assessed by averaging over all frames. These errors, quantified in function of the regularisation weight, are shown in Fig. 10.4 and Fig. 10.5

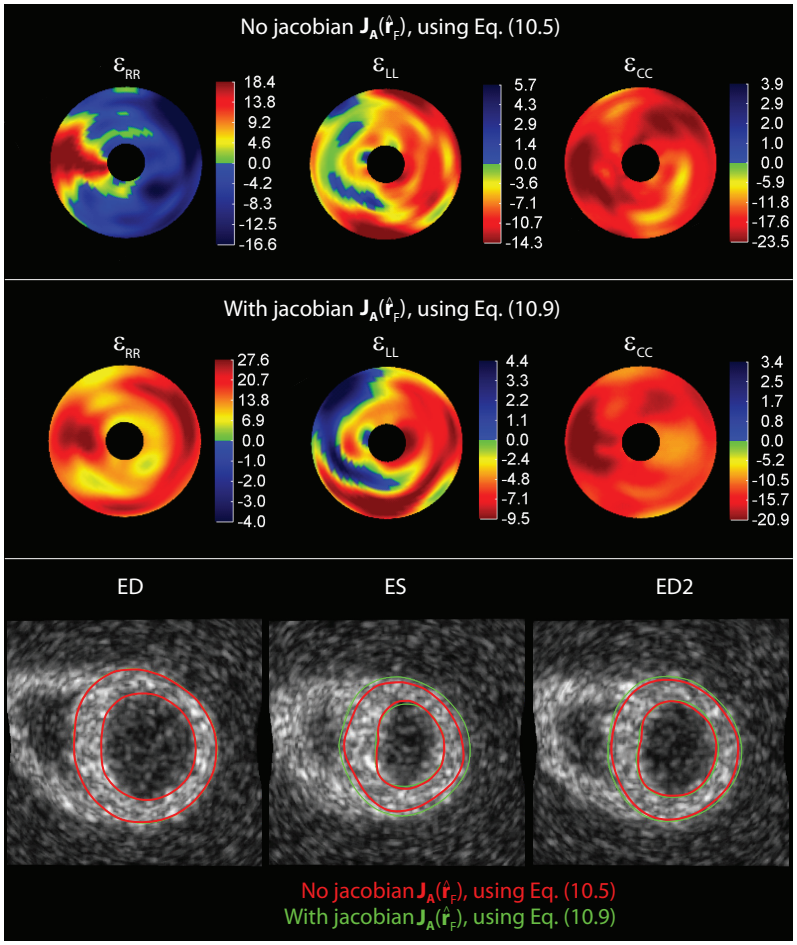

Figure 10.3: Neglecting the jacobian $\mathbf{J_A}(\hat{\mathbf{r}}_F)$ of the anatomical unfolding in the volume conservation penalty (top) or taking it into account in the AFFD model (middle) influences end-systolic strain estimates. The differences in terms of tracking the endo- and epicardial borders in a mid short-axis slice is shown in the bottom panel at different frames during the cardiac cycle.

respectively. Using the obtained optimal weights, segmental strain curves for both regularisation techniques were estimated and plotted in Fig. 10.6.

Finally, the influence of the SNR on displacement and strain accuracy is summarized in Fig. 10.7. The four SNR datasets described in section 8.2 (table 8.1) were used for this purpose.

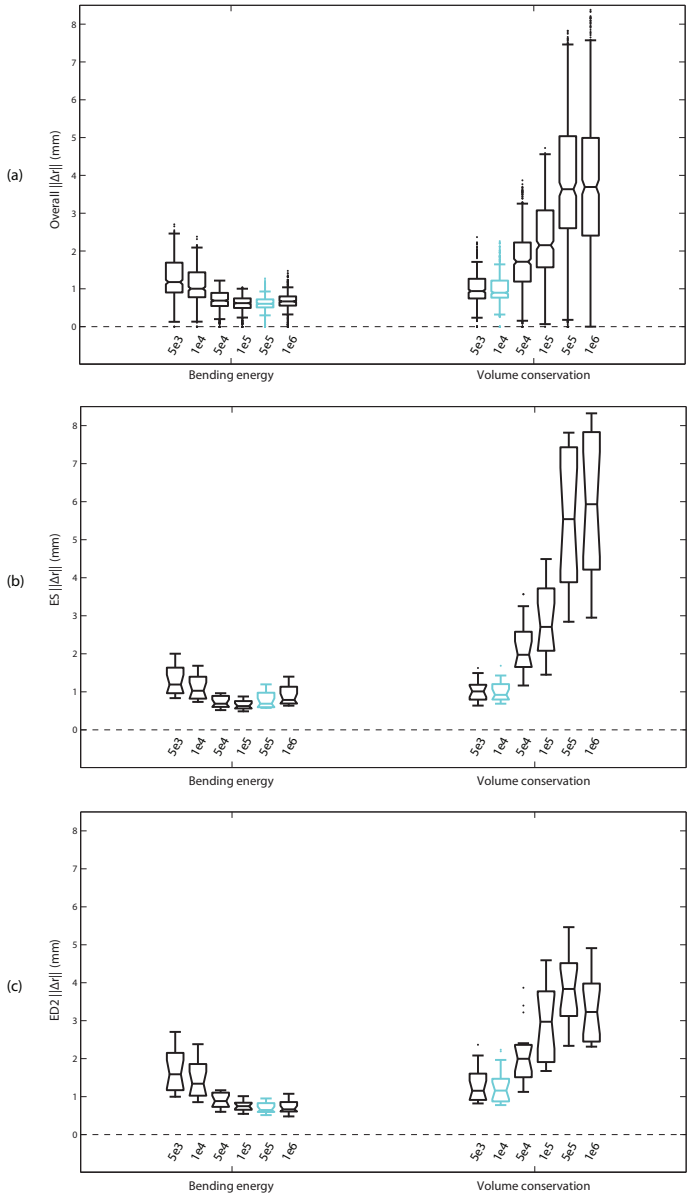

Figure 10.4: Displacement errors $\|\mathbf{r}\|$ averaged over the whole cardiac cycle (a), at end-systole only (b) or at the end of the cardiac cycle (c), expressed in terms of either the bending energy penalty weight (left) or the volume conservation penalty weight (right). The optimal weights are highlighted.

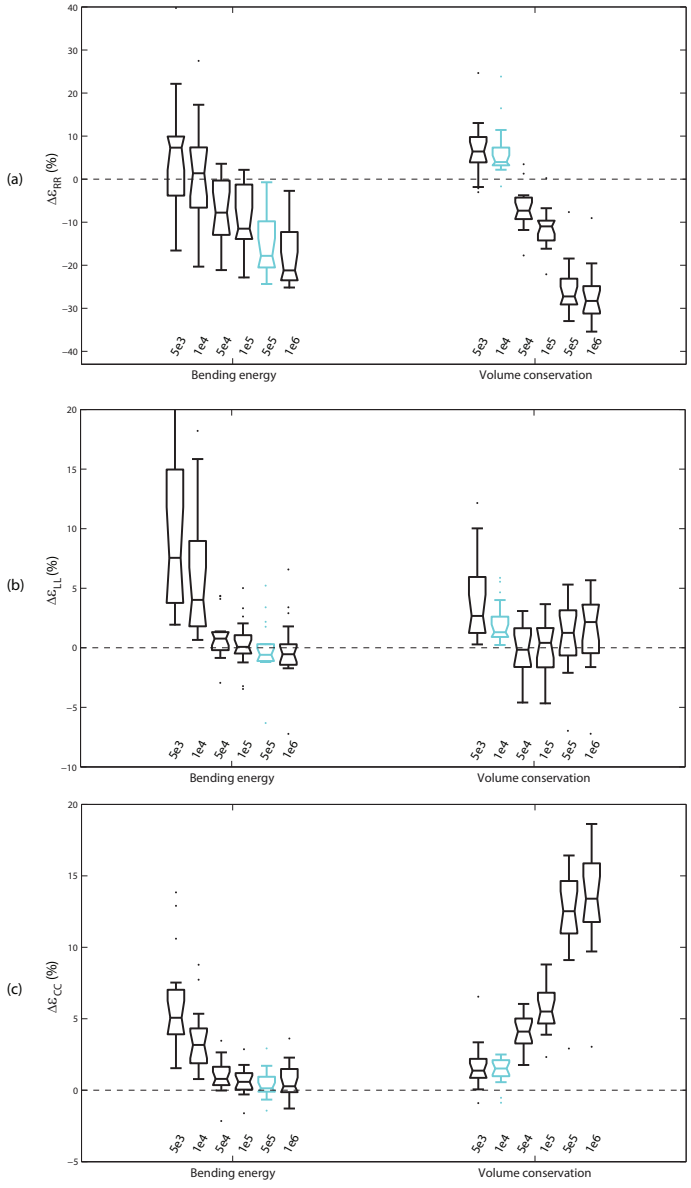

Figure 10.5: End-systolic (a) $\varepsilon_{\mathrm{RR}}$, (b) $\varepsilon_{\mathrm{LL}}$ and (c) $\varepsilon_{\mathrm{CC}}$ strain errors, expressed in terms of either the bending energy penalty weight (left) or the volume conservation penalty weight (right). The optimal weights are highlighted.

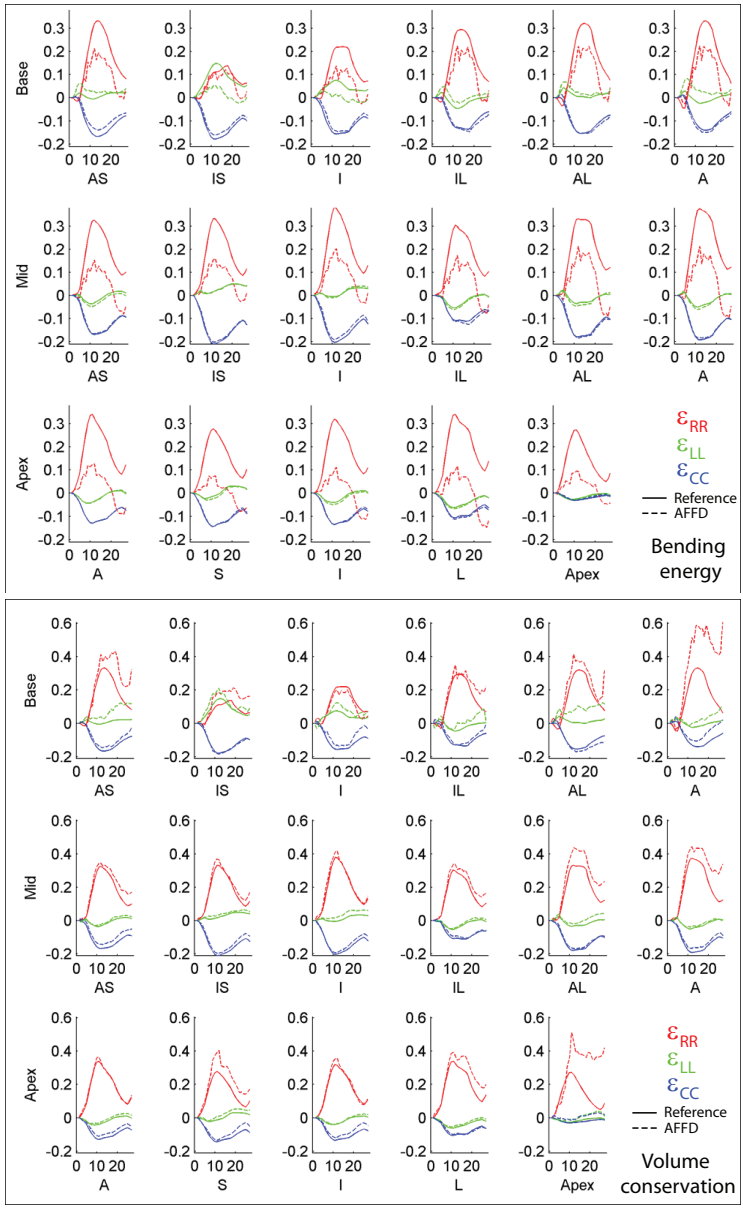

Figure 10.6: Segmental strain curves using a bending energy (top; $\omega = 5e5$) or a volume conservation as a penalty term (bottom; $\omega = 1e4$). red=$\varepsilon_{\mathrm{RR}}$, green=$\varepsilon_{\mathrm{LL}}$, blue=$\varepsilon_{\mathrm{CC}}$, full/dotted line = reference/estimated, AS/IS=antero/inferoseptal, AL/IL=antero/inferolateral, A/I=anterior/inferior.

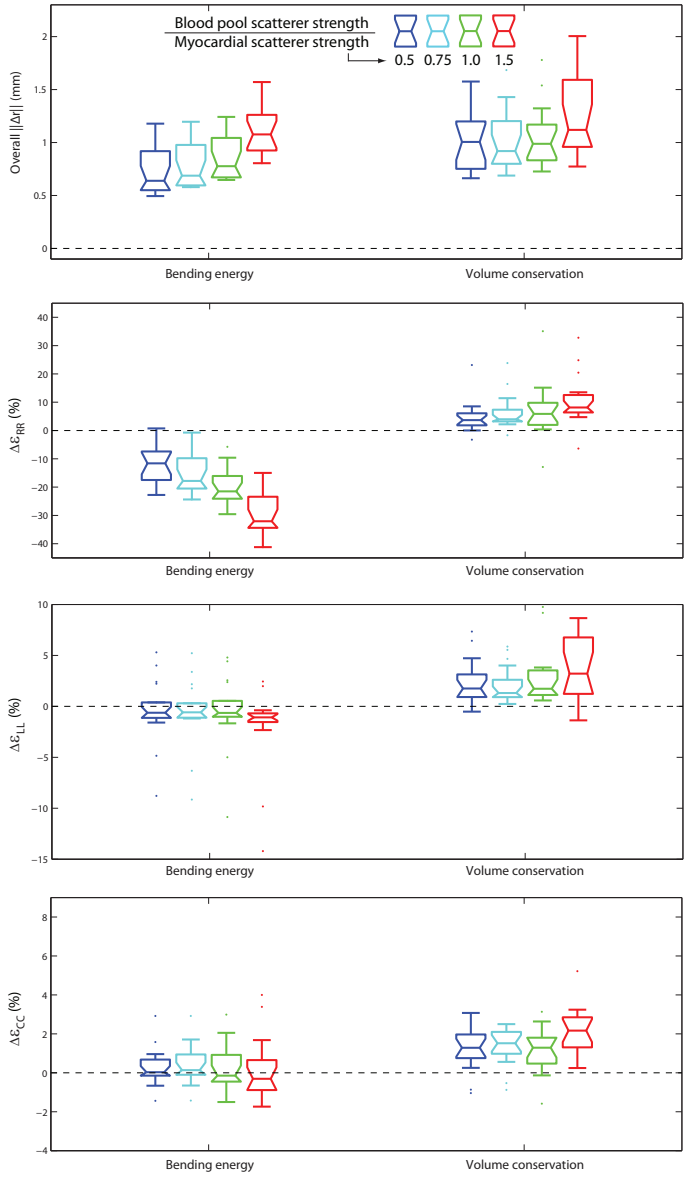

Figure 10.7: Sensitivity of end-systolic displacement and end-systolic strain accuracy to different SNRs: (a) displacement errors, (b) $\varepsilon_{\mathrm{RR}}$ errors, (c) $\varepsilon_{\mathrm{LL}}$ errors, and (d) $\varepsilon_{\mathrm{CC}}$ errors. The highest SNR is shown in blue, the lowest in red. Light blue corresponds to the dataset used in Figs 10.4 and 10.5 with optimal weights $\omega = 5e5$ for the bending energy, and $\omega = 1e4$ for volume conservation.

10.5 Discussion

In this chapter, the potential to regularise cardiac motion with a volume conservation penalty was further investigated. From a mathematical point-of-view it is logic to take the determinant of the Jacobian of the anatomical unfolding process into account. Indeed, Fig. 10.3 shows that this has a profound impact on strain estimates in the AFFD model if this would be neglected (top panel). Using the initial formulation of Eq. (10.5), which would be valid in Cartesian space, results in a striking underestimation of radial strain when simply applied in anatomical space. As can be noted from the bottom panel, the majority of the myocardial wall does not display thickening during systole, apart from a small region near the septum. This observation is also reflected in the radial bullseye plot in the top panel, showing primarily near-zero radial strain. This is most likely related to the fact that the inward radial motion, which is translated to a horizontal thickening motion here, is simply not a volume conserving deformation anymore when viewed in anatomical space. The imposed volume conservation penalty therefore tries to solve this apparent contradiction by only horizontally translating the myocardium, which would be a volume conserving deformation if the image would have been represented in Cartesian space. Including the fact that volume changes associated with a certain deformation are spatially varying in anatomical space, improves radial strain estimates greatly (middle panel). Please note that the inversed positive strain pattern seen in the $\varepsilon_{\mathrm{LL}}$ bullseye plot is purely related to the underlying simulations (see Fig 8.3 bottom).

Next, both regularisation strategies were compared quantitatively by extracting motion and strain from the same dataset, and by varying the penalty weight within a range of 5e3 to 1e6 relative to the image similarity metric. Fig. 10.4a illustrates that the smallest overall displacement errors occured at different weights, which were considered to be the optimal values in this study: $\omega = 5e5$ for the bending energy penalty and $\omega = 1e4$ for the volume conservation penalty. This error was slightly higher, and had a higher variance compared to the bending energy. However, this difference became less evident at end-systole (panel b), and seems to be most likely related to the drift occuring at the end of the cardiac cycle (panel c). The volume penalty also appeared more sensitive to the investigated tuning range.

Interestingly, analysing these errors in terms of radial strain (Fig. 10.5a), favored the volume conservation regularisation since the error was both lower (with a slight overestimation of $\varepsilon_{\mathrm{RR}}$) and more precise at the optimal weights. Over the whole range of investigated weights, it also showed less variance. Sadly, this advantage did not carry over to the other strain components (panels b and c). Both $\varepsilon_{\mathrm{LL}}$ and $\varepsilon_{\mathrm{CC}}$ were slightly higher compared to using a bending energy

term, but still within an acceptable range with average strain errors at ES under 2%.

Fig. 10.6 shows segmental strain curves for both regularisation strategies. The AFFD model using the bending energy penalty underestimates $\varepsilon_{\mathrm{RR}}$ at ES (top panel), whereas this error is lower if volume conservation is used (bottom panel). Errors for the other components were slightly higher. These observations are in agreement with the previously observed trends. However, it can also be noted that the radial strain curves are smoother when volume conservation is imposed, which can be mostly seen in the segments at a mid ventricular level. Finally, the AFFD model with the volume conservation penalty appears to perform better during systole compared to diastole with drift occuring for all strain components. This may be related to the current formulation of the volume conservation penalty which is currently assymetric in nature: an equal amount of compression or expansion is penalised differently. In the future, the drift behaviour may therefore improve if the penalty term would be modified to become symmetric, e.g. by using a logarithmic operation as proposed in [201] and [218]. Futhermore, it may also be worthwhile to investigate whether making the weight of the volume conservation penalty dependent on the optimizer iteration, would improve convergence as proposed by Shi *et al.* [218]. Indeed, one of the disadvantages of the volume conservation penalty is its tendency to not move away from the initial undeformed configuration as this corresponds to a local minimum of the penalty term.

The influence of the SNR on tracking performance is visualised in Fig. 10.7. Please note that the results for the bending energy weight shown in this figure are slightly different compared to those presented in Fig. 8.4 since the AFFD model including the circumferential cyclicity constraints was not used yet in that chapter. It can be seen that the average overall errors were more stable for the volume conservation penalty (panel a). However, the variation increased considerably, especially in the lowest SNR scenario. Breaking this down into the individual strain components, revealed that it was mostly the $\varepsilon_{\mathrm{LL}}$ component which performed suboptimally (panel c). Radial strain on the other hand became much less sensitive to the SNR compared to the method using bending energy as a regularizer (panel b). Circumferential strain errors also stayed fairly constant with decreasing image quality, although still slighty overestimating deformation (panel d).

10.6 Conclusions

In this section, the performance of a volume conservation regularizer was investigated. While overall displacement errors were slightly higher compared to a regularizer using the bending energy, it was shown to be advantageous in estimating radial strain. It was less susceptible to changes in SNR, and smoother radial strain curves closer to the reference measures were obtained. However, errors for the other strain components were slightly higher, but still within an acceptable range. Whether this also improves strain outcomes in clinical datasets remains the topic of future work.

Chapter 11

Non-rigid image registration using a transformation model adapted to the heart: Automating the 3D strain estimation workflow

This work was published in:
B. Heyde, D. Barbosa, A. Daraban, R. Jasaityte, P. Claus, F. Maes, and J. D'hooge. An automated pipeline for regional strain estimation from volumetric ultrasound data. In *IEEE International Ultrasonics Symposium*, Prague, Czech Republic, 21-25 July 2013. *In press*

11.1 Motivation

The AFFD model currently requires a time-consuming delineation of the endocardium to transform the images to anatomical space. This in turn may jeopardize its use in daily clinical practice. Furthermore, estimating strain within a region-of-interest requires manually delineating the whole LV for both the CFFD and AFFD model. Given this manual delineation, strain outcomes may therefore be subject to a considerable observer variability. This has already been demonstrated in clinical practice using commercial software tools [122].

In this chapter a fully automated strain estimation strategy with minimal user input is therefore proposed. The AFFD model is coupled with a real-time segmentation procedure [16]. The different conceptual steps are shown in Fig. 11.1 and are summarized in section 11.2. The pipeline is fully automated, and only requires two user interactions in the final step (Fig. 11.1F). Its applicability is illustrated in a realistic clinical setting, and its performance is compared against a traditional strategy involving manual contouring.

11.2 Automated workflow

A. LV pose detection

To detect the pose of the left ventricle, the long axis (LAx) and the mitral valve plane were sequentially detected (Fig. 11.1A). This in turn, allows for a fast ellipsoid fitting procedure to initialize the endocardial segmentation required in step B.

A robust edge detector based on the phase of the monogenic signal was first used to detect the endocardial border in several consecutive C-planes. Since the endocardium has a circular shape in these 2D planes, applying the Hough transform for circles returns the most likely position for the center of the LV cavity in each of these image slices. Dynamic programming was then utilized to estimate the most probable LAx orientation. The mitral valve plane was detected by finding the plane perpendicular to this LAx which had a brighter average appearance compared to its immediate parallel planes, while also noting that the mitral valve plane usually forms a dark-to-bright transition with respect to its upper neighboring planes. The interested reader is referred to [15] for more implementation details.

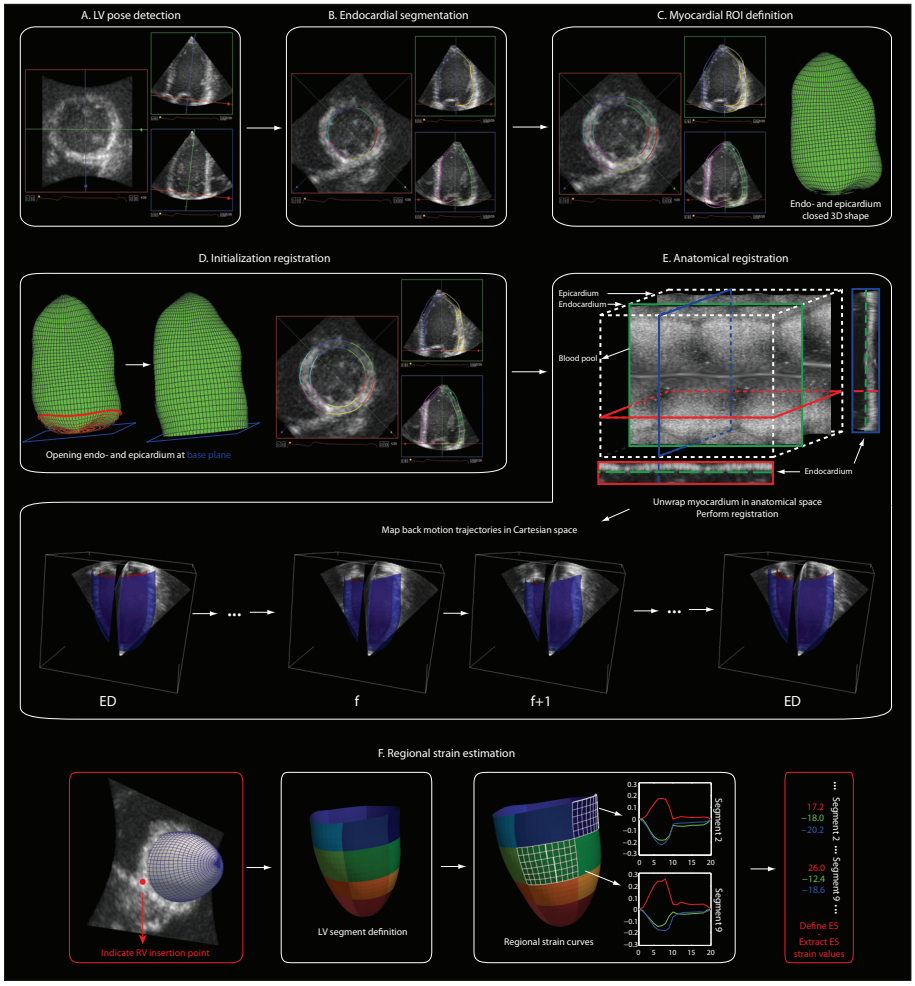

Figure 11.1: Overview of the proposed automated workflow for regional strain estimation. Consecutive steps are labeled alphabetically and are described more in detail under the corresponding headings of section 11.2. Regions highlighted in red indicate steps which require user interaction, the others are performed fully automatic.

B. Endocardial segmentation

Next, the endocardium is segmented using a B-spline Explicit Active Surfaces (BEAS) framework, which is a generic 3D segmentation algorithm introduced by Barbosa *et al.* [16]. The fundamental concept of BEAS is to regard the boundary of an object as an explicit function, where one of the coordinates of the points within the surface, x_1, is given explicitly as a function of the remaining coordinates, i.e. $x_1 = \psi(x_2, \cdots, x_n) = \psi(\mathbf{x}^*)$. This reduces the dimensionality of the segmentation problem. Since ψ is defined in the spherical domain, i.e. $\rho = \psi(\theta, \varphi)$, we can describe the endocardial surface $\mathbf{S}(\theta, \varphi)$ simply as

$$\mathbf{S}(\theta, \varphi) = [\psi(\theta, \varphi)\, cos\, \theta\, cos\, \varphi,\ \psi(\theta, \varphi)\, sin\, \theta\, cos\, \varphi,\ \psi(\theta, \varphi)\, sin\, \varphi] \tag{11.1}$$

Furthermore, ψ is defined as a linear combination of B-spline basis functions, where the segmented surface is explicitly controlled through the B-spline coefficients $c[\theta, \varphi]$ [16]. Both of these concepts lend the algorithm real-time segmentation properties.

The endocardial surface $\mathbf{S}$ is initialized as an ellipsoid with the initial dimensions given by the LV pose detection step described in step A. The segmentation is then allowed to evolve to the true endocardium by minimizing a localized means separation energy, explicitly taking the darker appearance of the blood with respect to the myocardial tissue into account [15]:

$$E_L = \int_\Omega \delta(\phi(\mathbf{x})) \int_\Omega B(\mathbf{x}, \mathbf{y})\, F_L(\mathbf{y}, H(\phi(\mathbf{y})))\, \mathrm{d}\mathbf{y}\, \mathrm{d}\mathbf{x}, \tag{11.2}$$

$$F_L(\mathbf{y}, H_\phi(\mathbf{y})) = (u_x - v_x), \tag{11.3}$$

where $B(\mathbf{x}, \mathbf{y})$ corresponds to a mask function in which the local means inside and outside the segmented interface, u_x and v_x respectively, are estimated. $\delta(\phi(\mathbf{x}))$ and $H(\phi(\mathbf{x}))$ are the Dirac and Heaviside operators respectively applied to the level-set like function $\phi(\mathbf{x}) = \psi(\mathbf{x}^*) - x_1$, which is defined over the image domain Ω. This implies that whenever $u_x > v_x$, this segmentation energy will have a positive value, which is thus penalized in the proposed minimization strategy. This energy can be directly minimized analytically with respect to the B-spline coefficients $c[\theta, \varphi]$ as described further in detail in [15]. Please note that the resulting endocardial surface is closed at the mitral valve plane due to the spherical formulation (Fig. 11.1B).

C. Myocardial ROI definition

In order to create a myocardial region-of-interest (ROI), we let the endocardial surface grow along its local normal direction $\boldsymbol{n}$. A plausible location of the epicardium is found when an intensity interface similar to the endocardium is detected. In practice, the optimal thickness t of the myocardium is obtained by minimizing the following objective function:

$$t = \arg\min_{\gamma} \int_{\Omega} \delta(\phi(\mathbf{x}))(I(\mathbf{x}) - I(\mathbf{x} + \gamma\, \boldsymbol{n}))^2, \tag{11.4}$$

with $\delta(\phi(\mathbf{x}))I(\mathbf{x})$ corresponding to the image intensity of the surface $\mathbf{S}$. To avoid an overinfluence of the papillary muscle on the resulting epicardium, i.e. to avoid concave areas, we take the convex hull of this surface to define the outer layer of the myocardium. This implies that the final myocardial ROI does not necessarily have a constant thickness (Fig. 11.1C).

D. Initialization registration

In order to perform the anatomical unfolding, both the endo- and epicardial surface should be open at the mitral valve plane since the l direction should be perpendicular to the mitral valve plane, and since we want to avoid an overinfluence of the mitral valve motion on the recovered motion field.

We open both meshes artificially near the basal level of the mesh having the highest mean local curvature $\bar{\kappa}$ (Fig. 11.1D left, red border), defined as [79]:

$$\bar{\kappa} = \frac{(\mathbf{S}_\theta \cdot \mathbf{S}_\theta).(\mathbf{S}_{\varphi\varphi} \cdot \mathbf{n}) - 2(\mathbf{S}_\theta \cdot \mathbf{S}_\varphi).(\mathbf{S}_{\theta\varphi} \cdot \mathbf{n}) + (\mathbf{S}_\varphi \cdot \mathbf{S}_\varphi).(\mathbf{S}_{\theta\theta} \cdot \mathbf{n})}{2\left[(\mathbf{S}_\theta \cdot \mathbf{S}_\theta).(\mathbf{S}_\varphi \cdot \mathbf{S}_\varphi) - (\mathbf{S}_\theta \cdot \mathbf{S}_\varphi)^2\right]}, \tag{11.5}$$

with $\mathbf{S}_i$ and $\mathbf{S}_{ij}$ $(i, j \in (\theta, \varphi))$ the vectors corresponding to the first and second partial derivatives of $\mathbf{S}(\theta, \varphi)$ respectively. This expression can be evaluated analytically given the formulation of the surface $\mathbf{S}$ in Eq. (11.1). We then use the spherical harmonics fitting procedure of Eq. (7.3) and Eq. (7.4), to extend the mesh down to the basal plane (Fig. 11.1D middle). This also uniformly resamples both surfaces in the [l,c] direction.

E. Anatomical registration

A detailed description of the AFFD model is given in chapter 7. Circumferential cyclicity was encoded directly in the B-spline transform as described in chapter 9. For the purpose of demonstrating the feasibility of the workflow, the bending energy penalty was used as a regularizer in this chapter. The volume conservation regularizer developed in chapter 10 can be used as well here, but was still in development when this study was performed.

Anatomical registration is visualised schematically in Fig. 11.1E. The whole image sequence is transformed first into an anatomically equivalent image sequence (Fig. 11.1E top right). The curved open endocardial surface obtained in step D is therefore mapped onto a horizontal plane in anatomical space (Fig. 11.1E, green dotted line). The complex systolic thickening of the myocardium during the cardiac cycle is therefore translated in a predominantly uni-directional thickening of a myocardial 'slab'. This in turn, makes motion estimation conceptually easier to perform. After tracking, motion trajectories are mapped back to Cartesian space for visualisation and strain computations (Fig. 11.1E bottom).

F. Regional strain estimation

Strain was estimated using the standard unit length extension used throughout this thesis, e.g. Eq. (A.1). In order to estimate regional strain curves, the LV is automatically divided in 18 segments (3 longitudinal levels, and 6 uniformly distributed circumferential sectors). Two user-interaction steps are required in this stage to extract regional end-systolic (ES) strain values. In order to orient the segments properly, the user is required to select the right ventricular (RV) septal insertion point (Fig. 11.1F left). Finally, the ES timing has to be indicated unless only the peak strain, or the temporal strain behavior is of interest (Fig. 11.1F right).

11.3 Experiments and Results

To test the proposed automated approach, volumetric data (32±3 Hz) was recorded in 3 healthy volunteers and 3 patients with an acute myocardial infarction, using a GE VividE9 (GE Vingmed, Horten, Norway) equipped with a 4V probe (1.7/3.3 MHz). The acquired data was processed using the automated method as outlined in section 11.2. The same recordings were also processed using a traditional manual pipeline, i.e. manually identifying the LAx, the mitral valve plane and contouring the myocardial ROI (steps A-D in Fig. 11.1 become manual).

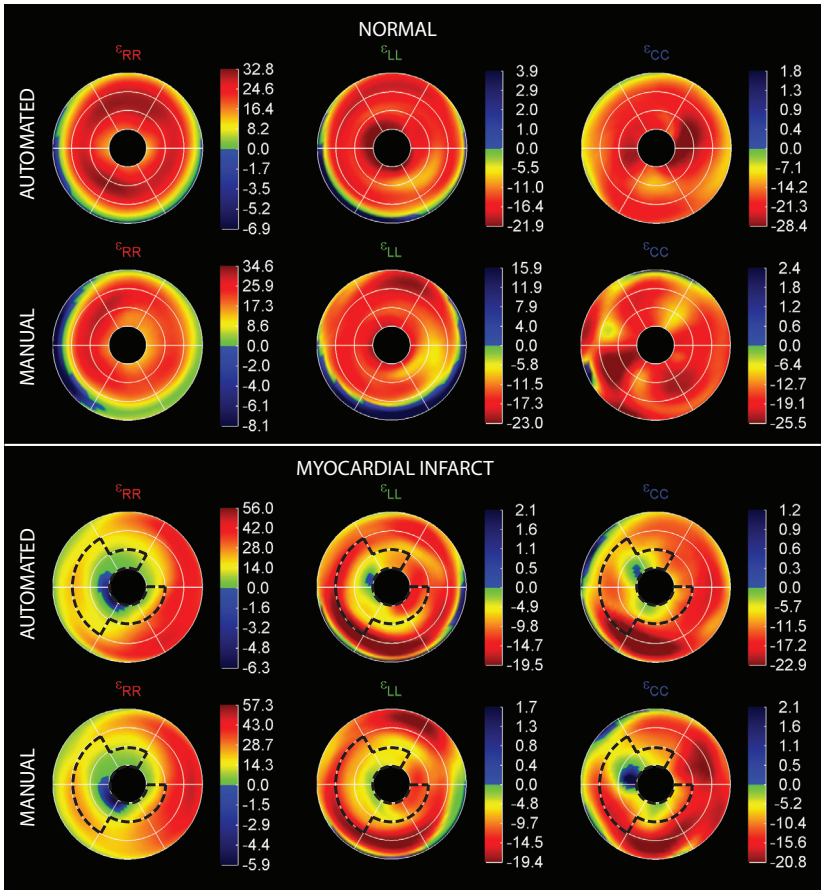

Figure 11.2: Bullseye plots of estimated end-systolic radial ($\varepsilon_{\mathrm{RR}}$), longitudinal ($\varepsilon_{\mathrm{LL}}$) and circumferential strain ($\varepsilon_{\mathrm{CC}}$) using (top) the automated method and (bottom) using manual contouring to initialize the pipeline, for (left) a healthy subject and (right) a patient with an acute myocardial infarct. The dysfunctional area as identified by wall motion scoring is highlighted.

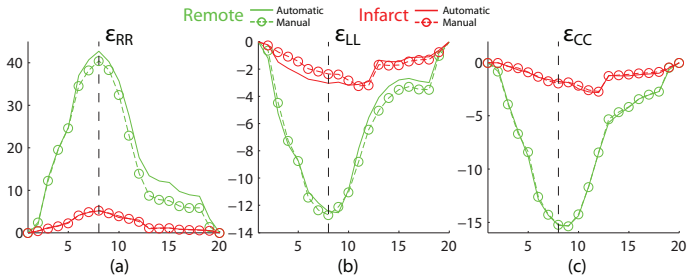

Figure 11.3: Temporal strain profiles for a patient with an acute myocardial infarct, obtained with the proposed automated method (full line) or when a manual time-consuming segmentation was used (circles). The radial (a), longitudinal (b) or circumferential strain (c) was averaged over the remote (green) or the infarct region (red). The vertical dashed line indicates ES.

The user interaction time for the automated method and the manual pipeline was 19±3 s versus 390±90 s respectively. Fig. 11.2 shows the bullseye plots at end-systole for a healthy volunteer and a patient with an acute myocardial infarct, processed with both pipelines. Fig. 11.3 illustrates the temporal strain profiles for the same patient, again obtained with both pipelines and averaged over either the infarct or remote region.

The end-systolic segmental strain differences between the automated and the manual pipeline, taking all subjects into account, were 0.6±3.5%, -0.3±3.6%, -0.7±3.4% for $\varepsilon_{\mathrm{RR}}$, $\varepsilon_{\mathrm{LL}}$ and $\varepsilon_{\mathrm{CC}}$ respectively. Please note that these differences are expressed in absolute strain, and are not relative errors. Comparing the infarct regions against the remote regions in the patient group, ES strain was reduced by 13.7%, 3.8% and 8.5% for the automated method, and by 12.3%, 5.0% and 9.0% if manually contoured, for $\varepsilon_{\mathrm{RR}}$, $\varepsilon_{\mathrm{LL}}$ and $\varepsilon_{\mathrm{CC}}$ respectively.

11.4 Discussion

In this section we compared our proposed automated approach against a traditional strategy involving manual contouring. The user interaction time for the automated method was considerably shorter and eliminated observer variability. Fig. 11.2 illustrates that healthy volunteers had a normal homogeneous ES strain pattern using the automated approach, while dysfunctional regions in patients could be identified. The spatial strain pattern is also comparable with a fully manual strategy (Fig. 11.2 bottom), although a blue inversed strain area could be noticed at the base for the normal subject.

This is most likely due to a mitral valve plane misplacement too far down towards the left atrium. Finally, Fig. 11.3 also demonstrates that the temporal strain profile between both strategies matches closely for the identification of dysfunctional regions.

The proposed automated approach currently requires only two user-inputs: indicating the right-ventricular insertion point to orient the tracked ROI and selecting ES for timing. Both user-inputs could be further automated in the future by e.g. detecting the LV outflow tract to orient the ROI (as proposed in [186]), and by using the ECG or detecting the timing of the aortic valve closure to automatically identify ES. As an alternative, the minimum of the global volume curve extracted from the tracked mesh could be used to set end-systole.

11.5 Conclusions

A fully automated strain estimation pipeline was developed in this chapter, showing reliable strain estimates which were in agreement with conventional manual analysis, but with a considerable lower user-interaction time. The proposed approach is an attractive solution for clinical practice.

Chapter 12

General conclusions

12.1 Main contributions

Ultrasound imaging plays a key role in clinical practice for the evaluation of cardiac morphology and function. One of the most significant developments in echocardiography of the last decade was the introduction of three-dimensional ultrasound imaging and its evolution from slow and labor-intense offline reconstruction to real-time volumetric imaging available today. Three-dimensional echocardiography has a bright future as it offers the possibility to improve and expand on the diagnostic capabilities of traditional 2D echocardiography. Analyzing these datasets however is a challenging endeavor as the spatial and temporal resolution is currently lower than in 2D and the large amount of data makes a manual evaluation cumbersome.

The main contribution of this thesis has therefore been the development of non-rigid registration techniques able to cope with the demanding conditions met in volumetric ultrasound imaging. We have illustrated that image registration is a viable technique for regional cardiac function estimation in a variety of cardiac ultrasound imaging scenarios.

The major contributions and strengths of this work can be summarized as follows:

- The **synergistic approach** in developing and validating the proposed image processing technique. Rather than designing the theoretical framework first, extensive validation has been an integral part of the development process, as reflected by the successive chapters of this work. This strategy promoted online feedback regarding the performance of the algorithm, helped in identifying bottlenecks earlier and allowed steering the development process more effectively.

- **An in-vitro experimental setup** was built in which tissue-mimicking phantoms could be deformed and the accuracy of the regional motion estimates could be assessed using sonomicrometry (in collaboration with the University of Warsaw, Poland). Some phantoms contained stiff inclusions to mimic dysfunctional areas (which would correspond to an infarct in patients). As such, we were the first to report on the discriminative power of a 3D strain method to detect inclusions (chapter 4).

- **An in-vivo animal study** was designed to acquire 3D US data in open-chest sheep subject to different conditions comparable to clinical situations, e.g. induction of ischemia (in collaboration with the University of Ghent, Belgium). Sonomicrometry was used to provide reference deformation estimates. We were the first to validate and report the performance of a registration-based technique for US-based regional strain estimation in an in-vivo context (chapter 5).

- **New regularisation methods** were proposed to improve cardiac deformation estimates. A strategy was derived to adapt the topology of the control point grid of the FFD models to the anatomy of the heart (chapters 6 and 7). It was shown that such a model is more suited for cardiac deformation estimation as model complexity and computation time was reduced considerably (chapter 9). Furthermore, it was shown that a volume conservation regulariser, solely imposed on the myocardium, resulted in both smoother and less noise sensitive radial strain curves (chapter 10).

- The AFFD model was **compared to other state-of-the art strain estimation techniques**, and was the method of choice in terms of displacement accuracy and had the lowest errors for the circumferential strain. The other strain compents were competitive (chapter 8).

- Efforts were made to **automate the strain estimation workflow** (chapter 11) and integrate this into a user-friendly research tool, simplifying its introduction in clinical practice [109].

- The method was completely implemented within a C++ programming environment using **state-of-the art image processing libraries** (ITK) in order to limit the computational processing burden.

It should be noted that the developed methodology remains relatively generic and is not restricted to a single modality. It has already led to an active contribution in **other applications**: it was applied within a small animal setting to assess global function from cine MRI images [70], and to assess regional function from tagged MRI images [124]. Simultaneously, the method was extended to include the time direction in the FFD transform for cardiac motion estimation from tagged MRI [168].

12.2 Future perspectives

The developed anatomical non-rigid registration algorithm (AFFD) was already extensively tested at increasing stages of realism: in-silico (chapters 7, 8 and 10), in-vitro and in-vivo (chapter 7). Its performance was evaluated positively on a small number of clinical cases (chapter 11). In order to **fully explore its clinical potential**, the method should be tested on a larger number of clinical images. Data acquired in the context of a large multi-center clinical study coordinated by the lab of this PhD thesis could provide further insights and valorisation given that the reference strain measurements of Doppler, 2D speckle tracking and tagged MRI are available [61].

The current implementation of the AFFD model is still fairly slow, requiring about 2 hours to extract deformation from a 30 frames sequence. This may potentially hamper its future use in clinical practice. Several **computational improvements** can still be made to speed up the registration process. The main bottleneck of the algorithm is the computation of the regularisation terms, which are currently calculated within every voxel. Closed-form integrals can be derived where the regularisation terms are directly calculated over the whole B-spline support, e.g. as proposed in [139] [215]. Other authors have suggested speeding up the registration process by efficient linear programming [78] or by using a stochastic optimizer, which only requires metric values and derivatives in a subset of voxels during every iteration of the optimization process [118][119].

Further significant reductions in calculation time could be obtained by parallellizing the algorithm. This can be achieved by distributing the individual pairwise registrations over multiple CPUs. This was already performed for the CFFD model since every inter-frame registration could be considered independent. For the AFFD model such strategy could not be used thus far

since the myocardial mask of the volume conservation penalty was propagated forward using the previous inter-frame registration. By using a fast global tracking strategy as e.g. proposed in [17], the myocardial mask could be deformed prior to applying non-rigid image registration, thereby opening the possibility to distribute the registration task over different CPUs. As an alternative, GPU accelerations could be used for the metric computations. Porting the whole framework to a GPU is far from trivial but significant execution time improvements have been reported previously [213].

Analyzing US images is challenging due to the image quality, which can be deteriorated by a number of artefacts [177]. As mentioned in chapter 4 static artefacts and reverberations may negatively affect intensity-based registration algorithms. Deriving strategies to **preprocess US images** to filter these artefacts prior to registration may further improve deformation estimates [34].

Finally, SSD has been used as a **similarity criterion** throughout this thesis, mostly for its computational simplicity and good performance for monomodality registration. It may be interesting in the future to compare the obtained results with those of other similarity measures, e.g. those that take speckle statistics explicitely into account [46]. Alternative metrics to provide even more robust deformation estimates could also be based on segmentation-energies, e.g. by adopting a regional formulation as described in [16].

Closing words

Summarizing four years of research...
...in a mere 100 words can be a daunting task.


strain
image
model
motion
deformation
estimation
registration
cardiac
tracking
AFFD
CFFD
data
images
used
methods
values
within
speckle
phantom
conservation
sonomicrometry
time
inclusion
techniques
every
ED
performed
obtained
circumferential
Chapter
field
region
space
myocardium
penalty
line
radial
also
using
see
However
along
models
proposed
ES
heart
transformation
two
study
order
estimates
left
Eq
frame
mm
displacement
energy
surface
one
points
cycle
LV
compared
method
myocardial
anatomical
longitudinal
performance
based
therefore
tissue
error
may
chapter
direction
wall
spatial
volume
clinical
crystal
datasets
point
imaging
shown
lower
respectively
estimated
grid
function
errors
Figure
ultrasound
different
due
segments
correlation
B-spline
apical
results
right

Appendix A

Background: Strain estimation

A.1 One-dimensional strain

A.1.1 Definitions

The most commonly used definition of strain is the **Lagrangian strain**, which is defined as the change in length of an object normalized to its original size:

$$\varepsilon_{\text{L}} = \frac{L - L_0}{L_0} \tag{A.1}$$

where L_0 and L are the initial and the deformed (instantaneous) length respectively. Its name originates from the description of the deformation in terms of the material coordinates (i.e. the undeformed reference state). Lagrangian strain is also referred to as **Cauchy strain** and **engineering strain**, or simply the **unit extension** of an object. This is the most commonly used definition in echocardiography, as it leads to an intuitive description of deformation since positive strain corresponds to stretching, whereas negative strain corresponds to shortening.

Eulerian strain is an alternative measure of strain and is formed by relating the incremental strain to its instantaneous length:

$$d\varepsilon_{\mathrm{E}} = \frac{dL}{L} \tag{A.2}$$

Integrating the incremental strain therefore leads to the definition of the **Eulerian strain**:

$$\varepsilon_{\mathrm{E}} = \int_{L_0}^{L} \frac{1}{L} dL = ln\left(\frac{L_0}{L}\right) \tag{A.3}$$

Its name originates from the description of the deformation in terms of spatial coordinates (i.e. from the perspective of the current deformation state). Eulerian strain is also known as the **true**, **logarithmic** or **natural strain**.

Lagrangian and Eulerian strain are related in the following way:

$$\varepsilon_{\mathrm{E}} = ln(\varepsilon_{\mathrm{L}} + 1) \tag{A.4}$$

If the strains are small (e.g. 5%), both strain definitions are approximately equal (i.e. differences are smaller than 0.1% strain). For large cardiac deformations, i.e. during systole, the difference becomes significant. In this thesis, the Lagrangian strain formulation is adopted in all chapters.

A.1.2 Tissue Doppler imaging and strain

This section aims to highlight that tissue Doppler imaging measures natural strain and strain rate, as opposed to lagrangian strain and strain rate which are typically extracted in clinical 2D and 3D strain estimation applications.

Strain rate (SR) expresses the speed at which the myocardial deformation occurs and has the unit s^{-1}. SR is thus the temporal derivative of strain:

$$\mathrm{SR} = \dot{\varepsilon} = \frac{d\varepsilon}{dt} \tag{A.5}$$

This definition is valid for both Lagrangian and Eulerian strain descriptors.

More specific, Eulerian SR can be expressed as a spatial velocity gradient (VG):

$$\dot{\varepsilon}_{\mathrm{E}} = \frac{d\varepsilon_{\mathrm{E}}}{dt} = \frac{\frac{dL}{L}}{dt} = \frac{v_2(t) - v_1(t)}{L(t)} = \frac{\mathrm{VG}}{L(t)} \tag{A.6}$$

where $v_2(t)$ and $v_1(t)$ are the local instantaneous velocities of an object with length $L(t)$, as shown in Fig. A.1.

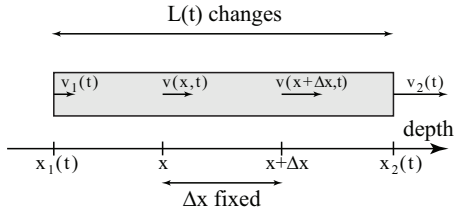

Figure A.1: Geometry used to clarify the different variables in the definition of natural SR and the SR estimator used in TDI.

In tissue Doppler imaging, the velocities of all pixels of the object along the image line are sampled simultaneously. Because it is not feasible to track the end points of the object, TDI-derived strain rate measures the velocity gradient of two points over a fixed distance Δx (see Fig. A.1), resulting in the following SR estimator:

$$\mathrm{SR} = \frac{v(x,t) - v(x+\Delta x,t)}{\Delta x} \tag{A.7}$$

Please note the difference between Eqs. (A.6) and (A.7). In the latter formulation Δx is kept constant, whereas the length of the object $L(t)$ changes in the former formulation.

Under the assumption of a linear, uniform strain within the object, the instantaneous velocity of a point within the object can be written as:

$$v(x,t) = v_1(t) + \frac{v_2(t) - v_1(t)}{L(t)} \cdot (x(t) - x_1(t)) \tag{A.8}$$

Substituting (A.8) into (A.7) shows that the SR measured by TDI is equal to the natural strain rate $\dot{\varepsilon}_{\mathrm{E}}$:

$$\mathrm{SR} = \frac{v(x) - v(x+\Delta x)}{\Delta x} \overset{(A.8)}{=} \frac{v_2(t) - v_1(t)}{L(t)} = \dot{\varepsilon}_{\mathrm{E}} \tag{A.9}$$

Instead of estimating SR with the velocity gradient over a fixed offset distance Δx, it can also be calculated as the slope of the regression line of all velocities within the offset distance Δx as described by Fleming *et al.* [71]. This assumes that the velocity distribution is homogeneous.

Once the strain rate is known, Eulerian strain can then be calculated by means of temporal integration:

$$\varepsilon_{\mathrm{E}} = \int \dot{\varepsilon}_{\mathrm{E}}\, dt \tag{A.10}$$

A.2 Three-dimensional strain

The theory of **continuum mechanics** makes a distinction between two deformation theories depending on the amount of local deformation:

- **Finite strain theory**, also called **large strain theory**, deals with large deformation in which the undeformed (reference) and deformed configuration are significantly different.
- **Infinitesimal strain theory**, also called **small strain theory**, is used for the analysis of small deformations, in which the undeformed (reference) and deformed configuration can be assumed identical.

A.2.1 Continuum mechanics

The present section provides a concise overview of the fundamentals of continuum mechanics of solid continuum bodies, meant to provide a sufficient background to formulate strain definitions. For a more complete treatment the reader is referred to e.g. Malvern *et al.* [153].

Assume a deformation $\mathcal{X}(\mathbf{X})$ which transforms a continuous body from the undeformed configuration B into the deformed configuration b (Fig. A.2). After deformation, each particle at a certain material position $\mathbf{X}$ will be displaced to a new spatial position $\mathbf{x}$:

$$\mathbf{x} = \mathbf{X} + \mathbf{u} \tag{A.11}$$

with $\mathbf{u}$ the **displacement vector**.

The deformation can be characterized by the **deformation gradient tensor** $\mathbf{F}$, which maps an arbitrary Lagrangian line segment $d\mathbf{X}$ onto its corresponding deformed Eulerian line segment $d\mathbf{x}$:

$$d\mathbf{x} = \mathbf{F} \cdot d\mathbf{X} \tag{A.12}$$

and is thus defined as the Lagrangian gradient of the Eulerian coordinates $\mathbf{x}$:

$$\mathbf{F} = \nabla\mathcal{X}, \quad \text{with} \quad F_{ij} = \frac{\partial x_i}{\partial X_j} \tag{A.13}$$

In the context of the FFD model used in this thesis, $\mathbf{F}$ is also called the spatial Jacobian of the transformation field $\mathbf{T}(\mathbf{r})$, e.g. see Eq. (4.5) or Eq. (B.25).

Similarly, a **displacement gradient tensor** $\mathbf{D}$ can be defined as the partial derivative of the displacement vector with respect to the material coordinates:

$$\mathbf{D} = \nabla\mathbf{u}, \quad \text{with} \quad D_{ij} = \frac{\partial u_i}{\partial X_j} \tag{A.14}$$

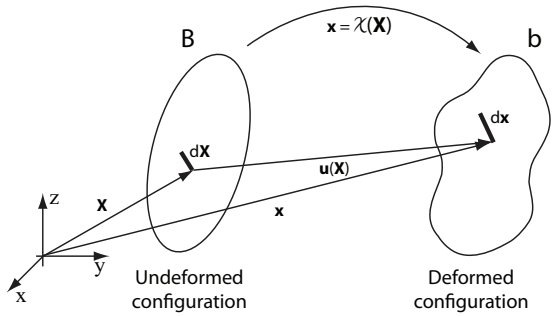

Figure A.2: Definitions used to describe the deformation of a continuous body.

Subsituting Eqs.(A.13) and (A.14) into Eq. (A.12) yields a relation between the deformation gradient tensor and the displacement gradient tensor:

$$\mathbf{F} = \mathbf{D} + \mathbf{I}, \quad \text{with} \quad F_{ij} = \frac{\partial u_i}{\partial X_j} + \delta_{ij} \tag{A.15}$$

where $\mathbf{I}$ represents the identity matrix, and δ_{ij} being the Kronecker delta.

It is often convenient to work with a rotation-independent measure of deformation in continuum mechanics. Given that a pure rotation should not induce any stresses in a deformable body, and given that a rotation followed by its inverse rotation results in no net change, rotation can be excluded from the deformation measure by multiplying the deformation gradient tensor F with its transpose. As such the **right Cauchy-Green deformation tensor C** can be defined as follows:

$$\mathbf{C} = \mathbf{F}^{\mathrm{T}} \cdot \mathbf{F}, \quad \text{with} \quad C_{ij} = \sum_{k=1}^{3} \frac{\partial x_k}{\partial X_i} \cdot \frac{\partial x_k}{\partial X_j} \tag{A.16}$$

Physically, this deformation tensor yields the squared local distance change due to the deformation:

$$\|d\mathbf{x}\|^2 = d\mathbf{X} \cdot \mathbf{C} \cdot d\mathbf{X} \tag{A.17}$$

A.2.2 Finite strain theory

The deformation tensors introduced in the previous section are then used to define the **Lagrangian finite strain tensor**, also called the **Green-Lagrangian strain tensor** or **Green–St.Venant strain tensor**:

$$\mathbf{E} = \frac{1}{2}(\mathbf{C} - \mathbf{I}) \tag{A.18}$$

Physically, the strain tensors are used to calculate the difference between the squared local distances before and after deformation:

$$\|d\mathbf{x}\|^2 - \|d\mathbf{X}\|^2 = 2d\mathbf{X} \cdot \mathbf{E} \cdot d\mathbf{X} \tag{A.19}$$

The Lagrangian finite strain tensor can be expressed in terms of the deformation gradient tensor $\mathbf{F}$ by substituting Eq. (A.16) into (A.18):

$$\mathbf{E} = \frac{1}{2}(\mathbf{F}^{\mathrm{T}} \cdot \mathbf{F} - \mathbf{I}), \quad \text{with} \quad E_{ij} = \frac{1}{2}\left(\sum_{k=1}^{3} \frac{\partial x_k}{\partial X_i} \cdot \frac{\partial x_k}{\partial X_j} - \delta_{ij}\right) \tag{A.20}$$

or as a function of the displacement gradient tensor $\mathbf{D}$ by substituting Eqs.(A.15) and (A.16) into (A.18):

$$\mathbf{E} = \frac{1}{2}\left((\mathbf{D}+\mathbf{I})^{\mathrm{T}} \cdot (\mathbf{D}+\mathbf{I}) - \mathbf{I}\right), \quad \text{with} \quad E_{ij} = \frac{1}{2}\left(\frac{\partial u_i}{\partial X_j} + \frac{\partial u_j}{\partial X_i} + \sum_{k=1}^{3} \frac{\partial u_k}{\partial X_i} \cdot \frac{\partial u_k}{\partial X_j}\right) \tag{A.21}$$

Strain in any given (unit) direction $\mathbf{N} = d\mathbf{X}/\|d\mathbf{X}\|$, can easily be extracted from the Lagrangian strain tensor $\mathbf{E}$ by projection unto this direction:

$$\varepsilon_{\mathbf{N}} = \mathbf{N}^{\mathrm{T}} \cdot \mathbf{E} \cdot \mathbf{N} \tag{A.22}$$

Please note that a capital letter $\mathbf{N}$ was used to indicate that this direction is defined in the undeformed state.

It is also important to stress that the strain $\varepsilon_{\mathbf{N}}$ extracted from $\mathbf{E}$ is different compared to the Lagrangian strain ε_L defined in Eq. (A.1). They are related in the following way:

$$\varepsilon_{\mathbf{N}} = \varepsilon_L + \frac{1}{2}\varepsilon_L^2 \tag{A.23}$$

This can easily be seen by rewriting both strain definitions. Starting from Eq. (A.19), this leads to:

$$2d\mathbf{X} \cdot \mathbf{E} \cdot d\mathbf{X} = \|d\mathbf{x}\|^2 - \|d\mathbf{X}\|^2,$$

$$2\|d\mathbf{X}\| \cdot \mathbf{N}^{\mathrm{T}} \cdot \mathbf{E} \cdot \mathbf{N} \cdot \|d\mathbf{X}\| = \|d\mathbf{x}\|^2 - \|d\mathbf{X}\|^2,$$

$$\varepsilon_N = \frac{\|d\mathbf{x}\|^2 - \|d\mathbf{X}\|^2}{2\|d\mathbf{X}\|^2} \tag{A.24}$$

Similarly, adapting Eq. (A.1) to the nomenclature of Fig. A.2 leads to:

$$\varepsilon_L = \frac{\|d\mathbf{x}\| - \|d\mathbf{X}\|}{\|d\mathbf{X}\|} \tag{A.25}$$

Combining Eq. (A.24) with (A.25) therefore leads to Eq. (A.23).

A.2.3 Infinitesimal strain theory

For small deformations, the non-linear or second-order terms of the finite strain tensor **E** in Eqs. (A.20) and (A.21) can be neglected, leading to the definition of the **infinitesimal strain tensor e**, also referred to as the **Cauchy strain tensor** or **small strain tensor** with the following components:

$$e_{ij} = \frac{1}{2}\left(\frac{\partial u_i}{\partial X_j} + \frac{\partial u_j}{\partial X_i}\right) \tag{A.26}$$

However, since the LV undergoes large deformations during the cardiac cycle, the assumption of infinitesimal strains is usually inaccurate.

A.2.4 Description of cardiac strain

In the field of echocardiography it is convenient to describe the 3D myocardial mechanics using a **3D extension of the one-dimensional Lagrangian strain** definition of Eq. (A.1) as follows:

$$\begin{pmatrix} \varepsilon_{xx} & \varepsilon_{xy} & \varepsilon_{xz} \\ \varepsilon_{yx} & \varepsilon_{yy} & \varepsilon_{yz} \\ \varepsilon_{zx} & \varepsilon_{zy} & \varepsilon_{zz} \end{pmatrix}, \quad \text{with} \quad \varepsilon_{ij} = \frac{\Delta i}{j} \tag{A.27}$$

As such, 3D deformation can be described by three normal strain components ε_{ii}, and six shearing strain components ε_{ij} (Fig. A.3).

In order to facilitate interpretation of strain measurements and to reduce the mathematical complexity required to describe deformation, choosing the appropriate coordinate system is important. Due to the approximately ellipsoidal shape of the left ventricle it is convenient to define a local rather then a global coordinate system, i.e. defining three mutually perpendicular axes in each point of the myocardium (see Fig. A.4), which leads to the following intuitive strain description:

$$\begin{pmatrix} \varepsilon_{\mathrm{RR}} & \varepsilon_{\mathrm{RL}} & \varepsilon_{\mathrm{RC}} \\ \varepsilon_{\mathrm{LR}} & \varepsilon_{\mathrm{LL}} & \varepsilon_{\mathrm{LC}} \\ \varepsilon_{\mathrm{CR}} & \varepsilon_{\mathrm{CL}} & \varepsilon_{\mathrm{CC}} \end{pmatrix} \tag{A.28}$$

where $\varepsilon_{\mathrm{RR}}$ corresponds to a strain component along the radial axis (pointing away from the cavity, perpendicular to the myocardial wall), $\varepsilon_{\mathrm{LL}}$ corresponding to a strain component along the longitudinal axis (tangent to the wall, pointing to the base), and $\varepsilon_{\mathrm{CC}}$ along the circumferential axis (tangent to the wall, pointing in the anti-clockwise direction when viewed from the apex). The off-diagonal elements correspond to shearing strain components, which will give rise to e.g. LV torsion during systole.

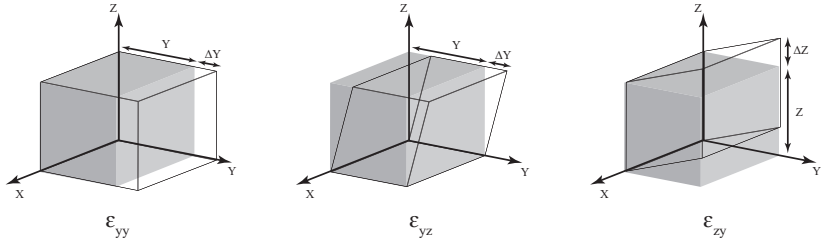

Figure A.3: Deformation of a 3D object illustrating one normal (left) and two shear strain components (middle and right).

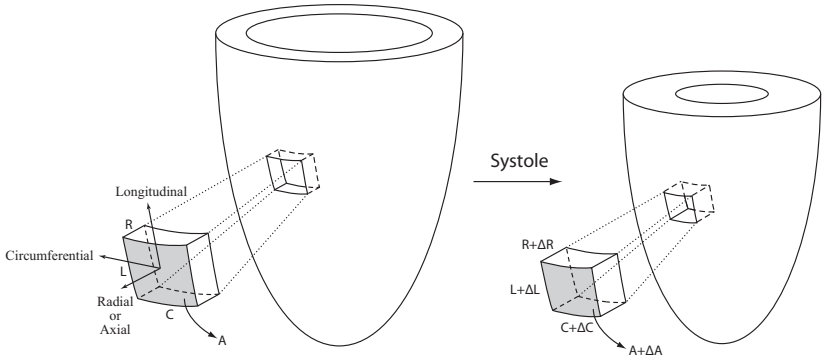

Figure A.4: Definition of the local heart coordinate system (see section A.2.4) together with the nomenclature to describe the change of a myocardial segment during systole (see section A.3).

As an alternative, some authors have proposed to report **principal strains** $\varepsilon_{\mathrm{PP}}$ which are independent of the coordinate system orientation (e.g. [64][176][189]). Given that the Lagrangian strain tensor $\mathbf{E}$ is symmetric, the principal strains can be extracted by performing an eigendecomposition of the matrix:

$$\mathbf{E} = \Omega \cdot \Lambda \cdot \Omega^{-1} = \Omega \cdot \begin{pmatrix} \varepsilon_{\mathrm{PP},1} & 0 & 0 \\ 0 & \varepsilon_{\mathrm{PP},2} & 0 \\ 0 & 0 & \varepsilon_{\mathrm{PP},3} \end{pmatrix} \cdot \Omega^{-1} \tag{A.29}$$

where $\varepsilon_{\mathrm{PP},i}$ represents the principal strain component along the principal strain direction, formed by the respective columns of Ω. While these measures are independent of the defined coordinate system in every point, it is important to note that their physiological or clinical value is more difficult to deduct as they do not relate to any cardiac direction.

Eq. (A.23) showed that strain derived from the Lagrangian strain tensor in continuum mechanics is different from the Lagrangian strain definitions of Eqs.(A.1) and (A.28). Nevertheless, it is still possible to derive an expression for the **classical Lagrangian strain in continuum mechanics**, by using the deformation gradient tensor $\mathbf{F}$. This is particularly interesting in the context of this thesis since $\mathbf{F}$ can be calculated in any given point from the FFD transformation model used in this thesis. By starting from Eq. (A.19), dividing both sides by $\|d\mathbf{X}\|^2$ and using $d\mathbf{X} = \mathbf{N} \cdot \|d\mathbf{X}\|$, we obtain:

$$\frac{\|d\mathbf{x}\|^2}{\|d\mathbf{X}\|^2} - 1 = 2 \cdot \mathbf{N}^{\mathrm{T}} \cdot \mathbf{E} \cdot \mathbf{N} \tag{A.30}$$

Taking the square root, and substracting 1 to obtain the unit extension leads to

$$\frac{\|d\mathbf{x}\|}{\|d\mathbf{X}\|} - 1 = \sqrt{2 \cdot \mathbf{N}^{\mathrm{T}} \cdot \mathbf{E} \cdot \mathbf{N} + 1} - 1 \tag{A.31}$$

Finally, by substituting Eq. (A.20) in Eq. (A.31), and noting that $\mathbf{N}^{\mathrm{T}} \cdot \mathbf{I} \cdot \mathbf{N} = 1$, we obtain an expression relating Lagrangian strain with the deformation gradient tensor $\mathbf{F}$:

$$\varepsilon_{\mathrm{L}} = \frac{\|d\mathbf{x}\| - \|d\mathbf{X}\|}{\|d\mathbf{X}\|} = \sqrt{\mathbf{N}^{\mathrm{T}} \cdot \mathbf{F}^{\mathrm{T}} \cdot \mathbf{F} \cdot \mathbf{N}} - 1 \tag{A.32}$$

This equation is used in for example chapter 4 to extract cardiac strain.

A.3 Radial strain estimation

Because a direct estimation of $\varepsilon_{\mathrm{RR}}$ remains difficult (see e.g. section 4.6.2), some authors have proposed to compute it from the other strain components [85][199][209]. This can be accomplished by assuming myocardial incompressibility, i.e. volume conservation, during the cardiac cycle.

Estimating $\varepsilon_{\mathrm{RR}}$ through $\varepsilon_{\mathrm{LL}}$ and $\varepsilon_{\mathrm{CC}}$

Consider a small myocardial element which deforms during the cardiac cycle, as shown in Fig. A.4. In reality, the surfaces of this element are curved, but locally this element can be considered a cube with initial dimensions $\mathrm{R}, \mathrm{L}, \mathrm{C}$ along the respective cardiac directions. Upon deformation, the lengths of the cube change with $\Delta\mathrm{R}, \Delta\mathrm{L}, \Delta\mathrm{C}$ respectively. A change in volume ($\Delta\mathrm{V}$) can thus be expressed as:

$$\Delta\mathrm{V} = (\mathrm{R} + \Delta\mathrm{R})(\mathrm{L} + \Delta\mathrm{L})(\mathrm{C} + \Delta\mathrm{C}) - \mathrm{RLC} \tag{A.33}$$

Setting $\Delta V = 0$ to impose myocardial incompressibility, and dividing by RLC leads to:

$$(1 + \frac{\Delta R}{R})(1 + \frac{\Delta L}{L})(1 + \frac{\Delta C}{C}) = 1 \tag{A.34}$$

Noting that $\Delta R/R$ is equal to ε_{RR}, and by reasoning in a similar fashion for ε_{LL} and ε_{CC}, one obtains the following relationship between the individual strain components:

$$(1 + \varepsilon_{RR})(1 + \varepsilon_{LL})(1 + \varepsilon_{CC}) = 1 \tag{A.35}$$

Therefore, ε_{RR} can be estimated as:

$$\varepsilon_{RR} = \frac{1}{(1 + \varepsilon_{LL})(1 + \varepsilon_{CC})} - 1 \tag{A.36}$$

Under the assumption of small deformations, i.e. $\varepsilon_{RR} \ll 1, \varepsilon_{LL} \ll 1$ and $\varepsilon_{CC} \ll 1$, Eq. (A.35) simplifies to:

$$\varepsilon_{RR} + \varepsilon_{LL} + \varepsilon_{CC} \approx 0 \tag{A.37}$$

and ε_{RR} can simply be calculated as the negative sum of ε_{LL} and ε_{CC}:

$$\varepsilon_{RR} \approx -(\varepsilon_{LL} + \varepsilon_{CC}) \tag{A.38}$$

While this formulation appears more intuitive with respect to Eq. (A.36), it is important to stress that this formulation only holds true for small deformations. The deviation from true volume conservation rapidly increases for larger strain values as shown in Fig. A.5. Nevertheless, up to strain values of 5% for both ε_{LL} and ε_{CC}, the error remains under 1% for ε_{RR}.

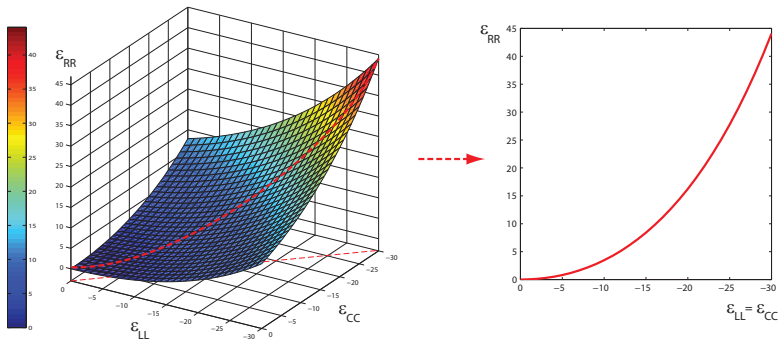

Figure A.5: Deviation from volume conservation expressed as an ε_{RR} error when using the simplified expression of Eq. (A.38) compared to its ideal value obtained through Eq. (A.36).

Estimating $\varepsilon_{\mathrm{RR}}$ through area strain $\varepsilon_{\mathrm{AS}}$

Area strain, sometimes also called **area change ratio** (e.g. in [209]), is defined as the relative change in (endocardial) surface area A during the cardiac cycle. Using the notations of Fig. A.4, this leads to:

$$\varepsilon_{\mathrm{AS}} = \frac{(\mathrm{A} + \Delta\mathrm{A}) - \mathrm{A}}{\mathrm{A}} = \frac{(\mathrm{L} + \Delta\mathrm{L})(\mathrm{C} + \Delta\mathrm{C}) - \mathrm{LC}}{\mathrm{LC}} \tag{A.39}$$

After dividing by LC this reduces to

$$\varepsilon_{\mathrm{AS}} = (1 + \varepsilon_{\mathrm{LL}})(1 + \varepsilon_{\mathrm{CC}}) - 1 \tag{A.40}$$

Finally, by imposing myocardial incompressibility, i.e. by combining Eq. (A.40) with Eq. (A.36), $\varepsilon_{\mathrm{RR}}$ can be expressed in terms of $\varepsilon_{\mathrm{AS}}$ as

$$\varepsilon_{\mathrm{RR}} = -\frac{\varepsilon_{\mathrm{AS}}}{\varepsilon_{\mathrm{AS}} + 1} \tag{A.41}$$

Again, if small deformations can be assumed, Eq. (A.40) reduces to

$$\varepsilon_{\mathrm{AS}} \approx (\varepsilon_{\mathrm{LL}} + \varepsilon_{\mathrm{CC}}) \tag{A.42}$$

Therefore, from Eq. (A.38) it is obvious that $\varepsilon_{\mathrm{RR}}$ is simply the negative of $\varepsilon_{\mathrm{AS}}$

$$\varepsilon_{\mathrm{RR}} \approx -\varepsilon_{\mathrm{AS}} \tag{A.43}$$

Appendix B

Background: Non-rigid image registration using FFD models

B.1 Image registration

General formulation

During image registration, one image (called the moving image, I_M) is deformed to match another image (the fixed image, I_F). Image registration is an optimization problem with the goal of finding a displacement field $\mathbf{u}_{F \to M}(\mathbf{r})$ in each point $\mathbf{r}$ that makes $I_M(\mathbf{r} + \mathbf{u}_{F \to M}(\mathbf{r}))$ spatially aligned with $I_F(\mathbf{r})$. Equivalently, registration is the problem of finding a transformation field $\mathbf{T}(\mathbf{r}) = \mathbf{r} + \mathbf{u}(\mathbf{r})$ that makes $I_M(\mathbf{T}(\mathbf{r}))$ spatially aligned with $I_F(\mathbf{r})$ [272]. The transformation is governed by the transformation parameters $\boldsymbol{\mu}$.

An image similarity metric S (e.g. sum of squared differences, cross-correlation or mutual information) measures the quality of the alignment after applying the transformation on the fixed image I_F. Additional a-priori knowledge of the transformation field can be incorporated in the motion estimation process by e.g. modeling the deformed image as a viscous fluid [51], or by imposing physical penalties on the transformation field (e.g. a smoothness [203] or a volume conservation penalty [140]). This regularisation term R is then combined with the image similarity metric S, into a cost function C:

$$C(I_F, I_M; \boldsymbol{\mu}) = S(I_F, I_M; \boldsymbol{\mu}) + \omega\, R(\boldsymbol{\mu}) \tag{B.1}$$

where ω is a hyperparameter controlling the influence of the regularisation term.

As such, image registration can be formulated as a minimization problem:

$$\boldsymbol{\mu}^* = \arg\min_{\boldsymbol{\mu}} C(I_F, I_M; \boldsymbol{\mu}) \tag{B.2}$$

To determine the optimal transformation parameters $\boldsymbol{\mu}^*$, an iterative optimization strategy can be used:

$$\boldsymbol{\mu}_{(k+1)} = \boldsymbol{\mu}_{(k)} + a_{(k)}\boldsymbol{d}_{(k)}, \quad k = 0, 1, 2, ... \tag{B.3}$$

with $\boldsymbol{d}_{(k)}$ the search direction at iteration (k), and $a_{(k)}$ a scalar gain factor controlling the step size along the search direction. Many optimization methods can be found in literature differing in the way $a_{(k)}$ and $\boldsymbol{d}_{(k)}$ are computed [121]. Many strategies exist to determine the gain factor $a_{(k)}$, e.g. it can be set as a constant or as a decaying function of (k), it can be determined by an *exact* line search that tries to minimize the cost function C along the current direction $\boldsymbol{d}_{(k)}$ (requiring many evaluations of C, and sometimes also of $\partial C/\partial\boldsymbol{\mu}$), or as an *inexact* line search that finds a gain factor a_k which sufficiently reduces C in iteration $(k+1)$. For gradient-based optimization schemes, the search direction $\boldsymbol{d}_{(k)}$ is based on $\partial C/\partial\boldsymbol{\mu}$.

For example, the gradient descent method [181], takes steps in the direction of the negative gradient of the cost function:

$$\boldsymbol{\mu}_{(k+1)} = \boldsymbol{\mu}_{(k)} - a_{(k)}\frac{\partial C}{\partial \boldsymbol{\mu}} \tag{B.4}$$

A popular alternative for large-scale optimization problems are the Newtonian optimizers which use the inverse of the Hessian matrix $\mathbf{H}$ of the cost function C at each iteration step (k). The use of second-order information gives the optimization better theoretical convergence properties:

$$\boldsymbol{\mu}_{(k+1)} = \boldsymbol{\mu}_{(k)} - [\mathbf{H}(\boldsymbol{\mu}_{(k)})]^{-1}\frac{\partial C}{\partial \boldsymbol{\mu}} \tag{B.5}$$

Quasi-Newtonian optimizers use an approximation of the Hessian matrix $\mathbf{H}(\boldsymbol{\mu}_{(k)}) \approx L_{(k)}$ since the computation of the Hessian matrix and its inverse are computationally expensive, especially when a large amount of parameters have to be optimized [58]. As such, matrix inversion operations can be avoided. There are several ways to construct the series $L_{(k)}$, e.g. as proposed in the Broyden-Fletcher-Goldfarb-Shanno (BFGS) method. For a review of other optimization strategies in the context of non-rigid image registration, the reader is referred to [121].

Non-rigid image registration

Elastic or non-rigid image registration methods use image warping techniques to estimate cardiac motion between frames. Free-form deformation (FFD) models where the cardiac displacement field is parametrized using smooth basis functions, have been an attractive approach [203]. In the case of 3D images, myocardial displacement of a point $\mathbf{r} = [x, y, z]$ between two images I_F and I_M can then be modelled with a three-dimensional third order B-spline tensor-product, defined on a cubic lattice [125][203]:

$$\mathbf{u}_{F\to M}(\mathbf{r}) = \sum_{i\in\mathcal{N}_i}\sum_{j\in\mathcal{N}_j}\sum_{k\in\mathcal{N}_k} \boldsymbol{\mu}^{ijk}\beta_x^3(\frac{x-\kappa_x^{ijk}}{\sigma_x})\beta_y^3(\frac{y-\kappa_y^{ijk}}{\sigma_y})\beta_z^3(\frac{z-\kappa_z^{ijk}}{\sigma_z}) \quad \text{(B.6)}$$

with κ_ξ^{ijk} and σ_ξ the control point location and spacing respectively, and N_ξ the set of control points within the compact support $\mathcal{N}$ of the B-spline β_ξ ($\xi \in \{x, y, z\}$). A large amount of parameters typically needs to be optimized when using a FFD model. For example, registering two 3D US images having a size of $256 \times 256 \times 256$ voxels, with an FFD model having a $10 \times 10 \times 10$ grid spacing requires optimizing approximately 47000 parameters.

Given the large number of parameters of the optimization problem, we use a popular limited-memory variant of the BFGS method (LBFGSB) in this thesis, which does not require storing $L_{(k)}$ in memory, and which also implements an inexact line search routine to determine the gain factor $a_{(k)}$ [36][271]. Eq. (B.5) therefore becomes:

$$\boldsymbol{\mu}_{(k+1)} = \boldsymbol{\mu}_{(k)} - a_{(k)}L_{(k)}\frac{\partial C}{\partial \boldsymbol{\mu}} \quad \text{(B.7)}$$

B.2 Image metrics and their derivatives

As evident from Eq. (B.7), finding the optimal transformation field assumes that $\partial C/\partial\boldsymbol{\mu}$ can be calculated, which in turns requires estimating the derivatives of the similarity measure S and the regularisation term R:

$$\frac{\partial C}{\partial \boldsymbol{\mu}} = \boldsymbol{\mu}_{(k)} - a_{(k)}\left(\frac{\partial S}{\partial \boldsymbol{\mu}} + \omega\frac{\partial R}{\partial \boldsymbol{\mu}}\right) \quad \text{(B.8)}$$

This section gives an overview of the different similarity metrics and regularisation terms used in this thesis, together with the calculation of their derivatives. They are formulated for a 3D image registration problem. They can easily be downscaled to 2D images by setting the z-components zero.

Sum of squared differences

The sum of squared differences (SSD) image metric between two images I_F and I_M is defined as:

$$S = \frac{1}{P} \sum_{\mathbf{r} \in I_F} \left[I_F(\mathbf{r}) - I_M(\mathbf{T}(\mathbf{r})) \right]^2 \tag{B.9}$$

with P the number of points $\mathbf{r}$. Its derivative wrt. the transformation parameters can therefore be easily calculated as

$$\frac{\partial S}{\partial \boldsymbol{\mu}} = \frac{2}{P} \sum_{\mathbf{r} \in I_F} \left[I_M(\mathbf{T}(\mathbf{r})) - I_F(\mathbf{r}) \right] \cdot \frac{\partial I_M(\mathbf{T}(\mathbf{r}))}{\partial \mathbf{T}(\mathbf{r})} \cdot \frac{\partial \mathbf{T}(\mathbf{r})}{\partial \boldsymbol{\mu}} \tag{B.10}$$

where $\partial I_M(\mathbf{T}(\mathbf{r}))/\partial \mathbf{T}(\mathbf{r})$ is the moving image derivative at a mapped location $\mathbf{T}(\mathbf{r})$ which stays constant during optimization.

Smoothness penalty

The smoothness penalty associated with a certain transformation field $\mathbf{T}(\mathbf{r})$ can be computed based upon the 3D equivalent of a 2D bending energy of a thin sheet of metal [203]:

$$R = \frac{1}{P} \sum_{\mathbf{r} \in I_F} \left\| \frac{\partial^2 \mathbf{T}(\mathbf{r})}{\partial \mathbf{r} \partial \mathbf{r}^T} \right\|_F^2 \tag{B.11}$$

$$= \frac{1}{P} \sum_{\mathbf{r} \in I_F} \sum_{\xi \in (x,y,z)} \left(\frac{\partial^2 T_\xi}{\partial x^2} \right)^2 + \left(\frac{\partial^2 T_\xi}{\partial y^2} \right)^2 + \left(\frac{\partial^2 T_\xi}{\partial z^2} \right)^2 + 2 \left(\frac{\partial^2 T_\xi}{\partial x \partial y} \right)^2 + 2 \left(\frac{\partial^2 T_\xi}{\partial x \partial z} \right)^2 + 2 \left(\frac{\partial^2 T_\xi}{\partial y \partial z} \right)^2 \tag{B.12}$$

where the subscript F denotes the Frobenius norm. Its derivative wrt. the transformation parameters is estimated as

$$\frac{\partial R}{\partial \boldsymbol{\mu}} = \frac{2}{P} \sum_{\mathbf{r} \in I_F} \sum_{\xi \in (x,y,z)} \left(\frac{\partial^2 T_\xi}{\partial x^2} \right) \cdot \left(\frac{\partial}{\partial \boldsymbol{\mu}} \frac{\partial^2 T_\xi}{\partial x^2} \right) + \left(\frac{\partial^2 T_\xi}{\partial y^2} \right) \cdot \left(\frac{\partial}{\partial \boldsymbol{\mu}} \frac{\partial^2 T_\xi}{\partial y^2} \right) + \left(\frac{\partial^2 T_\xi}{\partial z^2} \right) \cdot \left(\frac{\partial}{\partial \boldsymbol{\mu}} \frac{\partial^2 T_\xi}{\partial z^2} \right) + 2 \left(\frac{\partial^2 T_\xi}{\partial x \partial y} \right) \cdot \left(\frac{\partial}{\partial \boldsymbol{\mu}} \frac{\partial^2 T_\xi}{\partial x \partial y} \right) + 2 \left(\frac{\partial^2 T_\xi}{\partial x \partial z} \right) \cdot \left(\frac{\partial}{\partial \boldsymbol{\mu}} \frac{\partial^2 T_\xi}{\partial x \partial z} \right) + 2 \left(\frac{\partial^2 T_\xi}{\partial y \partial z} \right) \cdot \left(\frac{\partial}{\partial \boldsymbol{\mu}} \frac{\partial^2 T_\xi}{\partial y \partial z} \right) \tag{B.13}$$

Volume conservation penalty

A volume conservation penalty can be used to constrain the space of allowable transformation fields $\mathbf{T}(\mathbf{r})$ by penalising relative volume changes as expressed by the determinant of the *spatial* Jacobian $\mathbf{J}$, defined as

$$\mathbf{J} = \frac{\partial \mathbf{T}(\mathbf{r})}{\partial \mathbf{r}} \tag{B.14}$$

Incompressibility can be enforced by penalising the deviation of Eq. (B.14) from unity, e.g. by adapting the formulation of [140]:

$$R = \frac{1}{P} \sum_{\mathbf{r} \in I_F} \left[\det(\mathbf{J}) - 1 \right]^2 \tag{B.15}$$

Its derivative wrt. the transformation parameters is computed as

$$\frac{\partial R}{\partial \boldsymbol{\mu}} = \frac{2}{P} \sum_{\mathbf{r} \in I_F} \left[\det(\mathbf{J}) - 1 \right] \cdot \frac{\partial \det(\mathbf{J})}{\partial \boldsymbol{\mu}} \tag{B.16}$$

B.3 Transform derivatives

The calculation of the metric values and their derivatives as described by Eqs. (B.9)–(B.16), requires B-spline transform derivatives in space or with respect to the B-spline parameters $\boldsymbol{\mu}$. While they are conceptually easy to calculate given their attractive mathematical properties [245], this task can nevertheless be daunting given the large matrices required to store these derivatives and the tedious management of the different B-spline parameters associated with each knot. The present section therefore aims to provide guidance for the interested reader.

Please note that the regularisation terms typically require first and second order *spatial* derivatives of the transformation field, i.e. the *spatial Jacobian* and *spatial Hessian*, whereas the optimization routine requires first order derivatives wrt. to the transformation parameters, i.e. the *Jacobian*. Again, formulations are presented in case of a 3D image registration problem which can easily be downscaled to 2D images if necessary by simply setting the z-components to zero. A superscript was added to the resulting transform derivative matrices to indicate their size.

Transform

Starting from the B-spline tensor product representing the displacement field defined in Eq. (B.6), and introducing the following short notations:

$$\boldsymbol{\mu}^{ijk} = [\mu_x^{ijk}, \mu_y^{ijk}, \mu_z^{ijk}] = [\mu_x^m, \mu_y^m, \mu_z^m] \tag{B.17}$$

$$b_{333}^{ijk} = \beta_x^3(\frac{x-\kappa_x^{ijk}}{\sigma_x})\beta_y^3(\frac{y-\kappa_y^{ijk}}{\sigma_y})\beta_z^3(\frac{z-\kappa_z^{ijk}}{\sigma_z}) = b_{333}^m \tag{B.18}$$

where index m was introduced to replace the running index ijk, and now runs over $m = 1..M$, with M being the total amount of parameters $\boldsymbol{\mu}$. As such, Eq. (B.6) can be rewritten in the following compact notation:

$$\mathbf{T}(\mathbf{r}) = \begin{bmatrix} T_x(\mathbf{r}) \\ T_y(\mathbf{r}) \\ T_z(\mathbf{r}) \end{bmatrix} = \begin{bmatrix} x \\ y \\ z \end{bmatrix} + \begin{bmatrix} \sum_m \mu_x^m b_{333}^m \\ \sum_m \mu_y^m b_{333}^m \\ \sum_m \mu_z^m b_{333}^m \end{bmatrix} \tag{B.19}$$

Furthermore, the following short notations for the **spatial partial derivatives** are introduced:

$$b_{233}^m = \tfrac{1}{\sigma_x}\left[\beta_x^2(\tfrac{x-\kappa_x^{ijk}}{\sigma_x}+\tfrac{1}{2}) - \beta_x^2(\tfrac{x-\kappa_x^{ijk}}{\sigma_x}-\tfrac{1}{2})\right] \cdot \beta_y^3(\tfrac{y-\kappa_y^{ijk}}{\sigma_y}) \cdot \beta_z^3(\tfrac{z-\kappa_z^{ijk}}{\sigma_z}) \tag{B.20}$$

$$b_{133}^m = \tfrac{1}{\sigma_x^2}\left[\beta_x^1(\tfrac{x-\kappa_x^{ijk}}{\sigma_x}+1) - 2\beta_x^1(\tfrac{x-\kappa_x^{ijk}}{\sigma_x}) + \beta_x^1(\tfrac{x-\kappa_x^{ijk}}{\sigma_x}-1)\right] \cdot \beta_y^3(\tfrac{y-\kappa_y^{ijk}}{\sigma_y}) \cdot \beta_z^3(\tfrac{z-\kappa_z^{ijk}}{\sigma_z}) \tag{B.21}$$

$$b_{223}^m = \tfrac{1}{\sigma_x}\tfrac{1}{\sigma_y}\left[\beta_x^2(\tfrac{x-\kappa_x^{ijk}}{\sigma_x}+\tfrac{1}{2}) - \beta_x^2(\tfrac{x-\kappa_x^{ijk}}{\sigma_x}-\tfrac{1}{2})\right] \cdot \left[\beta_y^2(\tfrac{y-\kappa_y^{ijk}}{\sigma_y}+\tfrac{1}{2}) - \beta_y^2(\tfrac{y-\kappa_y^{ijk}}{\sigma_y}-\tfrac{1}{2})\right] \cdot \beta_z^3(\tfrac{z-\kappa_z^{ijk}}{\sigma_z}) \tag{B.22}$$

with similar expressions for $b_{323}^m, b_{332}^m, b_{313}^m, b_{331}^m, b_{322}^m$ and b_{232}^m.

Please note that only a small subset S of the parameters $\boldsymbol{\mu}$ are required to calculate the **partial derivatives wrt. to the B-spline parameters**. As such, the resulting matrices will be sparse. The non-zero contributions therefore loop from $m = 1..S$.

Jacobian

$$\frac{\partial \mathbf{T}(\mathbf{r})}{\partial \boldsymbol{\mu}} = \begin{bmatrix} \frac{\partial T_x}{\partial \mu_x^1} & \cdots & \frac{\partial T_x}{\partial \mu_x^M} & \frac{\partial T_x}{\partial \mu_y^1} & \cdots & \frac{\partial T_x}{\partial \mu_y^M} & \frac{\partial T_x}{\partial \mu_z^1} & \cdots & \frac{\partial T_x}{\partial \mu_z^M} \\ \frac{\partial T_y}{\partial \mu_x^1} & \cdots & \frac{\partial T_y}{\partial \mu_x^M} & \frac{\partial T_y}{\partial \mu_y^1} & \cdots & \frac{\partial T_y}{\partial \mu_y^M} & \frac{\partial T_y}{\partial \mu_z^1} & \cdots & \frac{\partial T_y}{\partial \mu_z^M} \\ \frac{\partial T_z}{\partial \mu_x^1} & \cdots & \frac{\partial T_z}{\partial \mu_x^M} & \frac{\partial T_z}{\partial \mu_y^1} & \cdots & \frac{\partial T_z}{\partial \mu_y^M} & \frac{\partial T_z}{\partial \mu_z^1} & \cdots & \frac{\partial T_z}{\partial \mu_z^M} \end{bmatrix}^{\textbf{(3 x 3M)}} \tag{B.23}$$

Substituting Eq. (B.19) into Eq. (B.23), and taking the sparsity of the resulting matrix into account yields:

$$\frac{\partial \mathbf{T}(\mathbf{r})}{\partial \boldsymbol{\mu}} = \begin{bmatrix} b_{333}^1 & \cdots & b_{333}^S & 0 & \cdots & 0 & 0 & \cdots & 0 \\ 0 & \cdots & 0 & b_{333}^1 & \cdots & b_{333}^S & 0 & \cdots & 0 \\ 0 & \cdots & 0 & 0 & \cdots & 0 & b_{333}^1 & \cdots & b_{333}^S \end{bmatrix}^{\textbf{(3 x 3S)}} \tag{B.24}$$

Spatial Jacobian

$$\frac{\partial \mathbf{T}(\mathbf{r})}{\partial \mathbf{r}} = \begin{bmatrix} \frac{\partial T_x}{\partial x} & \frac{\partial T_x}{\partial y} & \frac{\partial T_x}{\partial z} \\ \frac{\partial T_y}{\partial x} & \frac{\partial T_y}{\partial y} & \frac{\partial T_y}{\partial z} \\ \frac{\partial T_z}{\partial x} & \frac{\partial T_z}{\partial y} & \frac{\partial T_z}{\partial z} \end{bmatrix}^{\textbf{(3x3)}} \tag{B.25}$$

Substituting Eq. (B.19) into Eq. (B.25) yields:

$$\frac{\partial \mathbf{T}(\mathbf{r})}{\partial \mathbf{r}} = \begin{bmatrix} 1 + \sum_m \mu_x^m b_{233}^m & \sum_m \mu_x^m b_{323}^m & \sum_m \mu_x^m b_{332}^m \\ \sum_m \mu_y^m b_{233}^m & 1 + \sum_m \mu_y^m b_{323}^m & \sum_m \mu_y^m b_{332}^m \\ \sum_m \mu_z^m b_{233}^m & \sum_m \mu_z^m b_{323}^m & 1 + \sum_m \mu_z^m b_{332}^m \end{bmatrix}^{\textbf{(3x3)}} \tag{B.26}$$

Jacobian of Spatial Jacobian

$$\frac{\partial}{\partial \boldsymbol{\mu}} \frac{\partial \mathbf{T}(\mathbf{r})}{\partial \mathbf{r}} = \Bigg\{ \frac{1}{\partial \mu_x^1} \frac{\partial \mathbf{T}(\mathbf{r})}{\partial \mathbf{r}}, \cdots, \frac{1}{\partial \mu_x^M} \frac{\partial \mathbf{T}(\mathbf{r})}{\partial \mathbf{r}}, \frac{1}{\partial \mu_y^1} \frac{\partial \mathbf{T}(\mathbf{r})}{\partial \mathbf{r}}, \cdots, \frac{1}{\partial \mu_y^M} \frac{\partial \mathbf{T}(\mathbf{r})}{\partial \mathbf{r}}, \frac{1}{\partial \mu_z^1} \frac{\partial \mathbf{T}(\mathbf{r})}{\partial \mathbf{r}}, \cdots, \frac{1}{\partial \mu_z^M} \frac{\partial \mathbf{T}(\mathbf{r})}{\partial \mathbf{r}} \Bigg\}^{\textbf{([3 x 3] x 3M)}} \tag{B.27}$$

Substituting Eq. (B.19) into Eq. (B.27), and taking the sparsity of the resulting matrix into account yields:

$$\frac{\partial}{\partial \boldsymbol{\mu}} \frac{\partial \mathbf{T}(\mathbf{r})}{\partial \mathbf{r}} = \Bigg\{ \begin{bmatrix} b_{233}^1 & b_{323}^1 & b_{332}^1 \\ 0 & 0 & 0 \\ 0 & 0 & 0 \end{bmatrix}, \cdots, \begin{bmatrix} b_{233}^S & b_{323}^S & b_{332}^S \\ 0 & 0 & 0 \\ 0 & 0 & 0 \end{bmatrix}, \begin{bmatrix} 0 & 0 & 0 \\ b_{233}^1 & b_{323}^1 & b_{332}^1 \\ 0 & 0 & 0 \end{bmatrix}, \cdots, \begin{bmatrix} 0 & 0 & 0 \\ b_{233}^S & b_{323}^S & b_{332}^S \\ 0 & 0 & 0 \end{bmatrix}, \begin{bmatrix} 0 & 0 & 0 \\ 0 & 0 & 0 \\ b_{233}^1 & b_{323}^1 & b_{332}^1 \end{bmatrix}, \cdots, \begin{bmatrix} 0 & 0 & 0 \\ 0 & 0 & 0 \\ b_{233}^S & b_{323}^S & b_{332}^S \end{bmatrix} \Bigg\}^{\textbf{([3 x 3] x 3S)}} \tag{B.28}$$

Spatial Hessian

$$\frac{\partial^2 \mathbf{T}(\mathbf{r})}{\partial \mathbf{r}^2} = \left\{ \begin{bmatrix} \frac{\partial^2 T_x}{\partial x^2} & \frac{\partial^2 T_x}{\partial x \partial y} & \frac{\partial^2 T_x}{\partial x \partial z} \\ \frac{\partial^2 T_x}{\partial y \partial x} & \frac{\partial^2 T_x}{\partial y^2} & \frac{\partial^2 T_x}{\partial y \partial z} \\ \frac{\partial^2 T_x}{\partial z \partial x} & \frac{\partial^2 T_x}{\partial z \partial y} & \frac{\partial^2 T_x}{\partial z^2} \end{bmatrix}, \begin{bmatrix} \frac{\partial^2 T_y}{\partial x^2} & \frac{\partial^2 T_y}{\partial x \partial y} & \frac{\partial^2 T_y}{\partial x \partial z} \\ \frac{\partial^2 T_y}{\partial y \partial x} & \frac{\partial^2 T_y}{\partial y^2} & \frac{\partial^2 T_y}{\partial y \partial z} \\ \frac{\partial^2 T_y}{\partial z \partial x} & \frac{\partial^2 T_y}{\partial z \partial y} & \frac{\partial^2 T_y}{\partial z^2} \end{bmatrix}, \begin{bmatrix} \frac{\partial^2 T_z}{\partial x^2} & \frac{\partial^2 T_z}{\partial x \partial y} & \frac{\partial^2 T_z}{\partial x \partial z} \\ \frac{\partial^2 T_z}{\partial y \partial x} & \frac{\partial^2 T_z}{\partial y^2} & \frac{\partial^2 T_z}{\partial y \partial z} \\ \frac{\partial^2 T_z}{\partial z \partial x} & \frac{\partial^2 T_z}{\partial z \partial y} & \frac{\partial^2 T_z}{\partial z^2} \end{bmatrix} \right\}^{\mathbf{(3 \times 3 \times 3)}} \tag{B.29}$$

Substituting Eq. (B.19) into Eq. (B.29) yields:

$$\frac{\partial^2 \mathbf{T}(\mathbf{r})}{\partial \mathbf{r}^2} = \left\{ \begin{bmatrix} \sum_m \mu_x^m b_{133}^m & \sum_m \mu_x^m b_{223}^m & \sum_m \mu_x^m b_{232}^m \\ \sum_m \mu_x^m b_{223}^m & \sum_m \mu_x^m b_{313}^m & \sum_m \mu_x^m b_{322}^m \\ \sum_m \mu_x^m b_{232}^m & \sum_m \mu_x^m b_{322}^m & \sum_m \mu_x^m b_{331}^m \end{bmatrix}, \begin{bmatrix} \sum_m \mu_y^m b_{133}^m & \sum_m \mu_y^m b_{223}^m & \sum_m \mu_y^m b_{232}^m \\ \sum_m \mu_y^m b_{223}^m & \sum_m \mu_y^m b_{313}^m & \sum_m \mu_y^m b_{322}^m \\ \sum_m \mu_y^m b_{232}^m & \sum_m \mu_y^m b_{322}^m & \sum_m \mu_y^m b_{331}^m \end{bmatrix}, \begin{bmatrix} \sum_m \mu_z^m b_{133}^m & \sum_m \mu_z^m b_{223}^m & \sum_m \mu_z^m b_{232}^m \\ \sum_m \mu_z^m b_{223}^m & \sum_m \mu_z^m b_{313}^m & \sum_m \mu_z^m b_{322}^m \\ \sum_m \mu_z^m b_{232}^m & \sum_m \mu_z^m b_{322}^m & \sum_m \mu_z^m b_{331}^m \end{bmatrix} \right\}^{\mathbf{(3 \times 3 \times 3)}} \tag{B.30}$$

Please note that every submatrix $\partial^2 T_\xi / \partial \mathbf{r}^2$ ($\xi \in x, y, z$) is symmetrical.

Jacobian of Spatial Hessian

$$\frac{\partial}{\partial \boldsymbol{\mu}} \frac{\partial^2 \mathbf{T}(\mathbf{r})}{\partial \mathbf{r}^2} = \Bigg\{ \frac{1}{\partial \mu_x^1} \frac{\partial^2 \mathbf{T}(\mathbf{r})}{\partial \mathbf{r}^2}, \cdots, \frac{1}{\partial \mu_x^M} \frac{\partial^2 \mathbf{T}(\mathbf{r})}{\partial \mathbf{r}^2}, \frac{1}{\partial \mu_y^1} \frac{\partial^2 \mathbf{T}(\mathbf{r})}{\partial \mathbf{r}^2}, \cdots, \frac{1}{\partial \mu_y^M} \frac{\partial^2 \mathbf{T}(\mathbf{r})}{\partial \mathbf{r}^2}, \frac{1}{\partial \mu_z^1} \frac{\partial^2 \mathbf{T}(\mathbf{r})}{\partial \mathbf{r}^2}, \cdots, \frac{1}{\partial \mu_z^M} \frac{\partial^2 \mathbf{T}(\mathbf{r})}{\partial \mathbf{r}^2} \Bigg\}^{\textbf{([3 x 3 x 3] x 3M)}} \tag{B.31}$$

Substituting Eq. (B.19) into Eq. (B.31), and taking the sparsity of the resulting matrix into account yields:

$$\begin{aligned}
\frac{\partial}{\partial \boldsymbol{\mu}} \frac{\partial^2 \mathbf{T}(\mathbf{r})}{\partial \mathbf{r}^2} = \Bigg\{ & \Bigg\{ \begin{bmatrix} b_{133}^1 & b_{223}^1 & b_{232}^1 \\ b_{223}^1 & b_{313}^1 & b_{322}^1 \\ b_{232}^1 & b_{322}^1 & b_{331}^1 \end{bmatrix}, \mathrm{O}^{(3\times3)}, \mathrm{O}^{(3\times3)} \Bigg\}, \cdots, \\
& \Bigg\{ \begin{bmatrix} b_{133}^S & b_{223}^S & b_{232}^S \\ b_{223}^S & b_{313}^S & b_{322}^S \\ b_{232}^S & b_{322}^S & b_{331}^S \end{bmatrix}, \mathrm{O}^{(3\times3)}, \mathrm{O}^{(3\times3)} \Bigg\}, \\
& \Bigg\{ \mathrm{O}^{(3\times3)}, \begin{bmatrix} b_{133}^1 & b_{223}^1 & b_{232}^1 \\ b_{223}^1 & b_{313}^1 & b_{322}^1 \\ b_{232}^1 & b_{322}^1 & b_{331}^1 \end{bmatrix}, \mathrm{O}^{(3\times3)} \Bigg\}, \cdots, \\
& \Bigg\{ \mathrm{O}^{(3\times3)}, \begin{bmatrix} b_{133}^S & b_{223}^S & b_{232}^S \\ b_{223}^S & b_{313}^S & b_{322}^S \\ b_{232}^S & b_{322}^S & b_{331}^S \end{bmatrix}, \mathrm{O}^{(3\times3)} \Bigg\}, \\
& \Bigg\{ \mathrm{O}^{(3\times3)}, \mathrm{O}^{(3\times3)}, \begin{bmatrix} b_{133}^1 & b_{223}^1 & b_{232}^1 \\ b_{223}^1 & b_{313}^1 & b_{322}^1 \\ b_{232}^1 & b_{322}^1 & b_{331}^1 \end{bmatrix} \Bigg\}, \cdots, \\
& \Bigg\{ \mathrm{O}^{(3\times3)}, \mathrm{O}^{(3\times3)}, \begin{bmatrix} b_{133}^S & b_{223}^S & b_{232}^S \\ b_{223}^S & b_{313}^S & b_{322}^S \\ b_{232}^S & b_{322}^S & b_{331}^S \end{bmatrix} \Bigg\} \Bigg\}^{\textbf{([3 x 3 x 3] x 3S)}}
\end{aligned} \tag{B.32}$$

where $\mathrm{O}^{(3\times3)}$ is a 3-by-3 null-matrix.

B.4 Implementation details

The concepts introduced in the previous sections can be implemented in numerous ways. A fair amount of publicly available ready-to-use software packages currently exists, some of them acting as black-boxes, while others being open-source, e.g. Plastimatch [213], Elastix [120], MIRT - Medical Image Registration Toolbox for Matlab [174], IRTK - Image Registration Toolkit [202], NiftyReg [164], medInria [103], ... Some of these implementations use the C++ libraries of ITK [266] as a foundation to perform image registration. These libraries are attractive due to their open-source model, good performance properties, and modular design. It also implies that the basic functionalities (such as memory allocation and class design) are thoroughly tested on a daily basis and therefore form a solid framework to build further upon. However, it is important to note that, while ITK already provides a variety of classes performing basic image processing tasks, the user still remains responsible to link these classes, and to implement the desired additional functionalities to built a robust application.

In order to remain flexible, gain thorough insight into image registration tasks, and have full access and control over the design of the algorithm, it was decided to build a custom-made software package for estimating cardiac motion from US sequences. For this purpose, a combination of 'vanilla' ITK classes (version 3.20), ITK classes found within elastix (version 4.4) and new classes, were merged. The goal of this section is not meant to provide an exhaustive guide of the implemented classes, but to describe the architecture from a broad perspective and highlight its non-trivial implementation nature.

In practice, the software was separated into two layers. The bottom layer consists of individual C++ classes which are responsible for the basic tasks within a registration framework (e.g. calculating the image similarity between two images using for example the sum-of-squared differences, interpolating an image, generating an image mask, reading or writing an image, ...). These classes are found within the modules shown in Fig. B.1, and often require setting a number of parameters (e.g. the number of resolutions and the final grid size of the B-spline transform, the penalty weight, the stop conditions for the optimizer, ...). These parameters can be read from a file or parsed through the command line at run-time. However, it is important to note that ITK uses an advanced inheritance class system which is heavily templated by nature. While this allows the code to be highly efficient, this also implies that template parameters (such as the image dimension, pixel type, B-spline order) cannot be determined at run-time. Furthermore, exchanging the class responsible for the task of a certain module is also not possible at run-time, e.g. switching the bending energy penalty for a volume conservation penalty, or adding cyclicity to

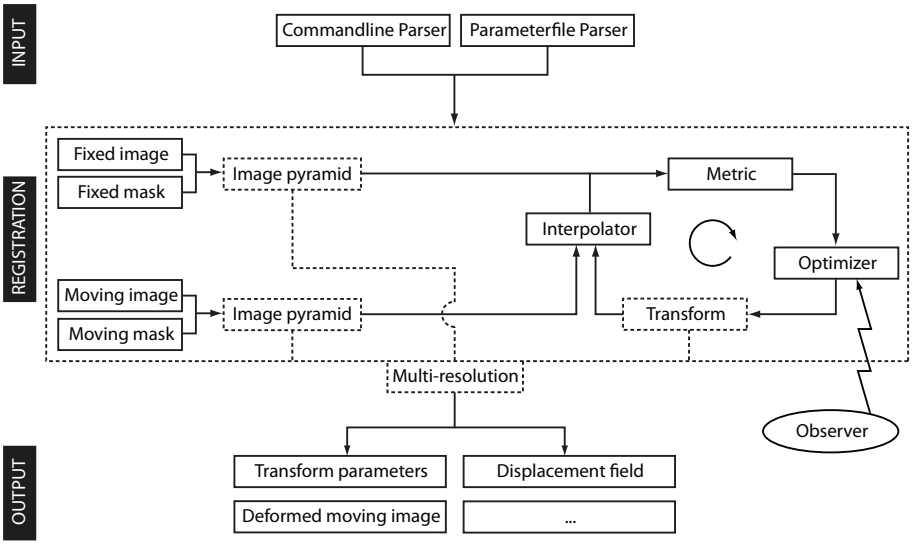

Figure B.1: Image registration framework for cardiac motion estimation using ITK modules. Arrows indicate how the top layer of the software connects the modules of the basic layer (rectangles). Dotted lines refer to those modules which play a role when following a multi-resolution image registration strategy.

a certain direction of the B-spline transform (see the circumferential direction in the AFFD model). A naive implementation would require recompiling the code for these scenarios.

In order to solve these issues, a second layer was added. This top layer is responsible for instantiating the correct components in every module and assigning the correct parameter values based on the input from a file, connecting all the modules (see Fig. B.1), and controlling input and output (e.g. parsing the correct filenames, writing the output as a displacement field or as a deformed moving image, print optimizer output, ...).

While the usage of this framework is not limited to US-based cardiac motion estimation, the next overview will only focus on the specifics within the context of the CFFD and AFFD model.

Multi-resolution strategy In order to speed up the registration and increase the convergence rate it is common practice to adopt a multi-resolution strategy. This can be done by either reducing the transform complexity and/or the image complexity. In general, 3 to 4 resolution stages were used for the FFD model, halving the B-spline grid in every stage, typically leading to a final grid spacing of approximately 2–4 mm (depending on the application and the image resolution). In order to reduce image complexity during image registration, a smoothing pyramid (generated by applying a Gaussian filter with an increasing variance), a shrinking pyramid (generated by increasing the amount of data subsampling), or a combination of both can be used. Typically, the number of levels within the pyramid was the same as the number of resolutions in the FFD model. The image pyramids were generated based on a power of 2 of the resolution level s (with level 1 being the finest level), e.g. for the shrinking pyramid the subsampling factor was $2^{(s-1)}$, and the variance of the Gaussian filter in the smoothing pyramid was $(2^{(s-1)}/2)^2$.

Image masks In order to assure that voxels outside the US sector scan did not contribute to the cost function, a simple threshold filter was applied on the fixed and moving image before image registration.

Transform The transform module uses the parameters parsed by the optimizer to deform the moving image and calculates the transform derivatives described in appendix B.3. It also takes care of the necessary functionalities to upsample the B-spline grids in the next resolution scale, or to define a cyclic B-spline transform in a certain direction, i.e. the adaptation of the local B-spline neighborhood near the borders and centering the B-spline grid as described in section 9.2.1. Third-order B-splines were used in the CFFD and AFFD model.

Interpolator In order to create the deformed moving image during the metric calculations, points are generally mapped to a non-grid position and image intensities therefore have to be interpolated. A linear interpolation scheme was used as this forms a good trade-off between computation time and accuracy.

Metric This module takes care of the actual calculation of the cost function and its derivative with respect to the transform parameters. The cost function can consist of any weighted combination of SSD, MI, the bending energy penalty and/or the volume conservation penalty. The tuning of the weights and the choice of these terms is motivated throughout the chapters of this thesis. The bending energy penalty was computed everywhere, regardless of the image masks, to ensure a smooth motion field when myocoardial segments would move in and outside the sector scan during the cardiac cycle.

Optimizer A limited-memory Broyden-Fletcher-Goldfarb-Shanno bound constrained optimizer was used [36]. Typically, the optimizer was allowed to run up to 200 iterations and a cost convergence tolerance of 1E-4 was used. An observer was also linked to the optimizer in order to track the progress of the registration, i.e. printing the current resolution and iteration, metric value and derivative, ...

Bibliography

[1] M. Alessandrini, A. Basarab, H. Liebgott, and O. Bernard. Myocardial motion estimation from medical images using the monogenic signal. *IEEE Trans Image Process*, 22(3):1084–1095, 2013.

[2] M. Alessandrini, H. Liebgott, D. Barbosa, and O. Bernard. Monogenic phase based optical flow computation for myocardial motion analysis in 3D echocardiography. In *STACOM - Statistical atlases and computational models of the heart*, volume 7746 of Lecture Notes in Computer Science, pages 159–168, 2012.

[3] M. Alessandrini, H. Liebgott, D. Friboulet, and O. Bernard. Simulation of realistic echocardiographic sequences for ground-truth validation of motion estimation. In *ICIP - International Conference on Image Processing*, 2012.

[4] B. Amundsen, T. Helle-Valle, T. Edvardsen, H. Torp, J. Crosby, E. Lyseggen, A. Stoylen, H. Ihlen, J. Lima, O. Smiseth, and S. Slordahl. Noninvasive myocardial strain measurement by speckle tracking echocardiography: validation against sonomicrometry and tagged magnetic resonance imaging. *J Am Coll Cardiol*, 47(4):789–793, 2006.

[5] E. Angelini and O. Gerard. Review of myocardial motion estimation methods from optical flow tracking on ultrasound data. In *28th IEEE EMBS Annual Int Conf*, pages 1537–1540, 2006.

[6] E. Angelini, A. Laine, S. Takuma, J. Holmes, and S. Homma. LV volume quantifiaction via spatiotemporal analysis of real-time 3-D echocardiography. *IEEE Trans Med Imaging*, 20:457–469, 2001.

[7] G. Angelini, G. Fraser, M. Koning, J. Smyllie, W. Hop, G. Sutherland, and P. Verdouw. Adverse hemodynamic effects and echocardiographic consequences of pericardial closure soon after sternotomy and pericardiotomy. *Circulation*, 82(5 Suppl):397–406, 1990.

[8] M. Ashraf, X. Li, Y. M, A. Jensen, J. Pemberton, L. Hui, P. Lysyansky, Z. Friedman, B. Park, and D. Sahn. Delineation of cardiac twist by a sonographically based 2-dimensional strain analysis method. *J Ultrasound Med*, 25(9):1193–1198, 2006.

[9] N. Bachner-Hinenzon, O. Ertracht, M. Lysiansky, O. Binah, and D. Adam. Layer-specific assessment of left ventricular function by utilizing wavelet denoising: a validation study. *Med Biol Eng Comput*, 49(1):3–13, 2011.

[10] M. Bansal, G. Cho, J. Chan, R. Leano, B. Haluska, and T. Marwick. Feasibility and accuracy of different techniques of two-dimensional speckle based strain and validation with harmonic phase magnetic resonance imaging. *J Am Soc Echocardiogr*, 21(12):1318–1325, 2008.

[11] M. Bansal, L. Jeffriess, R. Leano, J. Mundy, and T. Marwick. Assessment of myocardial viability at dobutamine echocardiography by deformation analysis using tissue velocity and speckle-tracking. *J Am Coll Cardiol: Cardiovasc Imaging*, 3(2):121–131, 2010.

[12] P. Baraldi, A. Sarti, C. Lamberti, A. Prandini, and F. Sgallari. Evaluation of differential optical flow techniques on synthesized echo images. *IEEE Trans Biomed Eng*, 43(3):259–272, 1996.

[13] D. Barbosa. 3D cardiac strain estimation based on non-rigid registration: optimization for in-vivo application. Master's thesis, KU Leuven, 2009.

[14] D. Barbosa, O. Bernard, O. Savu, T. Dietenbeck, B. Heyde, P. Claus, D. Friboulet, and J. D'hooge. Coupled B-spline active geometric functions for myocardial segmentation: a localized region-based approach. In *IEEE Int Ultrasonics Symposium*, pages 1648–1651, 2010.

[15] D. Barbosa, T. Dietenbeck, B. Heyde, H. Houle, D. Friboulet, J. D'hooge, and O. Bernard. Fast and fully automatic 3-D echocardiographic segmentation using B-spline explicit active surfaces: feasibility study and validation in a clinical setting. *Ultrasound Med Biol*, 39(1):89–101, 2013.

[16] D. Barbosa, T. Dietenbeck, J. Schraerer, J. D'hooge, D. Friboulet, and O. Bernard. B-spline explicit active surfaces: an efficient framework for real-time 3-D region-based segmentation. *IEEE Trans Image Process*, 21(1):241–251, 2012.

[17] D. Barbosa, B. Heyde, T. Dietenbeck, D. Friboulet, J. D'hooge, and O. Bernard. Fast left ventricle tracking in 3D echocardiographic data using anatomical affine optical flow. In *FIMH - Functional Imaging and Modeling of the Heart*, volume LNCS 7945, pages 191–199, London, UK, 20-22 June 2013.

[18] D. Barbosa, G. Kiss, P. Claus, K. Hristova, B. Amundsen, D. Loeckx, F. Orderud, H. Torp, and J. D'hooge. A comparison between methods for automatic quantification of global left ventricular function. In *IEEE Int Ultrasonics Symposium*, pages 313–316, 2009.

[19] D. Barbosa, H. Krasimira, D. Loeckx, F. Rademakers, P. Claus, and J. D'hooge. 3D motion and strain estimation of the heart: initial clinical findings. In *SPIE Med Imaging*, volume 7629, pages 4–9, 2010.

[20] J. Barron, D. Fleet, and S. Beauchemin. Performance of optical flow techniques. *Int J Comput Vision*, 12(1):43–77, 1994.

[21] M. Becker, R. Hoffmann, H. Kuhl, H. Grawe, M. Katoh, R. Kramann, A. Bucker, P. Hanrath, and N. Heussen. Analysis of myocardial deformation

based on ultrasonic pixel tracking to determine transmurality in chronic myocardial infarction. *Eur Heart J*, 27(21):2560–2566, 2006.

[22] V. Behar, D. Adam, P. Lysyansky, and Z. Friedman. Improving motion estimation by accounting for local image distortion. *Ultrasonics*, 43(1):57–65, 2004.

[23] M. Belohlavek, V. Bartleson, and M. Zobitz. Real-time strain rate imaging: validation of peak compression and expansion rates by a tissue-mimicking phantom. *Echocardiography*, 18(7):565–571, 2001.

[24] J. Bernard, P. Wouters, M. Doursout, B. Florence, J. Chelly, and R. Merin. Effects of sevoflurane and isoflurane on cardiac and coronary dynamics in chronically instrumented dogs. *Anesthesiology*, 72(4):659–662, 1990.

[25] B. Bijnens, P. Claus, F. Weidemann, J. Strotmann, and G. Sutherland. Investigating cardiac function using motion and deformation analysis in the setting of a coronary artery disease. *Circulation*, 116(21):2453–2464, 2007.

[26] A. Bistoquet, J. Oshinski, and O. Skrinjar. Myocardial deformation recovery from cine MRI using a nearly incompressible biventricular model. *Med Image Analysis*, 12(1):69–85, 2008.

[27] S. Bjaerum, H. Torp, and K. Kristoffersen. High frame rate tissue Doppler imaging. In *IEEE Int Ultrasonics Symposium*, pages 1417–1421, 2001.

[28] J. Bogaert and F. Rademakers. Regional nonuniformity of normal adult human left ventricle. *Am J Physiol Heart Circ Physiol*, 280(2):H610–H620, 2001.

[29] L. Bohs and G. Trahey. A novel method for angle independent ultrasonic imaging of blood flow and tissue motion. *IEEE Trans Biomed Eng*, 38(3):280–286, 1991.

[30] J. Bosch, S. Mitchell, B. Lelieveldt, F. Nijland, O. Kamp, M. Sonka, and J. Reiber. Automatic segmentation of echocardiographic sequences by active appearance motion models. *IEEE Trans Med Imaging*, 21(11):1374–1383, 2002.

[31] D. Boukerroui, A. Noble, and M. Brady. Velocity estimation in ultrasound images: a block matching approach. In *IPMI - Information Processing in Medical Imaging*, volume 18, pages 586–598, 2003.

[32] A. Bowman and S. Kovác. Assessment and consequences of the constant-volume attribute of the four-chambered heart. *Am J Physiol Heart Circ Physiol*, 285(5):H2027–H2033, 2003.

[33] M. Buhmann. Radial basis functions. *Acta Numerica*, 9:1–38, 2000.

[34] N. Bylund. *Spatio-temporal filtering of ultrasound image sequences*. PhD thesis, Linköping University, 2004.

[35] B. Byram, G. Holley, D. Giannantonio, and G. Trahey. 3-D phantom and in vivo cardiac speckle tracking using a matrix array and raw echo data. *IEEE Trans Ultrason Ferroelectr Freq Control*, 57(4):839–854, 2010.

[36] R. Byrd, P. Lu, J. Nocedal, and C. Zhu. A limited memory algorithm for bound constrained optimization. *SIAM Journal on Scientific Computing*, 16(5):1190–1208, 1995.

[37] M. Cerqueira, N. Weissman, V. Dilsizian, A. Jacobs, S. Kaul, W. Laskey, D. Pennell, J. Rumberger, T. Ryan, and V. Mario. Standardized myocardial segmentation and nomenclature for tomographic imaging of the heart. *Circulation*, 105(4):539–542, 2002.

[38] I. Céspedes, Y. Huang, J. Ophir, and S. Spratt. Methods for estimation of subsample time delays of digitized echo signals. *Ultrason Imaging*, 17(2):142–171, 1995.

[39] V. Chalana, D. Linker, D. Haynor, and Y. Kim. A multiple active contour model for cardiac boundary detection on echocardiographic sequences. *IEEE Trans Med Imaging*, 15(3):290–298, 1996.

[40] J. Chan, L. Hanekom, C. Wong, R. Leano, G.-Y. Cho, and T. Marwick. Differentation of subendocardial and transmural infarction using two-dimensional strain rate imaging to assess short-axis and long-axis myocardial function. *J Am Coll Cardiol*, 48(10):2026–2033, 2006.

[41] R. Chandrashekara, R. Mohiaddin, and D. Rueckert. Analysis of myocardial motion and strain patterns using a cylindrical B-spline transformation model. In *IS4TM - International Symposium on Surgery Simulation and Soft Tissue Modelling*, volume 2673 of Lecture Notes in Computer Science, pages 88–99, 2003.

[42] R. Chandrashekara, R. Mohiaddin, and D. Rueckert. Analysis of 3-D myocardial motion in tagged mr images using nonrigid image registration. *IEEE Trans Med Imaging*, 23(10):1245–1250, 2004.

[43] X. Chen, H. Xie, R. Erkamp, K. Kim, C. Jia, J. Rubin, and M. O'Donnell. 3-D correlation-based speckle tracking. *Ultrason Imaging*, 27(1):21–36, 2005.

[44] Y. Chunke, K. Terada, and S. Oe. Motion analysis of echocardiograph using optical flow method. In *IEEE Int. Conf. Systems, Man and Cybernetics*, volume 1, pages 672–677, 1996.

[45] P. Claus, H. Choi, J. D'hooge, and F. Rademakers. On the calculation of principle curvatures of the left-ventricular surfaces. In *IEEE Engineering in Medicine and Biology Society Conference*, pages 961–964, 2008.

[46] B. Cohen and I. Dinstein. New maximum likelihood motion estimation schemes for noisy ultrasound images. *Pattern Recogn*, 35(2):455–463, 2002.

[47] C. Compas, E. Wong, X. Huang, S. Sampath, B. Lin, X. Papademetris, K. Thiele, D. Dione, A. Sinusas, M. O'Donnell, and J. Duncan. A combined shape tracking and speckle tracking approach for 4D deformation analysis in echocardiography. In *ISBI - International Symposium on Biomedical Imaging*, pages 458–461, 2012.

[48] G. Constantine, K. Shan, S. Flamm, and M. Sivananthan. Role of MRI in clinical cardiology. *Lancet*, 363(9427):2162–2171, 2004.

[49] S. Cournane, L. Cannon, J. Browne, and A. Fagan. Assessment of the accuracy of an ultrasound elastography liver scanning system using a pva-cryogel phantom with optimal acoustic and mechanical properties. *Phys Med Biol*, 55(19):5965–5983, 2010.

[50] J. Crosby, B. Amundsen, T. Hergum, E. Remme, S. Langeland, and H. Torp. 3-D speckle tracking for assessment of regional left ventricular function. *Ultrasound Med Biol*, 35(3):458–471, 2009.

[51] E. D'Agostino, F. Maes, D. Vandermeulen, and P. Suetens. A viscous fluid model for multimodal non-rigid image registration using mutual information. *Med Image Analysis*, 7(4):565–575, 2003.

[52] M. Dandel. Echocardiographic strain and strain rate imaging - clinical applications. *Int J Cardiol*, 132(1):11–24, 2009.

[53] M. De Craene, P. Allain, H. Gao, A. Prakosa, S. Marchesseau, O. Somphone, L. Hilpert, A. Manrique, H. Delingette, S. Makram-Ebeid, N. Villain, J. D'hooge, M. Sermesant, and E. Saloux. Computational and physical phantom setups for the second cardiac motion analysis challenge (cMAC2). In *STACOM - Statistical atlases and computational models of the heart*, volume 7746 of Lecture Notes in Computer Science, pages 125–133, 2012.

[54] M. De Craene, S. Marchesseau, B. Heyde, H. Gao, M. Alessandrini, O. Bernard, G. Piella, A. Porras, E. Saloux, L. Tautz, A. Hennemuth, A. Prakosa, H. Liebgott, O. Somphone, P. Allain, S. Makram-Ebeid, H. Delingette, M. Sermesant, and J. D'hooge. 3D strain assessment in ultrasound (straus): A synthetic comparison of five tracking methodologies. *IEEE Trans Med Imaging*, 32(9):1632–1646, 2013.

[55] M. De Craene, G. Piella, O. Camara, N. Duchateau, E. Silva, A. Doltra, J. D'hooge, J. Brugada, M. Sitges, and A. Frangi. Temporal diffeomorphic free-form deformation: application to motion and strain estimation from 3D echocardiography. *Med Image Analysis*, 16(2):427–450, 2012.

[56] M. De Craene, G. Piella, N. Duchateau, E. Silva, A. Doltra, H. Gao, J. D'hooge, O. Camara, J. Brugada, M. Sitges, and A. Frangi. Temporal diffeomorphic free-form deformation for strain quantification in 3D-US images. In *MICCAI - Medical Image Computing and Computer-Assisted Intervention*, volume 6362 of Lecture Notes in Computer Science, pages 1–8, 2010.

[57] X. Deng and T. Denney. Three-dimensional myocardial strain reconstruction from tagged MRI using a cylindrical B-spline model. *IEEE Trans Med Imaging*, 23(7):861–867, 2004.

[58] J. Dennis and J. More. Quasi-Newtonian methods, motivation and theory. *SIAM Review*, 19(1):46–89, 1977.

[59] J. D'hooge, B. Bijnens, J. Thoen, F. Van de Werf, G. Sutherland, and P. Suetens. Echocardiographic strain and strain-rate imaging: a new tool to study regional myocardial function. *IEEE Trans Med Imaging*, 21(9):1022–1030, 2002.

[60] J. D'hooge, A. Heimdal, F. Jamal, T. Kukulski, B. Bijnens, F. Rademakers, L. Hatle, P. Suetens, and G. Sutherland. Regional strain and strain rate measurements by cardiac ultrasound: principles, implementation and limitations. *Eur J Echocardiogr*, 1(3):154–170, 2000.

[61] DOPPLER-CIP European multi-center clinical study: Determining Optimal non-invasive Parameters for the Prediction of Left vEntricular

morphologic and functional Remodelling in Chronic Ischemic Patients. http://www.dopplercip.be/.

[62] Q. Duan, E. Angelini, S. Herz, C. Ingrassia, K. Costa, J. Holmes, S. Homma, and A. Laine. Region-based endocardium tracking on real-time three-dimensional ultrasound. *Ultrasound Med Biol*, 35(2):256–265, 2009.

[63] Q. Duan, E. Angelini, S. Herz, C. Ingrassia, O. Gerard, K. Costa, J. Holmes, S. Homma, and A. Laine. Dynamic cardiac information from optical flow using four dimensional ultrasound. In *EMBS - Engineering in Medicine and Biology Society*, pages 4465–4468, 2005.

[64] Q. Duan, K. Parker, A. Lorsakul, E. Angelini, E. Hyodo, S. Homma, J. Holmes, and A. Laine. Quantitative validation of optical flow based myocardial strain measures using sonomicrometry. In *ISBI - International Symposium on Biomedical Imaging*, pages 454–457, 2009.

[65] N. Duchateau, A. Doltra, E. Silva, M. De Craene, G. Piella, M. Castel, L. Mont, J. Brugada, A. Frangi, and M. Sitges. Atlas-based quantification of myocardial motion abnormalities: added-value for understanding the effect of cardiac resynchronization therapy. *Ultrasound Med Biol*, 38(12):2186–2197, 2012.

[66] T. Edvardsen, B. Gerber, J. Garot, D. Bluemke, J. Lima, and O. Smiseth. Quantitative assessment of intrinsic regional myocardial deformation by doppler strain rate echocardiography in humans: validation against three-dimensional tagged magnetic resonance imaging. *Circulation*, 106(1):50–56, 2002.

[67] A. Elen, H. Choi, D. Loeckx, H. Gao, P. Claus, P. Suetens, F. Maes, and J. D'hooge. 3D cardiac strain estimation using spatio-temporal elastic registration of ultrasound images: a feasibility study. *IEEE Trans Med Imaging*, 27(11):1580–1591, 2008.

[68] A. Elen, D. Loeckx, H. Choi, H. Gao, P. Claus, F. Maes, S. P, and J. D'hooge. Estimation of 3D cardiac deformation using spatio-temporal elastic registration of non-scanconverted ultrasound data. In *SPIE Med Imaging*, volume 6920, pages 0R1–0R9, San Diego, USA, 17-21 February 2008.

[69] A. Fenster, D. Downey, and H. Cardinal. Three-dimensional ultrasound imaging. *Phys Med Biol*, 46(5):R67–R99, 2001.

[70] V. Ferferieva, P. Claus, B. Heyde, F. Rademakers, and J. D'hooge. Early left ventricular remodeling in a rat model of chronic myocardial infarction. In *EuroEcho*, Budapest, Hungary, 7-10 December 2011. poster presentation.

[71] D. Fleming, X. Xia, W. McDicken, G. Sutherland, and L. Fenn. Myocardial velocity gradients detected by doppler imaging. *Br J Radiol*, 67(799):679–688, 1994.

[72] A. Frangi, W. Niessen, and M. Viergever. Three-dimensional modeling for functional analysis of cardiac images: a review. *IEEE Trans Med Imaging*, 20(1):2–25, 2001.

[73] B. Friemel, L. Bohs, and G. Trahey. Relative performance of two-dimensional speckle tracking techniques: normalized correlation, non-normalized correlation and sum-absolute-difference. In *IEEE Int Ultrasonics Symposium*, pages 1481–1484, 1995.

[74] F. Fromageau, E. Brusseau, G. Vray D, Giminez, and P. Delechartre. Characterization of PVA cryogel for intravascular ultrasound elasticity imaging. *IEEE Trans Ultrason Ferroelectr Freq Control*, 50(10):1318–1323, 2003.

[75] J. Ganame, P. Claus, B. Eyskens, A. Uyttebroeck, M. Renard, J. D'hooge, M. Gewillig, B. Bijnens, G. Sutherland, and L. Mertens. Acute cardiac functional and morphological changes after Anthracycline infusions in children. *Am J Cardiol*, 99(7):974–977, 2007.

[76] H. Gao, H. Choi, P. Claus, S. Boonen, S. Jaecques, G. Van Lenthe, G. Van Der Perre, W. Lauriks, and J. D'hooge. A fast convolution-based methodology to simulate 2-D/3-D cardiac ultrasound images. *IEEE Trans Ultrason Ferroelectr Freq Control*, 56(2):404–409, 2009.

[77] E. Gayat, H. Ahmad, L. Weinert, R. Lang, and V. Mor-Avi. Reproducibility and inter-vendor variability of left ventricular deformation measurements by three-dimensional speckle-tracking echocardiography. *J Am Soc Echocardiogr*, 24(8):878–885, 2011.

[78] B. Glocker, N. Paragios, N. Komodakis, G. Tziritas, and N. Navab. Inter and intra-modal deformable registration: continuous deformations meet efficient optimal linear programming. In *IPMI - Information Processing in Medical Imaging*, volume 20, pages 408–420, 2007.

[79] R. Goldman. Curvature formulas for implicit curves and surfaces. *Comp Aided Geom Design*, 22(7):632–658, 2005.

[80] J. Gorcsan, D. Strum, W. Mandarino, V. Gulati, and M. Pinsky. Quantitative assessment of alterations in regional left ventricular contractitlity with color-coded tissue doppler echocardiography. *Circulation*, 95:2423–2433, 1997.

[81] B. Guth, R. Savage, F. White, A. Hagan, L. Samtoy, and C. Bloor. Detection of ischemic wall dysfunction - comparison between m-mode echocardiography and sonomicrometry. *Am Heart J*, 107(3):449–457, 1984.

[82] E. Haber and J. Modersitzki. Numerical methods for volume preserving image registration. *Inverse problems*, 20(5):1621–1638, 2004.

[83] L. Hanekom, C. Jenkins, L. Jeffries, C. Case, J. Mundy, C. Hawley, and T. Marwick. Incremental value of strain rate analysis as an adjunct to wall-motion scoring for assessment of myocardial viability by dobutamine echocardiography: a follow-up study after revascularization. *Circulation*, 112(25):3892–3900, 2005.

[84] J. Hansegård, S. Urheim, K. Lunde, S. Malm, and S. Rabben. Semi-automated quantification of left ventricular volumes and ejection fraction by real-time three-dimensional echocardiography. *Cardiovascular Ultrasound*, 7:18, 2009.

[85] A. Heimdal. 4D strain: advanced research application for quantitative echocardiography. Technical report, GE Healthcare, 2011.

[86] A. Heimdal, A. Stoylen, H. Torp, and T. Skjaerpe. Real-time strain rate imaging of the left ventricle by ultrasound. *J Am Soc Echocardiogr*, 11(11):1013–1019, 1998.

[87] T. Helle-Valle, J. Crosby, T. Edvardsen, E. Lyseggen, B. Amundsen, H.-J. Smith, B. Rosen, J. Lima, H. Torp, H. Ihlen, and O. Smiseth. New noninvasive method for assessment of left ventricular rotation: speckle tracking echocardiography. *Circulation*, 112(20):3149–3156, 2005.

[88] B. Heyde, D. Barbosa, P. Claus, F. Maes, and J. D'hooge. Three-dimensional cardiac motion estimation based on non-rigid image registration using a novel transformation model adapted to the heart. In *STACOM - Statistical Atlases and Computational Models of the Heart*, volume 7746 of Lecture Notes in Computer Science, pages 142–150, 2012.

[89] B. Heyde, D. Barbosa, P. Claus, F. Maes, and J. D'hooge. Influence of the grid topology of free-form deformation models on the performance of 3D strain estimation in echocardiography. In *FIMH - Functional Imaging and Modeling of the Heart*, volume LNCS 7945, pages 308–315, London, UK, 20-22 June 2013.

[90] B. Heyde, D. Barbosa, A. Daraban, R. Jasaityte, P. Claus, F. Maes, and J. D'hooge. An automated pipeline for regional strain estimation from volumetric ultrasound data. In *IEEE Int Ultrasonics Symposium*, Prague, Czech Republic, 21-25 July 2013. [In press].

[91] B. Heyde, D. Barbosa, R. Jasaityte, S. Bouchez, P. Wouters, F. Maes, P. Claus, and J. D'hooge. Three-dimensional myocardial strain estimation from volumetric ultrasound data using a novel transformation model adapted to the heart. In *IEEE Int Ultrasonics Symposium*, pages 1086–1089, Dresden, Germany, 7-10 October 2012.

[92] B. Heyde, S. Bouchez, S. Thieren, M. Vandenheuvel, R. Jasaityte, D. Barbosa, P. Claus, F. Maes, P. Wouters, and J. D'hooge. Elastic image registration to quantify 3D regional myocardial deformation from volumetric ultrasound: Experimental validation in an animal model. *Ultrasound Med Biol*, 39(9):1688–1697, 2013.

[93] B. Heyde, P. Claus, R. Jasaityte, D. Barbosa, S. Bouchez, M. Vandenheuvel, P. Wouters, F. Maes, and J. D'hooge. Motion and deformation estimation of cardiac ultrasound sequences using an anatomical B-spline transformation model. In *ISBI - International Symposium on Biomedical Imaging*, pages 266–269, Barcelona, Spain, 2-5 May 2012.

[94] B. Heyde, S. Cygan, H. Choi, B. Lesniak-Plewinska, D. Barbosa, A. Elen, P. Claus, D. Loeckx, K. Kaluzynski, and J. D'hooge. Regional cardiac motion and strain estimation in three-dimensional echocardiography: A validation study in thick-walled univentricular phantoms. *IEEE Trans Ultrason Ferroelectr Freq Control*, 59(4):668–682, 2012.

[95] B. Heyde, R. Jasaityte, D. Barbosa, V. Robesyn, S. Bouchez, P. Wouters, F. Maes, P. Claus, and J. D'hooge. Elastic image registration versus speckle tracking for 2D myocardial motion estimation: a direct comparison in-vivo. *IEEE Trans Med Imaging*, 32(2):449–459, 2013.

[96] B. Heyde, R. Jasaityte, S. Bouchez, M. Vandenheuvel, D. Loeckx, P. Claus, P. Wouters, and J. D'hooge. Three-dimensional myocardial strain estimation

from volumetric ultrasound: experimental validation in an animal model. In *IEEE Int Ultrasonics Symposium*, pages 1862–1865, Orlando, USA, 18-21 October 2011.

[97] E. Hoffman and R. E. Invariant total heart volume in the intact thorax. *Am J Physiol*, 249(4 Pt 2):H883–H890, 1985.

[98] R. Hoffmann, H. Lethen, T. Marwick, M. Arnese, P. Fioretti, A. Pingitore, E. Picano, T. Buck, R. Erbel, F. Flachskampf, and P. Hanrath. Analysis of interinstitutional observer agreement in interpretation of dobutamine stress echocardiograms. *J Am Coll Cardiol*, 27(2):330–336, 1996.

[99] M. Holden. A review of geometric transformations for nonrigid body registration. *IEEE Trans Med Imaging*, 27(1):111–128, 2008.

[100] B. Horn and B. Schunck. Determining optical flow. *Artif Intell*, 17(1-3):185–203, 1981.

[101] H. Hurlburt, G. Aurigemma, J. Hill, A. Narayanan, W. Gaasch, C. Vinch, T. Meyer, D. Phil, and D. Tighe. Direct ultrasound measurement of longitudinal, circumferential, and radial strain using 2-dimensional strain imaging in normal adults. *Echocardiography*, 24(7):723–731, 2007.

[102] C. Ingul, E. Rozis, S. Slordahl, and T. Marwick. Incremental value of strain rate imaging to wall motion analysis for prediction of outcome in patients undergoing dobutamine stress echocardiography. *Circulation*, 115(10):1252–1259, 2007.

[103] Inria (Asclepios, Athena, Parietal and Visages), Software package: medInria 2. `http://med.inria.fr/`.

[104] G. Jacob, A. Noble, C. Behrenbruch, A. Kelion, and A. Banning. A shape-space-based approach to tracking myocardial borders and quantifying regional left-ventricular function applied in echocardiography. *IEEE Trans Med Imaging*, 21(3):226–238, 2002.

[105] L. Jacobs, I. Salgo, S. Goonewardena, L. Weinert, P. Coon, D. Bardo, O. Gerard, P. Allain, J. Zamorano, L. de Isla, V. Mor-Avi, and R. Lang. Rapid online quantification of left ventricular volume from real-time three-dimensional echocardiographic data. *Eur Heart J*, 27(4):460–468, 2006.

[106] F. Jamal, C. Bergerot, L. Argaud, J. Loufouat, and M. Ovize. Longitudinal strain quantitates regional right ventricular contractile function. *Am J Physiol Heart Circ Physiol*, 285(6):H2842–H2847, 2003.

[107] R. Jasaityte, J. D'hooge, L. Herbots, A. Daraban, and F. Rademakers. Consistent regional heterogeneity of passive diastolic stretch and systolic deformation in the healthy heart: age-related changes in left ventricle contractility. *Ultrasound Med Biol*, 2013. In press: 10.1016/j.ultrasmedbio.2013.09.005.

[108] R. Jasaityte, B. Heyde, and J. D'hooge. Current state of three-dimensional myocardial strain estimation using echocardiography. *J Am Soc Echocardiogr*, 26(1):15–28, 2013.

[109] R. Jasaityte, B. Heyde, V. Ferferieva, B. Amundsen, D. Barbosa, D. Loeckx, G. Kiss, F. Orderud, P. Claus, H. Torp, and J. D'hooge. Comparison of a

new methodology for the assessment of 3D myocardial strain from volumetric ultrasound with 2D speckle tracking. *Int J Cardiovascular Imaging*, 28(5):1049–1060, 2012.

[110] C. Jenkins, K. Bricknell, L. Hanekom, and T. Marwick. Reproducibility and accuracy of echocardiographic measurements of left ventricular parameters using real-time three-dimensional echocardiography. *J Am Coll Cardiol*, 44(4):878–886, 2004.

[111] J. Jensen. *Estimation of blood velocities using ultrasound*. Cambridge University Press, 1996.

[112] F. Kallel and J. Ophir. A least-squares strain estimator for elastography. *Ultrason Imaging*, 19(3):195–208, 1997.

[113] K. Kaluzynski, X. Chen, S. Emelianov, A. Skovoroda, and M. Donnell. Strain rate imaging using two-dimensional speckle tracking. *IEEE Trans Ultrason Ferroelectr Freq Control*, 48(4):1111–1123, 2001.

[114] H. Kanai, H. Hasegawa, N. Chubachi, Y. Koiwa, and M. Tanaka. Noninvasive evaluation of local myocardial thickening and its color-coded imaging. *IEEE Trans Ultrason Ferroelectr Freq Control*, 44(4):752–768, 1997.

[115] K. Khairy and J. Howard. Spherical harmonics-based parametric deconvolution of 3D surface images using bending energy minimization. *Med Image Analysis*, 12(2):217–227, 2008.

[116] G. Kiss, E. Nielsen, F. Orderud, and H. Torp. Performance optimization of block matching in 3D echocardiography. In *IEEE Int Ultrasonics Symposium*, pages 1403–1406, 2009.

[117] S. Kleijn, M. Aly, C. Terwee, A. van Rossum, and O. Kamp. Reliability of left ventricular volumes and function measurements using three-dimensional speckle tracking echocardiography. *Eur Heart J Cardiovasc Imaging*, 13(2):159–168, 2012.

[118] S. Klein, J. Pluim, M. Staring, and M. Viergever. Adaptive stochastic gradient descent optimisation for image registration. *J Comput Vision*, 81(3):227–239, 2009.

[119] S. Klein, M. Staring, P. Andersson, and J. Pluim. Preconditioned stochastic gradient descent optimisation for monomodal image registration. In *MICCAI - Medical Image Computing and Computer-Assisted Intervention*, volume 6892 of Lecture Notes in Computer Science, pages 549–556, 2011.

[120] S. Klein, M. Staring, K. Murphy, M. Viergever, and J. Pluim. Elastix: a toolbox for intensity based medical image registration. *IEEE Trans Med Imaging*, 29(1):196–205, 2010.

[121] S. Klein, M. Staring, and J. Pluim. Evaluation of optimization methods for nonrigid medical image registration using mutual information and B-splines. *IEEE Trans Image Process*, 16(12):2879–2890, 2007.

[122] L. Koopman, C. Slorach, W. Hui, C. Manlhiot, B. McCrindle, M. Friedberg, E. Jaeggi, and L. Mertens. Comparison between different speckle tracking

and color tissue Doppler techniques to measure global and regional myocardial deformation in children. *J Am Soc Echocardiogr*, 23(9):919–928, 2010.

[123] J. Korinek, J. Wang, P. Sengupta, C. Miyazaki, J. Kjaergaard, E. McMahon, T. Abraham, and M. Belohlavek. Two-dimensional strain - a doppler-indepent ultrasound method for quantitation of regional deformation: validation in vitro and in vivo. *J Am Soc Echocardiogr*, 18(12):1247–1253, 2005.

[124] F. Kremer, T. Dresselaers, B. Heyde, V. Ferferieva, E. Caluwé, H. F. Choi, P. Claus, W. Oosterlinck, S. Janssens, U. Himmelreich, and J. D'hooge. 2D strain assessment in the mouse through spatial compounding of myocardial velocity data: In-vivo feasibility. *Ultrasound Med Biol*, 39(10):1848–1860, 2013.

[125] J. Kybic and M. Unser. Fast parametric elastic image registration. *IEEE Trans Image Process*, 12(11):1427–1442, 2003.

[126] C. Lamberti, A. Sarti, and F. Bertucci. Topology of optical flow in 3D echocardiography. In *Computers in cardiology*, pages 227–230, 1997.

[127] S. Langeland, J. D'hooge, T. Claessens, P. Claus, P. Verdonck, P. Suetens, G. Sutherland, and B. Bijnens. RF-based two-dimensional cardiac strain estimation: a validation study in tissue-mimicking phantom. *IEEE Trans Ultrason Ferroelectr Freq Control*, 51(11):1537–1546, 2004.

[128] S. Langeland, J. D'hooge, H. Torp, B. Bijnens, and P. Suetens. Comparison of time-domain displacement estimators for two-dimensional RF tracking. *Ultrasound Med Biol*, 29(8):1177–1186, 2003.

[129] S. Langeland, J. D'hooge, P. Wouters, A. Leather, P. Claus, B. Bijnens, and G. Sutherland. Experimental validation of a new ultrasound method for the simultaneous assessment of radial and longitudinal myocardial deformation independent of insonation angle. *Circulation*, 112(14):2157–2162, 2005.

[130] S. Langeland, P. Wouters, P. Claus, A. Leather, B. Bijnens, G. Sutherland, F. Rademakers, and J. D'hooge. Experimental assessment of a new research tool for the estimation of two-dimensional myocardial strain. *Ultrasound Med Biol*, 32(10):1509–1513, 2006.

[131] M. Larsson, F. Kremer, P. Claus, L. Brodin, and J. D'hooge. A novel measure to express tracking quality in ultrasound block matching. In *IEEE Int Ultrasonics Symposium*, pages 1636–1639, 2010.

[132] M. Ledesma-Carbayo, J. Kybic, M. Desco, A. Santos, M. Suhling, P. Hunziker, and M. Unser. Spatio-temporal nonrigid registration for ultrasound cardiac motion estimation. *IEEE Trans Med Imaging*, 24(9):1113–1126, 2005.

[133] M. Leitman, P. Lysyansky, S. Sidenko, V. Shir, E. Peleg, M. Binenbaum, E. Kaluski, R. Krakover, and Z. Vered. Two-dimensional strain - a novel software for real-time quantitative echocardiographic assessment of myocardial function. *J Am Soc Echocardiogr*, 17(10):1021–1029, 2004.

[134] B. Lesniak-Plewinska, S. Cygan, K. Kaluzynski, J. D'hooge, E. Zmigrodzki, E. Kowalik, M. Kordybach, and M. Kowalski. A dual-chamber, thick-walled cardiac phantom for use in cardiac motion and deformation imaging by ultrasound. *Ultrasound Med Biol*, 36(7):1145–1156, 2010.

[135] E. Leung, M. Danilouchkine, M. van Stralen, N. de Jong, A. van der Steen, and J. Bosch. Left ventricular border tracking using cardiac motion models and optical flow. *Ultrasound Med Biol*, 37(4):605–616, 2011.

[136] J. Li and T. Denney. Left ventricular motion reconstruction with a prolate spheroidal B-spline model. *Phys Med Biol*, 51(3):517–537, 2006.

[137] N. Lin and J. Duncan. Generalized robust point matching using an extended free-form deformation model: application to cardiac images. In *ISBI - International Symposium on Biomedical Imaging*, volume 1, pages 320–323, Arlington, USA, 15-18 April 2004.

[138] Y. Liu, R. Bahn, and E. Ritman. Dynamic intramyocardial blood volume: evaluation with a radiological opaque marker method. *Am J Physiol*, 263(3 Pt 2):H963–H967, 1992.

[139] D. Loeckx. *Automated non-rigid intra-patient image registration using B-splines*. PhD thesis, PSI-ESAT, Katholieke Universiteit Leuven, Leuven, Belgium, 2006.

[140] D. Loeckx, S. Diris, F. Maes, D. Vandermeulen, G. Marchal, and P. Suetens. Plaque and stent artifact reduction in subtraction CT angiography using nonrigid registration and a volume penalty. In *MICCAI - Medical Image Computing and Computer-Assisted Intervention*, volume 3750 of Lecture Notes in Computer Science, pages 361–368, 2005.

[141] D. Loeckx, F. Maes, D. Vandermeulen, and P. Suetens. Nonrigid image registration using free-form deformations with a local rigidity constraint. In *MICCAI - Medical Image Computing and Computer-Assisted Intervention*, volume 3216 of Lecture Notes in Computer Science, pages 639–646, 2004.

[142] R. Lopata, H. Hansen, M. Nillesen, J. Thijssen, and C. de Korte. Comparison of one-dimensional and two-dimensional least-squares strain estimators for phased array displacement data. *Ultrason Imaging*, 31(1):1–16, 2009.

[143] R. Lopata, M. Nillesen, I. Gerrits, J. Thijssen, L. Kapusta, and C. de Korte. 4D cardiac strain imaging: Methods and initial results. In *IEEE Int Ultrasonics Symposium*, pages 872–875, 2007.

[144] R. Lopata, M. Nillesen, I. Gerrits, J. Thijssen, L. Kapusta, F. van de Vosse, and C. de Korte. Performance evaluation of methods for two-dimensional displacement and strain estimation using ultrasound radio frequency data. *Ultrasound Med Biol*, 35(5):796–812, 2009.

[145] R. Lopata, M. Nillesen, J. Thijssen, L. Kapusta, and C. de Korte. 4D RF-based cardiac strain imaging in healthy children: initial in vivo experience. In *IEEE Int Ultrasonics Symposium*, pages 587–590, 2010.

[146] R. Lopata, M. Nillesen, J. Thijssen, L. Kapusta, and C. de Korte. Three-dimensional cardiac strain imaging in healthy children using RF-data. *Ultrasound Med Biol*, 37(9):1399–1408, 2011.

[147] M. Lotfi-Tokaldany, S. Majidi, F. Nikdoust, Z. Roomi, M. Sheikhfathollahi, and H. Sadeghian. Normal values for longitudinal tissue velocity and strain rate imaging in individual segments of the left and right ventricles of healthy adult hearts. *J Ultrasound Med*, 32(3):463–474, 2013.

[148] M. Lubinski, S. Emelianov, and M. O'Donnell. Speckle tracking methods for ultrasonic elasticity imaging using short-time correlation. *IEEE Trans Ultrason Ferroelectr Freq Control*, 46(1):82–96, 1999.

[149] B. Lucas and T. Kanade. An iterative image registration technique with an application to stereo vision. In *DARPA Image Understanding Workshop*, pages 121–130, 1981.

[150] F. Maffessanti, H. Nesser, L. Weinert, R. Steringer-Mascherbauer, J. Niel, W. Gorissen, L. Sugeng, R. Lang, and V. Mor-Avi. Quantitative evaluation of regional left ventricular function using three-dimensional speckle tracking echocardiography in patients with and without heart disease. *Am J Cardiol*, 104(12):1755–1762, 2009.

[151] T. Mäkelä, P. Clarysse, O. Sipilä, N. Pauna, Q. Pham, T. Katila, and I. Magnin. A review of cardiac image registration methods. *IEEE Trans Med Imaging*, 21(9):1011–1021, 2002.

[152] T. Malan, J. DiNardo, R. Isner, E. Frink, M. Goldberg, P. Fenster, E. Brown, R. Depa, L. Hammond, and H. Mata. Cardiovascular effects of sevoflurane compared to those of isoflurane in volunteers. *Anesthesiology*, 83(5):918–928, 1995.

[153] L. Malvern. *Introduction to the mechanics of a continuous medium*. Prentice-Hall, Englewood Cliffs, NJ, 1969.

[154] T. Mansi, X. Pennec, M. Sermesant, H. Delingette, and N. Ayache. iLogDemons: a demons-based registration algorithm for tracking incompressible elastic biological tissues. *Int J Comput Vision*, 92(1):92–111, 2010.

[155] S. Marchesseau, H. Delingette, M. Sermesant, M. Sorine, K. Rhode, S. Duckett, C. Rinaldi, R. Razavi, and N. Ayache. Preliminary specificity study of the Bestel-Clément-Sorine electromechanical model of the heart using parameter calibration from medical images. *J Mech Behavior Biomed Materials*, 20:259–271, 2013.

[156] E. Marieb and K. Hoehn. *Anatomy & physiology*. Chapter 17 - The cardiovascular system: the heart, pages 595-624. Pearson International Edition, third edition edition, 2008.

[157] T. Marwick. Measurement of strain and strain rate by echocardiography: ready for prime time? *J Am Coll Cardiol*, 47(7):1313–1327, 2006.

[158] T. Marwick. Will standardization make strain a standard measurement? *J Am Soc Echocardiogr*, 25(11):1204–1206, 2012.

[159] T. Marwick, R. Leano, J. Brown, J.-P. Sun, R. Hoffmann, P. Lysyansky, M. Becker, and J. Thomas. Myocardial strain measurement with 2-dimensional speckle-tracking echocardiography: definition of normal range. *J Am Coll Cardiol: Cardiovasc Imaging*, 2(1):80–84, 2009.

[160] K. Matre, C. Moen, T. Fanneløp, G. Dahle, and K. Grong. Multilayer radial systolic strain can identify subendocardial ischemia: an experimental tissue Doppler imaging study of the porcine left ventricular wall. *Eur J Echocardiogr*, 8(6):420–430, 2007.

[161] K. McLeod, A. Prakosa, T. Mansi, M. Sermesant, and X. Pennec. An incompressible log-domain demons algorithm for tracking heart tissue. In *STACOM - Statistical atlases and computational models of the heart*, volume 7085 of Lecture Notes in Computer Science, pages 55–67, 2012.

[162] K. McLeod, C. Seiler, M. Sermesant, and X. Pennec. A near-incompressible poly-affine motion model for cardiac function analysis. In *STACOM - Statistical atlases and computational models of the heart*, volume 7746 of Lecture Notes in Computer Science, pages 288–297, 2013.

[163] L. Mertens, J. Ganame, P. Claus, N. Goemans, D. Thijs, B. Eyskens, D. Van Laere, B. Bijnens, J. D'hooge, G. Sutherland, and G. Bruyse. Early regional myocardial dysfunction in young patients with Duchenne muscular dystrophy. *J Am Soc Echocardiogr*, 21(9):1049–1054, 2008.

[164] R. G. Modat, M, Z. Taylor, M. Lehmann, J. Barnes, D. Hawkes, N. Fox, and S. Ourselin. Fast free-form deformation using graphics processing units. *Comput Methods Programs Biomed*, 98(3):278–284, 2010. Software: NiftyReg - `http://www0.cs.ucl.ac.uk/staff/M.Modat/Marcs_Page/Software.html`.

[165] C. Moen, P. Salminen, G. Dahle, J. Hjertaas, K. Grong, and K. Matre. Multi-layer radial systolic strain vs. one-layer strain for confirming reperfusion from a significant non-occlusive coronary stenosis. *Eur Heart J Cardiovasc Imaging*, 14(1):24–37, 2013.

[166] V. Mor-Avi, C. Jenkins, H. Kühl, H. Nesser, T. Marwick, A. Franke, C. Ebner, B. Freed, R. Steringer-Mascherbauer, H. Pollard, L. Weinert, J. Niel, L. Sugeng, and R. Lang. Real-time 3-dimensional echocardiographic quantification of left ventricular volumes: multicenter study for validation with magnetic resonance imaging and investigation of sources of error. *J Am Coll Cardiol: Cardiovasc Imaging*, 1(4):413–423, 2008.

[167] V. Mor-Avi, R. Lang, L. Badano, M. Belohlavek, N. Cardim, G. Derumeaux, M. Galderisi, T. Marwick, S. Nagueh, P. Sengupta, R. Sicari, O. Smiseth, B. Smulevitz, M. Takeuchi, J. Thomas, M. Vannan, J. Voigt, and J. Zamorano. Current and evolving echocardiographic techniques for the quantitative evaluation of cardiac mechanis: ASE/EAE consensus statement of methodology and indications. *J Am Soc Echocardiogr*, 24(3):277–313, 2011.

[168] P. Morais, B. Heyde, D. Barbosa, S. Queirós, P. Claus, and J. D'hooge. Cardiac motion and deformation estimation from tagged MRI sequences using a temporal coherent image registration framework. In *FIMH - Functional Imaging and Modeling of the Heart*, volume LNCS 7945, pages 316–324, London, UK, 20-22 June 2013. poster presentation.

[169] A. Morsy and O. von Ramm. Flash correlation: A new method for 3-D ultrasound tissue motion tracking and blood velocity estimation. *IEEE Trans Ultrason Ferroelectr Freq Control*, 46(3):728–736, 1999.

[170] R. Mukherjee, C. Sprouse, A. Pinheiro, T. Abraham, and P. Burlina. Computing myocardial motion in 4-dimensional echoardiography. *Ultrasound Med Biol*, 38(7):1284–1297, 2012.

[171] K. Munk, N. Andersen, S. Nielsen, B. Bibby, H. Botker, T. Nielsen, and S. Poulsen. Global longitudinal strain by speckle tracking for infarct size estimation. *Eur J Echocardiogr*, 12(2):156–165, 2011.

[172] D. Muraru, L. Badano, G. Piccoli, P. Gianfagna, L. Del Mestre, D. Ermacora, and A. Proclemer. Validation of a novel automated border-detection algorithm for rapid and accurate quantitation of left ventricular volumes based on three-dimensional echocardiography. *Eur J Echocardiogr*, 11(4):359–368, 2010.

[173] P. Muyan-Ozcelik, J. Owens, J. Xia, and S. Samant. Fast deformable registration on the GPU: a CUDA implementations of Demons. In *ICCSA - Int Conf on Computat Sciences and its Applications*, pages 223–233, 2008.

[174] A. Myronenko. Software package: MIRT - Medical Image Registration Toolbox. `https://sites.google.com/site/myronenko/research/mirt`.

[175] A. Myronenko, X. Song, and D. Sahn. LV motion tracking from 3D echocardiography using textural and structural information. In *MICCAI - Medical Image Computing and Computer-Assisted Intervention*, volume 4792 of Lecture Notes in Computer Science, pages 428–435, 2007.

[176] A. Myronenko, X. Song, and D. Sahn. Maximum likelihood motion estimation in 3D echocardiography through non-rigid registration in spherical coordinates. In *FIMH - Functional Imaging and Modeling of the Heart*, volume 5528 of Lecture Notes in Computer Science, pages 427–436, 2009.

[177] T. Nelson, D. Pretorius, A. Hull, M. Riccabona, M. Sklasky, and G. James. Sources and impact of artifacts on clinical three-dimensional ultrasound imaging. *Ultrasound Obstet Gynecol*, 16(4):374–383, 2000.

[178] H. Nesser and S. Winter. Speckle tracking in the evaluation of left ventricular dyssynchrony. *Echocardiography*, 26(3):324–336, 2009.

[179] M. Nillesen, R. Lopata, I. Gerrits, L. Kapusta, H. Huisman, J. Thijssen, and C. de Korte. Segmentation of the heart muscle in 3-D pediatric echocardiographic images. *Ultrasound Med Biol*, 33(9):1453–1462, 2007.

[180] J. Noble and D. Boukerroui. Ultrasound image segmentation: a survey. *IEEE Trans Med Imaging*, 25(8):987–1010, 2006.

[181] J. Nocedal and S. Wright. *Numerical Optimization*. Springer-Verlag, New York, 1999.

[182] R. Norris, P. Barnaby, P. Brandt, G. Geary, R. Whitlock, C. Wild, and B. Barratt-Boyes. Prognosis after recovery from first acute myocardial infarction: Determinants of reinfarction and sudden death. *Am J Cardiol*, 53(4):408–413, 1984.

[183] Y. Notomi, P. Lysyansky, R. Setser, T. Shiota, Z. Popovic, M. Martin-Miklovic, J. Weaver, S. Oryszak, N. Greenberg, R. White, and J. Thomas. Measurement of ventricular torsion by two-dimensional ultrasound speckle tracking imaging. *J Am Coll Cardiol*, 45(12):2034–2041, 2005.

[184] F. Orderud, J. Hånsgard, and S. Rabben. Real-time tracking of the left ventricle in 3D echocardiography using a state estimation approach. In *MICCAI -*

Medical Image Computing and Computer-Assisted Intervention, volume 4791 of Lecture Notes in Computer Science, pages 858–865, 2007.

[185] F. Orderud and S. Rabben. Real-time 3D segmentation of the left ventricle using deformable subdivision surfaces. In *Comp Vision and Patt Recognition*, pages 1–8, 2008.

[186] F. Orderud, H. Torp, and S. Rabben. Automatic alignment of standard views in 3D echocardiograms using real-time tracking. In *SPIE Med Imaging*, volume 7625, 2009.

[187] J. Ortiz-Pérez, J. Rodríguez, S. Meyers, D. Lee, C. Davidson, and E. Wu. Correspondence between the 17-segment model and coronary arterial anatomy using contrast-enhanced cardiac magnetic resonance imaging. *J Am Coll Cardiol: Cardiovasc Imaging*, 1(3):282–293, 2008.

[188] X. Papademetris, A. Sinusas, D. Dione, T. Constable, and J. Duncan. Estimation of 3-D left ventricular deformation from medical images using biomechanical models. *IEEE Trans Med Imaging*, 21(7):786–800, 2002.

[189] X. Papademetris, A. Sinusas, D. Dione, and J. Duncan. Estimation of 3D left ventricular deformation from echocardiography. *Med Image Analysis*, 5(1):17–28, 2001.

[190] L. Pérez de Isla, D. Balcones, C. FernÃąndez-Golfin, P. Marcos-Alberca, C. AlmerÃŋa, J. Rodrigo, C. Macaya, and J. Zamorano. Three-dimensional-wall motion tracking: A new and faster tool for myocardial strain assessment: Comparison with two-dimensional-wall motion tracking. *J Am Soc Echocardiogr*, 22(4):325–330, 2009.

[191] E. Picano, F. Lattanzi, A. Orlandini, C. Marini, and A. L'Abbate. Stress echocardiography and the human factor: the importance of being expert. *J Am Coll Cardiol*, 17(3):666–669, 1991.

[192] G. Piella, A. Porras, M. De Craene, and N. Duchateau. Temporal diffeomorphic free form deformation to quantify changes induced by left and right bundle branch block and pacing. In *STACOM - Statistical atlases and computational models of the heart*, pages 134–141, 2012.

[193] B. Pirat, D. Khoury, C. Hartley, L. Tiller, L. Rao, D. Schulz, S. Nagueh, and W. Zoghbi. A novel feature-tracking echocardiographic method for the quantitation of regional myocardial function - validation in an animal model of ischemia-reperfusion. *J Am Coll Cardiol*, 51(6):651–659, 2008.

[194] Z. Popovic, C. Benejam, J. Bian, N. Mal, J. Drinko, K. Lee, F. Forudi, R. Reeg, N. Greenberg, J. Thomas, and M. Penn. Speckle-tracking echocardiography correctly identifies segmental left ventricular dysfunction induced by scarring in a rat model of myocardial infarction. *Am J Physiol Heart Circ Physiol*, 292(6):H2809–H2816, 2007.

[195] A. Prakosa, K. McLeod, M. Sermesant, and X. Pennec. Evaluation of iLogDemons algorithm for cardiac motion tracking in synthetic ultrasound sequence. In *STACOM - Statistical atlases and computational models of the heart*, volume 7746 of Lecture Notes in Computer Science, pages 178–187, 2013.

[196] A. Prakosa, M. Sermesant, H. Delingette, S. Marchesseau, E. Saloux, P. Allain, N. Villain, and N. Ayache. Generation of synthetic but visually realistic time series of cardiac images combining a biophysical model and clinical images. *IEEE Trans Med Imaging*, 32(1):99–109, 2013.

[197] M. Quiñones, B. Greenberg, H. Kopelen, C. Koilpillai, M. Limacher, D. Shindler, B. Shelton, and D. Weiner. Echocardiographic predictors of clinical outcome in patients with left ventricular dysfunction enrolled in the SOLVD registry and trials: significance of left ventricular hypertrophy. *J Am Coll Cardiol*, 35(5):1237–1244, 2000.

[198] B. Ramamurthy and G. Trahey. Potential and limitations of angle-independent flow detection algorithms using radio-frequency and detected echo signals. *Ultrason Imaging*, 13(3):252–268, 1991.

[199] P. Reant, L. Barbot, C. Touche, M. Dijos, F. Arsac, X. Pillois, M. Landelle, R. Roudaut, and S. Lafitte. Evaluation of global left ventricular systolic function using three-dimensional echocardiography speckle tracking strain parameters. *J Am Soc Echocardiogr*, 25(1):68–79, 2012.

[200] P. Reant, L. Labrousse, S. Lafitte, P. Bordachar, X. Pillois, L. Tariosse, S. Bonoron-Adele, P. Padois, C. Deville, R. Roudaut, and P. Dos Santos. Experimental validation of circumferential, longitudinal, and radial 2-dimensional strain during dobutamine stress echocardiography in ischemic conditions. *J Am Coll Cardiol*, 51(2):149–157, 2008.

[201] T. Rohlfing, C. Maurer, D. Bluemke, and M. Jacobs. Volume-preserving nonrigid registration of mr breast images using free-form deformation with an incompressibility constraint. *IEEE Trans Med Imaging*, 22(6):730–741, 2003.

[202] D. Rueckert. Software package: IRTK - Image Registration Toolkit. `http://www.doc.ic.ac.uk/~dr/software/`.

[203] D. Rueckert, L. Sonoda, D. Hill, M. Leach, and D. Hawkes. Nonrigid registration using free-form deformations: application to breast MR images. *IEEE Trans Med Imaging*, 18(8):712–721, 1999.

[204] D. Sahn, M. Ashraf, T. Balbach, and K. DesRochers. A new 3D strain method for processing of 4D echo images can delineate regional myocardial dysfunction: validation against sonomicrometry. In *J Am Coll Cardiol*, volume 57(suppl), page E707, 2011.

[205] K. Saito, H. Okura, N. Watanabe, A. Hayashida, K. Obase, K. Imai, T. Maehama, T. Kawamoto, Y. Neishi, and K. Yoshida. Comprehensive evaluation of left ventricular strain using speckle tracking echocardiography in normal adults: Comparison of three-dimensional and two-dimensional approaches. *J Am Soc Echocardiogr*, 22(9):1025–1030, 2009.

[206] N. Schiller, P. Shah, M. Crawford, D. A, D. R, F. H, G. H, N. Reichek, D. Sahn, and I. Schnittger. Recommendations for quantitation of the left ventricle by two-dimensional echocardiography. american society of echocardiography committee on standards, subcommittee on quantitation of two-dimensional echocardiograms. *J Am Soc Echocardiogr*, 2(5):358–367, 1989.

[207] J. Schnabel, D. Rueckert, M. Quist, J. Blackall, A. Castellano-Smith, T. Hartkens, G. Penney, W. Hall, H. Liu, C. Truwit, F. Gerritsen, D. Hill, and D. Hawkes. A generic framework for non-rigid registration based on non-uniform multi-level free-form deformations. In *MICCAI - Medical Image Computing and Computer-Assisted Intervention*, pages 573–581, 2001.

[208] T. Sederberg and S. Parry. Free-form deformation of solid geometric models. *ACM Siggraph Computer Graphics*, 20(4):151–160, 1986.

[209] Y. Seo, T. Ishizu, Y. Enomoto, H. Sugimori, and K. Aonuma. Endocardial surface tracking for assessment of regional LV wall deformation with 3D speckle tracking imaging. *J Am Coll Cardiol: Cardiovasc Imaging*, 4(4):358–365, 2011.

[210] Y. Seo, T. Ishizu, Y. Enomoto, H. Sugimori, M. Yamamoto, T. Machino, R. Kawamura, and K. Aonuma. Validation of 3-dimensional speckle tracking imaging to quantify regional myocardial deformation. *Circulation Cardiovascular Imaging*, 2(6):451–459, 2009.

[211] M. Sermesant, R. Chabiniok, P. Chinchapatnam, T. Mansi, F. Billet, P. Moireau, J. Peyrat, K. Wong, J. Relan, K. Rhode, M. Ginks, P. Lambiase, H. Delingette, M. Sorine, C. Rinaldi, D. Chapelle, R. Razavi, and N. Ayache. Patient-specific electromechanical models of the heart for the prediction of pacing acute effects in CRT: A preliminary clinical validation. *Med Image Analysis*, 16(1):201–215, 2012.

[212] M. Sermesant, H. Delingette, and N. Ayache. An electromechanical model of the heart for image analysis and simulation. *Med Image Analysis*, 25(5):612–625, 2006.

[213] J. Shackleford, N. Kandasamy, and G. Sharp. On developing B-spline registration algorithms for multi-core processors. *Phys Med Biol*, 55(21):6329–6351, 2010.

[214] J. Shackleford, N. Kandasamy, and G. Sharp. *High performance deformable image registration algorithms for manycore processors*. Chapter 5 - Deformable registration using optical-flow methods, pages 95-106. Morgan Kaufmann, 2013.

[215] J. Shackleford, Q. Yang, A. Lourenço, N. Shusharina, N. Kandasamy, and G. Sharp. Analytic regularization of uniform cubic B-spline deformation fields. In *MICCAI - Medical Image Computing and Computer-Assisted Intervention*, volume 7511 of Lecture Notes in Computer Science, pages 122–129, 2012.

[216] R. Shams, P. Sadeghi, K. R, and R. Hartley. A survey of medical image registration on multicore and the GPU. *IEEE Signal Processing Magazine*, 27(2):50–60, 2010.

[217] S. Shaw, D. Fox, and S. Williams. The development of left ventricular torsion and its clinical relevance. *Int J Cardiol*, 130(3):319–325, 2008.

[218] W. Shi, X. Zhuang, H. Wang, S. Duckett, D. Luong, C. Tobon-Gomez, K. Tung, P. Edwards, K. Rhode, R. Razavi, S. Ourselin, and D. Rueckert. A comprehensive cardiac motion estimation framework using both untagged and 3-D tagged MR images based on nonrigid registration. *IEEE Trans Med Imaging*, 31(6):1263–1275, 2012.

[219] H. Skulstad, K. Andersen, T. Edvardsen, K. Rein, T. Tonnessen, P. Hol, E. Fosse, and H. Ihlen. Detection of ischemia and new insight into left ventricular physiology by strain Doppler and tissue velocity imaging: assessment during coronary bypass operation of the beating heart. *J Am Soc Echocardiogr*, 17(12):1225–1233, 2004.

[220] G. Small, G. Wells, T. Schindler, B. Chow, and T. Ruddy. Advances in cardiac SPECT and PET imaging: overcoming the challenges to reduce radiation exposure and improve accuracy. *Canadian Journal of Cardiology*, 29(3):275–284, 2013.

[221] S. Smith, H. Pavy, and O. von Ramm. High-speed ultrasound volumetric imaging system - part i: transducer design and beam steering. *IEEE Trans Ultrason Ferroelectr Freq Control*, 38(2):100–108, 1991.

[222] O. Soliman, B. Krenning, M. Geleijnse, A. Nemes, J. Bosch, R. van Geuns, S. Kirschbaum, A. Anwar, T. Galema, W. Vletter, and F. ten Cate. Quantification of left ventricular volumes and function in patients with cardiomyopathies by real-time three-dimensional echocardiography: A head-to-head comparison between two different semiautomated endocardial border detection algorithms. *J Am Soc Echocardiogr*, 20(9):1042–1049, 2007.

[223] O. Somphone, C. Dufour, B. Mory, L. Hilpert, and S. Makram-Ebeid. Motion estimation in 3D echocardiography using smooth field registration. In *STACOM - Statistical atlases and computational models of the heart*, pages 151–158, 2012.

[224] X. Song, A. Myronenko, and D. Sahn. Speckle tracking in 3D echocardiography with motion coherence. In *Comp Vision and Patt Recognition*, pages 1–7, 2007.

[225] A. Sotiras, C. Davatzikos, and N. Paragios. Deformable medical image registration: a survey. *IEEE Trans Med Imaging*, 23(7):1153–1190, 2013.

[226] S. Srinivasan, T. Krouskop, and J. Ophir. Comparing elastographic strain images with modulus images obtained using nanoidentation: preliminary results using phantoms and tissue samples. *Ultrasound Med Biol*, 30(4):329–343, 2004.

[227] M. Staring, S. Klein, and J. Pluim. A rigidity penalty term for nonrigid registration. *Med Phys*, 34(11):4098–4108, 2007.

[228] P. Suetens. *Fundamentals of medical imaging*. Chapter 6 - Ultrasound imaging, pages 128-158. Cambridge University Press, second edition edition, 2009.

[229] M. Suffoletto, K. Dohi, M. Cannesson, S. Saba, and J. Gorcsan. Novel speckle-tracking radial strain from routine black-and-white echocardiographic images to quantify dyssynchrony and predict response to cardiac resynchronization therapy. *Circulation*, 113(7):960–968, 2006.

[230] M. Suhling, M. Arigovindan, C. Jansen, P. Hunziker, and M. Unser. Myocardial motion analysis from B-mode echocardiograms. *IEEE Trans Image Process*, 14(4):525–536, 2005.

[231] K. Surry, H. Austin, A. Fenster, and T. Peters. Poly(vinyl alcohol) cryogel phantoms for use in ultrasound and MR imaging. *Phys Med Biol*, 49(24):5529–5546, 2004.

[232] G. Sutherland, G. Di Salvo, P. Claus, J. D'hooge, and B. Bijnens. Strain and strain rate imaging: a new clinical approach to quantifying regional myocardial function. *J Am Soc Echocardiogr*, 17(7):788–802, 2004.

[233] G. Sutherland, L. Hatle, P. Claus, J. D'hooge, and B. Bijnens. *Doppler myocardial imaging: a textbook*. Chapter 3 - The principles of ultrasound based motion and deformation estimation, pages 23-48. BSWK bvba, Scientific Consulting and Publishing, 2006.

[234] G. Sutherland, M. Stewart, W. Groundstroem, C. Moran, A. Fleming, F. Guell-Peris, R. Riemersma, L. Fenn, K. Fox, and W. McDicken. Color Doppler myocardial imaging: a new technique for the assessment of myocardial function. *J Am Soc Echocardiogr*, 7(5):441–458, 1994.

[235] T. Szabo. *Diagnostic ultrasound imaging: inside out*. Chapter 12 - Nonlinear acoustics and imaging, pages 381-428. Elsevier Academic Press, 2004.

[236] A. Tamhane. Multiple comparisons in model I one-way ANOVA with unequal variances. *Communications in Statistics - Theory and Methods*, 6(1):15–32, 1977.

[237] L. Tautz, A. Hennemuth, and H. Peitgan. Quadrature filter based motion analysis for 3D ultrasound sequences. In *STACOM - Statistical atlases and computational models of the heart*, pages 169–177, 2012.

[238] A. Teske, B. De Boeck, P. Melman, G. Sieswerda, P. Doevendans, and M. Cramer. Echocardiographic quantification of myocardial function using tissue deformation imaging, a guide to image acquisition and analysis using tissue doppler and speckle tracking. *Cardiovascular Ultrasound*, 5(27), 2007.

[239] P. Theroux, J. Ross, D. Franklin, W. Kemper, and S. Sasyama. Regional myocardial function in the conscious dog during acute coronary occlusion and responses to morphine, propranolol, nitroglycerin, and lidocaine. *Circulation*, 53(2):302–314, 1976.

[240] J. Thirion. Image matching as a diffusion process: an analogy with Maxwell's demons. *Med Image Analysis*, 2(3):243–260, 1998.

[241] J. Thomas and Z. Popovic. Assessment of left ventricular function by cardiac ultrasound. *J Am Coll Cardiol*, 48(10):2012–2025, 2006.

[242] A. Thorstensen, H. Dalen, B. Amundsen, S. Aase, and A. Stoylen. Reproducibility in echocardiographic assessment of the left ventricular global and regional function, the hunt study. *Eur J Echocardiogr*, 11(2):149–156, 2010.

[243] L. Tong, H. Gao, and J. D'hooge. Multi-transmit beam forming for fast cardiac imaging - a simulation study. *IEEE Trans Ultrason Ferroelectr Freq Control*, 60(8):1719–1731, 2013.

[244] G. Trahey, J. Allison, and O. Von Ramm. Angle independent ultrasonic detection of blood flow. *IEEE Trans Biomed Eng*, 34(12):965–967, 1987.

[245] M. Unser. Splines: a perfect fit for signal and image processing. *IEEE Signal Processing Magazin*, 16(6):22–38, 1999.

[246] S. Urheim, T. Edvardsen, H. Torp, B. Angelsen, and O. Smiseth. Myocardial strain by Doppler echocardiography: validation of a new method to quantify regional myocardial function. *Circulation*, 102(10):1158–1164, 2000.

[247] D. Škerl, B. Likar, and Pernuš. A protocol for evaluation of similarity measures for non-rigid registration. *Med Image Analysis*, 12(1):42–54, 2008.

[248] K. Ustüner. High information rate volumetric ultrasound imaging. Technical report, Siemens Healthcare, 2008.

[249] M. van Stralen, J. Bosch, M. Voormolen, G. van Burken, B. Krenning, R. van Geuns, C. Lancée, N. de Jong, and J. Reiber. Left ventricular volume estimation in cardiac three-dimensional ultrasound: A semiautomatic border detection approach. *Acad Radiol*, 12(10):1241–1249, 2005.

[250] T. Varghese, J. Ophir, and I. Céspedes. Noise reduction in elastograms using temporal stretching with multicompression averaging. *Ultrasound Med Biol*, 22(8):1043–1052, 1996.

[251] T. Vartdal, H. Brunvand, E. Pettersen, H. Smith, E. Lyseggen, T. Helle-Valle, H. Skulstad, H. Ihlen, and T. Edvardsen. Early prediction of infarct size by strain Doppler echocardiography after coronary reperfusion. *J Am Coll Cardiol*, 49(16):1715–1721, 2007.

[252] T. Vercauteren, X. Pennec, A. Perchant, and N. Ayache. Symmetric log-domain diffeomorphic registration: a demons-based approach. In *MICCAI - Medical Image Computing and Computer-Assisted Intervention*, volume Pt 1, pages 754–761, 2008.

[253] T. Vercauteren, X. Pennec, A. Perchant, and N. Ayache. Diffeomorphic demons: efficient non-parametric image registration. *Neuroimage*, 45(1 Suppl):S61–S72, 2009.

[254] F. Viola and W. Walker. A comparison of the performance of time-delay estimators in medical ultrasound. *IEEE Trans Ultrason Ferroelectr Freq Control*, 50(4):392–401, 2003.

[255] O. Von Ramm, S. Smith, and H. Pavy. High-speed ultrasound volumetric imaging system - part ii: parallel processing and image display. *IEEE Trans Ultrason Ferroelectr Freq Control*, 38(2):109–115, 1991.

[256] H. Wang and A. Amini. Cardiac motion and deformation recovery from MRI: a review. *IEEE Trans Med Imaging*, 31(2):487–503, 2012.

[257] Y. Wang, B. Georgescu, D. Comaniciu, and H. Houle. Learning-based 3D myocardial motion flow estimation using high frame rate volumetric ultrasound data. In *ISBI - International Symposium on Biomedical Imaging*, pages 1097–1100, 2010.

[258] Y. Wang, B. Georgescu, H. Houle, and D. Comaniciu. Volumetric myocardial mechanics from 3D+t ultrasound data with multi-modal tracking. In *STACOM - Statistical atlases and computational models of the heart*, volume 6364 of Lecture Notes in Computer Science, pages 184–193, 2010.

[259] F. Weidemann, C. Dommke, B. Bijnens, P. Claus, J. D'hooge, P. Mertens, E. Verbeken, A. Maes, F. Van de Werf, I. De Scheerder, and G. Sutherland. Defining the transmurality of a chronic myocardial infarction by ultrasonic strain-rate imaging: implications for identifying intramural viability: an experimental study. *Circulation*, 107(6):883–888, 2003.

[260] H. White, R. Norris, M. Brown, R. Whitlock, and C. Wild. Left ventricular end-systolic volume as the major determinant of survival after recovery from myocardial infarction. *Circulation*, 76(1):44–51, 1987.

[261] D. Winchester, D. Wymer, R. Shifrin, S. Kraft, and J. Hill. Responsible use of computed tomography in the evaluation of coronary artery disease and chest pain. *Mayo Clin Proc*, 85(4):358–364, 2010.

[262] World Health Organisation. Cardiovascular diseases, fact sheet 317. `http://www.who.int/mediacentre/factsheets/fs317/en/index.html`, 2013.

[263] F. Yeung, S. Levinson, and K. Parker. Multilevel and motion model-based ultrasonic speckle tracking algorithms. *Ultrasound Med Biol*, 24(3):427–441, 1998.

[264] F. Yin, C. Chan, and R. Judd. Compressibility of perfused passive myocardium. *Am J Physiol*, 271(5 Pt 2):H1864–H1870, 1996.

[265] T. Yingchoncharoen, S. Agarwal, Z. Popović, and T. Marwick. Normal ranges of left ventricular strain: a meta analysis. *J Am Soc Echocardiogr*, 26(2):185–191, 2013.

[266] T. Yoo, M. Ackerman, L. W, W. Schroeder, V. Chalana, S. Aylward, M. D, and R. Whitaker. Engineering and algorithm design for an image processing API: a technical report on ITK - The Insight Toolkit. In *Studies in Health Technology and Informatics, Proceedings of Medicine Meets Virtual Reality*, volume 85, pages 586–592, 2002.

[267] W. Yu, P. Yan, A. Sinusas, K. Thiele, and J. Duncan. Towards pointwise motion tracking in echocardiographic image sequences - comparing the reliability of different features for speckle tracking. *Med Image Analysis*, 10(4):495–508, 2006.

[268] L. Zhang, J. Gao, M. Xiz, P. Yin, W. Liu, Y. Li, B. Klas, R. Balluz, and S. Ge. Three-dimensional global longitudinal strain analysis of left ventricle by real-time 3-D speckle tracking imaging in pediatric population: feasibility, reproducibility, maturational changes, and normal ranges. In *Circulation*, volume I24(suppl), page A10777, 2011.

[269] Z. Zhang, D. Sahn, and X. Song. Temporal diffeomorphic motion analysis from echocardiographic sequences by using intensity transitivity consistency. In *STACOM - Statistical atlases and computational models of the heart*, volume 7085 of Lecture Notes in Computer Science, pages 274–284, 2012.

[270] Z. Zhang, X. Song, and D. Sahn. Cardiac motion estimation from 3D echocardiography with spatiotemporal regularization. In *FIMH - Functional Imaging and Modeling of the Heart*, volume 6666 of Lecture Notes in Computer Science, pages 350–358, 2011.

[271] C. Zhu, R. Byrd, P. Lu, and J. Nocedal. L-BFGS-B: Algorithm 778: Fortran subroutines for large-scale bound-constrained optimization. *ACM Trans on Mathematical Software*, 23(4):550–560, 1997.

[272] B. Zitova and J. Flusser. Image registration methods: a survey. *Image Vision Comput*, 21(11):977–1000, 2003.

List of publications

International Journal

1. **B. Heyde**, S. Cygan, H. Choi, B. Lesniak-Plewinska, D. Barbosa, A. Elen, P. Claus, D. Loeckx, K. Kaluzynski, and J. D'hooge. Regional cardiac motion and strain estimation in three-dimensional echocardiography: A validation study in thick-walled univentricular phantoms. *IEEE Trans Ultrason Freq Control*, 59(4):668–682, 2012.

2. R. Jasaityte, **B. Heyde**, V. Ferferieva, B. Amundsen, D. Barbosa, D. Loeckx, G. Kiss, F. Orderud, P. Claus, H. Torp, and J. D'hooge. Comparison of a new methodology for the assessment of 3D myocardial strain from volumetric ultrasound with 2D speckle tracking. *Int J Cardiovascular Imaging*, 28(5):1049–1060, 2012.

3. D. Barbosa, **B. Heyde**, T. Dietenbeck, D. Friboulet, O. Bernard, H. Houle, and J. D'hooge. Quantification of left ventricular volume and global function using a fast fully automated segmentation tool: Validation in a clinical setting. *Int J Cardiovascular Imaging*, 29(2):309–316, 2012.

4. **B. Heyde**, R. Jasaityte, D. Barbosa, V. Robesyn, S. Bouchez, P. Wouters, F. Maes, P. Claus, and J. D'hooge. Elastic image registration versus speckle tracking for 2D myocardial motion estimation: a direct comparison in-vivo. *IEEE Trans Med Imaging*, 32(2):449–459, 2013.

5. R. Jasaityte, **B. Heyde**, and J. D'hooge. Current state of 3D myocardial strain estimation using echocardiography. *J Am Soc of Echocardiogr*, 26(1):15–28, 2013.

6. D. Barbosa, T. Dietenbeck, **B. Heyde**, H. Houle, D. Friboulet, J. D'hooge, and O. Bernard. Fast and fully automatic 3D echocardiographic segmentation using B-spline explicit active surfaces: feasibility

study and validation in a clinical setting. *Ultrasound Med Biol*, 39(1):89–101, 2013.

7. **B. Heyde**, S. Bouchez, S. Thieren, M. Vandenheuvel, R. Jasaityte, D. Barbosa, P. Claus, F. Maes, P. Wouters, and J. D'hooge. Elastic image registration to quantify 3D regional myocardial deformation from volumetric ultrasound: Experimental validation in an animal model. *Ultrasound Med Biol*, 39(9):1688–1697, 2013.

8. F. Kremer, T. Dresselaers, **B. Heyde**, V. Ferferieva, E. Caluwé, H. F. Choi, P. Claus, W. Oosterlinck, S. Janssens, U. Himmelreich, and J. D'hooge. 2D strain assessment in the mouse through spatial compounding of myocardial velocity data: In-vivo feasibility. *Ultrasound Med Biol*, 39(10):1848–1860, 2013.

9. M. De Craene, S. Marchesseau, **B. Heyde**, H. Gao, M. Allesandrini, O. Bernard, G. Piella, A. Porras, E. Saloux, L. Tautz, A. Hennemuth, A. Prakosa, H. Liebgott, O. Somphone, P. Allain, S. Makram Ebeid, H. Delingette, M. Sermesant, and J. D'hooge. 3D strain assessment in ultrasound (straus): A synthetic comparison of five tracking methodologies. *IEEE Trans Med Imaging*, 32(9):1632–1646, 2013.

10. D. Barbosa, **B. Heyde**, M. Cikes, T. Dietenbeck, P. Claus, D. Friboulet, O. Bernard, and J. D'hooge. Interactive 3D real-time segmentation of echocardiographic data through user-based deformation of B-spline explicit active surfaces. *Computerized Med Imaging and Graphics*, 2013. [In press]

International Conference: Published in Proceedings

11. **B. Heyde**, S. Cygan, H. Choi, B. Lesniak-Plewinska, D. Barbosa, A. Elen, P. Claus, D. Loeckx, K. Kaluzynski, and J. D'hooge. Three-dimensional cardiac motion and strain estimation: A validation study in thick-walled univentricular phantoms. In *IEEE Int Ultrasonics Symposium*, pages 1534 – 1537, San Diego, USA, 11-14 October 2010. [Young Investigator Award, Talk, Poster]

12. D. Barbosa, O. Bernard, O. Savu, T. Dietenbeck, **B. Heyde**, P. Claus, D. Friboulet, and J. D'hooge. Coupled B-spline active geometric functions for myocardial segmentation in cardiac ultrasound. In *IEEE Int Ultrasonics Symposium*, pages 1648–1651, San Diego, USA, 11-14 October 2010. [Poster]

13. **B. Heyde**, R. Jasaityte, S. Bouchez, M. Vandenheuvel, P. Claus, P. Wouters, and J. D'hooge. Performance of elastic image registration against speckle tracking for 2D cardiac motion and strain estimation. In *IEEE Int Ultrasonics Symposium*, pages 931–934, Orlando, USA, 18-21 October 2011. [Talk]

14. **B. Heyde**, R. Jasaityte, S. Bouchez, M. Vandenheuvel, D. Loeckx, P. Claus, P. Wouters, and J. D'hooge. Three-dimensional myocardial strain estimation from volumetric ultrasound: experimental validation in an animal model. In *IEEE Int Ultrasonics Symposium*, pages 1862–1865, Orlando, USA, 18-21 October 2011. [Talk]

15. D. Barbosa, O. Bernard, T. Dietenbeck, **B. Heyde**, D. Friboulet, H. Houle, and J. D'hooge. Fast 3D echocardiographic segmentation using B-Spline explicit active surfaces: a validation study in a clinical setting. In *IEEE Int Ultrasonics Symposium*, pages 1854–1857, Orlando, USA, 18-21 October 2011. [Talk]

16. M. Larsson, F. Kremer, **B. Heyde**, L. Brodin, and J. D'hooge. Ultrasound-based speckle tracking for 3D strain estimation of the arterial wall - an experimental validation study in a tissue mimicking phantom. In *IEEE Int Ultrasonics Symposium*, pages 725–728, Orlando, USA, 18-21 October 2011. [Talk]

17. F. Kremer, T. Dresselaers, **B. Heyde**, V. Ferferieva, E. Caluwe, W. Oosterlinck, S. Janssens, U. Himmelreich, and J. D'hooge. 2D myocardial strain in the mouse through spatial compounding: in-vivo feasibility study. In *IEEE Int Ultrasonics Symposium*, pages 939–942, Orlando, USA, 18-21 October 2011. [Talk]

18. **B. Heyde**, P. Claus, R. Jasaityte, D. Barbosa, S. Bouchez, M. Vandenheuvel, P. Wouters, F. Maes, and J. D'hooge. Motion and deformation estimation of cardiac ultrasound sequences using an anatomical B-spline transformation model. In *ISBI - International Symposium on Biomedical Imaging*, pages 266–269, Barcelona, Spain, 2-5 May 2012. [Poster]

19. D. Barbosa, T. Dietenbeck, **B. Heyde**, H. Houle, D. Friboulet, J. D'hooge, and O. Bernard. Fast and fully automatic 3D echocardiographic segmentation using B-spline explicit active surfaces. In *ISBI - International Symposium on Biomedical Imaging*, pages 1088–1091, Barcelona, Spain, 2-5 May 2012. [Poster]

20. **B. Heyde**, D. Barbosa, P. Claus, F. Maes, and J. D'hooge. Three-dimensional cardiac motion estimation based on non-rigid image registration using a novel transformation model adapted to the heart. In

STACOM - International Workshop on Statistical Atlases and Computational Models of the Heart: Motion tracking challenge, volume 7746, pages 142–150, Nice, France, 5 October 2012. [Talk]

21. **B. Heyde**, D. Barbosa, R. Jasaityte, S. Bouchez, P. Wouters, F. Maes, P. Claus, and J. D'hooge. Three-dimensional myocardial strain estimation from volumetric ultrasound data using a novel transformation model adapted to the heart. In *IEEE Int Ultrasonics Symposium*, pages 1086–1089, Dresden, Germany, 7-10 October 2012. [Talk]

22. D. Barbosa, O. Bernard, **B. Heyde**, T. Dietenbeck, H. Houle, D. Friboulet, and J. D'hooge. B-spline Explicit Active Tracking of Surfaces (BEATS): Application to real-time 3D segmentation and tracking of the left ventricle in 3D echocardiography. In *IEEE Int Ultrasonics Symposium*, pages 224–227, Dresden, Germany, 7-10 October 2012. [Talk]

23. M. Larsson, F. Kremer, **B. Heyde**, E. Widman, and J. D'hooge. Carotid strain estimation using an ultrasound-based speckle tracking algorithm - A comparison of standard clinical ultrasound and high-resolution ultrasound in tissue mimicking phantoms. In *IEEE Int Ultrasonics Symposium*, pages 1394–1397, Dresden, Germany, 7-10 October 2012. [Poster]

24. D. Bibicu, D. Barbosa, **B. Heyde**, D. Friboulet, O. Bernard, L. Moraru, P. Claus, and J. D'hooge. An integrated solution for semi-automatic segmentation of volumetric ultrasound data based on B-spline explicit active surfaces. In *IEEE Int Ultrasonics Symposium*, pages 2643–2646, Dresden, Germany, 7-10 October 2012. [Poster]

25. **B. Heyde**, D. Barbosa, P. Claus, F. Maes, and J. D'hooge. Influence of the grid topology of free-form deformation models on the performance of 3D strain estimation in echocardiography. In *FIMH - Functional Imaging and Modeling of the Heart*, volume LNCS 7945, pages 308–315, London, UK, 20-22 June 2013. [Talk]

26. D. Barbosa, **B. Heyde**, T. Dietenbeck, D. Friboulet, J. D'hooge, and O. Bernard. Fast left ventricle tracking in 3D echocardiographic data using anatomical affine optical flow. In *FIMH - Functional Imaging and Modeling of the Heart*, volume LNCS 7945, pages 191–199, London, UK, 20-22 June 2013. [Talk]

27. P. Morais, **B. Heyde**, D. Barbosa, S. Queirós, P. Claus, and J. D'hooge. Cardiac motion and deformation estimation from tagged MRI sequences using a temporal coherent image registration framework. In *FIMH -*

Functional Imaging and Modeling of the Heart, volume LNCS 7945, pages 316–324, London, UK, 20-22 June 2013. [Poster]

28. S. Queirós, D. Barbosa, **B. Heyde**, P. Morais, D. Friboulet, P. Claus, O. Bernard, and J. D'hooge. A fast fully automatic segmentation of the myocardium in 2D MR images. In *FIMH - Functional Imaging and Modeling of the Heart*, volume LNCS 7945, pages 71–79, London, UK, 20-22 June 2013. [Poster]

29. **B. Heyde**, D. Barbosa, A. Daraban, R. Jasaityte, P. Claus, F. Maes, and J. D'hooge. An automated pipeline for regional strain estimation from volumetric ultrasound data. In *IEEE Int Ultrasonics Symposium*, Prague, Czech Republic, 21-25 July 2013. [Talk, In press]

30. H. Gao, **B. Heyde**, and J. D'hooge. 3D intracardiac flow estimation using speckle tracking: a feasibility study in synthetic ultrasound data. In *IEEE Int Ultrasonics Symposium*, Prague, Czech Republic, 21-25 July 2013. [Talk, In press]

31. D. Barbosa, O. Bernard, **B. Heyde**, T. Dietenbeck, D. Friboulet, and J. D'hooge. Hybrid energy approach for real-time B-spline explicit active tracking of surfaces (heartBEATS). In *IEEE Int Ultrasonics Symposium*, Prague, Czech Republic, 21-25 July 2013. [Talk, In press]

32. D. Barbosa, O. Bernard, **B. Heyde**, T. Dietenbeck, D. Friboulet, and J. D'hooge. Towards online real-time strain estimation: feasibility study and initial clinical validation. In *IEEE Int Ultrasonics Symposium*, Prague, Czech Republic, 21-25 July 2013. [Poster, In press]

33. M. Larsson, P. Verbrugghe, M. Smoljkić, **B. Heyde**, N. Famaey, P. Herijgers, and J. D'hooge. Assessment of longitudinal strain in the carotid artery wall using ultrasound-based speckle tracking - validation in a sheep model. In *IEEE Int Ultrasonics Symposium*, Prague, Czech Republic, 21-25 July 2013. [Talk, In press]

34. E. Widman, K. Caidahl, J. D'hooge, **B. Heyde**, and M. Larsson. Speckle tracking strain estimation of a carotid artery plague phantom - validation via sonomicrometry. In *IEEE Int Ultrasonics Symposium*, Prague, Czech Republic, 21-25 July 2013. [Talk, In press]

International Conference: Abstract or Not Published

35. M. Larsson, F. Kremer, **B. Heyde**, L. Brodin, and J. D'hooge. 3D Strain imaging of the arterial wall: An experimental validation study

of an ultrasound-based speckle tracking algorithm. In *Biomechanics in vascular biology and cardiovascular disease*, Rotterdam, The Netherlands, 14-15 April 2011. [Talk]

36. R. Jasaityte, **B. Heyde**, D. Barbosa, D. Loeckx, P. Claus, and J. D'hooge. Echocardiographic differentiation of hypo-perfused from normally perfused segments: comparison of a 3D strain imaging with 2D speckle tracking. In *European Society of Cardiology*, Paris, France, 27-31 August 2011. [Poster]

37. V. Ferferieva, P. Claus, **B. Heyde**, F. Rademakers, and J. D'hooge. Early left ventricular remodeling in a rat model of chronic myocardial infarction. In *EuroEcho*, Budapest, Hungary, 7-10 December 2011. [Poster]

38. S. Bouchez, **B. Heyde**, M. Vandenheuvel, Y. Wang, H. Houle, J. D'hooge, and P. Wouters. In-vivo validation of a new 3D myocardial strain estimation tool. In *American Society of Echocardiography*, National Harbor, MD, USA, 25-29 August 2012. [Poster]

39. R. Jasaityte, **B. Heyde**, F. Rademakers, P. Claus, and J. D'hooge. Longitudinal and circumferential stretch-strain relationship can be obtained by 2D speckle tracking. In *EuroEcho*, Istanbul, Turkey, 11-14 December 2013. [Poster]

National or International Contributions (Invited Talks)

40. **B. Heyde**. Validating 3D motion and strain estimation in LV phantoms. In *Leuven symposium on myocardial velocity and deformation imaging*, Leuven, Belgium, 10-11 February 2011. [Talk]

41. **B. Heyde**. Experimental validation of different 3D strain methods against sonomicrometry. In *EuroEcho*, Budapest, Hungary, 7-10 December 2011. [Talk]

42. **B. Heyde**. A new method for improved myocardial deformation assessment. In *Leuven symposium on myocardial velocity and deformation imaging*, Leuven, Belgium, 9-10 February 2012. [Talk]

43. **B. Heyde**. Speckle tracking versus elastic registration for cardiac motion estimation: a direct comparison in-vivo. In *Bi-annual meeting of the Dutch society on ultrasound in medicine and biology*, Leuven, Belgium, 18 April 2012. [Talk]

44. **B. Heyde**. Comparison of different methodologies for 3D echocardiographic strain estimation. In *Leuven symposium on myocardial velocity and deformation imaging*, Leuven, Belgium, 7-8 February 2013. [Talk]

45. **B. Heyde**. Estimating regional cardiac function using 3D ultrasound imaging. In *Invited talk Department of Medical Engineering, Royal Institute of Technology, KTH*, Stockholm, Sweden, 19 April 2013. [Talk]

46. **B. Heyde**. Imaging myocardial mechanics by 3-D strain imaging-ready for clinical use? In *American society of echocardiography, 24th annual scientific sessions*, Minneapolis, MN, USA, 30 June 2013. [Talk]

47. **B. Heyde**. Registration-based motion estimation In *USART Training Course*, Leuven, Belgium, 5-6 December 2013. [Talk]

Internal Report and Seminars

48. **B. Heyde**. Recent developments in cardiac deformation imaging. In *Seminars - KU Leuven*, Leuven, Belgium, 1 July 2010. [Talk]

49. **B. Heyde**. Myocardial motion and strain estimation for the assess-ment of regional cardiac function using echocardiography. In *Research seminar - KU Leuven*, Leuven, Belgium, 7 September 2011. [Talk]

Theses

50. **B. Heyde**, C. Camerlinck, K. Schellinck, M. Vandenhaute, and G. Schoukens. Recycling polymers - current practices for PET reuse. Bachelor's thesis, University of Ghent, June 2007.

51. **B. Heyde**, N. Christiaen, and M. De Beule. Development of a validated finite element model for a polypropylene ankle-foot orthosis. Master's thesis, University of Ghent, June 2009.

DEPARTMENT OF CARDIOVASCULAR SCIENCES
CARDIOVASCULAR IMAGING AND DYNAMICS
Herestraat 49 box 7003
3000 Leuven, Belgium
brecht.heyde@med.kuleuven.be